

Université du Québec  
Institut National de la Recherche Scientifique  
Centre Énergie Matériaux Télécommunications

# **Study of (Co,Ni)O coated Cu-Ni-Fe anodes for Al electrolysis**

by

**Saeed Mohammadkhani**

A thesis submitted for the achievement of the  
degree of *Philosophiae doctor* (Ph.D.) in Energy and Materials Science  
December 2021

## **Jury Members**

President of the jury and internal examiner: Prof. Ana Tavares (INRS-EMT)

External examiner: Prof. Houshang Darvishi-Alamdari (Université de Laval)

External examiner: Prof. Gervais Soucy (Université de Sherbrooke)

Director of research: Prof. Daniel Guay (INRS-EMT)

Codirector of research: Prof. Lionel Roué (INRS-EMT)



## Abstract

The substitution of consumable carbon anodes emitting CO<sub>2</sub> with inert O<sub>2</sub>-evolving anodes for the primary production of aluminum would reduce considerably the emissions of carbon dioxide and perfluorocarbons from this industry. However, the design of inert anodes is a major challenge because of the severe Al electrolysis conditions that require materials with excellent resistance to corrosion and thermal shock, as well as adequate electrochemical properties and low dissolution in molten cryolite. Based on previous works carried out in our laboratory, single phase Cu<sub>65</sub>Ni<sub>20</sub>Fe<sub>15</sub> (wt%) alloy, is a promising material for inert anodes due to its ability to form a protective NiFe<sub>2</sub>O<sub>4</sub> layer upon Al electrolysis. However, this protective layer needs time to form at the surface of Cu-Ni-Fe alloys, during which fluorination can occur, causing premature degradation of the electrode.

In this thesis, first the possibility of producing single phase (Co,Ni)O powders with various Co/Ni ratios that could be used as raw materials for thermal spraying of protective coatings onto Cu-Ni-Fe anodes was evaluated. Two synthesis methods, namely mechanical alloying and calcination, which are both low-cost and easily scalable processes, were evaluated. The crystalline structure, thermal stability and powder morphology of the produced (Co,Ni)O powders were characterized. It was shown that prolonged high energy ball-milling led to significant contamination of the produced solid solutions due to the erosion of the WC milling tools. In contrast, pure (Co,Ni)O solid solutions is formed over the whole composition range using Co<sub>3</sub>O<sub>4</sub> and NiO powders as raw materials through a heat treatment process. Thermogravimetric analyzes (TGA) results revealed that at 1000 °C, Co<sub>x</sub>Ni<sub>1-x</sub>O solid solutions are stable over the whole composition range. In contrast, at 800 and 700 °C, Co<sub>x</sub>Ni<sub>1-x</sub>O are only stable for  $x \leq 0.54$  and  $x \leq 0.78$ , respectively. For a higher Co content, the formation of Co<sub>3</sub>O<sub>4</sub> was observed.

Then, a novel approach in the preparation of thick, dense, uniform and single phase (Co,Ni)O coatings using thermal spray techniques including suspension plasma spray (SPS) and high velocity oxygen fuel (HVOF) was investigated. In this context, (Co,Ni)O powders in large quantity (more than 1 kg per batch) with required particle sizes were prepared as raw materials for SPS and HVOF. The effects of spraying parameters on the composition and structure of the coatings were studied. Using the optimized spray conditions, coatings with more than 100 μm thickness were obtained by both SPS and HVOF. Coatings prepared with HVOF were single phase

while in coatings deposited with SPS, undesired reduction of NiO to Ni was observed. Then, the behaviour at 1000 °C of the coating/substrate ensembles and the influence of the coating and substrate compositions on their behaviour was studied at 1000 °C in dry inert and oxidizing atmospheres. The results demonstrated that after 20 h of heat treatment in air, (Co,Ni)O coatings on Cu-rich substrates are sandwiched between a top CuO and a bottom Cu<sub>2</sub>O layer. However, increasing the nickel content of the (Co,Ni)O coating decreases the Cu and O diffusivity, which results in thinner CuO, Cu<sub>2</sub>O and bottom oxide scale. In the case of Ni-rich Cu-Ni-Fe alloy, Cu diffusion to react with O and form CuO and Cu<sub>2</sub>O is less of an issue because the diffusion of Cu atoms in Ni-rich Cu-Ni-Fe alloys is considerably slowed down. In that case, a nickel ferrite scale is formed between the HVOF coating and the substrate. The thickness of the NiFe<sub>2</sub>O<sub>4</sub> layer decreases slightly (~ 15%) as the Ni content of the (Co,Ni)O coating is increased. Finally, the solubility of Co and Ni from Co<sub>x</sub>Ni<sub>1-x</sub>O materials in molten KF and NaF-based electrolytes was measured at 700 and 1000 °C and the use of metallic Cu-Ni-Fe anodes protected by single phase Co<sub>x</sub>Ni<sub>1-x</sub>O coatings for the primary production of aluminum was studied. It was shown that all compositions of (Co,Ni)O have very low solubility in sodium and potassium-based electrolyte and the total cobalt and nickel contaminations from (Co,Ni)O solid solutions in molten cryolites were less than 70 ppm. The electrolysis results at 1000 °C revealed that HVOF (Co,Ni)O coating layer increases the corrosion resistance of Cu-Ni-Fe anode and it is effective in providing required time for the formation of nickel ferrite layer as well as in preventing Cu-Ni-Fe alloy from fluorination.

*Keywords:* (Co,Ni)O solid solution, mechanical alloying, thermal stability, suspension plasma spray, high velocity oxygen fuel, high-temperature oxidation, inert anode, Al electrolysis.

## Résumé

La substitution des anodes de carbone consommables, émettant du CO<sub>2</sub>, par des anodes inertes, émettant de l'O<sub>2</sub>, pour la production primaire d'aluminium réduirait considérablement les émissions de dioxyde de carbone et de perfluorocarbures issu de cette industrie. Cependant, la conception d'anodes inertes est un défi majeur en raison des conditions sévères d'électrolyse d'aluminium qui nécessitent des matériaux présentant une excellente résistance à la corrosion et aux chocs thermiques, ainsi que des propriétés électrochimiques adéquates et une faible dissolution dans la cryolithe fondue. Sur la base de travaux antérieurs réalisés dans notre laboratoire, l'alliage monophasé Cu<sub>65</sub>Ni<sub>20</sub>Fe<sub>15</sub> (en %pds) est avancé comme un matériau prometteur pour les anodes inertes en raison de sa capacité à former une couche protectrice NiFe<sub>2</sub>O<sub>4</sub> lors de l'électrolyse de l'aluminium. Cependant, cette couche protectrice a besoin de temps pour se former à la surface des alliages Cu-Ni-Fe, au cours de laquelle une fluoration peut se produire, provoquant une dégradation prématurée de l'électrode.

Dans cette thèse, la possibilité de produire des poudres monophasées (Co,Ni)O avec différents rapports Co/Ni pouvant être utilisées comme matières premières pour la projection thermique de revêtements protecteurs sur des anodes Cu-Ni-Fe, a été évaluée. Deux méthodes de synthèse, à savoir le broyage mécanique à haute énergie et la calcination, qui sont à la fois des procédés peu coûteux et facilement évolutifs, ont été évaluées. La structure cristalline, la stabilité thermique et la morphologie des poudres de (Co, Ni)O produites ont été caractérisées. Il a été montré qu'un broyage prolongé à haute énergie entraînait une contamination importante des solutions solides produites en raison de l'érosion des outils de broyage constitués de WC. En revanche, des solutions solides pures de (Co, Ni) O sont formées sur toute la plage de composition en utilisant des poudres de Co<sub>3</sub>O<sub>4</sub> et NiO comme matières premières grâce à un processus de traitement thermique. Les résultats des analyses thermogravimétriques (TGA) ont révélé qu'à 1000 °C, les solutions solides de Co<sub>x</sub>Ni<sub>1-x</sub>O sont stables sur toute la plage de composition. En revanche, à 800 et 700 °C, les Co<sub>x</sub>Ni<sub>1-x</sub>O ne sont stables que pour x = 0,54 et x = 0,78, respectivement. Pour une teneur en Co plus élevée, la formation de Co<sub>3</sub>O<sub>4</sub> a été observée.

Par la suite, une nouvelle approche de préparation de revêtements (Co,Ni)O épais, denses, uniformes et monophasés à l'aide de deux techniques de pulvérisation thermique, soient la projection HVOF (High Velocity Oxy-Fuel) et la projection SPS (suspension plasma spray), a été

étudiée. Dans ce contexte, des poudres de (Co,Ni)O en grande quantité avec les granulométries requises ont été préparées comme matière première pour SPS et HVOF. Les effets des paramètres de pulvérisation sur la composition et la structure des revêtements ont été investigués. En utilisant les conditions de pulvérisation optimisées, des revêtements de plus de 100  $\mu\text{m}$  d'épaisseur ont été obtenus à la fois par SPS et HVOF. Les revêtements préparés par HVOF étaient monophasiques, tandis que dans les revêtements déposés par SPS, une réduction indésirable de NiO en Ni a été observée. Subséquemment, une étude du comportement à 1000 °C sous atmosphère sèche inerte et oxydante de l'ensemble des revêtements/substrats ainsi que l'analyse de l'influence de leur composition sur leur comportement ont été effectuées. Les résultats ont démontré qu'après 20 h de traitement thermique sous air, les revêtements (Co,Ni)O sur des substrats riches en Cu sont pris en sandwich entre une couche supérieure de CuO et une couche inférieure de Cu<sub>2</sub>O. Cependant, l'augmentation de la teneur en nickel du revêtement (Co,Ni)O diminue la diffusivité du Cu et de l'O, ce qui entraîne des écailles de CuO, Cu<sub>2</sub>O et d'oxyde du fond plus fine. Dans le cas des alliages Cu-Ni-Fe riches en Ni, la diffusion de Cu pour réagir avec O et former CuO et Cu<sub>2</sub>O est moins problématique car la diffusion des atomes de Cu dans les alliages Cu-Ni-Fe riches en Ni est considérablement ralentie. Dans ce cas, une calamine en ferrite de nickel se forme entre le revêtement obtenu par HVOF et le substrat. L'épaisseur de la couche de NiFe<sub>2</sub>O<sub>4</sub> diminue légèrement (~ 15%) à mesure que la teneur en Ni du revêtement (Co,Ni)O augmente. Enfin, la solubilité du Co et du Ni des matériaux Co<sub>x</sub>Ni<sub>1-x</sub>O dans les électrolytes fondus à base de KF et de NaF a été mesurée à 700 et 1000 °C et l'utilisation d'anodes métalliques Cu-Ni-Fe protégées par des revêtements monophasés Co<sub>x</sub>Ni<sub>1-x</sub>O pour la production primaire d'aluminium a été étudiée. Il a été montré que toutes les compositions de (Co,Ni)O ont une très faible solubilité dans les électrolytes à base de sodium et de potassium et que les contaminations totales en cobalt et nickel des solutions solides de (Co,Ni)O dans les cryolites fondues étaient inférieures à 70 ppm. Les résultats de l'électrolyse à 1000 °C ont révélé que la couche de revêtement par HVOF de (Co,Ni)O augmente la résistance à la corrosion de l'anode Cu-Ni-Fe et qu'elle est efficace pour fournir le temps requis pour la formation de la couche de ferrite de nickel ainsi que pour empêcher la formation d'alliage de Cu-Ni-Fe issu de la fluoration.

*Mots-clés : solution solide de (Co,Ni)O, mécano-alliage, stabilité thermique, pulvérisation plasma en suspension, oxygène combustible à grande vitesse, oxydation à haute température, anode inerte, électrolyse d'aluminium.*

## Acknowledgement

This thesis represents an important part of my life which would have never been possible without precious help of all the people who have supported and encouraged me. It is difficult, if not impossible, to express in just a few lines the immense gratitude I feel towards the many people who have helped or accompanied me during my PhD study.

First, I would like to express my sincere gratitude to my supervisor, Professor Daniel Guay for giving me the chance to work on this project and for his great expertise, immense knowledge, and patience. His advice on both research and my career has been invaluable. I would like to also thank my co-supervisor, Professor Lionel Roué for his generosity, availability, kindness, and supervision. This work would not be possible without wise advice, continued support, and positivity of my supervisors. Their guidance helped me throughout the research and writing of this thesis. I am extremely grateful for their unconditional support and for helping me find the right direction both in my academic research and my new life in Canada.

I want to acknowledge to Christophe Chabanier and Catalin Harnagea for their training and continued help with the characterization devices. A huge thank to Julie Gaudet for her enthusiasm and her presence in our laboratories to ensure the routine and the safe operation of the laboratories.

A significant part of this thesis was carried out at “Thermal spray and multiphase flow laboratories” at Concordia university. I would like to thank Professor Christian Moreau and Professor Ali Dolatabadi for welcoming me in their laboratory. Their knowledge and expertise allowed me to understand better the complex mechanisms in thermal spray techniques. Many thanks to Fadhel, research associate, Vahid and Alexandre, PhD students, at Professor Moreau’s group for their friendly and positive attitude.

Special thanks to two postdocs I have worked with at INRS, Emanuel and Etienne for their countless help and practical advice. Also, I would like to express my gratitude to my friends and colleagues at INRS, Mohamed, Sylvain, Quentin, Victor, Lucas, Alexandre, Youling and Samuel, for your good humor in the office and in the laboratory as well as for the good memories on the soccer field or on the foosball table.

I thank particularly my parents who always encouraged me. They have always been role models for me and have taught me never to give up no matter what, because the best is yet to come.

Finally, all my gratitude goes to the woman of my life, my dear Ellie, who accompanied me to live on the other side of the world, far from our families and friends. Thank you for believing in me, for your support and your presence, words cannot express how grateful I am to you.

# Contents

<b>Abstract</b>	<b>i</b>
<b>Résumé</b>	<b>iii</b>
<b>Acknowledgement</b>	<b>v</b>
<b>List of Figures</b>	<b>ix</b>
<b>List of tables</b>	<b>xi</b>
<b>Introduction</b>	<b>1</b>
<b>I. Chapter 1: Literature review</b>	<b>3</b>
<b>I.1. Aluminum</b>	<b>4</b>
I.1.1. General information on aluminum production	4
I.1.2. Current aluminum production and the Hall-Héroult process	5
I.1.3. Environmental issues of current aluminum production	9
<b>I.2. Inert anodes</b>	<b>10</b>
I.2.1. Environmental impacts related to the implantation of inert anodes	11
I.2.2. Selection criteria for inert anode materials	13
I.2.3. Electrolysis and configuration of electrolysis cell	16
<b>I.3. Cu-Ni-Fe anodes</b>	<b>18</b>
I.3.1. Production of Cu-Ni-Fe alloy	18
I.3.2. Anodic behaviour of Cu-Ni-Fe alloys	20
I.3.3. Problematic with Cu-Ni-Fe anodes	24
<b>I.4. (Co,Ni)O synthesis and coating inert anodes</b>	<b>26</b>
I.4.1. CoO-NiO phase diagram and high-temperature behaviour	27
I.4.2. Physical and chemical properties of CoO, NiO and (Co,Ni)O	30
I.4.3. Synthesis by mechanical alloying	35
I.4.4. Principles of mechanical alloying	36
I.4.5. Mechano-synthesis of oxide solid solution	38
I.4.6. Ball-milling parameters	39
I.4.7. Synthesis by calcination	43
<b>I.5. Thermal spray techniques</b>	<b>44</b>
I.5.1. Suspension Plasma Spray (SPS)	46
I.5.2. Spray parameters in SPS	48
I.5.3. High Velocity Oxygen Fuel (HVOF)	51
I.5.4. Particle temperature and velocity in HVOF	52
I.5.5. Fuel/oxygen (F/A) ratio	52
<b>References</b>	<b>53</b>
<b>II. Chapter 2: Experimental details and characterisation methods</b>	<b>63</b>
<b>II.1. Powder synthesis</b>	<b>64</b>
<b>II.2. Thermal spray</b>	<b>65</b>
II.2.1. Suspension plasma spray	65
II.2.2. High velocity oxygen fuel	66
<b>II.3. Characterization techniques</b>	<b>67</b>
II.3.1. X-ray diffraction (XRD)	67
II.3.2. Rietveld refinement analysis	69
II.3.3. Calculation of lattice parameter and composition of solid solution	69
II.3.4. Scanning electron microscopy (SEM) equipped with EDS	70

II.3.5.	Thermogravimetric analysis (TGA)	72
II.3.6.	Inductively coupled plasma atomic emission spectroscopy	73
II.3.7.	Particle size distribution measurement (PSD)	73
<b>II.4.</b>	<b>High temperature dry oxidation tests of coated anodes</b>	<b>74</b>
<b>II.5.</b>	<b>Aluminum electrolysis</b>	<b>75</b>
II.5.1.	Electrolysis cell	75
II.5.2.	Chronoamperometry	76
<b>References</b>		<b>78</b>
<b>III.</b>	<b>Chapter 3: Articles and unpublished results</b>	<b>79</b>
III.1.	A summary of article 1	80
III.2.	A summary of article 2	81
III.3.	A summary of article 3	83
III.4.	Article 1: Synthesis and thermal stability of (Co,Ni)O solid solutions	84
III.5.	Article 2: Suspension plasma spray deposition of $\text{Co}_x\text{Ni}_{1-x}\text{O}$ coatings	100
III.6.	Article 3: High-temperature behaviour of HVOF (Co,Ni)O coated Cu-Ni-Fe anodes	124
III.7.	Solubility in molten cryolite and anodic behaviour of (Co,Ni)O coated Cu-Ni-Fe electrodes	153
	<b>General conclusions and perspective</b>	<b>169</b>
	<b>Étude d'anodes Cu-Ni-Fe revêtues de (Co,Ni)O pour l'électrolyse de l'aluminium</b>	<b>173</b>

## List of Figures

Figure I.1.	Schematic representation of industrial Hall- Héroult electrolysis cell.	5
Figure I.2.	Inert anode cell voltage and power distribution for a Hall-Héroult cell at 960 °C working at 95% CE, 4.20 V and 960 °C for (a) traditional carbon anodes and (b) inert anodes [8].	8
Figure I.3.	World average perfluorocarbon emissions from aluminum production, from 1990 to 2019 [14].	10
Figure I.4.	Phase diagram of (a) NaF-AlF <sub>3</sub> [27] and (b) KF-AlF <sub>3</sub> [28] systems.	16
Figure I.5.	Ternary diagram of the NiO – CoO – ½ O <sub>2</sub> system in air [58].	28
Figure I.6.	Temperature-composition diagram of NiO-CoO-O <sub>2</sub> system in air as a function of temperature [58].	28
Figure I.7.	Relationship between molar fractions of NiO and lattice parameters of NiO-CoO solid solutions prepared at (a) 1000 and (b) 1100 °C [62].	29
Figure I.8.	Relationship between molar fractions of Ni <sub>3</sub> O <sub>4</sub> and lattice parameters of Ni <sub>3</sub> O <sub>4</sub> - Co <sub>3</sub> O <sub>4</sub> solid solutions prepared at 600 °C [62].	29
Figure I.9.	Electrical conductivity of NiO as a function of temperature in air [58].	31
Figure I.10.	Electrical conductivity of (1) CoO, (2) Co <sub>0.9</sub> Ni <sub>0.1</sub> O, (3) Co <sub>0.667</sub> Ni <sub>0.333</sub> O and (4) Co <sub>0.5</sub> Ni <sub>0.5</sub> O as a function of temperature in air [58].	31
Figure I.11.	Calculated oxygen potential phase diagram of Co-O system [63].	32
Figure I.12.	Oxygen potential phase diagram of Ni-O system [64].	32
Figure I.13.	Oxygen over-potentials of (Co,Ni)O and Co <sub>3</sub> O <sub>4</sub> coatings measured at 930 °C in molten cryolite [57].	33

Figure I.14. Oxygen over-potentials of (1) $\text{Co}_{0.85}\text{Ni}_{0.15}\text{O}$ coating, (2) $\text{NiFe}_2\text{O}_4$ coating on metallic anode and (3) carbon anode measured at 930 °C in molten cryolite [57].	34
Figure I.15. Schematic of different stages of the mechanical alloying leading to the formation of an alloy.	36
Figure I.16. (a) SPEX 8000 mill and (b) 2D representation of the crucible movement.	40
Figure I.17. (a) Union process, model S-1 Laboratory attritor and (b) schematic of the interior of the crucible.	40
Figure I.18. Schematic representation of a thermal plasma spraying process.	44
Figure I.19. Schematic presentation of the combination of process temperature and velocity for the different spray processes [99].	45
Figure I.20. Different spray parameters in thermal spray processes [47].	46
Figure I.21. Schematic side view of an axial feed system in DC plasma torches [100].	47
Figure I.22. Gas composition and plasma power effects on (a) particle velocity and (b) particle temperature, redrawn from [102].	49
Figure I.23. Variation of gas temperature as a function of richness ratio [112].	53
Figure II.1. Suspension plasma spray with a Mettech's Axial III gun.	66
Figure II.2. Diamond Jet 2700-hybrid HVOF gun with a convergent-divergent nozzle from Oerlikon Metco.	67
Figure II.3. Bruker D8 X-ray diffractometer used in this thesis.	68
Figure II.4. Different interactions between an electron and an atom producing (a) a secondary electron, (b) a backscattered electron and (c) a characteristic x-ray.	71
Figure II.5. Tescan Vega3 scanning electron microscope equipped with a Bruker XFlash® 6   10 Detector energy dispersive X-ray spectroscopy (EDX) used in this thesis.	72

Figure II.6.	Muffle and tubular furnaces used in this thesis.	75
Figure II.7.	Schematic illustration of aluminum electrolysis cell.	77
Figure II.8.	Schematic illustration of an anode before the electrolysis	77
Figure II.9.	Aluminum electrolysis cell and an anode before the electrolysis.	78

## List of tables

Table I.1.	CO <sub>2</sub> equivalent emissions from the various processes involved in the production of aluminum depending on the means of electricity production, reported by [8].	12
Table I.2.	Performance Targets for Inert Anodes.	14
Table II.1.	Characteristics of powders used for (Co,Ni)O synthesis.	64

## Introduction

Aluminum is the second most widely used metal in the world. However, primary Al production by electrolysis is still carried out using the Hall-Héroult process which results in heavy CO<sub>2</sub> emissions. The substitution of consumable carbon anodes emitting CO<sub>2</sub> with inert O<sub>2</sub>-evolving anodes for the primary production of aluminum would reduce considerably the emissions of carbon dioxide and perfluorocarbons from this industry. This substitution would eliminate about 6 Mt of CO<sub>2</sub> eq produced annually by Canadian aluminum smelters, which is equivalent to the amount of CO<sub>2</sub> generated annually by about 2 million cars. However, the design of inert anodes is a major challenge because of the severe Al electrolysis conditions that require materials with excellent resistance to corrosion and thermal shock, as well as adequate electrochemical properties. Among the numerous materials studied so far, Cu-Ni-Fe-based alloys appear to be promising, due to their ability to produce a protective nickel ferrite (NiFe<sub>2</sub>O<sub>4</sub>) in low-temperature (700 °C) potassium-based cryolite. However, this protective layer needs time to form at the surface of Cu-Ni-Fe alloys, during which fluorination can occur, causing premature degradation of the electrode.

In this context, the use of (Co,Ni)O protective coatings for metallic anode appears promising. In fact, CoO can work as a barrier for the fluorination of Ni-Fe alloys and the transformation of CoO to CoF<sub>2</sub> occurs only at very low oxygen pressure in cryolite medium and adding Ni atoms to CoO and forming (Co,Ni)O solid solutions helps in preventing the undesired decomposition of CoO to Co<sub>3</sub>O<sub>4</sub> at elevated temperatures. Coating Cu-Ni-Fe alloys with a single phase, dense and crack-free (Co,Ni)O protective coating, using conventional methods such as electrodeposition of metallic Co-Ni alloy followed by an oxidation step, is very difficult, since cracks are formed in the coating layer due to the change of densities upon oxidation of the metallic Co-Ni alloy. However, in thermal spraying techniques (high velocity oxygen fuel (HVOF) and suspension plasma spray (SPS)), thick coatings can be obtained in a single step with a relatively high efficiency.

Thus, in this thesis the following main objectives were investigated:

- Optimize the synthesis conditions to produce single phase Co<sub>x</sub>Ni<sub>1-x</sub>O solid solutions with a scalable, cost and time efficient process.

- Investigate thermal stability and dissolution rate in molten cryolite of (Co,Ni)O materials at elevated temperatures.
- Optimize SPS and HVOF spray parameters in order to obtain dense, uniform and single phase (Co,Ni)O coatings on Cu-Ni-Fe anodes.
- Study the dry oxidation behavior at high temperature of Cu-Ni-Fe alloys coated with  $\text{Co}_x\text{Ni}_{1-x}\text{O}$  solid solutions.
- Study the anodic behaviour of coated Cu-Ni-Fe alloys during the aluminum electrolysis conditions and characterize the oxide layers formed on the surface of the anodes to evaluate the impact of coating layer on the corrosion resistance of the alloy.

This thesis consists of three chapters. The first chapter is a bibliographical review of the current aluminum production process as well as the potential impacts and challenges of replacing carbon anodes with inert anodes. Then, Cu-Ni-Fe and Co-Ni-O systems as well as synthesis and coating procedures are introduced. In the second chapter, the different experimental and characterization procedures used in this thesis are presented. Finally, the third chapter presents the experimental obtained results and published articles.

**I. Chapter 1**

**Literature review**

## I.1. Aluminum

Aluminum is the third most abundant element in the Earth's crust (8.1 wt%) after oxygen and silicon. Despite being the most present metal in the Earth's crust, aluminum was not discovered until 1808 by Humphry Davy. Because of its high chemical activity, aluminum can be found only in oxide or silicate forms in the nature and not in its metallic form. Bauxite is the main aluminum ore composed of aluminum oxide, silica, iron oxides and titanium dioxide. In 1845, a German chemist named Friedrich Wöhler succeeded to separate aluminum from oxygen and produce sufficient quantity of metallic aluminum to study its properties. During the 19<sup>th</sup> century, the price of aluminum was even higher than that of gold, since it was very difficult to refine, and its usage remained uncommon. In 1886, an American engineer Charles Martin Hall and a French engineer Paul Héroult, discovered independently and simultaneously that it is possible to produce pure metallic aluminum by performing electrolysis on the dissolved aluminum oxide in molten cryolite ( $\text{Na}_3\text{AlF}_6$ ). The process that is called "Hall-Héroult process" lowered the aluminum production cost, made aluminum much more available to the public and led to extensive use of aluminum in different industries. Current aluminum production is still carried out by extracting bauxite and its conversion to alumina using the Bayer process followed by electrolytic aluminum production using the "Hall-Héroult" process.

### I.1.1. General information on aluminum production

Aluminum is the second most widely used metal in the world (after iron) due to its excellent properties such as light weight, good electrical and thermal conductivity, oxidation resistance, ductility and recyclability. Although the mechanical strength of metallic aluminum is very low, some aluminum alloys have even better mechanical properties than steel alloys. Aluminum is widely used in household equipment, building, chemical and pharmaceutical industries, automotive and aerospace industries, electronics, etc.

China is the main aluminum producer in the world with more than half of the total aluminum production followed by Russia (6.0%), Canada (5.3%) and India (5.3%). 9 out of 10 Canadian aluminum smelters are located in Quebec which makes it the major aluminum producer

in Canada [1]. The annual global aluminum production is expected to increase from 63 million tonnes in 2017 to more than 100 million tonnes in 2050 [2].

### I.1.2. Current aluminum production and the Hall-Héroult process

As mentioned above, industrial production of primary aluminum from alumina ore ( $\text{Al}_2\text{O}_3$ ) is still carried out in alumina reduction cells working by the Hall- Héroult process. In this process, alumina is dissolved in an electrolyte consisting mainly of liquid cryolite ( $\text{Na}_3\text{AlF}_6$ ) at 950-1000 °C. The application of a current between two carbon electrodes allows the reduction of dissolved  $\text{Al}^{3+}$  ions to metallic aluminum at the cathode. Since the density of aluminum is higher than that of electrolyte, it deposits at the bottom of cell forming a bath of liquid aluminum. At the same time, oxygen anions react with the carbon anode and produce carbon dioxide. The carbon anode is thus consumed which necessitates its regular replacement (every 25 days approximately) and generates a significant amount of  $\text{CO}_2$  according to the overall following reaction:



Canadian aluminum smelters produce annually more than 6 Mt of  $\text{CO}_2$  (reported in 2014), which is equivalent to the pollution generated annually by 2 million cars.

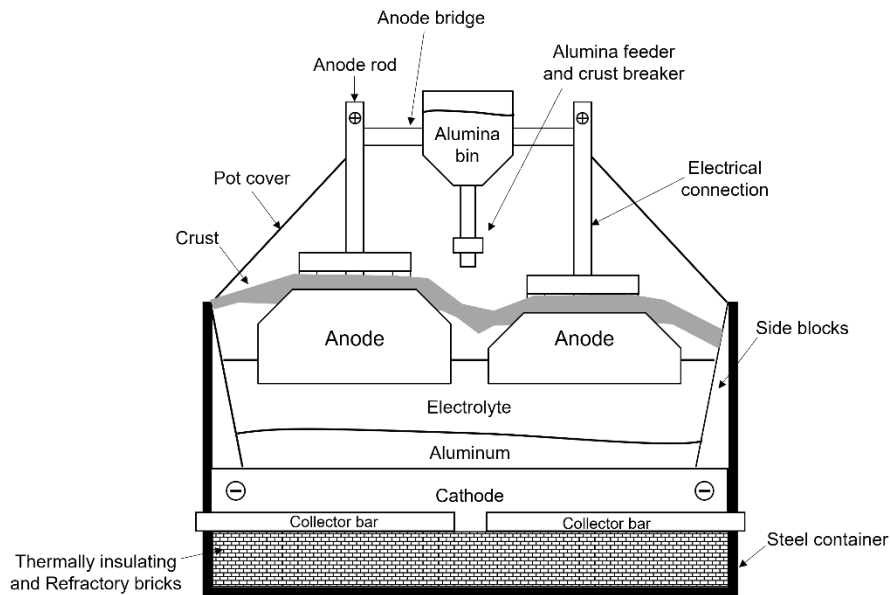


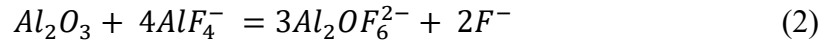
**Figure I.1. Schematic representation of an industrial Hall- Héroult aluminum electrolysis cell.**

A schematic representation of an industrial aluminum electrolysis cell is illustrated in Fig. I.1. In aluminum electrolysis cells, carbon anodes are immersed in the electrolyte at a certain and consistent distance from the liquid aluminum on the carbon cathode. The carbon anodes are blocks of carbon made of petroleum coke and coal tar pitch that can be categorized into two groups, pre-baked and Søderberg anodes, based on their production procedures. In pre-baked anodes, the solid carbon block is produced by heating a mixture of petroleum coke with coal tar pitch that acts as a binder. A press or a vibro-compactor is used to give a parallelepiped shape to the paste prior to the baking process. A pre-baked pot is composed of several single anodes that are electrically connected to a rod. Pre-baked anodes stay in the electrolysis cell for a specific time, usually 25 to 30 days, then they are removed from the cell, before being completely consumed. Søderberg anodes contain more than 25 wt% of coal tar pitch compared to 13-18 wt% for prebaked anodes. Søderberg anodes are made in-situ and a Søderberg cell has only one big anode that is placed in a steel container in the shape of the anode. The paste of petroleum coke and coal tar pitch is introduced into this container from the top and while moving toward the bottom, it bakes. The quality of Søderberg anode is therefore lower than that of pre-baked anode which results in a lower energy efficiency and higher cell voltage. Although using pre-baked anode requires periodic shutdowns for the anode replacement, more than 80% of aluminum plants in the world operate with pre-baked anodes because of their lower carbon consumption, higher aluminum quality and higher energy efficiency.

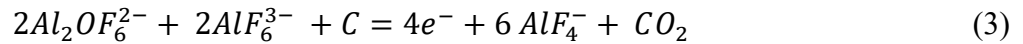
The cathode in aluminum smelter consists of carbon blocks, made by anthracite and graphite or semi-graphitized carbon, located at the bottom of the cell underneath a metal pool as shown in Fig. I.1. The electrolysis is performed at 950 to 980 °C and at an anode current density of about 0.8 A.cm<sup>-2</sup>. Since the aluminum cell works at a high temperature, on the top of carbon anodes, a crust is formed which is a protective layer made of mixed alumina and electrolyte residue. The formation of this crust is beneficial as it reduces heat loss and evaporation from the bath and avoids burning of anode to air. The dissolved alumina in the electrolyte is consumed to produce aluminum, hence, it is required to add alumina regularly to the bath. An alumina feeder, usually equipped with a crust breaker, is located above the crust. Liquid aluminum is regularly drained out of the cell.

The electrolyte in modern aluminum smelters consists of mainly cryolite ( $\text{Na}_3\text{AlF}_6$ ) with an excess of  $\text{AlF}_3$  and  $\text{Al}_2\text{O}_3$ . Other additives such as  $\text{CaF}_2$ ,  $\text{LiF}$  and  $\text{MgF}_2$  might be added to improve the properties of electrolyte such as reducing its melting temperature, increasing the faradic efficiency and increasing its electrical conductivity.

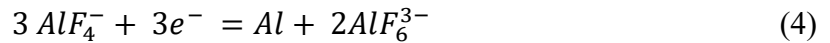
The reactions observed during electrolysis are more complex than the simplified overall reaction (1). First, alumina is dissolved in the cryolite bath to form  $\text{Al}_x\text{O}_y\text{F}_z$  ( $3x-2y-z$ ) type aluminum oxyfluorides according to the following reaction:



At the anode/bath interface, aluminum fluorides and oxyfluorides species react with the carbon anode and form carbon dioxide as described by the following reaction:



On the cathode side,  $\text{AlF}_4^-$  ions are reduced to form liquid aluminum which is deposited on the cathode with the following cathodic reaction:



The electrolyte composition can be measured with the cryolite ratio (CR) which is the molar ratio of  $\text{NaF}$  and  $\text{AlF}_3$ :

$$\text{CR} = \frac{[\text{NaF}]}{[\text{AlF}_3]} \quad (5)$$

The electrolyte properties such as its melting point, alumina solubility, electrical conductivity and its viscosity depend on cryolite ratio. A decrease in cryolite ratio results in lower melting point and higher faradic efficiency but lower alumina solubility and lower electrical conductivity as well [3,4]. The electrolyte composition can also be measured with the weight percentages of  $\text{NaF}$  and  $\text{AlF}_3$  which is called weight ratio:

$$\text{WR} = \frac{\text{mass of NaF}}{\text{mass of AlF}_3} \quad (6)$$

The cryolite ratio in industrial aluminum smelters is between 2.12 and 2.30 (i.e., 30 mol%  $\text{AlF}_3$ ) with an alumina concentration of up to 5 wt%. The alumina concentration is kept below its saturation (8 wt%) to increase the electrolysis efficiency. With this composition, the electrical conductivity of electrolyte is about  $2.2 \text{ S}\cdot\text{cm}^{-1}$ . In industrial cells for an anode current density of  $0.8 \text{ A}\cdot\text{cm}^{-2}$ , the anode overvoltage is usually about 400-500 mV. However, due to the formation of  $\text{CO}_2$  bubbles with a typical diameter of 2-10 mm at the anode surface, the active surface of the anode will be reduced resulting in an anode overpotential of 100-350 mV [4–6].

With all the technological improvements in the industrial aluminum electrolysis cells, the energy efficiency has increased approximately 75% and the required energy to produce one kilogram of aluminum has decreased to 13-15 kWh, with a world average of  $14.2 \text{ kWh}\cdot\text{kg}^{-1} \text{ Al}$  [7]. Haupin and Kvande [8,9] showed that at a faradic efficiency of 95% and a cell potential of 4.2 V, one kilogram of Al can be produced with 13.2 kWh, as shown in Fig. I.2.a.

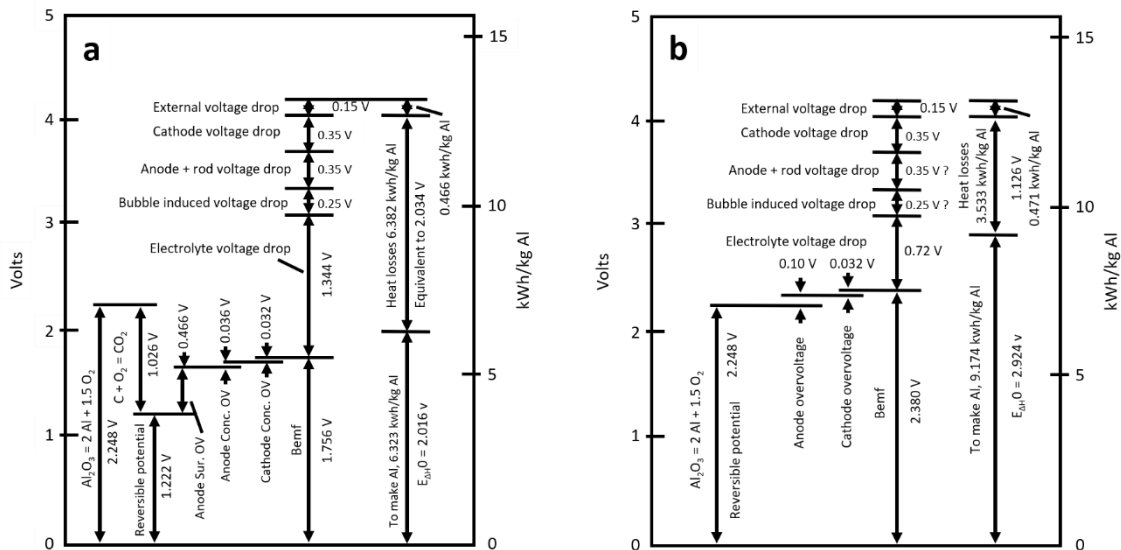


**Figure I.2. Inert anode cell voltage and power distribution for a Hall-Héroult cell at 960 °C working at 95% CE, 4.20 V and 960 °C for (a) traditional carbon anodes and (b) inert anodes [8].**

The cell potential of 4.2 V includes different overpotentials such as  $\sim 0.5 \text{ V}$  for anode overvoltage,  $\sim 0.03 \text{ V}$  for cathode overvoltage and  $\sim 1.2 \text{ V}$  for decomposition potential of alumina. Also, 1.3 V is included for voltage drop of electrolyte and 1.1 V for additional ohmic drop of other components (anode, cathode, external circuit). It must be noted that a significant amount of electrical energy is consumed to maintain the cell at the operating temperature. In fact, the

theoretical required energy for production of 1 kilogram of aluminum at 960 ° C is 6.32 kWh.kg<sup>-1</sup> Al. As shown in Fig. I.2.b, the potential of a cell equipped with inert anodes can be the same as that of a traditional cell by adjusting certain operational parameters, particularly the anode-to-cathode distance. In fact, the anode overvoltage for inert anode depends on the nature of the material from which it is made, on the nature of the electrolytic bath and on the temperature. The experimental measurements carried out for different types of inert anodes have shown that the overvoltage in inert anodes is much lower than in carbon anodes [10–12].

### I.1.3. Environmental issues of current aluminum production

As mentioned earlier, in current aluminum smelters, carbon anode is consumed in a reaction with oxygen. To produce 1 kg of Al, 0.46 kg of carbon is consumed and 1.5 kg of CO<sub>2</sub> is produced. Since electricity is supplied for Al production, the emitted CO<sub>2</sub> to generate electricity must be included in the total CO<sub>2</sub> emitted to produce one kilogram of aluminum. In countries such China and Australia where fossil fuels are the primary means of electricity generation, the overall average CO<sub>2</sub> emissions due to the electrolysis of aluminum was estimated at about 13 kg CO<sub>2</sub> / kg Al in 2015. In Quebec where hydroelectricity is used in aluminum smelters, the CO<sub>2</sub> emission in aluminum industries is about 2 kg CO<sub>2</sub> / kg Al in 2017 [13].

In addition to CO<sub>2</sub> emission, perfluorocarbons (PFCs) such as CF<sub>4</sub> and C<sub>2</sub>F<sub>6</sub> are emitted into the atmosphere during the primary aluminum production due to an undesired phenomenon known as “anode effect”. The anode effect happens when the alumina concentration in the bath decreases to less than 2 wt% which leads to an interruption in normal reactions that produce aluminum. Then, perfluorocarbons (CF<sub>4</sub> and C<sub>2</sub>F<sub>6</sub>) gases are formed through other electrochemical reactions. These gases produce bubbles on the anode surface, forming an insulation layer which is accompanied by a drastic increase in cell potential to 10 – 50 volts. To resolve the anode effect problem, the alumina concentration must be increased to its normal concentration as soon as possible and the gas layer formed on the anode surface must be removed. In modern aluminum smelters, when the anode effect is detected by computers, up and down movements of anode as well as an alumina overfeeding will be applied by the control system to return the cell to its normal conditions. Fortunately, over the past two decades with improvements in the aluminum pots and a

better control of anode effect phenomenon, the production of PFCs is considerably reduced from more than 5 kg CO<sub>2eq</sub> / kg Al to 0.57 kg CO<sub>2eq</sub> / kg Al as shown in Fig. I.3 [14].

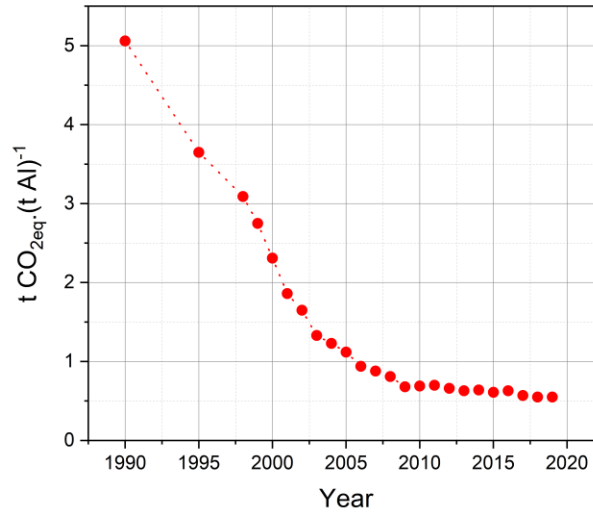


**Figure I.3. World average perfluorocarbon emissions from aluminum production, from 1990 to 2019 [14].**

## I.2. Inert anodes

Substitution of consumable carbon anodes with inert (O<sub>2</sub>-evolving) anodes in the electrochemical cells to produce aluminum has significant environmental benefits because it eliminates the emissions of carbon dioxide and perfluorocarbons associated with consumption of the carbon anode. Also, the periodic replacement of carbon anodes causes interruptions in aluminum production and risks to the safety of operators. By using non-consumable oxygen-evolving anodes, the overall reaction in alumina reduction cells will be:



which would reduce GHGs by 75 to 100% depending on the type of emissions (CO<sub>2</sub>, CF<sub>x</sub>, NO<sub>x</sub>, SO<sub>x</sub>, etc.). However, the design of inert anodes is a major challenge because of the severe Al electrolysis conditions which require materials with excellent resistance to corrosion and thermal shock as well as adequate electrochemical properties. In fact, the idea of replacing carbon anodes

with inert anodes has existed since the invention of the Hall-Héroult process. Hall noticed the consumption of graphite anode during aluminum electrolysis and investigated the possibility of its replacement with a metallic anode. However, after an intensive study on copper-based anodes, he gave up his idea due to inconclusive results.

Based on reaction (7), unlike carbon anodes, inert anodes are not involved in the reactions to produce aluminum, however, because of the severe aluminum electrolysis conditions, no material is completely inert in cryolithic medium. A possible material for an inert anode (ceramics, cermets or metallic alloys) must produce a protective oxide layer on its surface. Since oxides are also soluble in cryolite, although with a very low dissolution rate, oxide layers formed on the surface of anodes will be dissolved in cryolite which makes inert anodes to be more or less consumed. Therefore, numerous studies have been conducted to find a material with very low dissolution rate, high corrosion resistance and good electrical conductivity under Al electrolysis conditions [15].

#### 1.2.1. Environmental impacts related to the implantation of inert anodes

The environmental impact of substitution of carbon anodes with inert anodes will be significant, as it will prevent gases emissions ( $\text{CO}_2$ , CO,  $\text{CF}_4$  and  $\text{C}_2\text{F}_6$  emissions). It can also eliminate  $\text{SO}_2$  emission linked to the presence of sulfur in the petroleum cokes which are used to produce carbon anodes. As mentioned above, a part of air pollution in aluminum production is related to electricity generation. In a study by Kvande et al. [8], total  $\text{CO}_2$  emission from aluminum production cell using carbon or inert anodes with different source of electricity was estimated, as shown in Table I.1.

The main source of  $\text{CO}_2$  emission from aluminum production is the electric power production. Although in Quebec, only hydro-electricity is used for aluminum production, about 40 % of global aluminum production is carried out using the combustion of coal or natural gas. Also, as mentioned in Table I.1, with the green sources of electricity for aluminum production and by substitution of carbon anode with inert anode, not only  $\text{CO}_2$  and  $\text{CF}_4$  emissions from electrolysis cells will be eliminated but also a significant reduction of  $\text{CO}_2_{\text{eq}}$  emission will occur (about 2.3 instead of 5.7 t  $\text{CO}_2_{\text{eq}}$  / t Al).

**Table I.1. CO<sub>2</sub> equivalent emissions from the various processes involved in the production of aluminum depending on the means of electricity production, reported by [8].**

(a) With carbon anodes				
CO <sub>2</sub> emission from aluminum cell with carbon anodes	Hydro-electric and nuclear power plant	Natural gas-fired power plant	Coal-fired power plant	Weighted world average
CO <sub>2</sub> from bauxite mining and alumina production	2.0	2.0	2.0	2.0
CO <sub>2</sub> from prebaked carbon anode baking	0.2	0.2	0.2	0.2
CO <sub>2</sub> from electrolysis cells	1.5	1.5	1.5	1.5
CO <sub>2</sub> equivalent of CF <sub>4</sub> emissions	2.0	2.0	2.0	2.0
CO <sub>2</sub> from electric power production	0	6.0	13.5	4.8
<b>Total emission (t CO<sub>2</sub> eq / t Al)</b>	<b>5.7</b>	<b>11.7</b>	<b>19.2</b>	<b>10.5</b>

(a) With inert anodes				
CO <sub>2</sub> emission from aluminum cell with inert anodes	Hydro-electric and nuclear power plant	Natural gas-fired power plant	Coal-fired power plant	Weighted world average
CO <sub>2</sub> from bauxite mining and alumina production	2.0	2.0	2.0	2.0
CO <sub>2</sub> from inert anode production	0.2-0.3	0.2-0.3	0.2-0.3	0.2-0.3
CO <sub>2</sub> from electrolysis cells	0	0	0	0
CO <sub>2</sub> equivalent of CF <sub>4</sub> emissions	0	0	0	0
CO <sub>2</sub> from electric power production	0	6.0	13.5	4.8
<b>Total emission (t CO<sub>2</sub> eq / t Al)</b>	<b>2.3</b>	<b>8.3</b>	<b>15.8</b>	<b>7.1</b>

As shown in Fig. I.2, the decomposition potential of alumina in a cell equipped with inert anodes is 1 V higher than that of a traditional cell equipped with carbon anodes (~2.2 V instead of ~1.2 V). Besides the decomposition potential of alumina, the cell potential is composed of different overpotentials such as cathode, anode, electrolyte, gas bubble and external connections overpotentials. So, the higher cell potential in inert anode which results in a significant increase in energy consumption for aluminum production, must be compensated. For example, by reducing the anode-to-cathode distance from 4.4 cm (in carbon anodes) to 2.2 cm or even to 1.9 cm, it is possible to obtain a cell potential as low as 4.2 V and reduce the energy consumption by 23 %

[8,16]. Reducing the anode-to-cathode distance for inert anode is achievable because of the formation of smaller oxygen bubbles on the surface of inert anodes compared to the CO<sub>2</sub> bubbles evolving on the surface of carbon anodes. In fact, the average diameter of CO<sub>2</sub> can be 20 to 100 times larger than that of oxygen bubbles (0.1 mm) [5]. Also, the bubble layer depth on inert anode is more than 60 % smaller than on carbon anode. Formation of smaller gas bubbles with smaller bubble layer depth on the surface of the anode, allows to reduce the anode-to-cathode distance and reduces the resistance at the interface of the anode and the electrolyte.

Reducing the anode-to-cathode distance can increase the risk of short-circuit by molten aluminum formed on the cathode surface. Therefore, to have an anode-to-cathode distance as small as possible, it is essential to have a cathode with an excellent aluminum wettability. Titanium diboride (TiB<sub>2</sub>) seems to be a promising wettable cathode as it has good electrical conductivity, low solubility in molten cryolite and molten aluminum, good thermal conductivity, good oxidation resistance and most importantly, excellent aluminum wettability. However, the production of industrial TiB<sub>2</sub> wettable cathode is still a problem. The possibility of deposition of a thick, single phase, crack-free and dense TiB<sub>2</sub> coating to be used as cathodes in Al electrolysis has been carried out at INRS in collaboration with Concordia university.

It must be noted that decreasing the anode-to-cathode distance will decrease the electrical resistance of the electrolytic bath. This resistance is converted into the heat and it is used to maintain the aluminum cell at its cell operating temperature. The cell temperature must be maintained thus by either supplying additional heat or using a better thermal insulation. However, supplying additional heat represents additional costs while a better thermal insulation causes the protective crust to not be formed and exposes the cell walls to a corrosive environment [8]. To overcome this issue, an optimized anode-to-cathode distance must be selected and aluminum electrolysis can be carried out at lower temperature.

### 1.2.2. Selection criteria for inert anode materials

To replace carbon anode with inert anode and obtain its benefits, inert anode material must meet several criteria for being used in industrial scale. US Department of Energy published an “Inert Anode Roadmap” in 1998 in which the expected and required potential benefits from inert anodes accompanied with wettable cathodes were established [15]. In the “Inert Anode Roadmap”,

different performance criteria were defined for inert anodes. These performance criteria were categorized into two sets, Essential (first tier) targets and Beneficial (second tier) targets, as presented in Table I.2.

**Table I.2. Performance Targets for Inert Anodes.**

<b>Essential (1st Tier)</b>		<b>Beneficial (2nd Tier)</b>
<b>Criterion</b>	<b>Target for Inert Anode</b>	<b>Criterion</b>
<b>Electrochemical and thermodynamic stability</b>	Erosion rate of <10 mm/yr with current density (0.8 amps/cm <sup>2</sup> )	Health and Safety
<b>Electrochemical behavior (Current density)</b>	Polarization voltage of <0.5 volts at 0.8 amps/cm <sup>2</sup>	Economics
<b>Electrical conductivity</b>	Voltage (continuous) drop no worse than with carbon anode - bus to electrolyte	Net Energy
<b>Mechanical properties</b>	Sufficiently robust to survive in normal plant conditions - must withstand cell vibrations - must support its own weight - must maintain mechanical integrity - must not suffer from thermal shock - must survive in normal bath - must handle heat-up from room to operating temperature range of 930 °C- 1100 °C	Opportunity for Retrofit
<b>Oxidation</b>	Stability in oxygen at 1,000 °C - should not spall - may be a higher/lower operating temperature	Potential for Bath Chemistry
<b>Metal quality</b>	No worse than today's quality - 0.1% Fe, 0.2% Si - meets today's market standards	Modification
<b>Environmental and safety Acceptability of the material</b>	Eliminate beryllium, chromium, radioactive and EPA-defined hazardous materials	Other Cell Construction
		Materials
		Thermal Conductivity
		Porosity
		Positive Influence on Cathode life

So far, several anode materials have been evaluated as inert (O<sub>2</sub>-evolving) anodes to substitute consumable carbon anodes. The materials studied so far, can be categorized in three groups: metals, ceramics and cermets (composites of a ceramic and a metal). Each of these groups has its advantages and disadvantages and here, inert anodes based on metals will be discussed in

detail. As mentioned before, the idea of using metals as inert anodes was first adopted by the co-founder of the Hall-Héroult process, Charles Martin Hall. He investigated the possibility of using copper anodes in aluminum electrolysis [17]. Although all his attempts were unsuccessful, this approach had a definite interest.

Metals provide an excellent electrical conductivity and are resistant to thermal shocks. Also, their production and processing cost is relatively low and it is very easy to shape and electrically connect them. However, their dissolution rate in the molten electrolyte is high and their corrosion and oxidation resistance is low. In fact, only noble metals such as gold and platinum are inert to oxidation and most of metals intend to react with oxygen even at relatively low oxygen pressures. Using noble metals as inert anodes is not practical due to their high costs. So, to use a metallic anode in the severe electrolysis conditions, the oxide layer formed on the surface of the metallic anode must protect it from further corrosion and oxidation. The growth kinetics of the oxide layer must be faster than its dissolution rate. Also, this oxide layer must be dense and crack-free to prevent the infiltration of electrolyte into the anode surface. This oxide layer must also be a barrier for diffusion of oxygen and fluorides. It must not cause a significant increase in the cell potential; therefore, the electrical conductivity of this oxide layer must be sufficiently high. Finally, the oxide layer must have good adhesion to the anode surface to reduce the possibility of delamination.

Among several possible metals, alloys with different compositions based on Ni, Fe, Cu, Co or Al elements have been widely studied. Cu-Al alloys have been used as inert anode in studies by Hyrn et al. [18,19]. Shi et al. [20] used Ni-Fe alloys as inert anodes and Simakov et al. [21] studied Ni-based anodes containing Fe, Cu and Al. With the obtained results, these alloys seemed to be promising inert anodes, however, the purity of produced aluminum was relatively low due to its contamination with iron or copper. Another approach was adopted to improve the performance of these alloys by De Nora et al [22–24] where the corrosion resistance of the anode was enhanced by depositing a layer of  $\text{NiFe}_2\text{O}_4$  or cerium oxide ( $\text{CeO}_2$ ) on Ni-Fe alloy. However, the deposition processes were very challenging especially in the industrial scale and it was required to improve the long-term chemical stability of the coated anode. The oxidation and electrolytic behaviour of different compositions of Cu-Ni-Fe alloys have been studied so far and these alloys seems to be

the most promising materials as inert anodes. The Cu-Ni-Fe system will be discussed in detail later.

### 1.2.3. Electrolysis and configuration of electrolysis cell

In aluminum electrolysis, molten electrolyte is used to dissolve alumina and provide a medium for transferring ions. The electrolyte that is used currently in industrial aluminum production is a sodium-based electrolyte at 1000 °C. The electrolyte composition has been optimized over the past few decades, e.g., a higher cryolite ratio (CR) is used to increase the current efficiency. Since one of the main concerns with inert anodes is their corrosion resistance, lowering the electrolysis temperature can be very beneficial. Lowering the electrolysis temperature will decrease the dissolution and the corrosion rates of metallic anodes in the cryolitic medium, however, it also decreases the alumina solubility in the molten cryolite. Theoretically, it is possible to lower electrolysis temperature with an NaF-based electrolyte by decreasing the cryolite ratio (higher amount of  $\text{AlF}_3$ ). However, in these conditions, the alumina solubility in molten cryolite will be relatively low. The solubility of alumina in NaF-based electrolyte drops from 8 to 3 wt% when the temperature decreases from 960 to 750 °C. Another approach to lower electrolysis temperature is to use potassium-based electrolyte. With KF-based electrolyte, it is possible to work at temperatures between 700 to 800 °C with a cryolite ratio of 0.7 to 1.5 [25] and the alumina solubility in KF-based electrolyte is 6.3 and 4.7 wt% at 750 and 700 °C, respectively [26]. The phase diagrams of KF- $\text{AlF}_3$  and NaF- $\text{AlF}_3$  systems are presented in Fig. I.4.

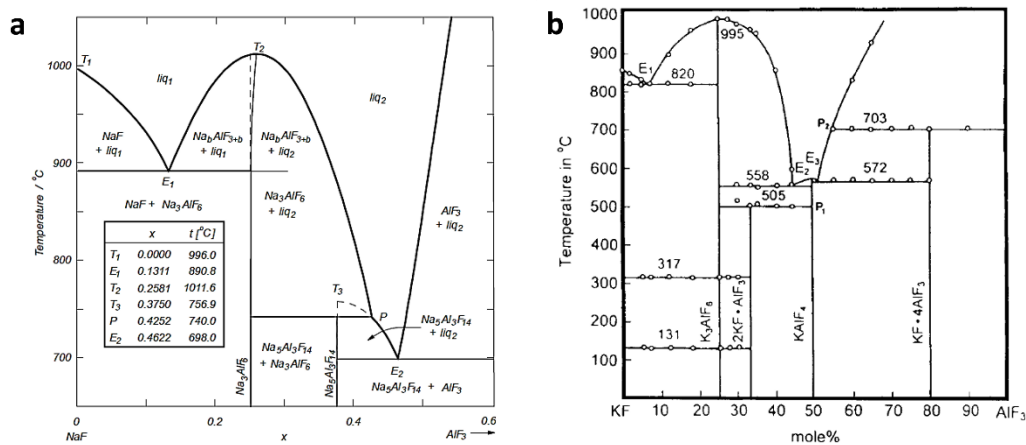


**Figure I.4. Phase diagram of (a) NaF- $\text{AlF}_3$  [27] and (b) KF- $\text{AlF}_3$  [28] systems.**

Although potassium-based cryolite exhibits higher alumina solubility, its electrical conductivity is lower than sodium-based cryolite. At 750 °C and the same cryolite ratio, the electrical conductivity of KF-based cryolite is 1.045 S.cm<sup>-1</sup> compared to 1.274 S.cm<sup>-1</sup> for NaF-based cryolite. The electrical conductivity decreases even more when alumina is added to the electrolyte [29]. This drop in conductivity leads to a higher release of heat from KF-based cryolite by Joule effect. So, it is essential to decrease the anode-to-cathode distance and thus, using wettable cathodes. In addition to lower electrical conductivity, potassium-based cryolite can penetrate into the carbon cathode and cause swelling and degradation of the cathode [30]. Also, since KF-based cryolite is more volatile than NaF-based cryolite, the chemistry of electrolyte might change and the level of bath might decrease during aluminum electrolysis [31]. This will increase the risk of anode effect and the interruption of aluminum production. With all these drawbacks associated with the use of potassium cryolite, it is necessary to precisely control electrolysis parameters and bath composition during aluminum electrolysis. However, despite these negative points, using KF-based electrolyte that allows reducing the electrolysis temperature seems to be a key factor to improve inert anodes performances. In order to use inert anode at high temperature electrolysis in NaF-based electrolyte, inert anode must be coated with a protective layer.

As mentioned earlier, replacing carbon anodes with inert anodes requires a complete redesigning of the electrolysis cell configuration. With all the technical difficulties linked with the use of inert anodes, especially at low temperatures, it is not possible to maintain the same cell geometry and configuration. Using a vertical electrode configuration and wettable cathodes as well as reducing the anode-to-cathode distance, electrolysis with inert anodes at low temperature can be economically and technically possible. Different cell configurations have been patented for electrolysis at lower temperatures. A bipolar cell was patented by Swiss Aluminum in 1976 with a SnO<sub>2</sub>-based ceramic anode and a carbon cathode. The cathode part is separated from the anode part with a layer of metal (Ni, Ag, Cu, Co or Mo) [32]. Beck et al. also patented an electrolysis cell made of a sequence of vertical anodes and cathodes in KF-based electrolyte working at 700 - 800 °C [33,34]. The bottom of the cell is also made of the anode materials and is electrically connected to the vertical anodes. With this configuration, the oxygen bubbles that are released from the bottom of the cell, keep the undissolved alumina particles suspended in the electrolyte. Therefore, it is possible to add a higher amount of alumina to the electrolyte and prevent the risk

of anode effect. The produced aluminum is also collected with a tube passing through the bottom of vertical cathodes.

### **I.3. Cu-Ni-Fe anodes**

As mentioned earlier, the design of inert anodes is a major challenge because of severe aluminum electrolysis conditions which require materials with excellent resistance to corrosion and thermal shock as well as adequate electrochemical properties. To date, there are no commercially available inert anodes that fully meet the requirements of the aluminum industry. So far, several anode materials have been evaluated as inert ( $O_2$ -evolving) anodes to substitute consumable carbon anodes. Among many materials studied so far, Cu-Ni-Fe-based alloys appear to be the most promising metallic anode materials, due to their ability to produce a protective nickel ferrite ( $NiFe_2O_4$ ) layer during Al electrolysis. However, these alloys might fluorinate during the electrolysis and form non-conductive nickel or iron fluoride which results in an increase in the cell voltage and a decrease in energy efficiency of the electrolysis process. Thus, a sacrificial protective layer must be deposited on the surface of the anode to increase its corrosion resistance and lifetime and provide the required time for the anode to form a nickel ferrite layer on its surface and prevent infiltration of fluorides into the anode surface. Here, a summary of studies carried out on the production and homogenization of Cu-Ni-Fe alloys as well as their behaviour during Al electrolysis will be presented.

#### **I.3.1. Production of Cu-Ni-Fe alloy**

Cu-Ni-Fe alloys have been prepared by ball-milling or fusion. Roué et al. [35] prepared different compositions of monophase Cu-Ni-Fe alloys by a 10 h high-energy ball-milling of metallic Cu, Ni and Fe powders using a vibratory mill (SPEX 8000). The ball-milling crucible was loaded and sealed under argon atmosphere. The produced powder was then consolidated to obtain dense electrodes for the electrolysis tests. As-milled powders were first sieved to get a particle size between 20 and 75  $\mu m$ . Then, sieved powders were heated up to 1000 °C under an Ar + H<sub>2</sub> (95/5) atmosphere to soften it and facilitate the following cold-pressing process. Then, the powders were cold-pressed at 26 ton.cm<sup>-2</sup> for 10 min to a disc-shape sample and then, the prepared pellet was

heated at 1000 °C under an Ar + H<sub>2</sub> (95/5) for 1 h. In another study [36], alloys with (Cu<sub>65</sub>Ni<sub>20</sub>Fe<sub>15</sub>)<sub>100-x</sub>O<sub>x</sub> compositions were prepared by a two-step ball-milling procedure. The Cu<sub>65</sub>Ni<sub>20</sub>Fe<sub>15</sub> alloy was first prepared as explained above by ball-milling under argon atmosphere, then the as-milled Cu<sub>65</sub>Ni<sub>20</sub>Fe<sub>15</sub> powder was introduced into the ball-milling crucible and the crucible was filled with oxygen gas, and the Cu-Ni-Fe powder was ball-milled again for 30 minutes. The oxygen content of the produced alloy was controlled by the number of times (0, 4, 9 and 18 times) that the crucible was filled with oxygen gas and was ball-milled again for 30 minutes. To fill the crucible with oxygen, it was opened and sealed in a glove bag in oxygen atmosphere at a pressure of 1 atm. The results showed that the obtained oxygen content was (Cu<sub>65</sub>Ni<sub>20</sub>Fe<sub>15</sub>)<sub>100-x</sub>O<sub>x</sub> with x = 0.3, 1.4, 3.3 and 7.2 wt%. The same procedure as explained above was applied to consolidate the powder prior to aluminum electrolysis tests. Also, in another work [37], to prevent multiple ball-milling steps, (Cu<sub>65</sub>Ni<sub>20</sub>Fe<sub>15</sub>)<sub>98.6</sub>O<sub>1.4</sub> (in wt%) was prepared by ball-milling nanosized Fe<sub>2</sub>O<sub>3</sub> and Cu-Ni-Fe alloy powders.

In another work, Roué et al. [38] prepared 16 kg of Cu-Ni-Fe powder using an attritor. The elemental Cu, Ni and Fe powders were ball-milled for 40 h at 200 rpm under Ar flow. The as-milled powder was then sieved to get a particle size between 20 and 75 µm. Then, 27 g of sieved powder was sintered to a pellet with a diameter of 20 mm and a thickness of 10 mm, using spark plasma sintering (SPS). The measured level of porosity in the sintered pellet was 5%. To prepare a larger size of anode for aluminum electrolysis, Cu<sub>65</sub>Ni<sub>20</sub>Fe<sub>15</sub> powder produced by an attritor, was deposited on a C63000 substrates using cold spray method [39]. 14 kg of Cu<sub>65</sub>Ni<sub>20</sub>Fe<sub>15</sub> powder was heat treated at 700 °C for 4 h under N<sub>2</sub>-30% H<sub>2</sub> and then sieved to remove particles larger than 75 µm. The coating process was carried out with N<sub>2</sub> carrier gas preheated at 800 °C and pressurized at 4.9 MPa. C63000 (Cu<sub>81.5</sub>Al<sub>10</sub>Ni<sub>5</sub>Fe<sub>3</sub>Mn<sub>0.5</sub> (wt%)) alloy with a diameter of 2.2 cm and a length of 25 cm was used as substrate. A coating with a thickness of 0.7-0.8 mm was obtained.

Although it is possible to use spark spray sintering (SPS) to consolidate Cu-Ni-Fe powder or to deposit it on a substrate by cold spraying, these methods are expensive and hardly scalable for production of anode at industrial scale. More recently, to prepare Cu-Ni-Fe anodes at the industrial scale, casting method was used by Roué et al. [40]. Elemental Cu, Ni and Fe powders were melted in a clay graphite crucible in air using an induction furnace at 1425 °C. 0.1 wt% of aluminum powder was also added to the liquid alloy to remove dissolved oxygen and the resulting

Al<sub>2</sub>O<sub>3</sub> was manually collected from liquid surface. The casting step was then performed with three different cooling rates of 5, 15 and 50 °C.min<sup>-1</sup> using iron, graphite and ceramic molds, respectively, to study the effect of cooling rates on the structure and the density of the as-cast alloys. Chemical segregation occurred in all as-cast alloys and their microstructure was composed of Ni-Fe-rich dendrites (Cu<sub>37</sub>Ni<sub>32</sub>Fe<sub>31</sub> (wt%)) embedded in a Cu-rich matrix (Cu<sub>86</sub>Ni<sub>9</sub>Fe<sub>5</sub> (wt%)). The results also showed that increasing the cooling rate led to an increase in the size of the pores inside the as-cast alloy but a decrease in the size of Ni-Fe-rich dendrites. The homogenization process was carried on the alloy casted in the graphite mold which had lower number of pores than the alloy casted in iron mold and smaller dendrite size of the alloy casted in ceramic mold. The as-cast alloy was successfully homogenized with a heat treatment at 1070 °C under 1 atm of Ar for 50 h followed by water quenching. The homogenization step is essential, since the bi-phase as-cast Cu-Ni-Fe alloy has a lower corrosion resistance during aluminum electrolysis; in fact, the iron-rich phase produces corrosion tunnels in the alloy [41].

### 1.3.2. Anodic behaviour of Cu-Ni-Fe alloys

As mentioned above, Cu-Ni-Fe alloys were studied as inert anodes for the first time by Beck and Brooks in 1994 [42]. Their work led to the determination of Cu-Ni-Fe alloys composition range in which the anodic behaviour of the alloy is acceptable. Following their work, between 1988 and 2005 a series of research was carried out in the United States where large anodes were produced by sintering and fusion of these alloys and electrolysis tests were conducted for hundreds of hours at 700 and 850 °C using TiB<sub>2</sub> as wettable cathodes [43]. Within these investigations, the effects of composition, microstructure and homogeneity of the alloy as well as electrolyte composition and electrolysis temperature were studied. Their work resulted in the publication of several articles and proved that a homogenous Cu-Ni-Fe alloy is a promising inert anode at low temperature electrolysis. In 2012, Gallino et al. [44] tested two compositions of Cu-Ni-Fe alloys (Cu<sub>25</sub>Ni<sub>40</sub>Fe<sub>35</sub> and Cu<sub>30</sub>Ni<sub>35</sub>Fe<sub>35</sub> in wt%) for electrolysis at 830 °C. The anodes were prepared by melting and homogenized with a following heat treatment. It was demonstrated that it is essential to have a ratio of Ni/Fe > 1, since a thick layer of NiO (~400 µm) and a continuous layer of NiFe<sub>2</sub>O<sub>4</sub> (~50 µm) was formed at the surface of Cu<sub>25</sub>Ni<sub>40</sub>Fe<sub>35</sub> alloy after 72 h electrolysis and a stable cell potential between 3.8 and 4.0 V was obtained. However, nickel and iron fluorides were formed at the oxide/alloy interface as well as at the grain boundaries of the alloy.

Since 2010, several studies have been conducted on the behaviour of Cu-Ni-Fe alloy as inert anode and TiB<sub>2</sub> as wettable cathodes for aluminum electrolysis in laboratory scale by Roué et al. [41]. A wide range of Cu-Ni-Fe alloys (Cu<sub>x</sub>Ni<sub>85-x</sub>Fe<sub>15</sub> with x = 0, 14, 32, 52, 60, 65, 70, 80 and 85 wt%) were tested for electrolysis at 700 °C with KF-based electrolyte. The iron content was set at 15 wt% as recommended by Beck et al. [42] and the effect of Cu and Ni content was examined. It was shown that when Cu content is lower than 32 wt%, the cell potential rapidly rises to 6.5 V due to the formation of nickel oxide and iron aluminate as well as the formation of KAlF<sub>4</sub> as a result of infiltration of electrolyte to the oxide/anode interface. When the Cu content is between 52 and 60 wt%, the cell potential stabilizes at 6.0 V and a complex oxide layer composed of sequences of layers of NiFe<sub>2</sub>O<sub>4</sub> - CuO + NiO - CuO was formed at the surface of anode. The best results were obtained when Cu content was between 65 and 85 wt% where a dense layer of oxide composed of mainly Cu<sub>2</sub>O with nickel ferrite particles dispersed in the vicinity of the oxide/alloy interface was formed and cell potential stabilized around 4.0 V. However, analyzing the purity of produced aluminum revealed that when the alloy contained more than 70 wt% of copper, the contamination of aluminum by Cu was too high. Roué et al. [45] then investigated more precisely the effect of Cu content on the prevention of the electrolyte infiltration into the anode surface by performing the same electrolysis conditions on anodes with Cu<sub>65</sub>Ni<sub>20</sub>Fe<sub>15</sub>, Cu<sub>55</sub>Ni<sub>25.7</sub>Fe<sub>19.3</sub> and Cu<sub>45</sub>Ni<sub>31.4</sub>Fe<sub>23.6</sub> compositions (in wt%). The most optimized composition was Cu<sub>65</sub>Ni<sub>20</sub>Fe<sub>15</sub> in which a layer of copper oxide was formed at the surface of the alloy which was then dissolved in electrolyte. The formation and dissolution of this copper oxide layer provided the time for the formation of an underlying nickel ferrite layer which thereafter protected the alloy from further corrosion. For lower copper content, the copper oxide layer was dissolved rapidly which exposed iron oxide to the electrolyte. As a result, iron oxide was dissolved before reacting with NiO and forming NiFe<sub>2</sub>O<sub>4</sub>. The optimal composition was identified as Cu<sub>65</sub>Ni<sub>20</sub>Fe<sub>15</sub> where the Cu content was high enough to assure the formation of a continuous nickel ferrite layer but low enough to maintain the purity of produced aluminum in an acceptable range.

Then the effect of iron content was studied using three compositions as (Cu<sub>3,25</sub>Ni)<sub>100-x</sub>Fe<sub>x</sub> (x = 0, 15 and 30 wt%) [35]. It was shown that when the alloy is iron free, a thick layer of copper and nickel oxides as well as a continuous layer of nickel fluoride (~ 50 µm) was formed during electrolysis which led to an increase in the cell potential. For alloys containing 15 and 30 wt% of iron, a continuous layer of nickel ferrite was formed and its thickness increased with iron content.

Although increasing the iron content led to the formation of a thicker protective nickel ferrite layer, the analysis on the purity of produced aluminum showed that it would also increase Al contamination. Moreover, for both alloys, a region composed of iron fluoride inclusions was formed which could be a problem for their long-term application as anodes.

To increase the purity of produced aluminum within the industrial standards, the Cu-Ni-Fe alloys were synthesized by ball-milling in an oxidizing atmosphere or by ball-milling a mixture of Cu-Ni-Fe and nanosized  $\text{Fe}_2\text{O}_3$  powders [37,44,46]. This would lead to the formation of  $\text{Fe}_2\text{O}_3$  particles dispersed in the as-prepared alloy and could help the alloy to form the nickel ferrite layer more rapidly. Thus, an alloy with  $(\text{Cu}_{65}\text{Ni}_{20}\text{Fe}_{15})_{98.6}\text{O}_{1.4}$  (wt%) composition was prepared and used in aluminum electrolysis. The results of electrolysis for a short duration (20 h) on small  $(\text{Cu}_{65}\text{Ni}_{20}\text{Fe}_{15})_{98.6}\text{O}_{1.4}$  anodes ( $\sim 4 \text{ cm}^2$ ) showed that the nickel ferrite layer was formed within the first few minutes of electrolysis and the total aluminum pollution was decreased to 0.24 wt% and the corrosion rate was estimated to be  $0.8 \text{ cm}\cdot\text{year}^{-1}$ .

To perform electrolysis tests in a more realistic condition, larger sizes of Cu-Ni-Fe anodes were prepared by cold spray and casting methods, as explained earlier. A 50 h electrolysis at  $700^\circ\text{C}$  using KF-based electrolyte was conducted on C63000 alloy coated with Cu-Ni-Fe alloy [39]. After 25 h electrolysis, a thick layer of oxide ( $\sim 400 \mu\text{m}$ ) was formed at the surface of the anode, however, in the subsequent 25 h electrolysis, the thickness of the oxide layer increased only  $25 \mu\text{m}$ , suggesting that a balance between the oxidation and dissolution rate was obtained. The EDS analysis of the anode after different electrolysis times, revealed that copper was the first element to be oxidized and a layer of CuO formed at the anode surface while the inward diffusion of oxygen led to the oxidation of nickel and iron. Thus, a layer of mixed NiO and  $\text{Fe}_2\text{O}_3$  was formed underneath the CuO layer where a non-continuous layer of nickel ferrite could be seen. Further electrolysis resulted in the continuous dissolution of CuO layer (due to its higher solubility in cryolite than NiO and  $\text{Fe}_2\text{O}_3$ ), formation of a continuous  $\text{NiFe}_2\text{O}_4$  layer and formation of a new  $\text{Cu}_2\text{O}$  layer at the interface of oxide/alloy. The thickness of nickel ferrite layer reached  $50 \mu\text{m}$  after 25 h electrolysis which explains the lower corrosion rate of the anode. However, delamination of Cu-Ni-Fe coating from C63000 substrate as well as detachment of oxide layer formed at the Cu-Ni-Fe coating surface was observed which could strongly affect the corrosion resistance of the

anode and purity of the produced aluminum. This is a major issue for the long-term viability of the Cu-Ni-Fe coated anode.

The as-cast and homogenized  $\text{Cu}_{65}\text{Ni}_{20}\text{Fe}_{15}$  and homogenized  $\text{Ni}_{65}\text{Fe}_{25}\text{Cu}_{10}$  (wt%) alloys were also used as anodes in aluminum electrolysis at 700 °C using KF-based electrolyte. The cell potential for the as-cast  $\text{Cu}_{65}\text{Ni}_{20}\text{Fe}_{15}$  anode started to increase after 11 h electrolysis suggesting the growth of a poorly conductive phase at its surface. After 20 h electrolysis, a 150  $\mu\text{m}$  thick oxide layer formed at the surface of the anode, composed of an outer 100  $\mu\text{m}$  porous CuO-rich areas surrounded by electrolyte and an inner mixed  $\text{Cu}_2\text{O}$ , NiO and  $\text{Fe}_2\text{O}_3$  layer where some discontinuous layers of nickel ferrite can be seen too. The EDS analysis of alloy/oxide interface showed that Cu-rich phase in the as-cast alloy was preferentially oxidized compared to the Ni-Fe-rich phase. Also,  $\text{NiF}_2$  and  $\text{FeF}_x$  phases were formed at the interface of the alloy which explains the increase in the cell potential. For homogenized  $\text{Cu}_{65}\text{Ni}_{20}\text{Fe}_{15}$  anode, a more stable cell potential was observed except for few rapid drops that might correspond to the detachment of poorly attached  $\text{NiAl}_2\text{O}_4$  layer formed at its surface. Underneath the delaminated  $\text{NiAl}_2\text{O}_4$  layer, a  $\text{CuO}_x$  region was observed where CuO is formed on top of  $\text{Cu}_2\text{O}$ . A continuous layer of nickel ferrite with 5 to 10  $\mu\text{m}$  thickness was observed beneath this  $\text{CuO}_x$  region followed by some discontinuous NiO +  $\text{Fe}_2\text{O}_3$  regions. The formation of continuous layer of  $\text{NiFe}_2\text{O}_4$  layer explains the more stable cell potential in the homogenized  $\text{Cu}_{65}\text{Ni}_{20}\text{Fe}_{15}$  anode. For homogenized  $\text{Ni}_{65}\text{Fe}_{25}\text{Cu}_{10}$  anode, a rapid increase of cell potential occurred only after 6 h of electrolysis due to the high infiltration of electrolyte into the porous oxide layer followed by the formation of an insulating layer. The cell voltage reached more than 9 V after 10 h electrolysis. The EDS analysis demonstrated that the thickness of the oxide layer formed at the surface of  $\text{Ni}_{65}\text{Fe}_{25}\text{Cu}_{10}$  anode varied between 20 to 100  $\mu\text{m}$  reflecting its partial delamination during Al electrolysis. Sequences of thin layers of oxides (5  $\mu\text{m}$ ) and layers of infiltrated electrolyte (10  $\mu\text{m}$ ) were observed on this alloy where the outer oxide layer was composed of mainly  $\text{NiAl}_2\text{O}_4$  and the oxide inner layers were constituted of NiO and  $\text{Fe}_2\text{O}_3$ . Nickel ferrite was not observed on this anode, probably because the NiO/ $\text{Fe}_2\text{O}_3$  ratio was not optimal to favor the formation of nickel ferrite.

### I.3.3. Problematic with Cu-Ni-Fe anodes

As discussed in this bibliographic study, after decades of scientific research, the substitution of carbon anodes with inert anodes has proven to be particularly difficult. Adopting inert anodes would require solving many technological issues. It would even be necessary to re-imagine the configuration of the electrolytic cells in order to reduce the inter-electrode distances, to develop new materials to thermally insulate the cells and to optimize the various systems controlling the evolution of the electrolytic bath chemistry (evolution CR, alumina concentration). Thus, it also requires finding a suitable wettable cathode such as  $\text{TiB}_2$ . Although, the main technological obstacle on which the majority of research has focused is finding a suitable anode material. Due to the highly corrosive conditions of the electrolytic medium and many corrosion mechanisms that may be involved, few anode materials have demonstrated stability greater than a few hundred hours. In addition, corrosion of the anodes makes it difficult to produce aluminum of a purity at least equal to that obtained with carbon anodes.

However, some materials exhibit properties close to the conditions required for their use as inert anode materials. Cu-Ni-Fe based alloys are promising inert anode materials for Al production. As shown in previous section, Cu-Ni-Fe alloys, especially homogenized  $\text{Cu}_{65}\text{Ni}_{20}\text{Fe}_{15}$  alloy, appear to be the most promising candidate due to their ability to form a protective layer of nickel ferrite ( $\text{NiFe}_2\text{O}_4$ ) on their surface during aluminum electrolysis. These alloys exhibit wear rates close to  $1 \text{ cm}\cdot\text{year}^{-1}$ . However, these alloys are sensitive to the fluorination reaction with the cryolitic medium, forming non-conductive nickel or iron fluoride at the metal/oxide interface, which increases the cell voltage and reduces energy efficiency of the electrolysis process. It is therefore essential to improve the corrosion resistance of these alloys with a protective coating layer.

To protect the Cu-Ni-Fe alloy from corrosion and prevent the infiltration of fluorides into the nickel ferrite layer, the use of (Co,Ni)O protective coatings for metallic anode appears promising. For that purpose, in a work by Nguyen and de Nora [24], a Co-Ni alloy was first electrodeposited onto the anode, which was followed by an oxidation treatment in air at high temperature to favor the formation of (Co,Ni)O coating. However, due to the change of densities upon oxidation of metallic Co-Ni alloy, this procedure may be challenging to produce coherent

and crack-free oxide layer as required for industrial Al production. A potentially relevant method to produce (Co,Ni)O coated inert anodes is by direct deposition of (Co,Ni)O oxide compounds or a mixture of CoO and NiO by thermal spray deposition techniques. It is worth noting that thermal spray can be used on Al production site to restore protective (Co,Ni)O coating on end-of-life inert anodes. Thermal spraying is a promising, fast and efficient method to deposit thick coatings for various applications in a single step [47]. Among various thermal spraying methods, suspension plasma spray (SPS), invented in the mid-1990s in the University of Sherbrooke, Canada [48], has demonstrated its capability to produce oxide coatings which are usually difficult to coat with other conventional coating methods such as electrodeposition, sintering and vacuum deposition. SPS includes injection of a suspension of submicron solid particles into the plasma jet, atomization and evaporation of the liquid phase, and then melting, acceleration, impact and deposition of the particles on a substrate [49,50]. SPS has been widely used to deposit coatings with different applications including biomaterials coating, wear and corrosion resistant coatings, thermal barrier coatings, coating fiber-reinforced composite materials and abradable coatings. This method has the advantages of high deposition rate, versatility, high scalability, moderate operating costs, and low thermal input into substrates. In SPS, thick coatings (from 10 to 300  $\mu\text{m}$ ) with sub-micrometer or nanometer scales structure can be produced. Therefore, the ability to create different distinct types of microstructures (columnar-grown, segmented, dense, and porous), the use of fine particles of single or multiphase composition and even the capability to combine different processes, opens a myriad of possibilities in terms of thermal spray engineering [51,52]. On the other hand, high velocity thermal spraying techniques are preferred to form coatings with low porosity and good adhesion to the substrate. In these methods, a mixture of oxygen and fuel such as hydrogen, propylene, ethylene or propane is used to produce a supersonic jet through a Laval nozzle. Powdered materials are injected into the flame, where the particles begin to melt while being accelerated towards a substrate. The high velocity of the particles causes them to form a dense stack of flattened droplets on the substrate, resulting in smooth, uniform coatings with good adhesion to the substrate. Usually, the residence time of the powder in the flame is shorter and the flame temperature is lower than in other thermal spray methods, which further reduces the possibility that the powder is reduced, oxidized or decomposed, or that undesired phase transformation occurs during spraying [47]. Different types of materials, including dense and porous metals, cermets and ceramics have been deposited by HVOF, and the targeted applications

are diverse such as wear and corrosion resistant coatings, and coatings acting as thermal barrier for high-temperature applications [53–55].

In this context, first, pure  $\text{Co}_x\text{Ni}_{1-x}\text{O}$  solid solutions must be synthesized over the whole composition range by a fast, scalable and cost-efficient method. Then, it is essential to determine their properties including thermal stability, dissolution rate in molten cryolite (NaF-based and KF-based cryolites) and electrical conductivity at temperatures ranging between 700 and 1000 °C. Then dense, uniform, and single phase  $\text{Co}_x\text{Ni}_{1-x}\text{O}$  coatings must be deposited on Cu-Ni-Fe substrates using thermal spray techniques. Thus, the effects of spraying parameters on the composition and structure of the coatings must be studied to obtain the optimized deposition conditions. Finally, the morphological and microstructural characteristics of the prepared coatings as well as their behaviour at 1000 °C in dry inert and oxidizing atmospheres and their electrochemical behaviour under Al electrolysis conditions must be investigated. Here, possible synthesis and coating procedures for (Co,Ni)O materials will be discussed in detail.

#### **I.4. (Co,Ni)O synthesis and coating inert anodes**

As explained above, single phase Cu-Ni-Fe alloys can form a protective  $\text{NiFe}_2\text{O}_4$  layer upon Al electrolysis. However, this protective nickel ferrite layer requires time to form at the surface of Cu-Ni-Fe alloys, during which Cu-Ni-Fe alloy may fluoride to form non-conductive nickel or iron fluorides. This will cause premature degradation of the electrode and a gradual increase in the cell voltage and a decrease in the energy efficiency of the electrolysis process. To protect the Cu-Ni-Fe alloy from corrosion and prevent the formation of metallic fluorides prior to the formation of a nickel ferrite layer, a protective coating can be used. This protective coating must be resistant to both oxidation and fluorination. Among different materials, oxides appear to be promising. In fact, it is known that CoO can work as a barrier for the fluorination and the transformation of CoO to  $\text{CoF}_2$  occurs only at very low oxygen pressure in cryolite medium. However, CoO tends to decompose to  $\text{Co}_3\text{O}_4$  at elevated temperatures [56], and formation of  $\text{Co}_3\text{O}_4$ , which is an n-type semiconductor, should be avoided as it would translate into higher overpotential during Al electrolysis due to its lower conductivity in comparison with p-type semiconductor oxides. The work of Nguyen and de Nora [57] demonstrated that adding Ni atoms to CoO phase and forming a (Co,Ni)O solid solution, makes it possible to avoid the transformation

of CoO to Co<sub>3</sub>O<sub>4</sub>. As explained above, to make a (Co,Ni)O-based protective coating, a Co-Ni alloy was first electrodeposited onto the anode, followed by an oxidation treatment in air at high temperature to favor the formation of a (Co,Ni)O solid solution. However, due to the change of densities upon oxidation of the metallic Co-Ni alloy, this manner of producing a cohesive, crack-free oxide layer on the inert anode may be challenging. It must be noted that NiO itself is not as resistant as CoO to fluorination and its electrical conductivity is lower than that of CoO or (Co,Ni)O at high temperatures [58]. To use (Co,Ni)O solid solutions as protective coatings for inert anodes, a time and cost-efficient process must be found to prepare large scale of these materials to be deposited directly through thermal spray techniques. The possible formation processes of (Co,Ni)O solid solutions by mechano-synthesis, calcination as well as during thermal spraying process will be discussed later.

#### I.4.1. CoO-NiO phase diagram and high-temperature behaviour

Both CoO and NiO have NaCl rock salt (*fcc*) crystal structure and comparable lattice parameters of 4.2667 and 4.1684 Å, respectively. These similarities provide the possibility of the formation of a solid solution over the whole composition range where the lattice parameter of Co<sub>x</sub>Ni<sub>1-x</sub>O changes linearly as a function of *x*. (Co,Ni)O solid solution can be produced by different methods. CoO-NiO-O<sub>2</sub> system was first studied by Moore and White in 1974 as conducting oxide electrodes in the fused carbonate fuel cells [58]. They investigated the equilibrium relationship between NiO and CoO in air from room temperature to 1000 °C. They studied the formation of the spinel NiCo<sub>2</sub>O<sub>4</sub> and the *fcc* CoO-NiO phases by converting the nickel and cobalt nitrates to oxides followed by heat treatment and quenching various ratios of the oxides at different temperatures. Then (Co,Ni)O solid solutions were brought to lower temperatures from 1000 to 800 °C and maintained at each temperature until they reached a constant weight. Thus, with thermodynamic considerations and experimental results, they predicted decomposition of single phase (Co,Ni)O solid solution to two phase (solid solution + Co<sub>3</sub>O<sub>4</sub>) in air at temperatures below 912 °C. They presented the isobaric ternary diagram of the NiO – CoO – ½ O<sub>2</sub> system in air as well as temperature-composition diagram of NiO-CoO-O<sub>2</sub> system in air at temperatures between 400 and 1000 °C, as shown in Fig. I.5 and I.6. Bergman and Agren [59] also studied thermodynamic properties of CoO-NiO system and discussed the formation of a second phase (Co<sub>3</sub>O<sub>4</sub>) using thermodynamic modeling.

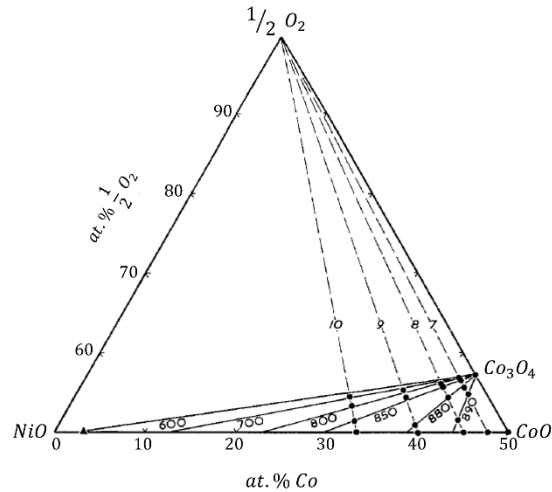


**Figure I.5. Ternary diagram of the NiO – CoO –  $\frac{1}{2}$  O<sub>2</sub> system in air [58].**

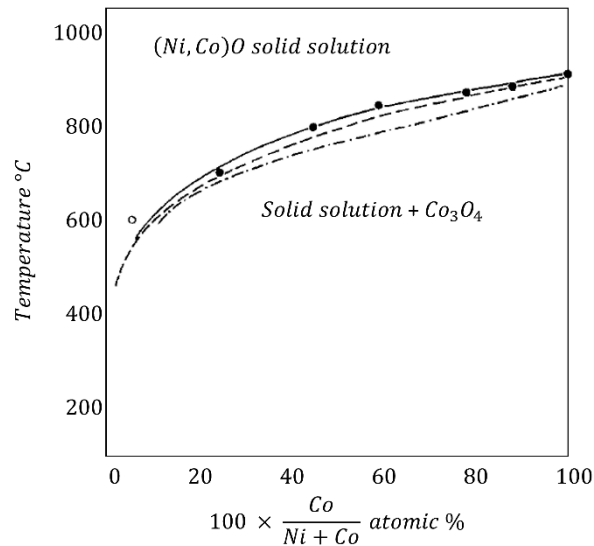


**Figure I.6. Temperature-composition diagram of NiO-CoO-O<sub>2</sub> system in air as a function of temperature [58].**

Sakata et al. [60] prepared different compositions of (Co,Ni)O by quenching mixtures of the cobalt and nickel carbonates from temperatures higher than 850 °C. It was shown that Co<sub>x</sub>Ni<sub>1-x</sub>O solid solution can be prepared, with the range of 0 ≤ x ≤ 1, by a calcination at 1000 °C in air of either various ratios of CoO and NiO powders [61]. Kuboon and Hu [62] also studied the possibility of CoO-NiO and Co<sub>3</sub>O<sub>4</sub>-Ni<sub>3</sub>O<sub>4</sub> solid solutions by heating different mixtures of Ni(NO<sub>3</sub>)<sub>2</sub> and Co(NO<sub>3</sub>)<sub>2</sub> at temperatures between 500 and 1000 °C. After these calcinations, they analyzed products with XRD and measured their lattice parameters. Their results revealed that Co<sub>3</sub>O<sub>4</sub> and

(Co,Ni)O solid solution are formed when the mixture is heated at temperatures below 800 °C. They calculated linear relationships between the molar fraction of NiO or Ni<sub>3</sub>O<sub>4</sub> and the lattice parameters of CoO-NiO or Co<sub>3</sub>O<sub>4</sub>-Ni<sub>3</sub>O<sub>4</sub> solid solutions which confirmed feasibility of Vegard's law for CoO-NiO and Co<sub>3</sub>O<sub>4</sub>-Ni<sub>3</sub>O<sub>4</sub> solid solutions. Relationships between molar fractions of NiO or Ni<sub>3</sub>O<sub>4</sub> and lattice parameters of NiO-CoO or Co<sub>3</sub>O<sub>4</sub>-Ni<sub>3</sub>O<sub>4</sub> solid solutions are shown in Fig. I.7 and I.8 and equations 8 and 9.

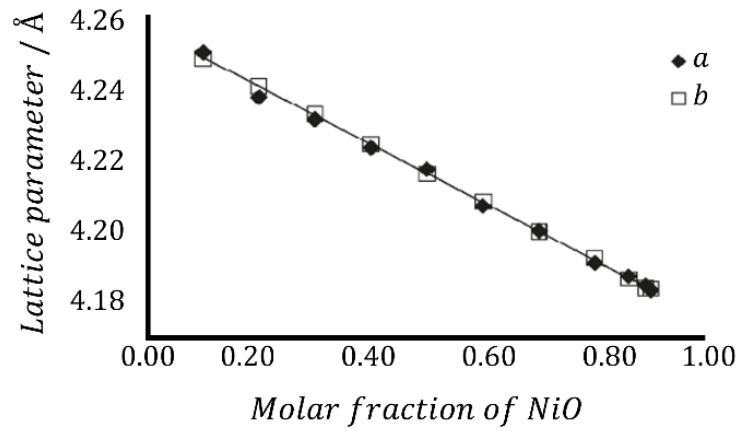


**Figure I.7. Relationship between molar fractions of NiO and lattice parameters of NiO-CoO solid solutions prepared at (a) 1000 and (b) 1100 °C [62].**

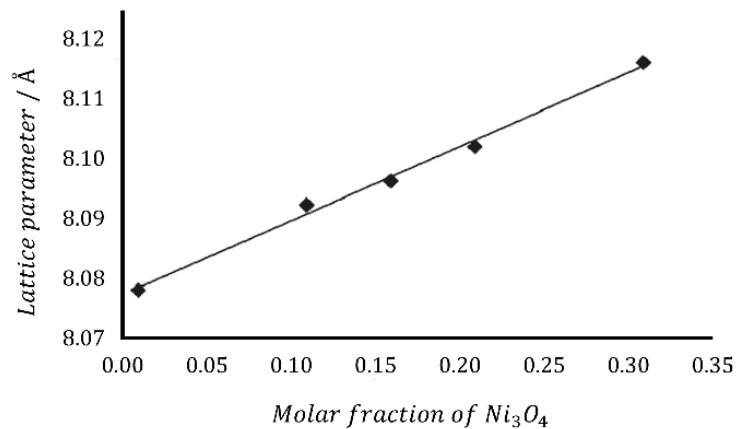


**Figure I.8. Relationship between molar fractions of Ni<sub>3</sub>O<sub>4</sub> and lattice parameters of Ni<sub>3</sub>O<sub>4</sub> - Co<sub>3</sub>O<sub>4</sub> solid solutions prepared at 600 °C [62].**

$$a_{CoO-NiO} = -0.0828 x_{NiO} + 4.2581 \quad (8)$$

$$a_{Co_3O_4-Ni_3O_4} = -0.1241 x_{Ni_3O_4} + 8.0813 \quad (9)$$

#### I.4.2. Physical and chemical properties of CoO, NiO and (Co,Ni)O

As explained before, to replace carbon anode with inert anode and obtain its benefits, materials used in inert anodes must meet several criteria for being used in industrial scale, such as good electrical conductivity, oxidation and corrosion resistance, thermal stability and low solubility in molten cryolite. To use (Co,Ni)O solid solutions as a protective coating for Cu-Ni-Fe anodes, it is essential to investigate their physical and chemical properties. However, to our knowledge, only few works have been published on physical and chemical properties of (Co,Ni)O materials. Here, a summary of studies on CoO, NiO and (Co,Ni)O characteristics will be presented.

Moore and White [58] studied the electrical conductivity of NiO, CoO and different compositions of (Co,Ni)O as a function of temperature in air atmosphere. They prepared pellets of these materials and then heat treated them at temperatures between 1150 and 20 °C and analyzed their electrical conductivity by measuring the potential drop between two platinum probes using a null current potentiometer with direct current passing through the pellet. Samples were held 12 hours at each temperature before measuring their electrical conductivity. The effects of temperature and composition on the electrical conductivity of  $Co_xNi_{1-x}O$  materials are given in Fig. I.9 and I.10. As shown in Fig. I.9 and I.10, the electrical conductivity of NiO, CoO and (Co,Ni)O increases with an increase in the temperature. This is expected as these materials are p-type semiconductors. Also, CoO and (Co,Ni)O have generally a better electrical conductivity than NiO. For  $Co_xNi_{1-x}O$  solid solutions, the electrical conductivity decreases as the NiO content in the solid solution increases.

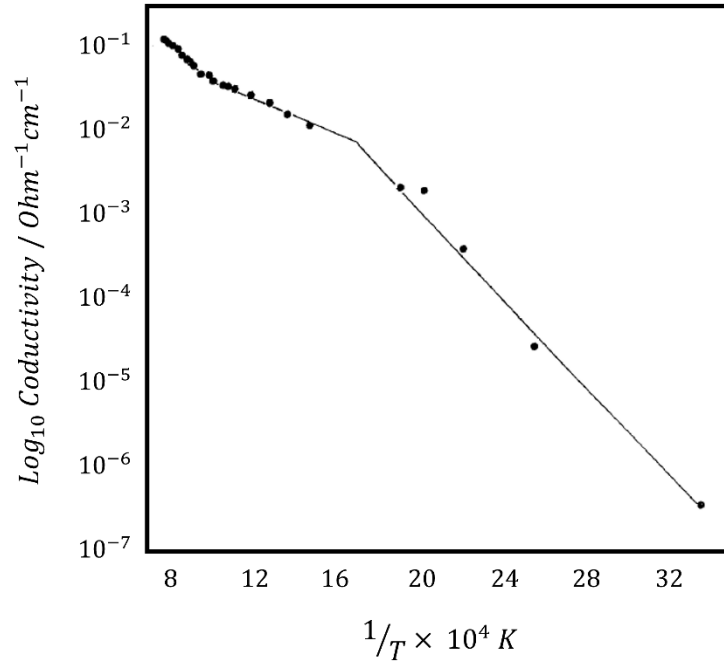


**Figure I.9.** Electrical conductivity of NiO as a function of temperature in air [58].

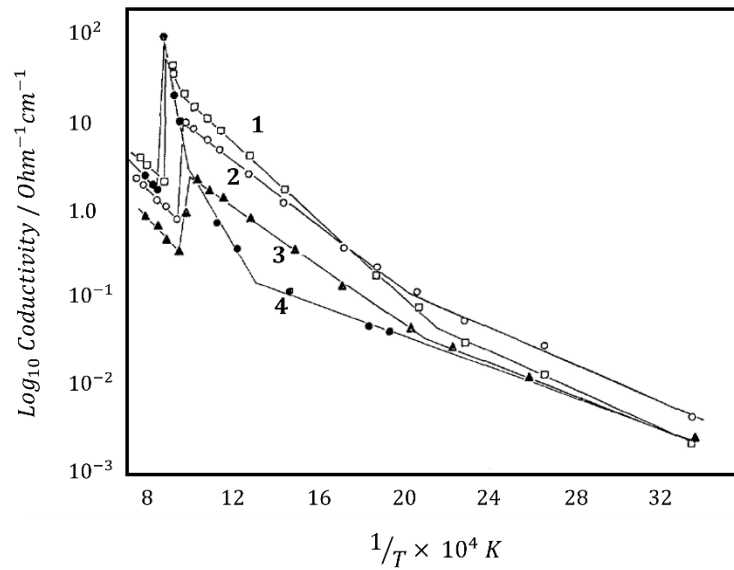


**Figure I.10.** Electrical conductivity of (1) CoO, (2) Co<sub>0.9</sub>Ni<sub>0.1</sub>O, (3) Co<sub>0.667</sub>Ni<sub>0.333</sub>O and (4) Co<sub>0.5</sub>Ni<sub>0.5</sub>O as a function of temperature in air [58].

Nguyen and de Nora [57] used Co<sub>x</sub>Ni<sub>1-x</sub>O as a protective coating for Ni-Fe alloy in aluminum electrolysis. CoO was chosen as it can work as a barrier for the fluorination of Ni-Fe alloys. However, CoO is likely to be converted into Co<sub>3</sub>O<sub>4</sub> under Al electrolysis conditions,

according to phase diagram of the Co-O system. The calculated oxygen potential phase diagrams of Co-O and Ni-O systems are demonstrated in Fig. I.11 and I.12.

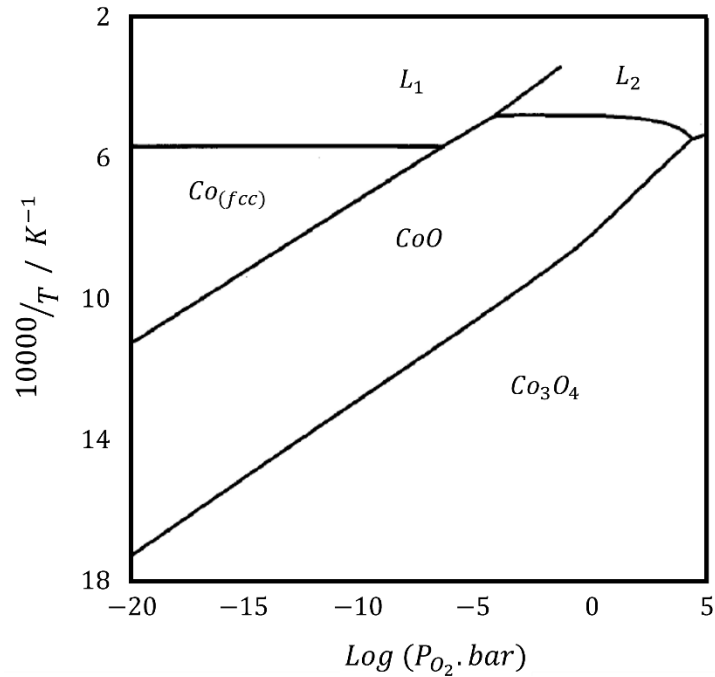


Figure I.11. Calculated oxygen potential phase diagram of Co-O system [63].

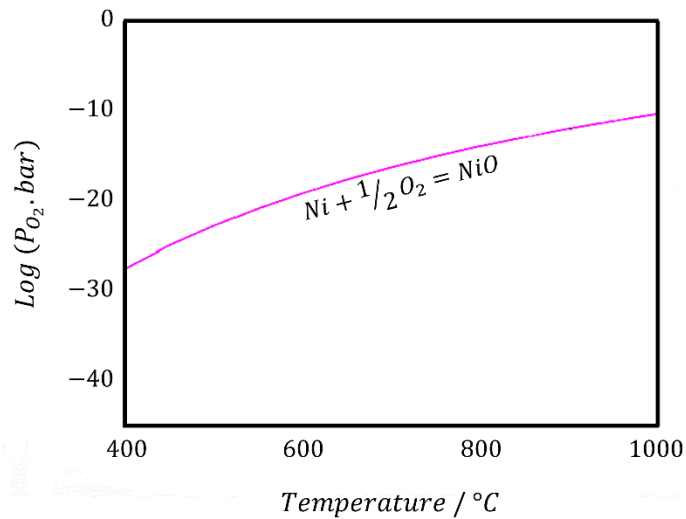
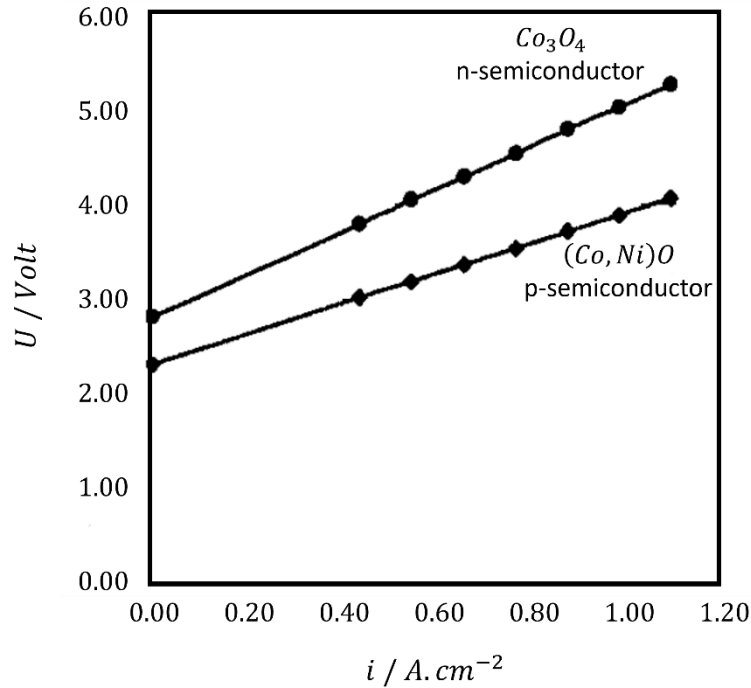


Figure I.12. Oxygen potential phase diagram of Ni-O system [64].

The formation of  $Co_3O_4$  is not desired as it is an n-type semiconductor that displays a significantly higher  $O_2$  evolution overpotential than p-type semiconductor  $CoO$ . The oxygen over-

potentials of CoO and Co<sub>3</sub>O<sub>4</sub> coatings measured at 930 °C in molten cryolite is presented in Fig. I.13.



**Figure I.13. Oxygen over-potentials of (Co,Ni)O and Co<sub>3</sub>O<sub>4</sub> coatings measured at 930 °C in molten cryolite [57].**

It has been shown that adding Ni atoms to CoO and forming (Co,Ni)O solid solutions helps in preventing the decomposition of CoO to Co<sub>3</sub>O<sub>4</sub> at elevated temperatures. Thus, to make a (Co,Ni)O-based protective coating, Nguyen and de Nora first electrodeposited a Co-Ni alloy onto the NiFe anode, then (Co,Ni)O solid solution coating was formed by a following oxidation treatment in air at high temperature. The electrolysis was carried out at 930 °C with a current density of 1 A.cm<sup>-1</sup> using a sodium-based electrolyte with addition of AlF<sub>3</sub>, CaF<sub>2</sub> and KF. Under these conditions, at least 15 % of nickel must be added to CoO to prevent its transformation to Co<sub>3</sub>O<sub>4</sub>. As explained before, formation of a nickel ferrite layer at the surface of the anode will prevent its further oxidation. Thus, to prevent any further over-potentials, the oxygen over-potential of (Co,Ni)O must be lower than that of NiFe<sub>2</sub>O<sub>4</sub>. Nguyen and de Nora measured the over-potential of carbon anode as well as NiFe<sub>2</sub>O<sub>4</sub> and Co<sub>0.85</sub>Ni<sub>0.15</sub>O coatings on metallic anode under operating conditions in electrolyte bath at 930 °C. Their results are shown in Fig. I.14.

Their results after a long electrolysis (2 months) showed that the metallic core of the anode was maintained intact under the protective (Co,Ni)O coating and an underlying oxide layer formed between the metallic anode and the oxide coating. The measured dissolution rate of (Co,Ni)O was about 3 mm per year. The cell voltage remained relatively stable around 4.5 V during the whole electrolysis time. Also, after 30 days electrolysis, the degree of metal contamination was measured and from 1340 ppm total metal impurities, the impurities of nickel and cobalt were 940 and 270 ppm, respectively [57].

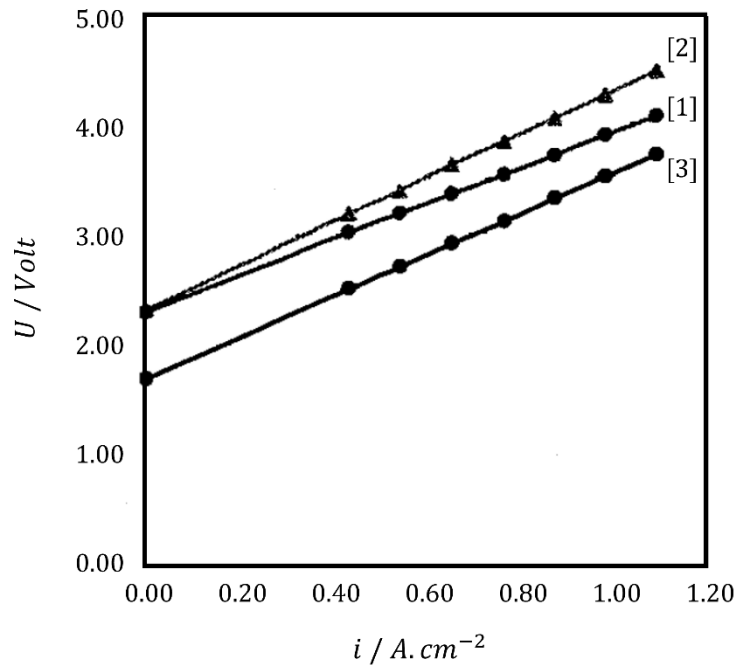


**Figure I.14. Oxygen over-potentials of (1)  $Co_{0.85}Ni_{0.15}O$  coating, (2)  $NiFe_2O_4$  coating on metallic anode and (3) carbon anode measured at 930 °C in molten cryolite [57].**

The solubility of NiO in molten cryolite-alumina at 1020 °C was also measured by Jentoftsen et al. [65]. They investigated the effects of temperature, cryolite composition and alumina concentration on the solubility of NiO in molten cryolite. Prior to their work, the nickel solubility at 1000 °C in pure cryolite and in cryolite with 6 wt% alumina was reported 0.32 and 0.25 wt%, respectively. Jentoftsen et al. prepared tablets of high purity NiO by sintering NiO powder at 1300 °C. Their experiments were carried out in a closed furnace in argon atmosphere and the nickel content of the samples was measured by Inductively coupled plasma (ICP) method. The Ni solubility in cryolite at 1020 °C in cryolite was 0.33 and 0.006 wt% for pure cryolite and cryolite with saturation of alumina, respectively.

These results confirmed that (Co,Ni)O are promising materials as a protective coating for NiFe anode. However, due to the change of densities upon oxidation of the metallic Co-Ni alloy, producing a cohesive, crack-free oxide layer on the inert anode as required for Al electrolysis, using electrodeposition + oxidation process may be challenging. It is thus essential to find a procedure to prepare thick, single phase, adherent and crack-free coating at the surface of metallic anodes, in a single step with a relatively high efficiency. A potentially more relevant method to produce (Co,Ni)O coated inert anodes, is through the direct deposition of (Co,Ni)O oxide compounds by thermal spray techniques such as suspension plasma spray (SPS) and high velocity oxygen fuel (HVOF). Although (Co,Ni)O solid solutions have been prepared previously using calcination method with multiple steps, large amount of (Co,Ni)O solid solution has never been produced with a single step method using ball-milling a mixture of CoO and NiO or Co<sub>3</sub>O<sub>4</sub> and NiO powders as well as using a single step calcination of Co<sub>3</sub>O<sub>4</sub> and NiO powders. The large-scale production methods as well as coating techniques used in this thesis to prepare and study (Co,Ni)O materials will be discussed below.

#### I.4.3. Synthesis by mechanical alloying

Mechanical alloying (MA) is a simple and scalable technique to synthesize equilibrium and metastable phases. Reactions in MA occur in the solid-state by providing mechanical energy instead of thermal energy; therefore, reactions in mechanical alloying do not always follow the phase diagrams restrictions and limitations. As a result, both equilibrium and non-equilibrium (metastable) materials can be prepared in powder form by MA process [66]. MA was invented in 1960 by Benjamin (The International Nickel Company (INCO)) and was used in industry from the beginning. His work consisted of hardening iron and nickel-based superalloys for aerospace applications by dispersing yttrium and thorium oxide particles which was not possible via common casting methods [67]. Subsequently during the 1970s and in the early 1980s, the reaction mechanisms in MA were widely studied [68–70] and amorphous Y-Co [71] and Ni-Nb [72] alloys were produced from their elementary powders through MA technique. Since then, MA has been widely used to manufacture amorphous materials [73], supersaturated [74], nanostructured [75], quasi-crystalline [76], novel alloys and composites [77] thanks to its versatility, high scalability and low production costs [78].

#### I.4.4. Principles of mechanical alloying

The mechanical alloying process consists of placing the powder mixture with intended proportion into the milling media (balls and crucible). Generally, the powder mixture is subjected to the high energy impacts of the milling balls together and with the crucible wall. Although the average amount of energy per collision as well as the rotation speed and direction, vary in different types of mills, the process mechanism is identical. This mechanism is comprised of repeated cold welding and fracture of the ingredients powder particles [69]. Fig. I.15 illustrates the different stages that occur during the mechanical alloying. The mechanisms occurring during the ball-milling may differ depending on the ductility of the starting powders.

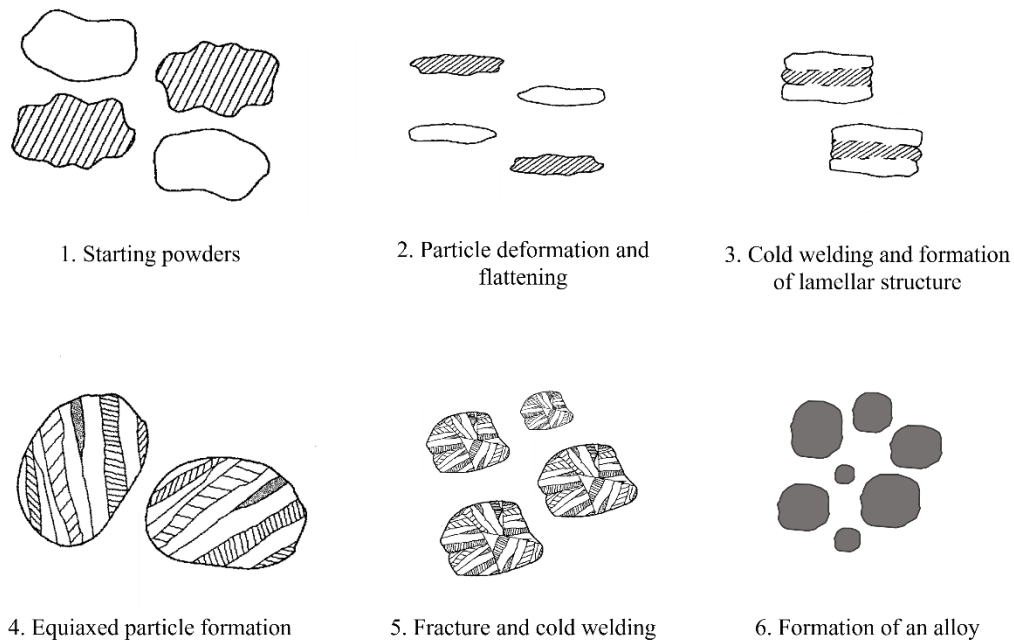


**Figure I.15. Schematic of different stages of the mechanical alloying leading to the formation of an alloy.**

In grinding two ductile materials, after the initial powder particles are mixed in the first step, particles tend to agglomerate in the elongated shapes as they are subjected to repeated high energy impacts. At this stage, the particles are plastically deformed to form thin and long lamellae. Cold-welding is the dominant phenomenon which causes the size of the particles increases, and different layers are welded together. Subsequently, the lamellae weld together to form a multilayer

lamellar structure, composed of a stack of layers, oriented in one direction with different compositions of those of the starting materials. By extending the grinding time, the powder particles are deformed plastically due to the high energy collisions, causing many defects in the crystalline structure of the starting materials. As the number of defects increases, the particles are hardened and cracks initiate, propagate and grow in the material. The particles are fractured in this stage and the fracturing rate is higher than the cold-welding rate, which decreases the size of the particles. As the grinding continues, a balance is then reached between the rates of cold-welding and fracturing. The particle size distribution is narrow because the size of the large particles decreases by fracturing at the same rate as the size of the small particles increases by cold-welding. The powder particles are deformed plastically due to the high energy collisions, causing significant number of defects in the crystalline structure of the starting materials including dislocations, gaps, stacking defects and grain boundaries. These structural defects combined with the localized increase in temperature and decrease in the distance between layers promote the interdiffusion of elements. The interdiffusion continues until all layers of a particle have the same composition. As a particle is broken down and welded to another particle, the same phenomenon will be repeated. This procedure must continue for the sufficient length of time until a steady state is reached when the composition of every powder particle is the same as the starting powder mixture composition and a homogeneous alloy is thus formed. Further milling does not lead to any noticeable change in the composition of the powder particles.

The mechanosynthesis can be used with a mixture of two powders with different hardness as in a metal-oxide mixture. In this case, the particle size of the hard powder decreases gradually, and by extending the grinding time, the fine fractured particles (brittle material) dispersed between the interlamellar spaces of the ductile material. It will enrich the ductile material with structural defects and lead to hardening and then fracturing. Thus, the ductile particles tend toward a narrow particle size distribution. If these two components have a low solubility or are insoluble, the ball-milling will lead to a uniform dispersion of the brittle phase in the ductile phase. If the two phases are soluble, an alloy will form. Oxide dispersion strengthened (ODS) type materials can be formed with such a mechanism [67].

Finally, in the mechanosynthesis of two hard powders, fracture is dominant, and the welding step never takes place. During grinding, the powders particle size decreases until they

reach their fracturing limit. This limitation is possible because below a certain size, the particles can deform plastically, reducing the tendency to fracture. Since there is a difference between the hardness of the fine powders, the hardest particles will be inserted into the most ductile ones to form granular particles. The plastic deformation is limited, thus, the lamellar particles will not form. Note that unlike the lamellar particles, in the granular particles, the diffusion distances are too great, and the density of defects is too low for interdiffusion to occur quantitatively to form an alloy. In this case, the formation of an alloy will be thermally activated. The collision of the particles and the grinding media will increase locally the temperature which will favor the interdiffusion of the elements between two neighboring particles to finally lead to the formation of an alloy. The formation of alloys from Si-Ge or Mn-Bi powders or from amorphous alloys or from intermetallic powders are examples of such a system [79].

#### I.4.5. Mechanosynthesis of oxide solid solution

Mechanical alloying is a suitable process for the synthesis of oxide solid solution powders given its simplicity, low cost and the possibility of production on an industrial scale. An oxide solid solution is usually composed of two oxides with the same crystal structure where one of them is considered as a host structure (the solvent) and the ions of the other oxide (the solute) dissolve and replace those of the solvent oxide. The purpose of using mixed oxides (oxide solid solution) is to relatively combine the properties of the pure oxides. To form an oxide solid solution over the whole composition range, the starting oxides must have similar crystal structures, quite close lattice parameters and ionic radius, as explained by Hume-Rothery rules [80]. Preparing the oxide solid solutions by traditional solid-state reactions requires either prolonged calcination at high temperatures or several manufacturing steps to obtain the final product. These manufacturing steps may include dissolving the metals in acids or organic compounds, followed by several heating steps and eliminating the organic contents. These materials can be prepared in a direct method at room temperature by mechanosynthesis without generating troublesome wastes or using of toxic organic solvents. Ball-milling can be used as a rather fast, simple and single step technique for producing oxide solid solutions over the whole composition range at room temperature by grinding the desired proportions of the constituent oxides. Indeed, mechanosynthesis has been widely used to prepare oxide solid solutions. For example, the formation of  $(\text{Sn,Ru})\text{O}_2$ ,  $(\text{Zr}_{1-x}\text{Ti}_x)\text{O}$ ,  $x\text{In}_2\text{O}_3(1-$

$x$ ) $\alpha$ -Fe<sub>2</sub>O<sub>3</sub>, (Mg<sub>x</sub>Ni<sub>1-x</sub>)O, Y<sub>2</sub>(Ti<sub>(1-y)</sub>Zr<sub>y</sub>)<sub>2</sub>O<sub>7</sub> from their pure oxide powders by mechanosynthesis has been reported [80–84].

#### 1.4.6. Ball-milling parameters

As previously explained, the solid-state reaction in mechanosynthesis process is based on energy transfer from the collisions of the powder particles with grinding media. Several parameters can affect this process and the properties of the obtained powder such as its particle size distribution, stoichiometry, microstructure and chemical homogeneity. The type of mill, milling time, grinding media, ball-to-powder mass ratio (BPR), and the use of a process control agent (PCA) are examples of these parameters. The influence of these variables on the final product obtained will be discussed in this section.

- **Type of mill**

Different types of grinding mills can be classified into attritor, planetary and shaker mills. These mills differ in terms of their capacities and efficiency of milling, grinding energy and the movements of crucible and balls. Some mills can be equipped with additional arrangements for cooling and heating as well as atmosphere to control the temperature and atmosphere during the grinding. Two types of mills that have been used in this thesis will be introduced in order of their typical capacities.

- *Shaker mills*

Shaker mills have the lowest powder capacity (up to 20 grams of the powder) and the highest crucible speed (about 1200 rpm). The SPEX 8000 is an example of such mills which usually consists of one crucible secured in a clamp. This crucible has an energetically back and forth motion while its end has lateral movements, simultaneously. The overall motion of the crucible appears as an 8 or infinity sign shape which forces the balls to move with high velocities (on the order of 5 m.s<sup>-1</sup>) and impact with great forces. This provides high frequency of impacts between the powder particles, the crucible walls and the milling balls. Fig. I.16 represents the SPEX 8000 which is most commonly used for laboratory investigations. The crucible in SPEX

ball-mill can be made of steel (hardened steel or stainless steel), ceramics (alumina, zirconia, silicon nitride), plastic and tungsten carbide.

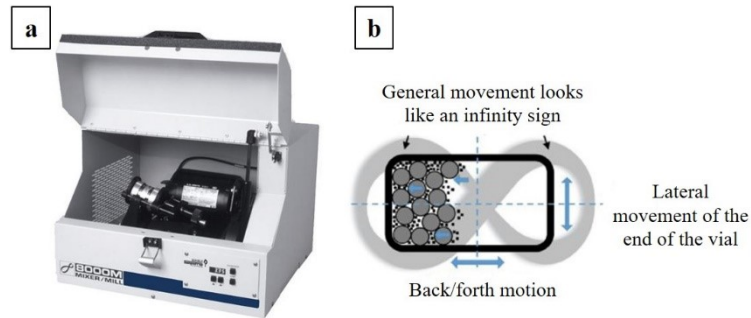


Figure I.16. (a) SPEX 8000 mixer/mill and (b) 2D representation of the crucible movement.

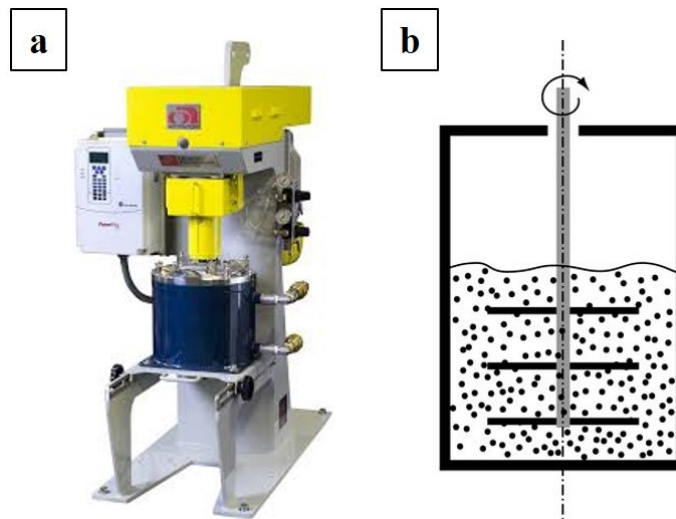


Figure I.17. (a) Union process, model S-1 laboratory attritor and (b) schematic of the interior of the crucible.

- *Attritors*

Attritors are used for large quantities powder milling (0.5 to 40 kg at a time) in laboratories and even in industries. Attritors consist of a large double wall container, half-filled with small balls, that can be cooled with water to control the grinding temperature, and a rotating shaft with arms. The grinding atmosphere can be controlled by introducing a gas flow into the crucible. The rotation of shaft agitates the balls and the powder within the crucible which makes the powder being ground (as shown in Fig. I.17). The grinding rate increases with the rotation speed of the

shaft. The velocity of the balls and the frequency of impacts in attritors ( $0.5 \text{ m}\cdot\text{s}^{-1}$  and 70 Hz) are much lower than those of shaker mills. Thus, longer grinding time is required in attritors.

- **Grinding medium**

As previously mentioned, the grinding media can be made of various materials including different types of steel (hardened, tempered, bearing or stainless steel), tungsten carbide, and different types of ceramic. Usually, the crucible and the balls are made of the same materials and the same material as the powder being milled, whenever possible, to prevent cross contamination. The materials used in the grinding medium must have a high hardness and a good erosion resistance to limit contamination of the powder while transferring the impact energy as much as possible.

The size of the grinding balls must be chosen carefully, as it can affect the milling efficiency and the products. The grinding balls with a large size will transfer more impact energy [85] and reduce the adhesion of powder to the grinding tools [86] while the smaller balls elevate the formation of amorphous phases [87,88]. A combination of large and small balls will randomize the motion of the balls and provide the most optimum milling conditions with the highest collision energy [66]. It has been reported that the geometry of the grinding tools has an influence on the product. Substitution of the ball with cylinders increases shear stresses in the powder particles instead of compression stresses, as a result, it reduces the contamination in the final product and promote the reduction of the particle size [89].

- **Ball-to-powder mass ratio (BPR)**

Although there is a wide range of ball-to-powder mass ratio (BPR) used by different investigators varying from 1:1 to 220:1, this variable must be chosen very carefully as it has a strong effect on the grinding time and the contamination in the final product. The higher BPR provides higher impact energy and results in shorter grinding time. An excessively high BPR may increase the contamination in the final product by the grinding materials [90]. On the other hand, a small BPR is useful to form metastable alloys, as using high BPR will increase the temperature inside the crucible and favors the formation of the thermodynamically stable crystalline phases [91,92]. Beside the materials being ground, BPR depends on the type of mill. For small capacity

mills like SPEX, usually ratio of 10:1 is most commonly used while for an attritor, it can be as high as 50:1 or even 100:1.

- **Process control agent (PCA)**

As explained earlier, cold-welding and fracturing are the main mechanisms in mechanosynthesis, and the formation of the new phases occurs only when there is a balance between these two mechanisms. Powder particles of the ductile materials have greater tendency in cold-welding than fracturing. As a result, powder particles can get agglomerated or stuck on the grinding tools. This is disadvantageous because it decreases the grinding yield and increases the contamination. It can also result in deviation from the desired composition if there is a preferential adhesion to the grinding tools in the ball-milled powders. A process control agent (PCA), acting as a surfactant, can easily solve this problem by reducing the cold-welding and limiting the agglomeration. The PCAs are mostly organic materials such as stearic acid, methanol, ethanol and hexane that absorb on the surfaces of the particles and prevent excessive cold-welding by decreasing their surface tension. It should be noted that the required amount of PCAs are mostly as low as 1 to 5 wt% of the total powder [66]. A large quantity of PCA results in decreasing the particle size, increasing the grinding time and contaminating the powder by carbon, oxygen or hydrogen while a lower addition of PCA reduces the powder yield. In fact, the required amount of PCA depends on the ductility and the quantity of the milled powder as well as chemical and thermal stability of the PCA material.

- **Contamination of the milled powder**

The contamination of the milled powder by grinding tools materials, atmosphere or by additives such as PCA, is one of the major problems of mechanosynthesis method. The level of contamination can be unacceptably high when reactive metals like titanium and zirconium are being milled or when a very long milling time is required. The ball-milling process continuously produces new surfaces with large surface area which favors the contamination of the milled powder. To overcome this problem, high-purity powder materials as well as high-purity atmosphere should be used, and the milling time must be as short as possible. In addition, the grinding tools (crucible and balls) must be chosen the same material as the powder being milled,

whenever possible. Otherwise, the grinding tools can be self-coated by the small amount of the milled material within a short grinding process, then the desired amount of powder can be milled.

#### I.4.7. Synthesis by calcination

Calcination is a process of heating a substance or a mixture of materials in a controlled temperature and atmosphere. In calcination, reactions occur in solid state without fusion by providing the required thermal energy. The objectives of calcination can be categorized into (a) manufacturing new materials (synthesis), (b) oxidizing a part or the whole of a substance, (c) removing volatile substances and (d) thermal decomposition or phase transition. The holding time, calcining temperature and atmosphere as well as heating and cooling rates can affect the calcination process and its final products. The synthesis temperature can be defined based on the calcination of similar compounds or by considering the phase diagrams. Thermal analysis methods such as thermogravimetric analysis (TGA) can effectively determine reactions occurring upon heating a material under the intended atmosphere. The kinetics of the reaction and the required calcination time must be investigated by an isothermal step at the onset temperature in the TGA graph. The holding time and temperature depend on heating rate, quantity of materials along with the physical and chemical properties of the substances, e.g., particle size and thermal conductivity. A longer calcining time is needed when the heating rate is too high to ensure all parts of sample reach the same temperature. To ensure the completion of reaction in calcination, all particles of the substances should be subjected to the same conditions and in case of heating under a gas flow, a sufficient quantity of gas should be supplied to provide the same environment. To perform calcination, furnaces with different size and shape are available in laboratory and industrial scales. These furnaces differ in terms of their sizes, maximum temperature, the possibility of controlling heating or cooling rates and introducing an atmosphere. Furnaces can be equipped with additional arrangements to control the atmosphere (oxidizing, reducing, inert, etc.) inside the furnace during the heat treatment.

## I.5. Thermal spray techniques

Thermal spray coating is a process in which thick coatings are prepared by the deposition of metallic and non-metallic materials in a molten or semi-molten condition. In thermal spray, a stream of high temperature gas is produced by plasma or combustion where powders, wires and suspensions are heated, melted (or semi-melted) and accelerated toward a substrate. The combination of thermal and kinetic energies allows an excellent bonding of the particles with the surface of the substrate upon impact. Thus, the final coating is comprised of layers of splats which are formed on the substrate by the deformation of accelerated molten (or semi-molten) particles or droplets as they reach the surface (Fig. I.18). It must be noted that the particle melting and solidification in thermal spray processes occur in a very short time (a few microseconds to a few milliseconds) with a very strong temperature gradient which can result in the formation of metastable phases [93].

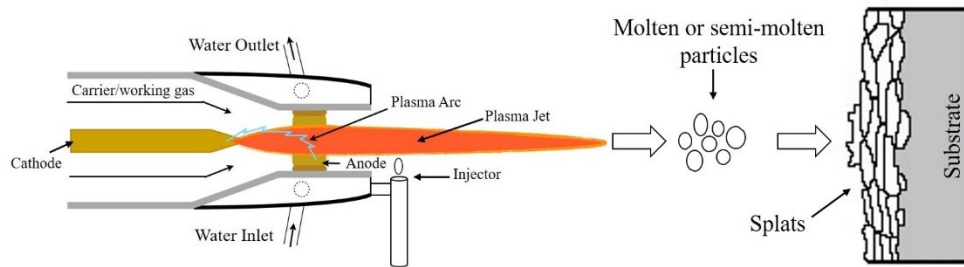


**Figure I.18. Schematic representation of a thermal plasma spraying process.**

Thermal spray was invented in the 1910s by M.U. Schoop who published several patents on different aspects of the flame and arc spray processes and commercialized them. In his patents, metallic or ceramic powders as well as wires or rods of various materials were used to deposit a coating through thermal spray methods. Schoop predicted the future developments of thermal spray and explained how layers of coating can be produced by atomizing the liquefied metal through a high velocity flow of air/inert gas or an electrical arc [94–96]. In the mid-1950s, Thermal Dynamics Corporation, Metco and Plasmadyne developed the first plasma spray torches which are the basis of many of the torches that are being used today. Before the invention of plasma spray torches, the thermal spray mostly consisted of flame or arc spray [47]. Since the 1960s, the

industrial requirements, especially in the aerospace industry, led to an accelerating pace of improvements in the thermal spray technology in terms of materials, applications, devices and processes. Thereafter, thermal spray has been widely used in aerospace, automotive, paper and printing, medical and dental, power, textile and chemical industries [97]. The applications of coatings obtained by thermal spray include wear and corrosion-resistant coatings, thermal insulation, abradable and abrasive coatings, biomaterials coatings and polymer coatings.

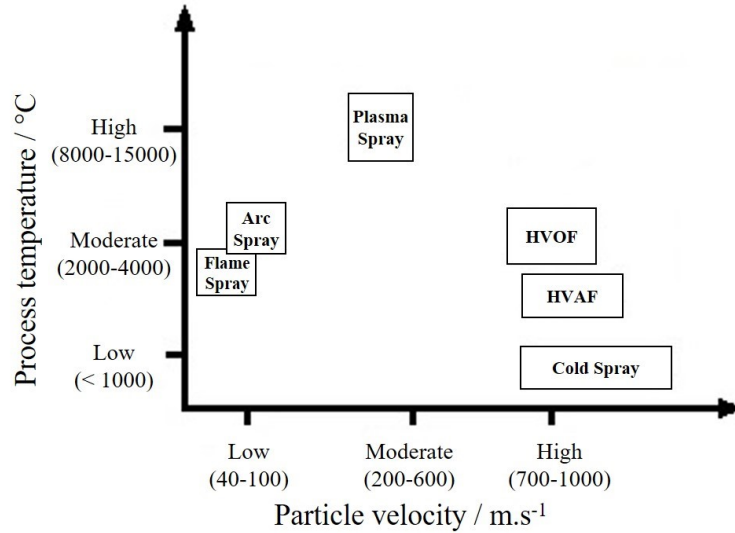


**Figure I.19. Schematic presentation of the combination of process temperature and velocity for the different spray processes [99].**

Thermal spray techniques can be categorized into two main groups based on the way energy or heat is provided. In the first category, the high temperature stream is created by a plasma which is produced by dissipation of electrical energy. Wire arc spraying, plasma transferred arc (PTA) deposition, atmospheric plasma spray (APS) and suspension plasma spray (SPS) are examples of this category. In the second group, the heat is provided through a combustion like the flame spraying of powders and wire as well as the high-velocity oxygen fuel (HVOF) and the high-velocity air fuel (HVAF) processes. Fig. I.19 shows the particle velocity and the process temperature in different thermal spray techniques. Among various thermal spraying methods, suspension plasma spray (SPS) and high-velocity oxygen fuel (HVOF) have demonstrated a great capability to produce oxide coatings which are usually difficult to coat with other conventional coating methods such as electrodeposition, sintering and vacuum deposition [98]. The principal

and the important variables in these two methods are explained below. Fig. I.20 summarizes some of the parameters affecting the thermal spray processes.

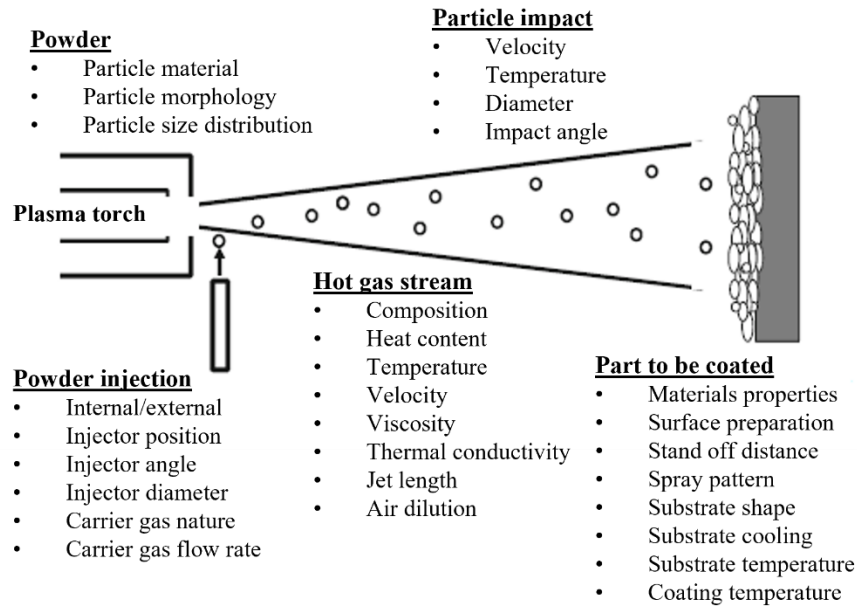


**Figure I.20. Different spray parameters in thermal spray processes [47].**

### I.5.1. Suspension Plasma Spray (SPS)

In plasma spraying, a plasma is generated by an electric arc between a cylindrical anode nozzle and a rod-shaped cathode. By injecting the plasma gas between the two electrodes, the gas is heated and accelerated which produces a jet with high temperature and high velocity. The temperature and velocity of the plasma gas depends on torch design, plasma gases, and operating parameters and may reach to a temperature as high as 12,000–15,000 K and a velocity range between 200 to 500 m.s<sup>-1</sup>. Powder particles, dispersed in a solvent (usually water or ethanol), are introduced into the plasma jet, heated and accelerated toward the substrate. Thus, SPS includes injection of a suspension of submicron solid particles into the plasma jet, atomization and evaporation of the liquid phase, and then melting and acceleration toward a substrate where the particles form layers of splats and eventually the coating. The SPS torch can move relative to the substrate and/or the substrate can move relative to the torch and thus a uniform coating can be

deposited all over the substrate surface. The thickness of coating is controlled by the number of plasma/particle jet passes over the substrate.

The difficulties associated with feeding, injection and then transportation of fine powder particles in a hot plasma jet, through the conventional powder plasma spray process such as atmospheric plasma spray, raise the need for a novel approach to overcome these problems. In fact, fine powder particles, due to their low weight, do not have enough momentum at the exit of the nozzle to properly enter the hot region of plasma jet.

Suspension plasma spray (SPS) was invented in 1994 by Gitzhofer et al. [48] in the University of Sherbrooke, Canada. Their invention consisted of an injection system for spraying a suspension of solid particles dispersed in a liquid carrier. This injection system resolved the feeding problems in conventional plasma spray system for spraying particles smaller than 10 microns.

The feed system in the primary SPS torches injected the suspension radially which raised several issues including the effective heat and momentum transfer from the plasma to the suspension droplets. To overcome these problems, Oberste-Berghaus et al. [100] filed a patent for a new axial feed system which can generate high gas velocities and plasma temperatures due to high total plasma power. Fig. I.21 shows a schematic of this feed system.

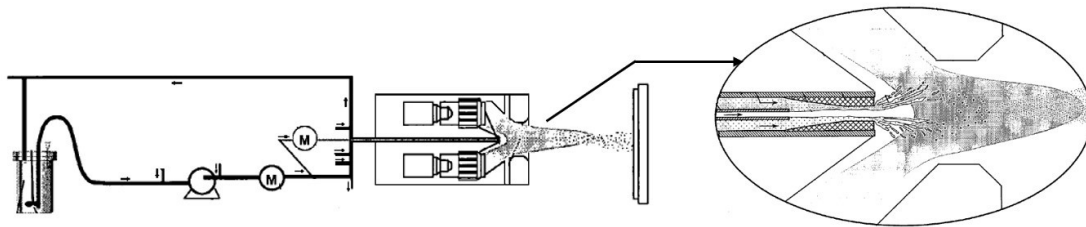


**Figure I.21. Schematic side view of an axial feed system in DC plasma torches [100].**

Sulzer-Metco developed a Triplex torch which is comprised of three cathodes supplied by three independent electric sources resulting in three arcs attaching at a single anode. The ring-shaped anode in this torch is separated from the cathode by some insulating rings. Such a design allows the generation of longer electric arcs, higher arc voltage and higher efficiency in heating the particles [101]. These improvements significantly enhance the efficiency of the process and

increase the application of SPS process in deposition of various coatings. Different types of coatings in terms of shape, coating porosity and materials composition can be prepared by SPS deposition. The spray conditions in SPS (high temperature and high velocity) make it the preferred method for spraying high temperature ceramics and oxides. However, to obtain a desirable coating thorough SPS process, several parameters must be adjusted.

### I.5.2. Spray parameters in SPS

More than 60 process parameters are adjustable in SPS process which allow the deposition of a wide range of materials on different substrates. However, controlling all these variables can be very complicated and requires special effort and knowledge. These operating parameters can be adjusted by a process control console which contains the safety interlocks too. The most important parameters in plasma spray process can be categorized into two groups: those related to the plasma torch e.g., arc current, plasma gas composition, and plasma jet environment, and those related to the particles and suspension e.g., feed rate, particle morphology and size distribution. Individually considering the effect of the SPS process parameters is very difficult since they are not usually independent. The impact of some of these variables is explained below.

- **Plasma gas composition and flow rate**

The gas composition and flow rates are controlled separately in the control console. Different combinations of gases can be mixed and introduced into the plasma torch. The most used gas as primary gas in SPS process is argon which is heavy enough to efficiently push the arc root downstream and has a low energy density to prevent the torch erosion. The secondary gas plays a key role in increasing the power density, gas velocity, and the heat transfer rates to powders. Helium, nitrogen and hydrogen are the most used ones as secondary gas in SPS. A combination of nitrogen and hydrogen as secondary gas could provide high deposition rates and high-power levels. Therefore, usually an optimal spray condition is obtained with a ternary gas mixture of Ar-N<sub>2</sub>-H<sub>2</sub> or Ar-N<sub>2</sub>-He. It must be noted that using helium instead of hydrogen in the plasma gas mixture may result in a less reductive environment.

The total gas flow and gas composition have an impact on the characteristics of the coating. Tarasi et al. [102] studied the effect of total plasma gas flow and gas composition on the properties

of the alumina-zirconia ceramics coatings deposited by SPS. They showed that using helium instead of hydrogen has the strongest influence on the obtained coating as it has higher viscosity at high temperatures which increases the plasma stability. Substitution of hydrogen with helium in SPS results in a slightly lower particle velocity but a higher heat conduction and thus a higher average particle temperature. The produced ceramic coatings had lower porosities when helium was used instead of hydrogen in the plasma gas. They also illustrated that increasing the total plasma gas flow rate will enhance both particles temperature and velocity. Although the parameters affecting the plasma spray conditions are not dependant, they concluded that the density of vertical and horizontal cracks in the coatings, increased when the total gas flow rate increased. Fig. I.22 shows the effect of the gas composition and the plasma power on particles temperature and velocity.

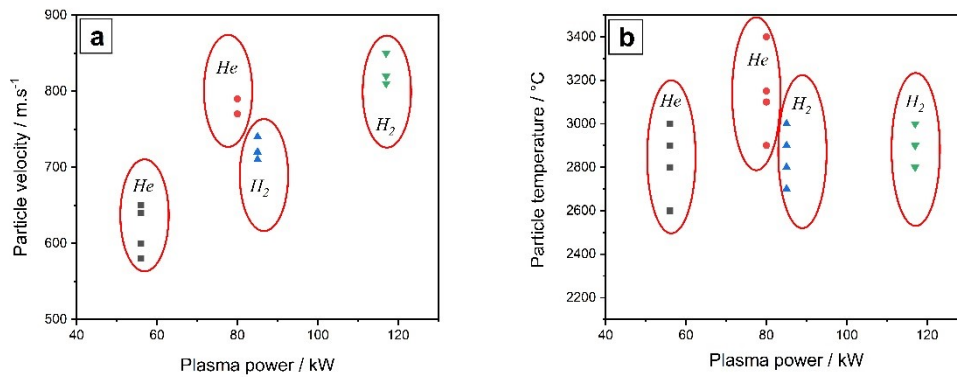


**Figure I.22. Gas composition and plasma power effects on (a) particle velocity and (b) particle temperature, redrawn from [102].**

- **Plasma power**

There are a lot of parameters that affect the plasma power such as plasma gas flow rate, plasma gas composition and current. It must be noted that torch power and plasma power are not identical, since a part of enthalpy in torch dissipates with the cooling water stream which is used in the torch to prevent it from overheating. Increasing the total gas flow rate leads a higher plasma power if all other parameters retain constant. Significantly higher plasma power can be obtained with a slight addition of H<sub>2</sub> to the plasma gas mixture. The impact of the plasma power on the quality of the coating is considerable. It has been shown that denser coatings and higher deposition

efficiencies are obtained when higher plasma powers were applied, since a better in-flight melting condition and a higher heat transfer efficiency were realized [103,104].

- **Particle morphology and size distribution**

The morphology and particle size distribution of the raw powders must be verified before the spray process. The size and shape of powders affects their flow and compaction properties. Typically, the suspension made of smaller particles has higher stability. The powder particles must be first analysed with optical or scanning electron microscopies to observe their morphology. Then the size and distribution widths of the powder particles must be measured through a particle size distribution (PSD) analysis. Many techniques used for measuring the particle size distribution make the general assumption that every particle is a sphere and report the equivalent value as its diameter. Therefore, it is necessary to observe the particle with microscopes to recognize the particles shapes. Suspension plasma spray process is developed to coat particles with submicron size, because the deposition of submicron particles with other thermal spray processes such as atmospheric plasma spray or HVOF can be very challenging. In SPS, generally it is essential to have powders with particle size smaller than 10  $\mu\text{m}$  ( $D_{90} < 10 \mu\text{m}$ ). However, to prevent clogging feeding system and increase the deposition efficiency, it is preferable to have particles smaller than 3  $\mu\text{m}$  ( $D_{90} < 3 \mu\text{m}$ ).

Morphology and shape of the particles have a strong effect on the temperature and velocity of the particles during the thermal spray. The heat transfer to the particles, specially in materials with poor thermal conductivities, may differ depending on the particle size and shape. The morphology of particles affects their aerodynamic behaviours which can result in different thermal conductivities, diffusivities and particle heat treatments. All these differences have a strong influence on the properties of the produced coating. Fauchais et al. [105] reported that the particle velocity and temperature are dependent to their size since the particle momentum during the plasma spray varies as a function of the cube of their diameter and a broader particle size distribution results in a more difference in particle momentums. The investigations of Kulkarni et al. [106] on the effect of particle size on the microstructure of the produced coating revealed that decreasing the average powder diameter can increase the velocity of depositing droplets, which yields thinner lamellae and affects the coating thermal conductivity. Also, Tarasi et al. [102]

showed that changing the particles from micron to nano size particles, decreases the in-flight particle temperature as well as the microcrack densities in the produced coating.

### 1.5.3. High Velocity Oxygen Fuel (HVOF)

High velocity oxygen fuel technique was invented in 1958 by Union Carbide (Praxair Surface Technology) but it was not introduced commercially until 1983 when James Browning patented a HVOF system to deposit WC–Co cermet coatings for aerospace industry application [107]. In HVOF, a mixture of an oxidizer (oxygen) and a fuel (a hydrocarbon molecule ( $C_xH_y$ ) such as propylene, ethylene or propane) is used to produce a combustion in a chamber. The produced supersonic jet goes through a convergent-divergent Laval nozzle, which is connected to the chamber, where a very high gas velocity can be achieved. In fact, the high velocity of particles in HVOF is obtained by using this convergent-divergent Laval nozzle and applying higher gas pressures inside the chamber. Coating materials can be injected in powder, liquid or suspension forms from a radial or an axial injector. Different types of materials, including metals, cermets and ceramics have been deposited by HVOF, and the targeted applications are diverse such as wear and corrosion resistant coatings, and coatings acting as thermal barrier for high-temperature applications [53–55,108–111].

Unlike plasma spray, the particles in HVOF usually are not completely melted during the deposition, since the process temperature in HVOF is much lower than in plasma spray, as shown in Fig. I.19. In HVOF, only small particles or a part of large particles are melted before depositing on the substrate, since the particle temperature is usually below the melting point of coating materials. However, the high velocity of the particles causes them to form a dense stack of flattened droplets on the substrate, resulting in smooth, uniform coatings with good adhesion to the substrate. Usually, the residence time of the powder in the flame is shorter and the flame temperature is lower than in plasma spray methods, which further reduces the possibility that the powder is reduced, oxidized or decomposed, or that undesired phase transformation occurs during spraying [47]. Therefore, HVOF is preferred to form coatings with low porosity and good adhesion to the substrate without any phase transformations.

#### I.5.4. Particle temperature and velocity in HVOF

As mentioned above, the velocity and temperature of particles are key parameters in HVOF spraying. The process temperature in HVOF is much lower than plasma spraying; also, particles travel from the torch to the substrate with much higher velocities. Combining a lower temperature and a higher velocity prevents undesired phase transformation that usually occurs at high temperatures, especially above the melting point. The temperature and velocity of particles in HVOF depends on several parameters such as particle size, fuel/oxygen ratio, carrier gas flow rate, chamber pressure, total gas flow rate, injection system (axial or radial), powder feed rate and using a shroud.

It has been shown that a slightly higher particle temperature is achieved when the gas pressure augments while the particle velocity linearly increases with increasing the gas pressure [112]. The particle temperature and velocity inside the chamber and after exiting the gun strongly depend on their size. Small particles (particles smaller than 10  $\mu\text{m}$ ) rapidly reach to the gas temperature inside gun but after exiting the gun, their temperature decreases drastically as their travel through air to reach the substrate. 10 to 20  $\mu\text{m}$  particles reach the gas temperature inside the gun and cooled down continuously as they exit the gun. Large particles (with diameters larger than 20  $\mu\text{m}$ ) never reach the gas temperature but their temperature remains almost unchanged until they deposit on the substrate because of their high thermal inertia. Particles with diameters smaller than 10  $\mu\text{m}$  travel with the highest velocity as they exit the gun while the velocity of larger particles decreases as their particle size increases [113,114].

#### I.5.5. Fuel/oxygen (F/A) ratio

One of the most important parameters in HVOF spraying is the F/A ratio (richness),  $R'$ , which is the ratio of fuel to oxygen. This ratio has a strong impact on velocity and temperature at the exit of HVOF torch. As explained above, in HOVF, the flame is produced with a reaction between a hydrocarbon molecule and an oxidizer. When the reaction is stoichiometric, all carbon and hydrogen atoms react with oxygen and the highest combustion temperature will be obtained. If there is an excess of oxygen or fuel, the reaction will not be stoichiometric; the excess of oxygen will not participate in the combustion reaction and will be heated to the combustion temperature

without being burned which results in a decrease in the final gas temperature. If there is an excess of fuel, it will be heated by the combustion and the final temperature will be lower as well. Different studies and simulations show that the flame temperature reaches a peak when the richness (fuel to oxygen ratio) is close to 1 [115,116], as shown in Fig. I.23.

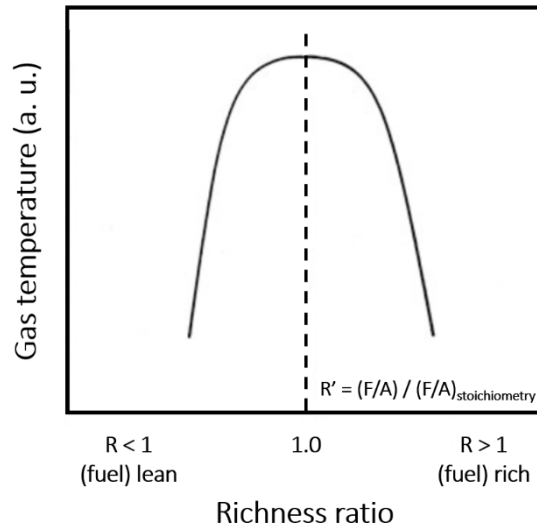


**Figure I.23. Variation of gas temperature as a function of richness ratio [112].**

## References

- [1] Aluminium Association of Canada. (AAC), Sustainable Development Report, 2017.
- [2] Energy Technology Transitions for Industry, OECD, 2009. doi:10.1787/9789264068612-en.
- [3] E. Skybakmoen, A. Solheim, Å. Sterten, Alumina solubility in molten salt systems of interest for aluminum electrolysis and related phase diagram data, *Metall. Mater. Trans. B.* 28 (1997) 81–86. doi:10.1007/s11663-997-0129-9.
- [4] J. Thonstad, P. Fellner, G.M. Haarberg, J. Hives, H. Kvarde, A. Sterten, *Aluminium Electrolysis: Fundamentals of the Hall-Herault Process*, 3rd ed, Aluminium-Verlag, Düsseldorf, Germany, 2001.
- [5] L. Cassayre, T.A. Utigard, S. Bouvet, Visualizing Gas Evolution on Graphite and Oxygen-Evolving Anodes, *J. Met.* (2002) 41–45. doi:https://doi.org/10.1007/BF02701696.
- [6] W.E. Haupin, A Scanning Reference Electrode for Voltage Contours in Aluminum

- Smelting Cells, *J. Met.* 23 (1971) 46–49. doi:<https://doi.org/10.1007/BF03355737>.
- [7] International Aluminum Institute (IAI), Primary Aluminum Production, Accessible at: <http://www.world-aluminium.org/statistics/>, Accessed on: 05/16/2019, n.d.
- [8] H. Kvande, W. Haupin, Inert anodes for Al smelters: Energy balances and environmental impact, *JOM.* 53 (2001) 29–33. doi:10.1007/s11837-001-0205-6.
- [9] W. Haupin, H. Kvande, Thermodynamics of Electrochemical Reduction of Alumina, in: *Essent. Readings Light Met.*, Springer International Publishing, Cham, 2016: pp. 160–165. doi:10.1007/978-3-319-48156-2\_22.
- [10] Y.X. Liu, J. Thonstad, Oxygen overvoltage on SnO<sub>2</sub>-based anodes in NaF-AlF<sub>3</sub>-Al<sub>2</sub>O<sub>3</sub> melts. Electrocatalytic effects of doping agents, *Electrochim. Acta.* 28 (1983) 113–116. doi:10.1016/0013-4686(83)85093-2.
- [11] J. Thonstad, A. Kiswa, J. Hives, Anode overvoltage on metallic inert anodes in low-melting bath, *Light Met.* 1 (2006) 373–380.
- [12] A.D. McLeod, J.S. Haggerty, D.R. Sadoway, Inert anode materials for Hall cells, *Light Met.* 1986. 2 (1986) 269–273.
- [13] International Aluminium Institute, Life cycle inventory data and environmental metrics for the primary aluminium industry, n.d. <http://www.world-aluminium.org/>.
- [14] International Aluminium Institute (IAI), Perfluorocarbon (PFC) Emissions, Accessible at: <http://www.world-aluminium.org/statistics/perfluorocarbon-pfc-emissions/>, Accessed on: 05/16/2019, n.d.
- [15] The Aluminum Association, Inert anode roadmap: A framework for technology development, Washington, 1998, (n.d.).
- [16] N. Jarrett, Production of aluminium and alumina, Volume 20, 1987. <http://books.google.com/books?id=949TAAAAMAAJ&pgis=1>.
- [17] H. Kvande, P.A. Drabløs, The Aluminum Smelting Process and Innovative Alternative Technologies, *J. Occup. Environ. Med.* 56 (2014) S23–S32. doi:10.1097/JOM.0000000000000062.
- [18] J.N. Hryn, D.R. Sadoway, Cell testing of metal anodes for aluminum electrolysis, *Light Met.* (1993) 475.
- [19] J.N. Hryn, M.J. Pellin, E.S. Division, M. Society, S. Diego, Dynamic inert metal anode, *Light Met.* (1999) 377.
- [20] Z. Shi, J. Xu, Z. Qiu, An Iron-Nickel Metal Anode for Aluminum Electrolysis, *Light Met. TMS (The Miner. Met. Mater. Soc.)* (2004) 1–5.

- [21] V.M.D. D.A. Simakov, E.V. Antipov, M.I. Borzenko, S.Y. Vassiliev, Y.A. Velikodny, Nickel and Nickel Alloys Electrochemistry in Cryolite-Alumina Melts, *Light Met. TMS (The Miner. Met. Mater. Soc. (2007) 489–493.*
- [22] V. De Nora, T.T. Nguyen, J.-J. Duruz, Aluminium electrowinning cells with metal-based anodes, WO2004035871A1, n.d.
- [23] J.J. Duruz, V. De Nora, The Dynamic Equilibrium of a Self-Forming Anode, Fall Meet. Electrochem. Soc. (1986).
- [24] T. Nguyen, V. de Nora, De Nora oxygen evolving inert metallic anode, *Light Met. (2006) 385–390.*
- [25] Siba P. Ray, X. Liu, J. A., Douglas Weirauch, Inert anode containing oxides of nickel iron and cobalt useful for the electrolytic production of metals - US6372119B1.pdf, US6372119B1, 2002.
- [26] A.P. Apisarov, A.E. Dedyukhin, A.A. Red'kin, O.Y. Tkacheva, Y.P. Zaikov, Physicochemical properties of KF-NaF-AlF<sub>3</sub> molten electrolytes, *Russ. J. Electrochem. 46 (2010) 633–639.* doi:10.1134/S1023193510060066.
- [27] A. Solheim, Å. Sterten, Activity Data for the System NaF-AlF<sub>3</sub>, in: Ninth Int. Symp. Light Met. Prod. Tromsø-Trondheim, Norw., n.d.: p. Proceedings, p. 225/34.
- [28] R. Chen, G. Wu, Q. Zhang, Phase Diagram of the System KF–AlF<sub>3</sub>, *98 (2000) 3196–3198.* doi:<https://doi.org/10.1111/j.1151-2916.2000.tb01703.x>.
- [29] J. Híveš, J. Thonstad, Electrical conductivity of low-melting electrolytes for aluminium smelting, *Electrochim. Acta. 49 (2004) 5111–5114.* doi:10.1016/j.electacta.2004.06.022.
- [30] Z. Fang, K. Zhang, X. Lü, L. Li, J. Zhu, J. Li, Alkali metals (K and Na) penetration and its effects on expansion of TiB<sub>2</sub>-C composite cathode during aluminum electrolysis, *Trans. Nonferrous Met. Soc. China. 23 (2013) 1847–1853.* doi:10.1016/S1003-6326(13)62669-2.
- [31] L. Cassayre, P. Palau, P. Chamelot, L. Massot, Properties of Low-Temperature Melting Electrolytes for the Aluminum Electrolysis Process: A Review, *J. Chem. Eng. Data. 55 (2010) 4549–4560.* doi:10.1021/je100214x.
- [32] H. Alder, Process for the electrolysis of a molten charge using inconsumable bi-polar electrodes, US3930967A, 1976.
- [33] T.R. Beck, R.J. Brooks, Electrolytic reduction of alumina, US5006209A, 1991.
- [34] T.R. Beck, C.W. Brown, Aluminum low temperature smelting cell metal collection, US6419812B1, 1991.
- [35] S. Helle, B. Brodu, B. Davis, D. Guay, L. Roué, Influence of the iron content in Cu-Ni based inert anodes on their corrosion resistance for aluminium electrolysis, *Corros. Sci. 53 (2011)*

- 3248–3253. doi:10.1016/j.corsci.2011.05.069.
- [36] S. Helle, M. Tresse, B. Davis, D. Guay, L. Roué, Mechanically Alloyed Cu-Ni-Fe-O Based Materials as Oxygen-Evolving Anodes for Aluminum Electrolysis, *J. Electrochem. Soc.* 159 (2012) E62. doi:10.1149/2.028204jes.
- [37] S. Helle, B. Davis, D. Guay, L. Roué, Ball-Milled (Cu-Ni-Fe + Fe<sub>2</sub>O<sub>3</sub>) Composite as Inert Anode for Aluminum Electrolysis, *J. Electrochem. Soc.* 160 (2013) E55–E59. doi:10.1149/2.084306jes.
- [38] L.R. G. Goupil, G. Bonnefont, H. Idrissi, D. Guay, Consolidation of mechanically alloyed Cu–Ni–Fe material by spark plasma sintering and evaluation as inert anode for aluminum electrolysis, *J. Alloys Compd.* 580 (2013) 256–261. doi:https://doi.org/10.1016/j.jallcom.2013.05.128.
- [39] S. Jucken, M.H. Martin, E. Irissou, B. Davis, D. Guay, L. Roué, Cold-Sprayed Cu-Ni-Fe Anodes for CO<sub>2</sub>-Free Aluminum Production, *J. Therm. Spray Technol.* 29 (2020) 670–683. doi:10.1007/s11666-020-01002-z.
- [40] S. Jucken, E. Schaal, B. Tougas, B. Davis, D. Guay, L. Roué, Impact of a post-casting homogenization treatment on the high-temperature oxidation resistance of a Cu-Ni-Fe alloy, *Corros. Sci.* 147 (2019) 321–329. doi:10.1016/j.corsci.2018.11.037.
- [41] L.R. S. Helle, M. Pedron, B. Assouli, B. Davis, D. Guay, Structure and high-temperature oxidation behaviour of Cu–Ni–Fe alloys prepared by high-energy ball milling for application as inert anodes in aluminium electrolysis, *Corros. Sci.* 52 (2010) 3348–3355. doi:https://doi.org/10.1016/j.corsci.2010.06.011.
- [42] T.R. Beck, A non-consumable metal anode for production of aluminum with low temperature fluoride melts, *Light Met.* (1995) 355. doi:10.1007/978-3-319-48200-2\_147.
- [43] N.C.W. T.R. Beck, C.M. MacRae, Metal Anode Performance in Low-Temperature Electrolytes for Aluminum Production, *Metall. Mater. Trans. B.* 42B (2011) 807–813. doi:10.1007/s11663-011-9511-8.
- [44] R.B. I. Gallino, M.E. Kassner, Oxidation and corrosion of highly alloyed Cu–Fe–Ni as inert anode material for aluminum electrowinning in as-cast and homogenized conditions, *Corros. Sci.* 63 (2012) 293–303. doi:https://doi.org/10.1016/j.corsci.2012.06.013.
- [45] L.R. E. Gavrilova, G. Goupil, B. Davis, D. Guay, On the key role of Cu on the oxidation behavior of Cu–Ni–Fe based anodes for Al electrolysis, *Corros. Sci.* 101 (2015) 105–113.
- [46] G. Goupil, S. Helle, B. Davis, D. Guay, L. Roué, Anodic behavior of mechanically alloyed Cu–Ni–Fe and Cu–Ni–Fe–O electrodes for aluminum electrolysis in low-temperature KF-AlF<sub>3</sub> electrolyte, *Electrochim. Acta.* 112 (2013) 176–182. doi:10.1016/j.electacta.2013.08.157.
- [47] P.L. Fauchais, J.V.R. Heberlein, M.I. Boulos, *Thermal Spray Fundamentals*, Springer US,

- Boston, MA, 2014. doi:10.1007/978-0-387-68991-3.
- [48] F. Gitzhofer, E. Bouyer, M.I. Boulos, Suspension Plasma Spray (SPS), US5609921A, 1994.
- [49] P. Fauchais, R. Etchart-Salas, V. Rat, J.F. Coudert, N. Caron, K. Wittmann-Ténèze, Parameters Controlling Liquid Plasma Spraying: Solutions, Sols, or Suspensions, *J. Therm. Spray Technol.* 17 (2008) 31–59. doi:10.1007/s11666-007-9152-2.
- [50] P. Fauchais, G. Montavon, R.S. Lima, B.R. Marple, Engineering a new class of thermal spray nano-based microstructures from agglomerated nanostructured particles, suspensions and solutions: an invited review, *J. Phys. D. Appl. Phys.* 44 (2011) 093001. doi:10.1088/0022-3727/44/9/093001.
- [51] M. Aghasibeig, F. Tarasi, R.S. Lima, A. Dolatabadi, C. Moreau, A Review on Suspension Thermal Spray Patented Technology Evolution, *J. Therm. Spray Technol.* 28 (2019) 1579–1605. doi:10.1007/s11666-019-00904-x.
- [52] F. Wu, Y. Huang, L. Song, X. Liu, Y. Xiao, J. Feng, J. Chen, Method for preparing porous hydroxyapatite coatings by suspension plasma spraying, US8877283B2, 2009.
- [53] M. Oksa, E. Turunen, T. Suhonen, T. Varis, S.-P. Hannula, Optimization and Characterization of High Velocity Oxy-fuel Sprayed Coatings: Techniques, Materials, and Applications, *Coatings*. 1 (2011) 17–52. doi:10.3390/coatings1010017.
- [54] M. Jones, A.. Horlock, P.. Shipway, D.. McCartney, J.. Wood, A comparison of the abrasive wear behaviour of HVOF sprayed titanium carbide- and titanium boride-based cermet coatings, *Wear*. 251 (2001) 1009–1016. doi:10.1016/S0043-1648(01)00702-5.
- [55] W. Brandl, D. Toma, J. Krüger, H.J. Grabke, G. Matthäus, The oxidation behaviour of HVOF thermal-sprayed MCrAlY coatings, *Surf. Coatings Technol.* 94–95 (1997) 21–26. doi:10.1016/S0257-8972(97)00470-2.
- [56] M. Chen, B. Hallstedt, L.J. Gauckler, Thermodynamic assessment of the Co-O system, *J. Phase Equilibria*. 24 (2003) 212–227. doi:10.1361/105497103770330514.
- [57] T. Nguyen, V. De Nora, De Nora oxygen evolving inert metallic anode, *TMS Light Met. In: Gallow* (2006) 385–390.
- [58] R.J. Moore, J. White, Equilibrium relationships in the system NiO-CoO-O<sub>2</sub>, *J. Mater. Sci.* 9 (1974) 1393–1400. doi:10.1007/BF00552924.
- [59] B. Bergman, J. Agren, Immiscibility in the CoO-NiO System, *J. Am. Ceram. Soc.* 69 (1986) C-248-C-250. doi:10.1111/j.1151-2916.1986.tb07352.x.
- [60] T. Sakata, K. Sakata, K. Kigoshi, On the Resistivity and Crystal Structure of Binary Oxide of Nickel and Cobalt, *J. Phys. Soc. Japan*. 10 (1955) 179–186. doi:10.1143/JPSJ.10.179.
- [61] K. Takizawa, A. Hagiwara, Behavior of CoO-NiO Solid Solution in Molten Carbonate, *J.*

- Electrochem. Soc. 148 (2001) A1034. doi:10.1149/1.1390345.
- [62] S. Kuboon, Y.H. Hu, Study of NiO–CoO and Co<sub>3</sub>O<sub>4</sub>–Ni<sub>3</sub>O<sub>4</sub> Solid Solutions in Multiphase Ni–Co–O Systems, *Ind. Eng. Chem. Res.* 50 (2011) 2015–2020. doi:10.1021/ie101249r.
- [63] M. Chen, B. Hallstedt, L.J. Gauckler, Thermodynamic assessment of the Co–O system, *J. Phase Equilibria*. 24 (2003) 212–227. doi:10.1361/105497103770330514.
- [64] Y. Wang, X. Lei, Y. Zhang, F. Chen, T. Liu, In-situ growth of metallic nanoparticles on perovskite parent as a hydrogen electrode for solid oxide cells, *J. Power Sources*. 405 (2018) 114–123. doi:10.1016/j.jpowsour.2018.10.023.
- [65] T.E. Jentoftsen, O.-A. Lorentsen, E.W. Dewing, G.M. Haarberg, J. Thonstad, Solubility of some transition metal oxides in cryolite-alumina melts: Part I. Solubility of FeO, FeAl<sub>2</sub>O<sub>4</sub>, NiO, and NiAl<sub>2</sub>O<sub>4</sub>, *Metall. Mater. Trans. B*. 33 (2002) 901–908. doi:10.1007/s11663-002-0073-7.
- [66] C. Suryanarayana, Mechanical alloying and milling, *Prog. Mater. Sci.* 46 (2001) 1–184. doi:10.1016/S0079-6425(99)00010-9.
- [67] J.S. Benjamin, Dispersion strengthened superalloys by mechanical alloying, *Metall. Trans.* 1 (1970) 2943–2951. doi:10.1007/BF03037835.
- [68] I.G. Wright, B.A. Wilcox, Observations on strengthening and oxidation behavior of a dispersion hardened Fe–Cr–Base alloy prepared by mechanical alloying, *Metall. Trans.* 5 (1974) 957–960. doi:10.1007/BF02643157.
- [69] S.N. Patankar, S.-Q. Xiao, J.J. Lewandowski, A.H. Heuer, The mechanism of mechanical alloying of MoSi<sub>2</sub>, *J. Mater. Res.* 8 (1993) 1311–1316. doi:10.1557/JMR.1993.1311.
- [70] J.S. Benjamin, Mechanical Alloying, *Sci. Am.* 234 (1976) 40–49. <http://www.jstor.org/stable/24950349>.
- [71] A.Y. Yermakov, Y.Y. Yurchikov, V.A. Barinov, Magnetic Properties of amorphous powders of Y–Co alloys produced by mechanical alloying, *Phys. Met. Metallogr.* 52 (1981) 50–58.
- [72] C.C. Koch, O.B. Cavin, C.G. McKamey, J.O. Scarbrough, Preparation of “amorphous” Ni<sub>60</sub>Nb<sub>40</sub> by mechanical alloying, *Appl. Phys. Lett.* 43 (1983) 1017–1019. doi:10.1063/1.94213.
- [73] L. Schultz, Formation of amorphous metals by mechanical alloying, *Mater. Sci. Eng.* 97 (1988) 15–23. doi:10.1016/0025-5416(88)90004-3.
- [74] H.J. Fecht, G. Han, Z. Fu, W.L. Johnson, Metastable phase formation in the Zr–Al binary system induced by mechanical alloying, *J. Appl. Phys.* 67 (1990) 1744–1748. doi:10.1063/1.345624.

- [75] Y. Chen, M.J. Conway, J.D. Fitzgerald, Carbon nanotubes formed in graphite after mechanical grinding and thermal annealing, *Appl. Phys. A Mater. Sci. Process.* 76 (2003) 633–636. doi:10.1007/s00339-002-1986-3.
- [76] J. Eckert, L. Schultz, K. Urban, Formation of quasicrystals by mechanical alloying, *Appl. Phys. Lett.* 55 (1989) 117–119. doi:10.1063/1.102394.
- [77] M. Sherif El-Eskandarany, Mechanical solid state mixing for synthesizing of SiCp/Al nanocomposites, *J. Alloys Compd.* 279 (1998) 263–271. doi:10.1016/S0925-8388(98)00658-6.
- [78] C. Suryanarayana, E. Ivanov, V. Boldyrev, The science and technology of mechanical alloying, *Mater. Sci. Eng. A.* 304–306 (2001) 151–158. doi:10.1016/S0921-5093(00)01465-9.
- [79] C.C.K. R.M. Davis, B. McDermott, Mechanical alloying of brittle materials, *Metall. Trans. A.* 19A (1988) 2867–2874.
- [80] J. Gaudet, A.C. Tavares, S. Trasatti, D. Guay, Physicochemical Characterization of Mixed RuO<sub>2</sub>-SnO<sub>2</sub> Solid Solutions, *Chem. Mater.* 17 (2005) 1570–1579. doi:10.1021/cm048129l.
- [81] L. Kong, J. Ma, W. Zhu, O. Tan, Phase formation and thermal stability of (Zr<sub>1-x</sub>Ti<sub>x</sub>)O<sub>2</sub> solid solution via a high-energy ball milling process, *J. Alloys Compd.* 335 (2002) 290–296. doi:10.1016/S0925-8388(01)01844-8.
- [82] M. Sorescu, T. Xu, L. Diamandescu, Synthesis and Characterization of Indium Oxide Doped Hematite xIn<sub>2</sub>O<sub>3</sub>·(1-x)α-Fe<sub>2</sub>O<sub>3</sub> Solid Solution, *MRS Proc.* 1309 (2011) mrsf10-1309-ee09-11. doi:10.1557/opl.2011.104.
- [83] N. Setoudeh, C. Zamani, M. Sajjadnejad, Mechanochemical Synthesis of Nanostructured Mg<sub>1-x</sub>Ni<sub>x</sub>O Compound by Mg-NiO Mixture, 50 (2017) 51–59. doi:10.7508/JUFGNSM.2017.01.07.
- [84] K.J. Moreno, R.S. Rodrigo, A.F. Fuentes, Direct synthesis of A<sub>2</sub>(Ti<sub>1-y</sub>Zr<sub>y</sub>)<sub>2</sub>O<sub>7</sub> (A=Gd<sup>3+</sup>, Y<sup>3+</sup>) solid solutions by ball milling constituent oxides, *J. Alloys Compd.* 390 (2005) 230–235. doi:10.1016/j.jallcom.2004.07.059.
- [85] W.J.S. D. Gavrilov, O. Vinogradov, Computer Simulation of Mechanical Alloying in a Shaker Ball Mill No Title, in: 10th Int. Conf. Vol 3; Process. Manuf. 1995; Whistler; Canada, Woodhead Publishing Limited, Whistler, 1995: pp. 11–18.
- [86] L. Takacs, M. Pardavi-Horvath, Nanocomposite formation in the Fe<sub>3</sub>O<sub>4</sub>-Zn system by reaction milling, *J. Appl. Phys.* 75 (1994) 5864–5866. doi:10.1063/1.355543.
- [87] K.B. Gerasimov, A.A. Gusev, E.Y. Ivanov, V. V. Boldyrev, Tribochemical equilibrium in mechanical alloying of metals, *J. Mater. Sci.* 26 (1991) 2495–2500. doi:10.1007/BF01130201.

- [88] W. Guo, S. Martelli, M. Magini, Effect of alloying addition on structure and thermal stability of Ti40Al60 prepared by mechanical alloying, *Acta Metall. Mater.* 42 (1994) 411–417. doi:10.1016/0956-7151(94)90496-0.
- [89] M.S. El-Eskandarany, K. Aoki, K. Suzuki, Rod milling for solid-state formation of Al30Ta70 amorphous alloy powder, *J. Less Common Met.* 167 (1990) 113–118. doi:10.1016/0022-5088(90)90295-U.
- [90] M.S. El-Eskandarany, K. Aoki, H. Itoh, K. Suzuki, Effect of ball-to-powder weight ratio on the amorphization reaction of Al50Ta50 by ball milling, *J. Less Common Met.* 169 (1991) 235–244. doi:10.1016/0022-5088(91)90072-C.
- [91] W. Guo, A. Iasonna, M. Magini, S. Martelli, F. Padella, Synthesis of amorphous and metastable Ti40Al60 alloys by mechanical alloying of elemental powders, *J. Mater. Sci.* 29 (1994) 2436–2444. doi:10.1007/BF00363438.
- [92] C. Suryanarayana, E. Ivanov, R. Noufi, M.A. Contreras, J.J. Moore, Phase selection in a mechanically alloyed Cu2013;In–Ga–Se powder mixture, *J. Mater. Res.* 14 (1999) 377–383. doi:10.1557/JMR.1999.0055.
- [93] P. Fauchais, M. Fukumoto, A. Vardelle, M. Vardelle, Knowledge Concerning Splat Formation: An Invited Review, *J. Therm. Spray Technol.* 13 (2004) 337–360. doi:10.1361/10599630419670.
- [94] Schoop M.U, Improvements in or connected with the coating of surfaces with metal, applicable also for Soldering or Uniting Metals and other Materials., 5,712, 1910. United Kingdom Patent No. A.D 5,712 U. K. P.
- [95] Schoop M.U, An Improved Process of Applying Deposits of Metal or Metallic Compounds to Surfaces., 21,066, 1911. United Kingdom Patent No. A.D.21066. U. K. P. Office.
- [96] Schoop M.U, Apparatus for Spraying Molten Metal and Other Fusible Substances., 1,133,507, 1915. USA Patent No.A1,133,507. U. S. P. Office.
- [97] B. Walser, The importance of thermal spray for current and future applications in key industries, *Spraytime.* 10 (2004) 1–7.
- [98] X. Fei, Y. Niu, H. Ji, L. Huang, X. Zheng, A comparative study of MoSi<sub>2</sub> coatings manufactured by atmospheric and vacuum plasma spray processes, *Ceram. Int.* 37 (2011) 813–817. doi:10.1016/j.ceramint.2010.10.018.
- [99] L.M. Berger, Application of hardmetals as thermal spray coatings, *Int. J. Refract. Met. Hard Mater.* 49 (2015) 350–364. doi:10.1016/j.ijrmhm.2014.09.029.
- [100] J. Oberste-Berghaus, S. Bouaricha, J.-G. Legoux, C. Moreau, B. Harvey, Method and Apparatus for Fine Particle Liquid, US8629371B2, 2005.
- [101] P. Fauchais, M. Vardelle, A. Vardelle, S. Goutier, What Do We Know, What are the Current

- Limitations of Suspension Plasma Spraying?, *J. Therm. Spray Technol.* 24 (2015) 1120–1129. doi:10.1007/s11666-015-0286-3.
- [102] F. Tarasi, M. Medraj, A. Dolatabadi, J. Oberste-Berghaus, C. Moreau, Effective Parameters in Axial Injection Suspension Plasma Spray Process of Alumina-Zirconia Ceramics, *J. Therm. Spray Technol.* 17 (2008) 685–691. doi:10.1007/s11666-008-9259-0.
- [103] D. Waldbillig, O. Kesler, Effect of suspension plasma spraying process parameters on YSZ coating microstructure and permeability, *Surf. Coatings Technol.* 205 (2011) 5483–5492. doi:10.1016/j.surfcoat.2011.06.019.
- [104] X. Chen, S. Kuroda, T. Ohnuki, H. Araki, M. Watanabe, Y. Sakka, Effects of Processing Parameters on the Deposition of Yttria Partially Stabilized Zirconia Coating During Suspension Plasma Spray, *J. Am. Ceram. Soc.* 99 (2016) 3546–3555. doi:10.1111/jace.14393.
- [105] P. Fauchais, G. Montavon, G. Bertrand, From Powders to Thermally Sprayed Coatings, *J. Therm. Spray Technol.* 19 (2010) 56–80. doi:10.1007/s11666-009-9435-x.
- [106] A. Kulkarni, A. Vaidya, A. Goland, S. Sampath, H. Herman, Processing effects on porosity-property correlations in plasma sprayed yttria-stabilized zirconia coatings, *Mater. Sci. Eng. A.* 359 (2003) 100–111. doi:10.1016/S0921-5093(03)00342-3.
- [107] J.A. Browning, Highly concentrated supersonic liquid material flame spray method and apparatus, 4,416,421, 1983.
- [108] J. Oberste Berghaus, J.-G. Legoux, C. Moreau, R. Hui, C. Decès-Petit, W. Qu, S. Yick, Z. Wang, R. Maric, D. Ghosh, Suspension HVOF Spraying of Reduced Temperature Solid Oxide Fuel Cell Electrolytes, *J. Therm. Spray Technol.* 17 (2008) 700–707. doi:10.1007/s11666-008-9249-2.
- [109] M. Gaona, R.S. Lima, B.R. Marple, Influence of particle temperature and velocity on the microstructure and mechanical behaviour of high velocity oxy-fuel (HVOF)-sprayed nanostructured titania coatings, *J. Mater. Process. Technol.* 198 (2008) 426–435. doi:10.1016/j.jmatprotec.2007.07.024.
- [110] F. Tarasi, M. Medraj, A. Dolatabadi, J. Oberste-Berghaus, C. Moreau, High-Temperature Performance of Alumina-Zirconia Composite Coatings Containing Amorphous Phases, *Adv. Funct. Mater.* 21 (2011) 4143–4151. doi:10.1002/adfm.201100471.
- [111] E. Turunen, T. Varis, J. Keskinen, T. Fält, S.P. Hannula, Improved Mechanical Properties by Nanoreinforced Ceramic Composite HVOF Coatings, *Adv. Sci. Technol.* 45 (2006) 1240–1245. doi:10.4028/www.scientific.net/AST.45.1240.
- [112] I. Glassman, *Combustion*, Academic Press, New York, 1977. doi:10.1016/B978-0-12-285850-5.X5001-6.
- [113] D. Cheng, Q. Xu, E.J. Lavernia, G. Trapaga, The effect of particle size and morphology on

the in-flight behavior of particles during high-velocity oxyfuel thermal spraying, *Metall. Mater. Trans. B.* 32 (2001) 525–535. doi:10.1007/s11663-001-0037-3.

- [114] V.R. Srivatsan, A. Dolatabadi, Simulation of Particle-Shock Interaction in a High Velocity Oxygen Fuel Process, *J. Therm. Spray Technol.* 15 (2006) 481–487. doi:10.1361/105996306X147126.
- [115] S. Gu, C.N. Eastwick, K.A. Simmons, D.G. McCartney, Computational Fluid Dynamic Modeling of Gas Flow Characteristics in a High-Velocity Oxy-Fuel Thermal Spray System, *J. Therm. Spray Technol.* 10 (2001) 461–469. doi:10.1361/105996301770349231.
- [116] Y.-M. Yang, H. Liao, C. Coddet, Simulation and Application of a HVOF Process for MCrAlY Thermal Spraying, *J. Therm. Spray Technol.* 11 (2002) 36–43. doi:10.1361/105996302770348952.

## II. Chapter 2:

# **Experimental details and characterisation methods**

## II.1. Powder synthesis

Small amount (~ 2 grams) of  $\text{Co}_x\text{Ni}_{1-x}\text{O}$  solid solution powders ( $x = 0.15 - 0.85$ ) were prepared by two different methods. In the first method, the solid solutions were synthesized by high energy ball-milling (HEBM) starting with CoO and NiO powders. CoO was itself prepared from  $\text{Co}_3\text{O}_4$  powder heated under argon at 900 °C for 3 hours, while NiO was purchased and used as-received. HEBM was performed using a SPEX 8000M laboratory mill. The powder mixture was introduced into a tungsten carbide crucible (capacity of 41 ml) with three tungsten carbide balls (two with a diameter of 7.5 mm and one with a diameter of 11 mm, total mass of 18.3 g). The ball-to-powder mass ratio (BPR) was fixed at 10:1. Stearic acid (0.5 wt %) was added to the initial powder mixture as process control agent (PCA) to prevent excessive cold welding. The ball-milling time was set at 20 hours. Since the powder synthesis using ball-milling resulted in a tungsten carbide (WC) contamination due to the erosion of the WC milling tools, in the second procedure, (Co,Ni)O solid solutions were prepared by a heat treatment procedure. In that case, as-received  $\text{Co}_3\text{O}_4$  and NiO powders were first mixed by hand or by a short (12 min) ball-milling and then heat treated in air at 1000 °C for 10 h. The (Co,Ni)O powders were let to cool down naturally at room temperature in air. These powders were used to determine the possibility of formation of (Co,Ni)O solid solutions over the whole composition range and investigate their thermal stability at elevated temperatures. A list of the materials used to synthesize (Co,Ni)O is presented in the Table II.1.

**Table II.1. Characteristics of powders used for (Co,Ni)O synthesis.**

Materials	Granulometry	Purity	Supplier
$\text{Co}_3\text{O}_4$	-325 mesh	$\geq 99.7\%$	Alfa Aesar
NiO	-325 mesh	$\geq 99\%$	Cerac
Stearic acid	---	$\geq 95\%$	Sigma-Aldrich

For deposition by SPS, a  $\text{Co}_{0.5}\text{Ni}_{0.5}\text{O}$  solid solution powder was prepared in kg quantity through a three-step process that involves 12 min ball-milling step of a mixture of NiO and  $\text{Co}_3\text{O}_4$  with the targeted 50 – 50 mol% of Co and Ni in an attritor, followed by a heat treatment at 1000 °C for 10 h and a final 3 h ball-milling step to reduce the powder particle size to under 3  $\mu\text{m}$  to

meet the SPS requirements. For other SPS depositions, mixtures of as-received CoO and NiO powders with different ratios were used as starting materials.

For deposition by HVOF,  $\text{Co}_x\text{Ni}_{1-x}\text{O}$  with  $x = 0.75$  and  $0.5$  was synthesized by mixing  $\text{Co}_3\text{O}_4$  and NiO powders followed by a 12 h heat treatment at  $1200\text{ }^\circ\text{C}$  in air. Cobalt oxide (CoO) was also prepared by heating  $\text{Co}_3\text{O}_4$  at  $1200\text{ }^\circ\text{C}$  for 12 hours under an argon flow, with a subsequent rapid cooling to prevent the conversion of CoO to  $\text{Co}_3\text{O}_4$  upon cooling. All powders were prepared in kg quantity. They were sieved with a -35 screen to remove large particles and avoid clogging the HVOF gun. They were also sieved with a +20  $\mu\text{m}$  screen to remove small particles and increase the powders flowability.

## **II.2. Thermal spray**

Two types of thermal spray techniques including suspension plasma spray (SPS) and high velocity oxygen fuel (HVOF) were used in this thesis to deposit (Co,Ni)O coatings on Cu-Ni-Fe alloys, as explained below. Experiments were performed at “Thermal spray and multiphase flow laboratories” at Concordia university.

### **II.2.1. Suspension plasma spray**

(Co,Ni)O coatings on stainless steel and Cu-Ni-Fe alloys were deposited by spraying a  $\text{Co}_{0.5}\text{Ni}_{0.5}\text{O}$  solid solution powder or mixtures of CoO and NiO using suspension plasma spray (SPS). Suspensions were prepared by mixing 10 wt% of oxide powders with the intended CoO and NiO ratio with 1 wt% of polyvinylpyrrolidone (PVP) as a dispersing agent in ethanol. All substrates were grit blasted and then rinsed with acetone prior to their use. Square-shaped stainless steel was used as substrate in the first series of experiments that were carried out to explore the optimum deposition parameters. The optimum spray parameters were then used to coat disc-shaped Cu-Ni-Fe substrates with a dense, crack-free and single phase (Co,Ni)O coating.

A Mettech’s Axial III plasma spray system, presented in Fig. II.1, is used to deposit SPS coatings in this thesis. This is a high-power, high-efficiency deposition device with axial injection capability in which injection of feedstock materials occurs directly into the center of the plasma plume. The injection setup for SPS is developed in-house [1]. The substrates were fixed on a

sample holder while the SPS gun traversed multiple passes horizontally over the substrates to cover it with a uniform coating. The coating thickness was then controlled by the number of these passes. A FLIR A320 infrared camera (FLIR Systems Inc., USA) was used to monitor substrate temperature during SPS.



**Figure II.1. Suspension plasma spray with a Mettech's Axial III gun.**

### II.2.2. High velocity oxygen fuel

CoO and (Co,Ni)O coatings were sprayed on Cu-Ni-Fe alloys using high velocity oxygen fuel method. Two compositions of Cu-Ni-Fe alloy, Cu-20Ni-15Fe and Ni-25Fe-10Cu (in wt%), were used as substrates. These alloys were previously produced by the casting method and were further homogenized by a heat treatment under argon [2,3]. These alloys were cut into disc-shaped substrates of 15 mm diameter and ~ 7 mm thickness. CoO and (Co,Ni)O powders were prepared by a heat treatment at 1200 °C as explained above. No inter pass pauses, air or water cooling was applied during the deposition process. The substrate temperature was about 450 °C and the deposition efficiency was 24%.

The HVOF coatings in this thesis were deposited using a Diamond Jet 2700-hybrid HVOF gun with a convergent-divergent nozzle from Oerlikon Metco (Westbury, NY, USA). The HVOF gun used in this thesis is shown in Fig. II.2. Propylene and nitrogen were used as fuel and powder

carrier gas, respectively. The substrate temperature was monitored during the HVOF coating process by a FLIR A320 infrared camera.

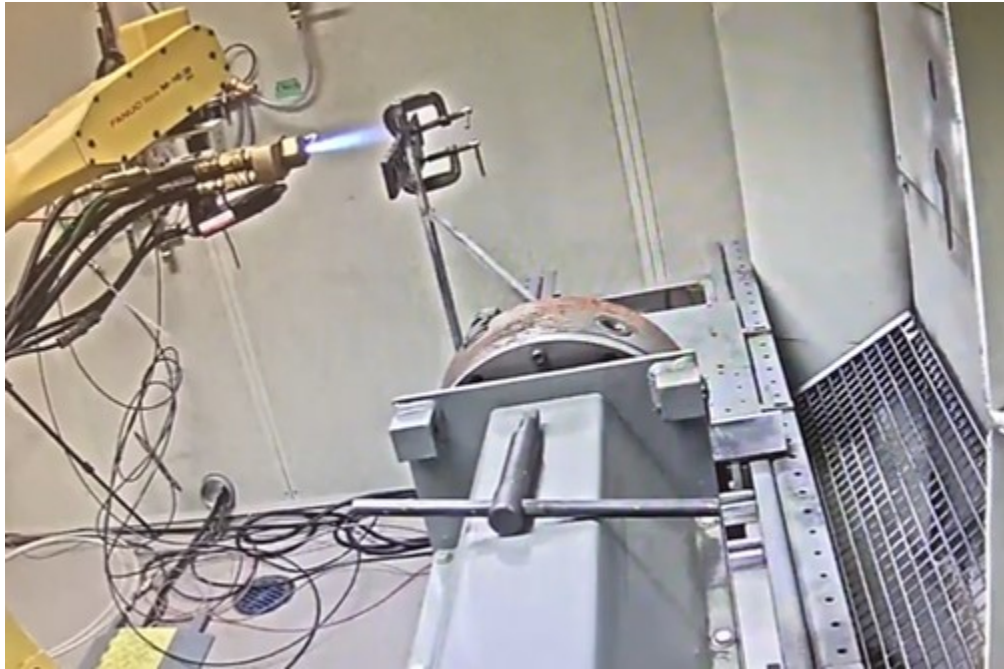


**Figure II.2. Diamond Jet 2700-hybrid HVOF gun with a convergent-divergent nozzle from Oerlikon Metco.**

### **II.3. Characterization techniques**

In this thesis, different characterization techniques were used to analyze as-received powders, prepared (Co,Ni)O solid solution powders, SPS and HVOF coating as well as samples after heat treatment or electrolysis tests. Here, these characterization techniques will be explained.

#### **II.3.1. X-ray diffraction (XRD)**

The X-ray diffraction technique (XRD) is a powerful tool to determine the phases present in a material as well as their crystal structure and orientation. A crystal is consisted of a periodic pattern of atoms in three dimensions that are arranged in planes of coordinates (h, k, l), spaced by a distance d. These sets of planes produce identical sets of cells in orientation, size and shape that are called unit cell. The unit cells can be defined by the lengths (a, b, c) of three vectors and the angles ( $\alpha$ ,  $\beta$ ,  $\gamma$ ) between them. These lengths (a, b, c) are the lattice parameters of the unit cell. When a beam of X-rays with the wavelength  $\lambda$  is incident a crystalline phase, atoms of the crystal

arranged in parallel planes, scatter the X-rays in all directions. The interferences between the scattered beams can be either constructive or destructive, depending on the wavelength  $\lambda$ , the angle of incidence  $\theta$  of the X-rays and the spacing  $d$  of the reticular planes. Interferences are constructive, forming diffraction peaks, if the inter-reticular distance is a product of an integer  $n$  and the wavelength  $\lambda$  of x-rays, summarized by Bragg's law:

$$n\lambda = 2d \sin \theta \quad (10)$$

More information on X-ray diffraction can be found in [4].

- **XRD equipment and protocols**

A Bruker D8 diffractometer, as shown in Fig. II.3, with Cu  $K_{\alpha}$  = 1.54060 Å radiation was used to analyze the crystalline structure of powders, alloys and coatings in a  $\theta$ - $2\theta$  configuration. In this device, while the goniometer (sample) is rotating at  $\theta$  angle, the detector moves simultaneously at  $2\theta$  angle and the X-ray source is fixed. The acquisition time varied from 2 to 30 seconds per step size of 0.02 to 0.1°. Determining the phases and indexing the diffraction peaks was carried out using EVA software. The position and the FWHM (Full Width at Half Maximum) of the peaks were measured by simulating the peaks by a function of the Pseudo-Voigt type. Further detailed analysis such as structural information and quantitative phase analysis was extracted using Rietveld refinement technique.



**Figure II.3. Bruker D8 X-ray diffractometer used in this thesis.**

### II.3.2. Rietveld refinement analysis

Rietveld refinement analysis was used to identify the crystalline structure and unit cell dimensions of (Co,Ni)O powders and (Co,Ni)O coatings deposited by thermal spray techniques. In these Rietveld refinement analyses, first the lattice parameters of  $\text{Co}_x\text{Ni}_{1-x}\text{O}$  solid solutions were extracted and then a quantitative analysis was carried out to obtain relative proportions of solid solution and metallic Ni phases (in coatings prepared by SPS) or that of solid solution and  $\text{Co}_3\text{O}_4$  phases formed after thermal stability measurements. To perform Rietveld refinement analysis, more intensive XRD patterns were obtained by reducing the step size and increasing the time per step.

Rietveld refinement is a multi-parameter curve-fitting procedure to extract structural information from the XRD pattern. In Rietveld refinement, XRD patterns are fitted and compared with reference or calculated patterns and backgrounds. Rietveld refinements were performed using the FULLPROF Suite program which is a set of crystallographic programs designed for Rietveld refinement.

### II.3.3. Calculation of lattice parameter and composition of solid solution

In a crystalline material, lattice parameters represent the dimensions of the unit cell while the interplanar spacing (d-spacing) is the distance between a set of (*hkl*) planes. For a cubic system where  $a = b = c$ , interplanar spacing can be calculated by:

$$\frac{1}{d^2} = \frac{(h^2 + k^2 + l^2)}{a^2} \quad (11)$$

Measuring the exact position of the diffraction peaks and using the Bragg's law (equation 10), the interplanar spacing for each phase, and thus the lattice parameter  $a$  can be calculated by:

$$a = \frac{\lambda\sqrt{(h^2 + k^2 + l^2)}}{2\sin\theta} \quad (12)$$

However, a more accurate measurement can be carried out using Rietveld refinement technique as mentioned above.

In XRD patterns of  $\text{Co}_x\text{Ni}_{1-x}\text{O}$  solid solution, any changes in the composition result in a slight displacement of the diffraction peaks. Therefore, accurate measurements of peak positions were necessary during the XRD analysis of as-prepared and heat treated  $\text{Co}_x\text{Ni}_{1-x}\text{O}$  solid solutions as well as two-phase (Co,Ni)O coatings deposited by suspension plasma spray. The exact composition of solid solution was extracted based on the existing linear relationship between the lattice parameter and the NiO molar fraction of the  $\text{Co}_x\text{Ni}_{1-x}\text{O}$  solid solution [5].

#### II.3.4. Scanning electron microscopy (SEM) equipped with EDS

Scanning electron microscopy (SEM) is a characterization tool that is based on the interaction between emitted electrons and atoms in a material. Electrons are emitted from a thermionic electron gun (filament) which will then be accelerated by applying a high positive voltage to the anode to form a primary electron beam towards the sample where they interact with the atoms. Different radiations are emitted from the surface of the sample which are collected by various detectors. The detectors convert these signals and transfer them to a computer where a very high-resolution image or a quantitative analysis can be produced.

When a primary electron beam strikes the sample surface, several signals are produced including secondary electrons (SE), back-scattered electrons (BSE), characteristic X-rays as illustrated in Fig. II.4 Each of these signals have different properties and they provide various information such as chemical composition and topology of the sample surface. Secondary electron, which is the most widely used signal in SEM, is produced when the incident primary electrons ionize the sample atoms (Fig. II.4.a). Secondary electrons have very low energy, less than 50 eV, and only those emitted from a region within few micrometers of material surface can be detected. Thus, secondary electrons provide accurate topological information such as texture and roughness of sample surface.

Another important signal in SEM is Backscattered electron (BSE). Both composition of the specimen and its topography can be revealed with BSE. BSEs are formed when the incident electrons collide the sample atomic nucleus (Fig. II.4.b), they will be reflected without losing much of their energy and as a result, BSEs usually possess high energy. In fact, elements with higher atomic number scatter more BSEs than light elements. Therefore, images with chemical contrast can be produced with BSEs.

When a secondary electron is emitted from an atom, the vacant position of that electron can be filled with an electron from an outer shell (Fig. II.4.c). Since there is a difference in energy between initial and final states of electron, an X-ray will be emitted to return the ionized atom to ground state. The energy of this X-ray photon is characteristic from one element to another and very useful chemical analysis can be acquired with characteristic x-rays.

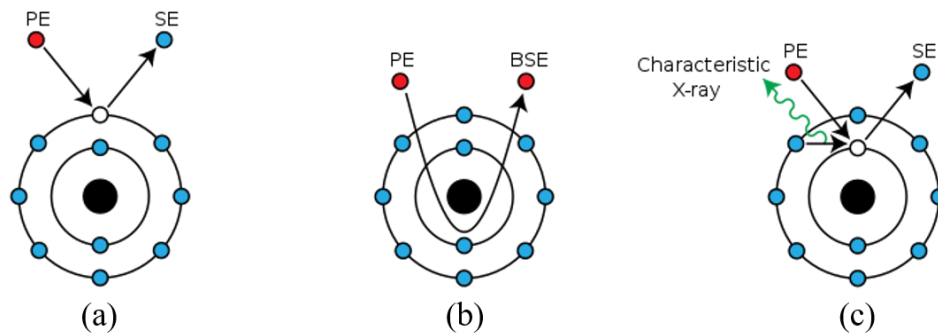


**Figure II.4. Different interactions between an electron and an atom producing (a) a secondary electron, (b) a backscattered electron and (c) a characteristic x-ray.**

- **SEM equipment and protocols**

The powder morphology and metallographic observation was carried out by scanning electron microscopy (SEM) in secondary electron (SE) mode operating at 20 kV and a working distance of 15 mm using a Tescan Vega3 scanning electron microscope. This SEM device, as shown in Fig. II.5, was equipped with a Bruker XFlash® 6 | 10 Detector energy dispersive X-ray spectroscope (EDX) to determine the composition of elements. All as-sprayed and heat treated coatings as well as coated anodes after aluminum electrolysis were embedded in epoxy resin and then cut using a precision cut-off machine (Secotom-15, Struers A/S, Denmark), then polished using standard metallographic procedures to a final finish of 0.4  $\mu\text{m}$  before being analyzed with SEM-EDS. To make the surface conductive, a 4 nm thick Pt / Pd layer was deposited using a 208HR apparatus (Cressington).



**Figure II.5. Tescan Vega3 scanning electron microscope equipped with a Bruker XFlash® 6 | 10 Detector energy dispersive X-ray spectroscope (EDX) used in this thesis.**

### II.3.5. Thermogravimetric analysis (TGA)

Thermal stability of  $\text{Co}_x\text{Ni}_{1-x}\text{O}$  solid solutions was determined at 800 and 1000 °C using Thermogravimetric analysis (TGA) technique. Solid solution powders were heated from room temperature up to 1000 °C, were held at 1000 °C for 1 min and then were cooled down to room temperature. Also, in other series of experiments, thermal stability of (Co,Ni)O powders were measured by raising the temperature up to 800 °C and maintaining it for 3 hours before decreasing it to room temperature. In all TGA measurements, the heating and cooling rates were fixed at 5 °C.min<sup>-1</sup>. TGA analysis were carried out at Centre de Recherche NanoQAM (Université du Québec à Montréal) using a TA Instruments (TGA Q500 / Discovery MS) equipment. TGA measurements were carried out under mixed flowing air/He gas (90 ml/min of air flow from the top and 10 ml/min of He from bottom). The same heat treatments were performed on (Co,Ni)O powders in a furnace and the powders were then analyzed by XRD, to investigate their thermal stability in air.

In thermogravimetric analysis (TGA), the variation in the mass of a material is measured as either functions of temperature or time as it is heated or cooled down under a controlled temperature in a controlled atmosphere. In TGA, up to 200 mg of a material can be analyzed with

a sensitivity of 0.1  $\mu\text{g}$  change in the mass and with a 0.01% accuracy. Materials can be placed in different types of pans that are supported with a high precision balance. These pans are made of alumina, aluminum or platinum to ensure that no reaction is happening between the specimens and the pans. Reactive or inert gas can be flown in the TGA furnace chamber with a controlled flow rate while the sample is heated or cooled down.

### II.3.6. Inductively coupled plasma atomic emission spectroscopy

The solubility of cobalt and nickel in molten cryolite was measured at 700 and 1000  $^{\circ}\text{C}$ . Sintered pellets of  $\text{Co}_x\text{Ni}_{1-x}\text{O}$  solid solutions were put under electrolyte mixture at the bottom of alumina crucibles. Electrolytes were heated at 700 and 1000  $^{\circ}\text{C}$  under argon flow and few grams of molten electrolyte were taken periodically using a graphite rod. Also, to quantify the pollution of the electrolyte by cobalt and nickel from coated anodes, a small amount of molten electrolyte was taken after aluminum electrolysis. The molten electrolyte which solidified on the cold surface of the graphite rod, was taken out to cool down to room temperature. Then it was crushed into powder with a mortar and pestle and was analyzed by inductively coupled plasma atomic emission spectroscopy (ICP-AES) at the INRS ETE center in Quebec with a Varian 725 device (Agilent).

In ICP-AES, samples are dissolved in an aqueous solution containing 10% HCl and 5%  $\text{HNO}_3$  and the solution is then injected into an argon plasma at a temperature of 10,000 K. The elements are ionized in the plasma and electrons in the excited atoms jump from an atomic orbital to another one with a different level of energy. The difference in the energy of these two atomic orbitals is emitted as a photon with a wavelength which is characteristic to every element. These photons are then collected with a detector and then concentration is measured by comparing the intensity of collected photons of each element with that of a standard sample. Except light elements such as hydrogen, carbon, oxygen, fluorine and chlorine that are not detectable by ICP, it is possible to use ICP to measure simultaneously the concentration of a large number of elements with a precision of ten ppb.

### II.3.7. Particle size distribution measurement (PSD)

As mentioned in previous chapter, it is necessary to analyze the size and morphology of the powder particles by SEM and PSD analysis. An observation with scanning electron

microscopes is required since most of PSD analysis devices consider all powder particles as a sphere, so they report the equivalent value as its diameter. In a particle size analysis, three different values (median, mean and mode) can be reported. The mode is the particle size most commonly found in the distribution. In fact, the mode is the peak in the PSD histogram while the mean is the average of the all particle sizes. The median is a value where half of the particles has larger size and half has smaller size. For a symmetric distribution, mode, mean and median are the same but in a non-symmetric distribution, they are three different values. To have a clear understanding of the powder particle size distribution, the value of the median ( $D_{50}$ ) as well as the upper ( $D_{90}$ ) and lower ( $D_{10}$ ) limits of the powder size distribution must be measured.  $D_{10}$  and  $D_{90}$  are the particle sizes which 10 and 90 percent of the distribution, respectively, have particle sizes smaller than them. Also, if the PSD is the distribution is bimodal (two-peaks in the size distribution), the values of the modes must be reported too.

Particle size distribution of CoO, NiO and  $\text{Co}_x\text{Ni}_{1-x}\text{O}$  powders were measured by laser diffraction using a Malvern Panalytical Spraytec instrument available at Concordia University. For particle size measurements, powders were put in a suspension in water and then were analyzed using a Malvern Wet Dispersion Accessory instrument. Raw powders for suspension plasma spray (SPS) must have particle size smaller than  $2\ \mu\text{m}$  ( $D_{90} < 3\ \mu\text{m}$ ) while for high velocity oxygen fuel spray, it is essential to have powders with particle size larger than  $10\ \mu\text{m}$  ( $D_{50} > 20\ \mu\text{m}$ ). The particle size ( $D_{90}$ ) of  $(\text{Co},\text{Ni})\text{O}$  powder produced by a two-step procedure (attrition + heat treatment) was reduced from  $17$  to  $3\ \mu\text{m}$  by a subsequent ball-milling step for 3 hours to fit the requirement of SPS procedure. Raw powders for HVOF were sieved with  $-35$  and  $+20\ \mu\text{m}$  screens to fit the requirement of HVOF procedure.

#### **II.4. High temperature dry oxidation tests of coated anodes**

Dry oxidation behaviour of coated Cu-Ni-Fe alloys was examined at  $1000\ ^\circ\text{C}$  in dry inert and oxidizing atmospheres. The as-coated samples were heated at  $1000\ ^\circ\text{C}$  for 20 h in static air and under an argon flow in a muffle furnace and a tubular furnace, respectively. The muffle and tubular furnaces used in this thesis to carry out heat treatments are presented in Fig. II.6. The heating rate was  $5\ ^\circ\text{C}\cdot\text{min}^{-1}$ . They were then taken out and analyzed with XRD. After XRD

analysis, they were embedded in epoxy resin and polished using standard metallographic procedures before being analyzed with SEM-EDS.

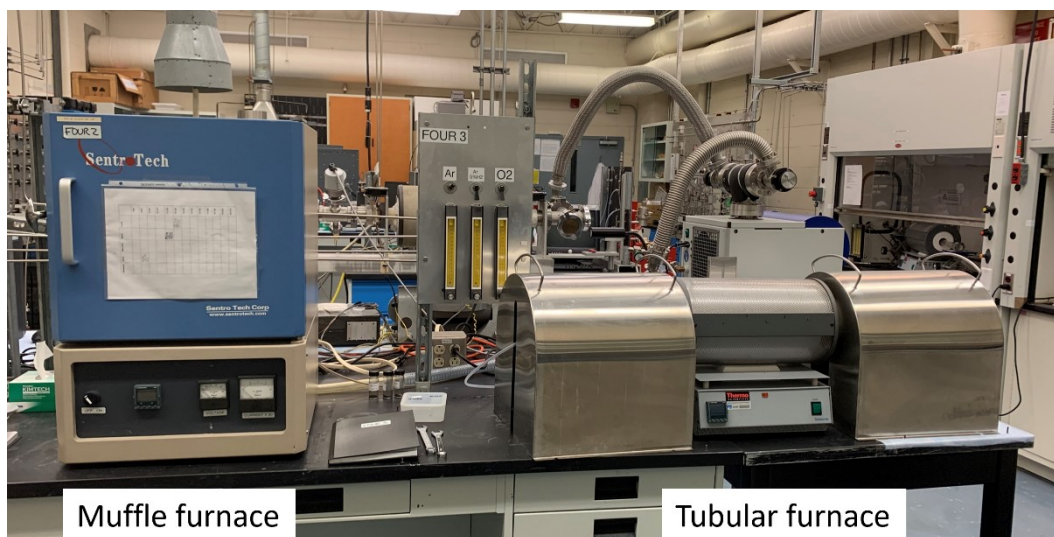


**Figure II.6. Muffle and tubular furnaces used in this thesis.**

## **II.5. Aluminum electrolysis**

Anodic behaviour of as-cast and coated Cu-Ni-Fe samples at temperatures between 700 and 1000 °C were studied in this thesis. Aluminum electrolysis tests were carried out in a laboratory electrolysis cell at INRS. Here, the electrolysis cell and setup used to perform aluminum electrolysis is explained.

### **II.5.1. Electrolysis cell**

A special electrochemical cell was designed to carry out the aluminum electrolysis as shown in Fig. II.7 and 9. The cell is made of stainless steel 310 and can be used for electrolysis at temperatures up to 1000 °C. It is closed by a water-cooled SS316 lid, equipped with 6 inlets sealed with Swagelok type connections. These inlets are designed to accommodate anode, cathode, gas in and out, thermocouple and alumina feeder. For aluminum electrolysis experiments, an alumina crucible was placed inside the SS310 cell as a secondary crucible to prevent any damages to the cell in case of a leakage. A graphite crucible containing the electrolyte was placed inside the secondary alumina crucible and was considered as the counter electrode. Alumina powder was

periodically added to the electrolyte with an automatic feeder to keep the alumina concentration at saturation during aluminum electrolysis. In this electrolysis cell, the gas-in and the alumina feeder inlets are connected to a T connection that allows alumina powder to be carried to the electrolyte surface where it dissolves. The ultra-high purity argon goes through a desiccator before entering the cell. An exhaust evacuates the gases inside the cell to a sodium carbonate-based neutralization system. The cell is placed inside a Carbolite Gero brand furnace.

### II.5.2. Chronoamperometry

Aluminum electrolysis was performed using chronoamperometry (CP) as an electrochemical technique. Chronoamperometry is a galvanostatic method in which the current at the anode (working electrode) is held constant. Then the cell potential is recorded as a function of time. Aluminum electrolysis was always carried out at an anode current density of  $0.5 \text{ A}\cdot\text{cm}^{-2}$  using a two-electrode configuration cell controlled by VMP3 multi-channel potentiostat/galvanostat (BioLogic Instrument). Anodes were placed inside the cell (5 cm above solid electrolyte) before being heated slowly ( $2 \text{ }^\circ\text{C}\cdot\text{min}^{-1}$ ) to the electrolysis temperature (700, 850 or 1000  $^\circ\text{C}$ ). The anode was then inserted into molten electrolyte. After electrolysis, anode was taken out of molten electrolyte but left inside the cell to slowly cool down to room temperature ( $\sim 2\text{-}4 \text{ }^\circ\text{C}\cdot\text{min}^{-1}$ ) to prevent the delamination of oxide layers due to thermal shock. The anode part above the bath was protected by a thick alumina-based cement coating, as shown in Fig. II.8 and 9. The electrolyte was composed of approximately 400 g of electrolyte, corresponding to a height of  $\sim 5 \text{ cm}$  and a cathode surface area of  $\sim 150 \text{ cm}^2$ . For electrolysis at 1000  $^\circ\text{C}$ , a NaF-based electrolyte (49 wt% NaF + 43 wt%  $\text{AlF}_3$  + 8 wt%  $\text{Al}_2\text{O}_3$ ) with a cryolite ratio (CR) of 2.3, and for electrolysis at 700 and 850  $^\circ\text{C}$ , a KF-based electrolyte (45 wt% KF + 50 wt%  $\text{AlF}_3$  + 5 wt%  $\text{Al}_2\text{O}_3$ ) with a cryolite ratio of 1.3 was used. All powders were dried in an oven at 150  $^\circ\text{C}$  for at least 24 h before the experiment.

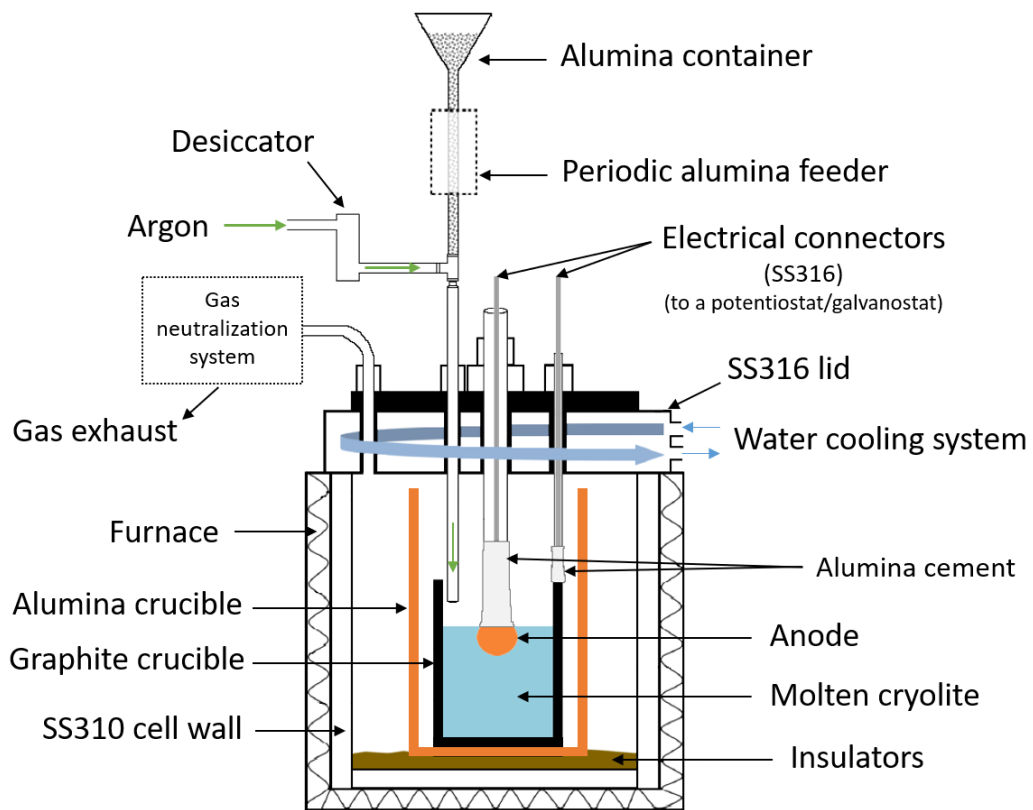


**Figure II.7. Schematic illustration of aluminum electrolysis cell.**

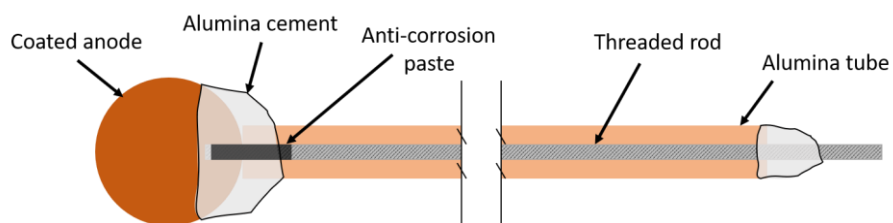


**Figure II.8. Schematic illustration of an anode before the electrolysis.**

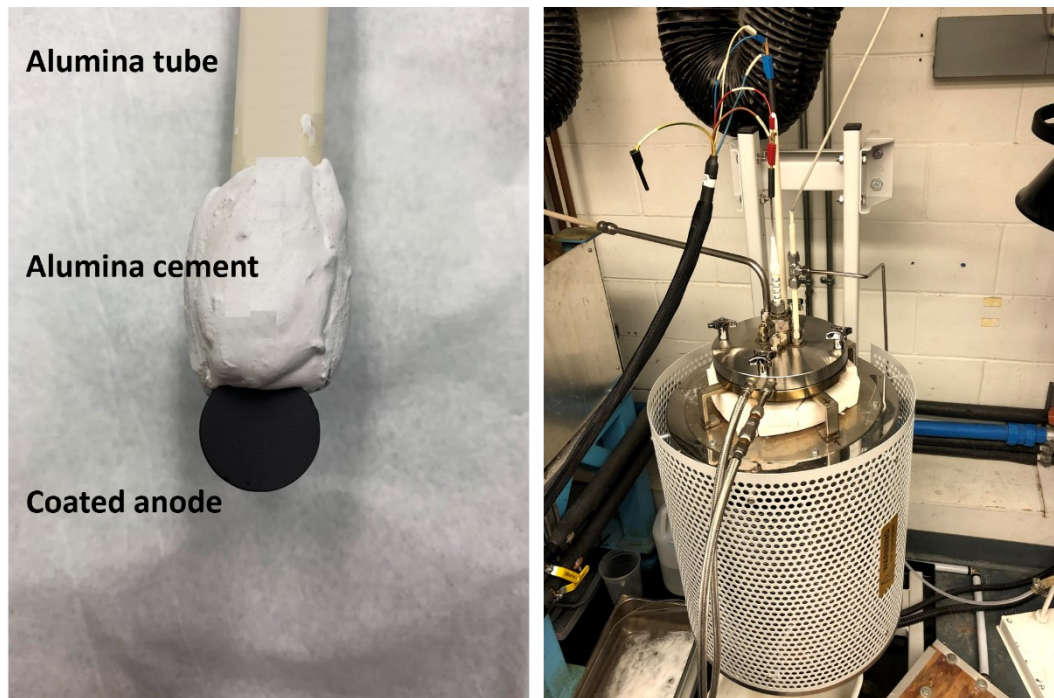


**Figure II.9. Aluminum electrolysis cell and an anode before the electrolysis.**

## References

- [1] F. Tarasi, M. Medraj, A. Dolatabadi, J. Oberste-Berghaus, C. Moreau, Enhancement of amorphous phase formation in alumina–YSZ coatings deposited by suspension plasma spray process, *Surf. Coatings Technol.* 220 (2013) 191–198. doi:10.1016/j.surfcoat.2012.10.054.
- [2] S. Jucken, E. Schaal, B. Tougas, B. Davis, D. Guay, L. Roué, Impact of a post-casting homogenization treatment on the high-temperature oxidation resistance of a Cu-Ni-Fe alloy, *Corros. Sci.* 147 (2019) 321–329. doi:10.1016/j.corsci.2018.11.037.
- [3] S. Jucken, B. Tougas, B. Davis, D. Guay, L. Roué, Study of Cu-Ni-Fe Alloys as Inert Anodes for Al Production in Low-Temperature KF-AlF<sub>3</sub> Electrolyte, *Metall. Mater. Trans. B.* 50 (2019) 3103–3111. doi:10.1007/s11663-019-01695-w.
- [4] B.D. Cullity, *Elements of X-RAY diffraction*, Addison-Wesley Publishing Company, Inc, 1978.
- [5] S. Mohammadkhani, E. Schaal, A. Dolatabadi, C. Moreau, B. Davis, D. Guay, L. Roué, Synthesis and thermal stability of (Co,Ni)O solid solutions, *J. Am. Ceram. Soc.* 102 (2019) 5063–5070. doi:10.1111/jace.16397.

**III. Chapter 3:**

**Articles and unpublished  
results**

In this chapter, three published articles are presented. These articles summarize the main results obtained within the framework of this thesis. The sequence of articles follows the progress of the work carried out. These articles explain the synthesis process of (Co,Ni)O solid solutions as well as their physical and chemical properties. Different thermal spray methods used to coat Cu-Ni-Fe alloys with a single phase and dense (Co,Ni)O layer and the high-temperature behaviour of the coated samples are also presented. Here, a summary of each article is presented. Then, all articles are introduced along with their bibliographic references that are listed independently at the end of each article. In the last part of this chapter, unpublished results on the solubility of (Co,Ni)O in molten cryolite and anodic behaviour of (Co,Ni)O coated Cu-Ni-Fe electrodes are presented.

### **III.1. A summary of article 1:**

#### Synthesis and thermal stability of (Co,Ni)O solid solutions

In the first article, two approaches are introduced for the production of (Co,Ni)O solid solutions. Two scalable solid-state synthesis methods, namely high-energy ball-milling (HEBM) and calcination, have been evaluated for the synthesis of (Co,Ni)O solid solutions. The produced powders were analyzed by XRD to evaluate the formation of a solid solution. In the first method, the solid solutions were synthesized by high energy ball-milling (HEBM) starting with CoO and NiO powders. HEBM was performed using a SPEX 8000M laboratory mill. Different milling times were tested (1, 4, 10, 20 and 30 h). In the second procedure,  $\text{Co}_x\text{Ni}_{1-x}\text{O}$  solid solutions were prepared by a mixed HEBM + heat treatment procedure. In that case, CoO and NiO powders were first ball-milled for a short period of time (12 min) and then heat treated in air at 1000 °C for 10 h. The (Co,Ni)O powders were let to cool down at room temperature in air. To compare the effect of using different starting materials, this second procedure was also applied to initial mixtures of  $\text{Co}_3\text{O}_4$  and NiO powders (instead of mixtures of CoO and NiO powders).

The results showed that it is possible to produce  $\text{Co}_x\text{Ni}_{1-x}\text{O}$  solid solutions and that 20 hours of ball-milling is required to obtain a solid solution. However, the produced solid solutions with HEBM were contaminated with tungsten carbide due to the erosion of ball-milling media. To obtain a WC-free solid solution, the ball-milling period was reduced to a minimum and a subsequent high temperature treatment was applied to favor interdiffusion of CoO and NiO to form

Co<sub>x</sub>Ni<sub>1-x</sub>O solid solutions. The obtained solid solutions with the second procedure were single phase and it was shown that it is possible to produce Co<sub>x</sub>Ni<sub>1-x</sub>O solid solutions over the whole composition range.

Then, thermal stability of different compositions of Co<sub>x</sub>Ni<sub>1-x</sub>O was studied using TGA and XRD. Also, the morphology of (Co,Ni)O powders was analyzed by SEM and PSD analyses. It was shown that at 1000 °C, Co<sub>x</sub>Ni<sub>1-x</sub>O solid solutions are stable over the whole composition range. In contrast, at 700 and 800 °C, Co<sub>x</sub>Ni<sub>1-x</sub>O are only stable for  $x \leq 0.22$  and  $x \leq 0.46$ , respectively. Thermal stability of (Co,Ni)O depends on temperature, oxygen pressure and composition of the solid solution. (Co,Ni)O solid solution particles have a spherical shape with not sharp edges. The particle size decreases regularly as the NiO content gets larger. However, the particle size of (Co,Ni)O powders prepared with mixed HEBM + heat treatment procedure is too small for APS and HVOF deposition and is too large for SPS deposition. Thus, further work is required to modify the particle size of (Co,Ni)O solid solutions for deposition with thermal spray techniques. Our preliminary results of the large-scale synthesis of (Co,Ni)O powders have shown that the size of (Co,Ni)O particles can be easily decreased by a short post-synthesis milling step (3 hours) to the micrometer size range compatible with deposition by suspension plasma spray (SPS).

### **III.2. A summary of article 2:**

#### **Suspension plasma spray deposition of Co<sub>x</sub>Ni<sub>1-x</sub>O coatings**

In the second article, two compositions of (Co,Ni)O coatings were prepared using Suspension Plasma Spray (SPS) process. The effects of SPS process parameters (plasma power, standoff distance, gas mixture, and substrate temperature) on the structure and composition of coatings were investigated. X-ray diffraction measurements, coupled with Rietveld refinement analysis, and scanning electron microscope (SEM) coupled with energy-dispersive X-ray spectroscopy (EDX) analyses were performed.

A first series of tests was performed to explore the deposition parameters space (Part 1, samples S1 to S5). Then, a series of three complementary tests were performed. In the first one, a 50 – 50 mol% CoO + NiO powder mixture was sprayed into water using different plasma powers. The particles were then collected from water, dried in an oven, and analyzed via XRD and SEM.

In the second one, NiO and CoO powders were deposited separately on a substrate. Finally, in the third complementary test, a  $\text{Co}_{0.5}\text{Ni}_{0.5}\text{O}$  solid solution powder was used as starting material to prepare coatings. Following these complementary tests, a second and a third series of tests were performed to obtain a single phase coating with low porosity and good adhesion. Also, possible causes for the formation of metallic nickel during spraying process is discussed.

It was shown that in the first two series of experiments where the substrate temperature was kept at low temperatures (below 600 and 300 °C), undesired reduction of NiO to Ni may occur and thus, the composition of the solid solution phase deviates from that of the starting materials. Uniform, adherent and non-porous  $\text{Co}_x\text{Ni}_{1-x}\text{O}$  coatings made of a single solid solution phase are obtained only in the third series of experiments where the substrate temperature is above 950 °C. Also, in the first complementary test where CoO and NiO particles were sprayed and then collected from water, XRD peaks of neither solid solution nor metallic nickel were observed. This suggests that the formation of solid solution and the reduction of NiO occurred mostly on the substrate, although it is possible that metallic Ni particles were reoxidized upon contact with water. In the second complementary test where CoO and NiO were sprayed separately, a coating that contains both NiO and metallic nickel phases was obtained when only NiO was sprayed while spraying only CoO particles using the same spray parameters produced a coating that contains only CoO. Finally, when a powder made of a  $\text{Co}_{0.5}\text{Ni}_{0.5}\text{O}$  solid solution was used as starting material (instead of a physical mixture of CoO and NiO) and a less reductive atmosphere, helium rather than hydrogen, was used in the plasma gas mixture, metallic Ni was also formed. Thus, the formation of metallic nickel during SPS occurs even if a solid solution is used as starting material and, most importantly, in the absence of a reductant in the plasma gas mixture. Based on different series of experiments carried out in this article and a bibliography review on the possibility of reduction of NiO to Ni in SPS, it was suggested that the reduction of NiO could occur by reducing C and H species resulting from the vaporization/decomposition/ionization of the liquid phase (ethanol) used to prepare the suspension for SPS. In fact, ethanol can reduce NiO to metallic Ni at temperatures between *ca* 375 - 825 °C. When the substrate temperature is kept as high as possible, metallic Ni is oxidized to NiO. Upon reaching a stable substrate temperature of *ca* 950 °C, oxidation of metallic Ni to NiO is fast compared to the transverse motion of the nozzle, allowing the formation of  $\text{Co}_x\text{Ni}_{1-x}\text{O}$  coating made of a single solid solution phase.

### III.3. A summary of article 3:

#### High-temperature behaviour of HVOF (Co,Ni)O coated Cu-Ni-Fe anodes

In the third article, high velocity oxygen fuel (HVOF) process was used to coat Cu-Ni-Fe alloys with dense, uniform, and single phase  $\text{Co}_x\text{Ni}_{1-x}\text{O}$  coatings (with  $x = 1, 0.75$  and  $0.5$ ). (Co,Ni)O and CoO powders were prepared in kg quantity with appropriate particle size for HVOF spraying. Prepared coatings were heated at  $1000\text{ }^\circ\text{C}$  for 20 h in static air and under an argon flow in a muffle furnace and a tubular furnace, respectively, to investigate the high-temperature behaviour of the samples. The as-sprayed and heat treated coatings were analyzed by XRD and SEM-EDS. The optimum HVOF spraying conditions were first determined. Three different sets of spray parameters were tested. In the optimum spray conditions where the fuel/oxygen ratio (richness) was close to 1, the observed splats formed a uniform structure since the particles were better accelerated/melted during the deposition process. The XRD results revealed that all prepared coatings using the optimum spray conditions were uniform and crack-free with very low porosity. The surface of coatings was smooth, and their thickness varied between 110 and  $125\text{ }\mu\text{m}$ . The composition of all coatings, as determined by EDS, was very close to that of their respective starting powders.

After heat treatment at  $1000\text{ }^\circ\text{C}$  in argon, iron diffusion was observed from both Cu-rich and Ni-rich substrates. The amount of diffused iron was slightly higher from Cu-rich substrate despite having lower iron content. Also, the iron diffusion was decreased as the Ni content of the  $\text{Co}_x\text{Ni}_{1-x}\text{O}$  coatings increased. After heat treatment in air, high-temperature behaviour of the samples depended strongly on the composition of the substrate. On Cu-rich alloy,  $\text{Co}_x\text{Ni}_{1-x}\text{O}$  coatings was sandwiched between two copper oxide layers and a thick layer of mixed iron, nickel and copper oxides was formed between  $\text{Co}_x\text{Ni}_{1-x}\text{O}$  coatings and Cu-rich substrates. Higher nickel content in the (Co,Ni)O slowed down oxygen diffusion to the substrate, as well as copper diffusion to the sample surface, thus the thickness of the oxide layer formed on Cu-rich substrate decreased with the increase in Ni content. On Ni-rich alloy, a  $\text{NiFe}_2\text{O}_4$  scale was formed between the substrate and the coating, and its thickness decreased as the Ni content of the  $\text{Co}_x\text{Ni}_{1-x}\text{O}$  coatings increased. These results confirmed that a (Co,Ni)O coating rich in nickel protects better the substrate from high temperature oxidation.

### III.4. Article 1: Synthesis and thermal stability of (Co,Ni)O solid solutions

**Authors:** Saeed Mohammadkhani <sup>a</sup>, Emmanuel Schaal <sup>a</sup>, Ali Dolatabadi <sup>b</sup>, Christian Moreau <sup>b</sup>, Boyd Davis <sup>c</sup>, Daniel Guay <sup>a</sup>, Lionel Roué <sup>a</sup>

<sup>a</sup> INRS-Énergie, Matériaux, Télécommunications, Varennes, Québec, Canada

<sup>b</sup> Department of Mechanical, Industrial & Aerospace Engineering, Concordia University, Montreal, Québec, Canada

<sup>c</sup> Kingston Process Metallurgy Inc., Kingston, Ontario, Canada

**Journal:** Journal of the American Ceramic Society

Published February 2019

**DOI:** <https://doi.org/10.1111/jace.16397>

#### **Contributions:**

The powder synthesis by ball-milling and heat treatment as well as characterizations of the prepared solid solutions by SEM, XRD, Rietveld refinement and Particle size distribution were carried out by the author of this thesis. The Thermogravimetric analysis (TGA) were performed at NanoQAM group at Université du Québec à Montréal (UQAM) and post-TGA calculation and data treatments were conducted by the author of this thesis. E. Schaal, A. Dolatabadi, C. Moreau, B. Davis, D. Guay, and L. Roué helped interpret the results and correct different versions of the article.

## Abstract

(Co,Ni)O solid solutions are considered as promising protective materials of O<sub>2</sub>-evolving anodes for Al production. In this context, two solid-state synthesis methods, namely high-energy ball milling (HEBM) and calcination, have been evaluated for the synthesis of (Co,Ni)O solid solutions. In all cases, Co<sub>x</sub>Ni<sub>1-x</sub>O solid solutions can be formed over the whole composition range. However, undesired WC contaminant is observed using the HEBM method due to the erosion of the milling tools. Their thermal stability in air has been analyzed by thermogravimetric analyses (TGA) complemented by X-ray diffraction (XRD) analyses. It is shown that Co<sub>x</sub>Ni<sub>1-x</sub>O solid solutions are stable at 1000 °C over the whole composition range whereas they are only stable for  $x \leq 0.46$  and  $x \leq 0.22$  at 800 °C and 700 °C, respectively. For higher Co contents, the formation of Co<sub>3</sub>O<sub>4</sub> is observed. This is a relevant information for their future use for Al production, which can be done at different temperatures (~ 700 - 1000 °C) depending on the electrolyte composition.

*Keywords:* (Co,Ni)O solid solution, mechanical alloying, calcination, thermal stability.

## 1. Introduction

Substitution of consumable carbon anodes with inert ( $O_2$ -evolving) anodes in the electrochemical cells for the production of aluminum has significant environmental benefits because it eliminates the emissions of carbon dioxide and perfluorocarbons associated with consumption of the carbon anode. However, the design of inert anodes is a major challenge because of the severe Al electrolysis conditions (cryolithic medium at 960 °C) which require materials with excellent resistance to corrosion and thermal shock as well as adequate electrochemical properties.<sup>1</sup>

In comparison with other available inert anodes materials (ceramic and cermet), metallic anodes have the advantages of high electrical conductivity, thermo-mechanical robustness, lower cost of fabrication and simplicity of electrical connection to the current lead.<sup>2</sup> However, the application of metallic anodes is still challenging. It is essential to find a material with very low dissolution rate and high corrosion resistance under Al electrolysis conditions. Among many metallic materials studied so far, Ni-Fe-Cu-based alloys appear to be promising in their ability to form a layer of nickel ferrite ( $NiFe_2O_4$ ) on the surface of the anode that is recognized for its low solubility in the cryolithic bath.<sup>3-5</sup> However, these alloys are sensitive to the fluoridation reaction with the cryolithic medium, forming non-conductive nickel or iron fluoride at the metal/oxide interface, which increases the cell voltage and reduces energy efficiency of the electrolysis process.<sup>6</sup> It is therefore essential to remedy this problem by protecting Ni-Fe-Cu anodes with an appropriate fluoridation barrier.

In this context, the use of CoO-based protective coatings for metallic anode appears promising as shown by Nguyen and de Nora.<sup>7</sup> However, CoO is likely to be converted into  $Co_3O_4$  under Al electrolysis conditions, according to phase diagram of the Co-O system, showing that dissociation of CoO to  $Co_3O_4$  occurs at  $\sim 960$  °C in 1 bar  $O_2$ .<sup>8</sup> This is not desired since  $Co_3O_4$  is an n-type semiconductor that displays a significantly higher  $O_2$  evolution overpotential than p-type semiconducting CoO.<sup>7</sup> It has been found that CoO can be stabilized under Al electrolysis conditions by adding about 15 wt% of Ni to form (Co,Ni)O solid solution. For that purpose, a Co-Ni alloy was first electrodeposited onto the anode, which was followed by an oxidation treatment in air at high temperature to favor the formation of (Co,Ni)O coating.<sup>7</sup> However, owing to the

change of densities upon oxidation of metallic Co-Ni alloy, this procedure may be challenging to produce coherent and crack-free oxide layer as required for industrial Al production.

A potentially more relevant method to produce (Co,Ni)O coated inert anodes is by direct deposition of (Co,Ni)O oxide compounds by thermal spray techniques such as atmospheric plasma spray (APS) and high velocity oxygen fuel (HVOF). They are well-established technologies for producing protective oxide coatings for various industrial applications (*e.g.* deposition of thermal barrier coatings on superalloys in energy and propulsion gas turbines).<sup>9</sup> New thermal spray coating technologies such as suspension plasma spray (SPS) in which solid particles are suspended in a liquid and injected into the thermal jet also offer new opportunities for controlling the coating phase structure and porosity.<sup>9</sup> Additionally, thermal spray could be used on Al production site to restore protective (Co,Ni)O coating on end-of-life inert anodes.

As a first step toward this goal, the objective of the present study is to evaluate the possibility of producing single phase (Co,Ni)O powders with various Co/Ni ratios that could be used as raw materials for the thermal spraying of protective coatings onto Ni-Fe-Cu inert anodes. Two synthesis methods are evaluated, namely mechanical alloying and calcination, which are both easily scalable processes. The crystalline structure, thermal stability and powder morphology of the produced (Co,Ni)O powders are characterized.

## 2. Experimental

### 2.1. Material synthesis

$\text{Co}_x\text{Ni}_{1-x}\text{O}$  solid solutions, with  $x$  varying from 0 to 1 were prepared by two different methods. In the first method, the solid solutions were synthesized by high energy ball milling (HEBM) starting with CoO and NiO powders. CoO was itself prepared from  $\text{Co}_3\text{O}_4$  powder (purity  $\geq 99.7\%$ , -400 mesh, Alfa Aesar) heated under argon at 900 °C for 3 hours, while NiO was purchased and used as-received (purity  $\geq 99\%$ , -325 mesh, Cerac). HEBM was performed using a SPEX 8000M laboratory mill. The powder mixture was introduced into a tungsten carbide crucible (capacity of 41 ml) with three tungsten carbide balls (two with a diameter of 7.5 mm and one with a diameter of 11 mm, total mass of 18.3 g). The ball-to-powder mass ratio (BPR) was fixed at 10:1. Stearic acid (0.5 wt %) was added to the initial powder mixture as process control

agent (PCA) to prevent excessive cold welding. Different milling times were tested (1, 4, 10, 20 and 30 h).

In the second procedure,  $\text{Co}_x\text{Ni}_{1-x}\text{O}$  solid solutions were prepared by a mixed HEBM + heat treatment procedure. In that case, CoO and NiO powders were first ball milled for a short period of time (12 min) and then heat treated in air at 1000 °C for 10 h. The (Co,Ni)O powders were let to cool naturally at room temperature under air. To compare the effect of using different starting materials, this second procedure was also applied to initial mixtures of  $\text{Co}_3\text{O}_4$  and NiO powders (instead of mixtures of CoO and NiO powders).

## 2.2. *Material characterization*

The crystalline structure of  $\text{Co}_x\text{Ni}_{1-x}\text{O}$  solid solutions was determined by X-ray diffraction (XRD) using a Bruker D8 diffractometer with  $\text{Cu K}_\alpha$  radiation. The crystalline structure and unit cell dimensions were obtained through the Rietveld refinement technique, which is a multi-parameter curve fitting procedure to extract structural information from powder diffraction data. Refinements of cell parameters were carried out using the program FULLPROF.<sup>10</sup>

The powder morphology was characterized by scanning electron microscopy (SEM) in secondary electron (SE) mode using a Tescan Vega3 scanning electron microscope equipped with a Bruker XFlash® 6 | 10 Detector energy dispersive X-ray spectroscope (EDX) to determine the composition of elements. Particle size distribution (PSD) of the (Co,Ni)O powders were measured in water suspension by laser diffraction using a Malvern Panalytical Spraytec instrument.

The thermal stability of the  $\text{Co}_x\text{Ni}_{1-x}\text{O}$  solid solutions was determined from thermogravimetric analyzes (TGA) performed using a TA Instruments (TGA Q500 / Discovery MS) equipment. The heating and cooling rates were fixed at 5 °C  $\text{min}^{-1}$ . TGA measurements were carried out under mixed flowing air/He gas (90 ml/min of air flow from the top and 10 ml/min of He from bottom). The measurements were performed by raising the temperature up to 1000 °C and maintaining it for 1 min before decreasing it.

### 3. Results and discussion

#### 3.1 Synthesis of (Co,Ni)O solid solutions

In a first series of experiments, CoO and NiO powders (with 85 and 15 mol%, respectively) were ball milled for different milling times from 1 to 30 hours. **Fig. 1A** shows the XRD patterns of as-milled (CoO + NiO) samples. After 1 h of ball milling, two sets of peaks can be seen in the XRD patterns. The main diffraction peaks occur at  $2\theta = 36.4^\circ, 42.3^\circ, 61.5^\circ, 73.8^\circ$  and  $77.6^\circ$  and are assigned to CoO phase. A second set of peaks are observed at  $2\theta = 37.2^\circ, 43.3^\circ, 62.8^\circ$  and  $75.5^\circ$  and are assigned to NiO. The diffraction peaks of NiO gradually disappears as milling is prolonged to 4 h and 10 h. In addition, a series of new peaks appear at  $2\theta = 31.4^\circ, 35.6^\circ$  and  $48.3^\circ$  that belongs to tungsten carbide. After 10 h also, the diffraction peaks of CoO are slightly displaced to larger  $2\theta$  value compared to the initial XRD pattern, suggesting that NiO is dissolved in CoO. The displacement of CoO peaks continues as the milling time is increased from 10 h to 20 h. Further milling does not lead to any noticeable change in the XRD patterns apart from a gradual increase of the intensity of WC peaks. Contamination of the milled powder is due to the erosion of WC crucible and balls during the milling process. This is confirmed by EDX measurement that shows a gradual increase of the W content as milling progresses (see **Table 1**). These data also show that the Co/(Co + Ni) does not evolve with milling time and is identical within experimental error to the initial composition, indicating there is no preferential sticking of either CoO or NiO on the milling tools.

The lattice parameter of the (Co,Ni)O phase,  $a$ , was determined as a function of milling time and is shown in **Fig. 1B**. There is a steady decrease of  $a$  from 4.263 to 4.249 Å as the milling time is increased from 0 to 20 h. Further milling does not induce any more variation of  $a$ , indicating that a steady state is reached. From now on, the milling time was set at 20 h.

The XRD patterns of  $x\text{CoO} + (1-x)\text{NiO}$  powder mixtures, with  $x = 0.85, 0.75, 0.625$  and  $0.50$ , after 20 h of milling are shown in **Fig. 1C**. In all cases, the XRD patterns consist of two series of peaks that are assigned to an *fcc* phase and WC. **Fig. 1D** shows that the lattice parameter of the *fcc* phase,  $a$ , decreases linearly from 4.26 (pure CoO) to 4.18 (pure NiO) as the NiO content is increased from 0 to 100 mol%. The equation of the regression line shown in **Fig. 1D** is

$$a_{(\text{Co,Ni})\text{O}} = -0.082(1) * (1-x)_{\text{NiO}} + 4.2583(9)$$

where  $(1-x)_{\text{NiO}}$  is the NiO mole fraction. The parameters of this linear relationship are in excellent agreement with those found by S. Kuboon and Y. H. Hu who have investigated Ni-Co-O solid solution materials prepared by calcination in air.<sup>11</sup>

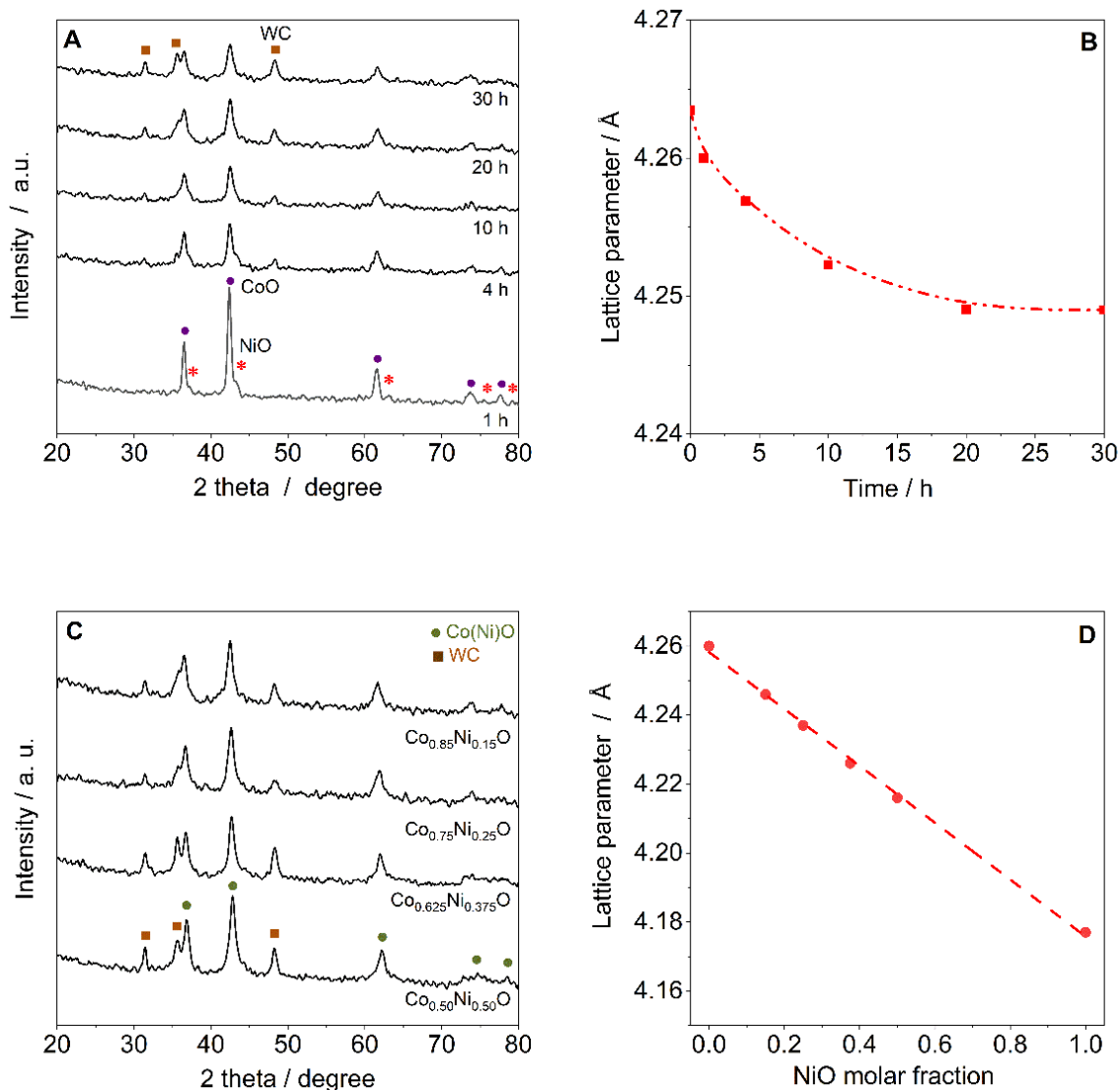


Figure 1. A, X-ray diffraction (XRD) patterns of 85 mol% CoO + 15 mol% NiO powder after different milling times. B, Variation of the lattice parameter of the (Co,Ni)O phase with milling time. C, XRD patterns of  $\text{Co}_x\text{Ni}_{1-x}\text{O}$  ( $x = 0.85, 0.75, 0.625, \text{ and } 0.50$ ) powders after 20 hours of milling. D, Variation of the lattice parameter of (Co,Ni)O solid solutions with respect to the molar fraction of NiO.

As seen in **Fig. 1C** and **Table 2**, there is a significant contamination of the milled powders with WC. Contamination of milled powders is an issue since WC is able to react at high temperature with  $\text{Co}_x\text{Ni}_{1-x}\text{O}$  to form  $\text{CoWO}_4$  (data not shown). Accordingly, a second procedure was devised to prepare WC-free  $\text{Co}_x\text{Ni}_{1-x}\text{O}$  solid solutions. This was achieved by reducing the ball

milling period to a minimum and relying on a subsequent high temperature treatment to favor interdiffusion of CoO and NiO to form  $\text{Co}_x\text{Ni}_{1-x}\text{O}$  solid solutions.

*Table 1. Composition of Co, Ni and W elements in the samples (85 mol% CoO + 15 mol% NiO) after different milling times. The composition was measured by EDX.*

Milling time (h)	Co (at%)	Ni (at%)	W (at%)	Co/(Co + Ni)
0	85.0	15.0	0	85.0
1	83.9	15.8	0.3	84.1
4	84.8	14.2	1.0	85.6
10	84.0	14.8	1.2	85.0
20	83.2	14.6	2.2	85.1

*Table 2. Composition of Co, Ni and W elements in  $\text{Co}_x\text{Ni}_{1-x}\text{O}$  solid solutions obtained after 20 h of HEBM. The composition was measured by EDX.*

x	Co (at%)	Ni (at%)	W (at%)	Co/(Co + Ni)
0.85	83.2	14.6	2.2	85.1
0.75	74.0	24.2	1.8	75.4
0.625	61.2	35.8	3.0	63.1
0.5	50.4	46.8	2.8	51.8

**Fig. 2A** displays the XRD patterns of different mixtures of  $x\text{CoO} + (1-x)\text{NiO}$  ball milled for 12 minutes and then heat treated at  $1000^\circ\text{C}$  in air for 10 h. For  $x = 0.625$  and  $0.50$ , only one series of peaks are observed that are assigned to *fcc*  $\text{Co}_x\text{Ni}_{1-x}\text{O}$  solid solutions. For  $x = 0.85$  and  $0.75$ , small peaks are observed at  $2\theta = 31.2^\circ, 44.6^\circ, 59.3^\circ$  and  $65.1^\circ$  besides the peaks corresponding to *fcc*  $\text{Co}_x\text{Ni}_{1-x}\text{O}$  solid solutions. This first series of peaks are assigned to  $\text{Co}_3\text{O}_4$ . **Fig. 2C** shows that the lattice parameter of *fcc*  $\text{Co}_x\text{Ni}_{1-x}\text{O}$  solid solutions slightly deviates from Vegard's law at the lowest NiO content. This is expected in view of the small amount of  $\text{Co}_3\text{O}_4$  formed in this range of composition. However, if the heat treatment step is performed at  $1100^\circ\text{C}$  (instead of  $1000^\circ\text{C}$ ),  $\text{Co}_3\text{O}_4$  is not observed anymore in the final product, which is then made of a single (Co,Ni)O solid solution (not shown).

It is known that  $\text{Co}_3\text{O}_4$  is not stable above *ca* 900 °C in air and will convert to  $\text{CoO}$ .<sup>8</sup> Therefore, instead of converting  $\text{Co}_3\text{O}_4$  to  $\text{CoO}$  prior to milling,  $\text{Co}_3\text{O}_4$  was used as starting materials (instead of  $\text{CoO}$ ). **Fig. 2B** shows the XRD patterns of  $(\text{Co}_3\text{O}_4 + \text{NiO})$  mixtures after 12 minutes of ball milling followed by a heat treatment at 1000 °C in air for 10 h. All XRD patterns depict only one set of peaks assigned to *fcc*  $\text{Co}_x\text{Ni}_{1-x}\text{O}$  solid solution with no trace of WC as confirmed from EDX analysis (data not shown). As seen in **Fig. 2C**, the variation of *a* with the NiO content closely follow Vegard's law. More interesting, the equation of the regression line shown in **Fig. 2C**

$$a_{(\text{Co,Ni})\text{O}} = -0.0842(6) * (1-x)_{\text{NiO}} + 4.2584(4)$$

is very similar to that observed previously for samples prepared by prolonged HEBM. Accordingly, this is going to be the preferred method to prepare pure  $\text{Co}_x\text{Ni}_{1-x}\text{O}$  solid solutions.

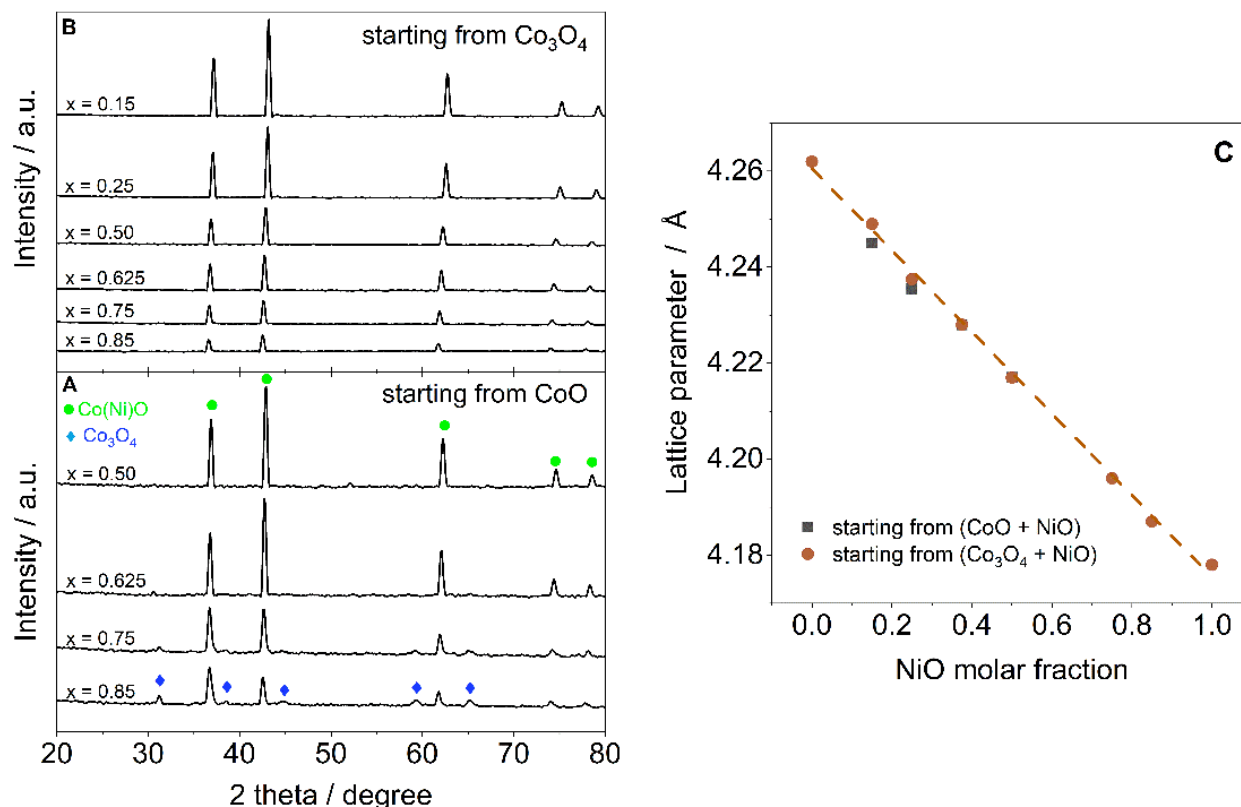


Figure 2. A, X-ray diffraction patterns of  $\text{Co}_x\text{Ni}_{1-x}\text{O}$  with  $x = 0.85, 0.75, 0.625,$  and  $0.50$  obtained after 12 minutes of ball milling of  $(\text{CoO} + \text{NiO})$  mixture followed by a heat treatment at 1000 °C for 10 hours in air. B, XRD patterns of  $\text{Co}_x\text{Ni}_{1-x}\text{O}$  with  $x = 0.85, 0.75, 0.625, 0.50, 0.25,$  and  $0.15$  obtained after 12 minutes of ball milling of  $(\text{Co}_3\text{O}_4 + \text{NiO})$  followed by a heat treatment at 1000 °C for 10 hours in air. C, Comparison of the relationship between lattice parameters of  $(\text{Co,Ni})\text{O}$  solid solutions and NiO molar fractions prepared from  $(\text{CoO} + \text{NiO})$  and  $(\text{Co}_3\text{O}_4 + \text{NiO})$ .

### 3.2 Thermal stability of (Co,Ni)O solid solutions

**Fig. 3** shows TGA curves of  $\text{Co}_x\text{Ni}_{1-x}\text{O}$  solid solutions. There is no mass change for  $\text{Co}_{0.15}\text{Ni}_{0.85}\text{O}$  and  $\text{Co}_{0.25}\text{Ni}_{0.75}\text{O}$ , which is not surprising considering these compounds are prepared through heat treatment at 1000 °C. At the opposite, mass changes are observed for  $\text{Co}_x\text{Ni}_{1-x}\text{O}$  with  $x \geq 0.50$ . In all cases, the mass starts to increase at *ca* 600 °C (point *a* in **Fig. 3**) to reach a maximum value at a temperature that varies with *x* (point *b*). Then the mass decreases and reaches a value at 1000 °C (point *c*) very close to the initial mass. Upon cooling down, the sample mass starts to increase again at a temperature that varies with *x* (point *d*). The net gain of mass (point *e*) also depends on *x*. These values are given in **Table 3**.

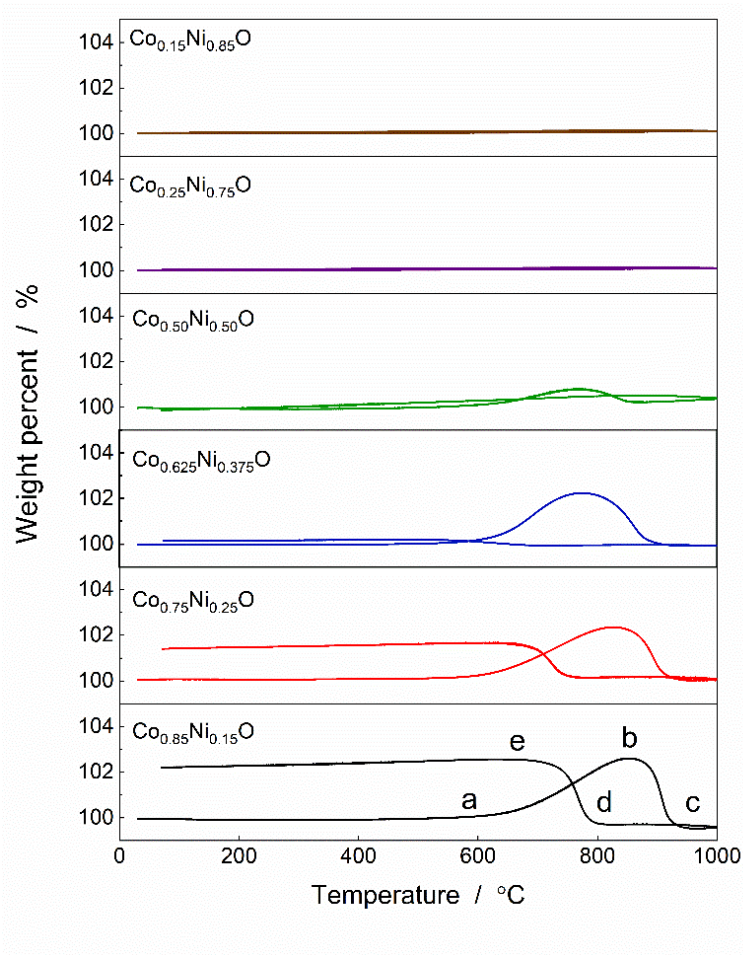


Figure 3. TGA curves of (Co,Ni)O solid solutions under air. The heating and cooling rates were 5 °C/min.

Table 3. Temperature and/or mass gain for some stages identified on the TGA curves of  $\text{Co}_x\text{Ni}_{1-x}\text{O}$  solid solutions.

x	Stage b		Stage d		Stage e	
	Temperature (°C)	Mass gain (%)	Temperature (°C)	Mass gain (%)	Temperature (°C)	Mass gain (%)
0.85	850	2.6	800	2.6	-	-
0.75	825	2.3	755	1.7	-	-
0.625	775	2.2	670	0.2	-	-
0.5	765	0.8	-	-	-	-

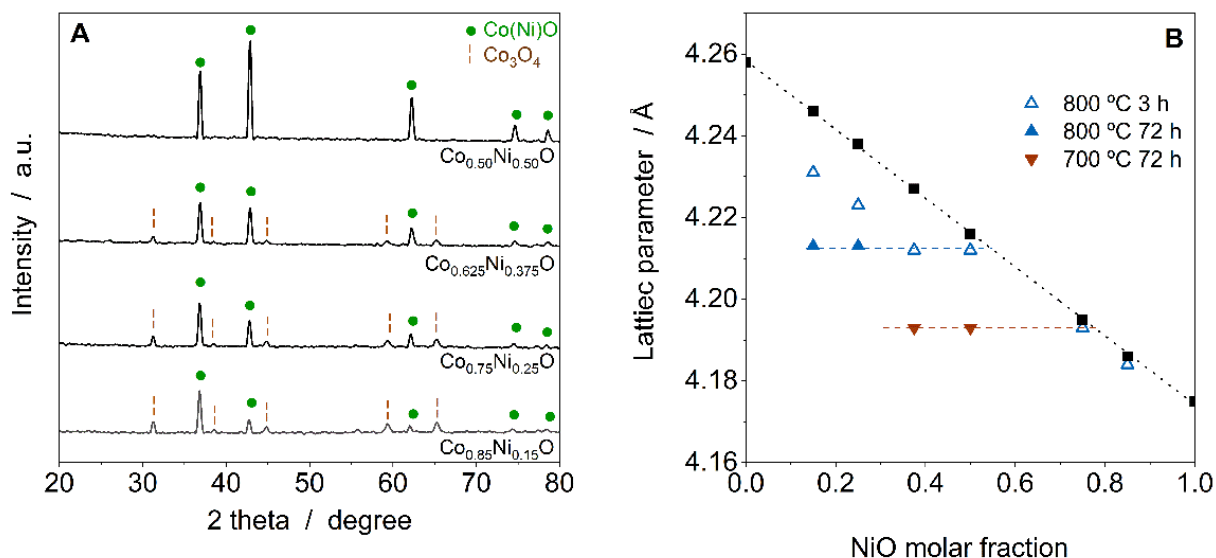


Figure 4. A, X-ray diffraction patterns of (Co,Ni)O solid solutions after heat-treatment at 800 °C for 3 hours; B, Variation of the lattice parameters of (Co,Ni)O solid solutions after heat-treatment at different temperatures and different periods of time. The linear relationship between the lattice parameter of  $\text{Co}_x\text{Ni}_{1-x}\text{O}$  solid solutions and the NiO molar fraction (from Figure 2B) is also shown as a reference (black dotted line).

For  $x \geq 0.50$ , the rapid mass increase observed from *ca* 600 °C is attributed to the partial decomposition of  $\text{Co}_x\text{Ni}_{1-x}\text{O}$  into  $\text{Co}_3\text{O}_4$  and  $\text{Co}_2\text{Ni}_{1-z}\text{O}$  with  $z < x$ , as confirmed by the XRD analyses presented hereafter (see Fig. 4). As  $\text{Co}_3\text{O}_4$  is not stable at high temperature, the decrease of mass observed at temperature above point b may be related the decomposition of  $\text{Co}_3\text{O}_4$  to  $\text{CoO}$ . However, as shown in Fig. 3 and Table 3, this mass loss onsets at a temperature lower than the decomposition temperature of  $\text{Co}_3\text{O}_4$  to  $\text{CoO}$  ( $\sim 920$  °C in air at 1 atm.)<sup>8</sup>, decreasing from 850 °C

for  $x = 0.85$  to  $765^\circ\text{C}$  for  $x = 0.50$ . Actually, this mass loss ( $\text{O}_2$  release) is due to decomposition of  $\text{Co}_3\text{O}_4$  to  $\text{CoO}$ , which is diluted by  $\text{NiO}$  from the existing  $\text{Co}_z\text{Ni}_{1-z}\text{O}$  phase, resulting in the reformation of the initial  $\text{Co}_x\text{Ni}_{1-x}\text{O}$  phase. The fact that the mass at point *c* is almost identical to the initial mass of the compound and that no  $\text{CoO}$  phase is observed in the XRD patterns of  $(\text{Co},\text{Ni})\text{O}$  solid solutions heated at  $1000^\circ\text{C}$  (**Fig. 2B**) is consistent with this reaction mechanism. It also agrees with the temperature-composition diagram of the  $\text{NiO-CoO-O}_2$  system in air, showing that the transition temperature between single phase  $(\text{Co},\text{Ni})\text{O}$  and two-phase  $\text{Co}_3\text{O}_4 + (\text{Co},\text{Ni})\text{O}$  decreases with the decreasing  $\text{Co},\text{Ni}$  content in the  $(\text{Co},\text{Ni})\text{O}$  solid solution (from  $\sim 900^\circ\text{C}$  for  $x \approx 0.95$  to  $\sim 600^\circ\text{C}$  for  $x \approx 0.05$ ).<sup>12</sup> Note that the formation of  $\text{Co}_3\text{O}_4$  was observed in ref. 12 whatever the  $\text{Co}$  content in the  $(\text{Co},\text{Ni})\text{O}$  phase, in contrast to the present study (only observed for  $x \geq 0.50$ ). The fact the  $\text{NiO-CoO-O}_2$  diagram was established under equilibrium conditions in contrast to the present TGA measurements can explain this difference. This suggests that the composition of the  $(\text{Co},\text{Ni})\text{O}$  solid solution not only impacts on the thermodynamic (temperature) of its decomposition/reformation but also affects its kinetic which seems to be much less favorable for  $x \leq 0.50$ . Assuming that the formation/decomposition of  $\text{Co}_3\text{O}_4$  is kinetically controlled by the diffusion of  $\text{O}^{2-}$  through the  $\text{Co-Ni-O}$  material, this suggests that  $\text{NiO}$ , present in larger proportion for  $x < 0.50$ , acts as oxygen diffusion barrier in the  $(\text{Co},\text{Ni})\text{O}$  solid solution. This is in accordance with the fact that oxygen diffusion in  $\text{NiO}$  is slower than in  $\text{CoO}$ .<sup>13</sup>

Upon cooling,  $\text{Co}_x\text{Ni}_{1-x}\text{O}$  solid solutions with  $x \geq 0.50$  are not stable at intermediate temperature (point *d*) and decomposes to  $\text{Co}_3\text{O}_4$ . This behaviour is reminiscent of that of  $\text{CoO}$ , which is stable at high temperature but is oxidized to  $\text{Co}_3\text{O}_4$  at intermediate temperature. In the case of  $x \geq 0.50$ , it is hypothesized that decomposition of  $(\text{Co},\text{Ni})\text{O}$  solid solutions formed at high temperature is observed in TGA measurements owing to the slow cooling rate. At the opposite, in a furnace,  $(\text{Co},\text{Ni})\text{O}$  heated at  $1000^\circ\text{C}$  are rapidly cooled down to room temperature, which prevents excessive decomposition. Accordingly, the XRD patterns of **Fig. 2B** are representative of the high temperature behaviour of the samples. Note that the mass gain due the formation of  $\text{Co}_3\text{O}_4$  is lower during the cooling step (point *e*) than during the heating step (point *b*) because of larger kinetic limitation at lower temperature. This is accentuated as  $x$  value is decreased, which confirms that the kinetic of  $\text{Co}_3\text{O}_4$  formation is slower as the  $\text{Co}$  content in  $(\text{Co},\text{Ni})\text{O}$  is decreased.

To further demonstrate the critical importance of cooling rate on the structure of the compound, **Fig. 4A** shows the XRD patterns of  $\text{Co}_x\text{Ni}_{1-x}\text{O}$  solid solutions (with  $x = 0.85, 0.75, 0.625$  and  $0.50$ ) heat treated at  $800\text{ }^\circ\text{C}$  in air for 3 h. For  $x = 0.85, 0.75$  and  $0.625$ , the XRD patterns exhibit two series of peaks attributed to  $\text{Co}_3\text{O}_4$  and  $(\text{Co,Ni})\text{O}$  solid solution. On the contrary, in the case of  $\text{Co}_{0.50}\text{Ni}_{0.50}\text{O}$ , there is only one set of peaks that belongs to  $(\text{Co,Ni})\text{O}$  solid solution. The lattice parameters  $a$  of  $(\text{Co,Ni})\text{O}$  solid solutions formed after heat treatment are shown in **Fig. 4B**. The lattice parameter of  $\text{Co}_x\text{Ni}_{1-x}\text{O}$  solid solutions with  $x > 0.50$  decreases after 3 h of heat treatment at  $800\text{ }^\circ\text{C}$ . In the case of  $\text{Co}_{0.85}\text{Ni}_{0.15}\text{O}$  and  $\text{Co}_{0.75}\text{Ni}_{0.25}\text{O}$ , increasing the heat treatment time from 3 to 72 h further decreases the lattice parameter. Based on the existing linear relationship between the lattice parameter and the NiO molar fraction of  $\text{Co}_x\text{Ni}_{1-x}\text{O}$  solid solution, it can be ascertained that only compounds with at least 54 mol% of NiO are stable at  $800\text{ }^\circ\text{C}$  (dashed blue line in **Fig. 4B**). At  $700\text{ }^\circ\text{C}$ , only  $\text{Co}_x\text{Ni}_{1-x}\text{O}$  solid solutions with at least 78 mol% of NiO are stable (dashed red line in **Fig. 4B**). These results are in very well accordance with the temperature-composition diagram of the NiO-CoO-O<sub>2</sub> system in air.<sup>12</sup> Regarding the  $\text{Co}_3\text{O}_4$  phase, its lattice parameter is similar for the different heat treatments ( $a = 8.08\text{ \AA}$  in accordance with JCPDS 43-1004 of  $\text{Co}_3\text{O}_4$ ), confirming that  $\text{Co}(\text{Ni})\text{O}_4$  solid solutions are not formed here. This agrees with the study of Kuboon and Hu, showing that  $\text{Co}(\text{Ni})\text{O}_4$  solid solutions are only formed when the Co-Ni-O material is subjected to calcination at a temperature lower than  $700\text{ }^\circ\text{C}$ .<sup>11</sup>

These results on the thermal stability of  $(\text{Co,Ni})\text{O}$  solid solutions indicate that for Al electrolysis at the usual temperature of  $\sim 960\text{ }^\circ\text{C}$ , the  $(\text{Co,Ni})\text{O}$  protective coating should be thermally stable whatever its stoichiometry. In contrast, for Al electrolysis at lower temperature (*e.g.*, at  $700 - 800\text{ }^\circ\text{C}$  in KF-AlF<sub>3</sub> based electrolyte)<sup>3-6</sup>, Ni-rich  $(\text{Co,Ni})\text{O}$  protective coatings should be selected in order to avoid the undesired formation of  $\text{Co}_3\text{O}_4$ . The impact of the stoichiometry of the  $(\text{Co,Ni})\text{O}$  coating on its protective properties under various Al electrolysis conditions will be evaluated in a near future.

### 3.3 Morphology of the $(\text{Co,Ni})\text{O}$ powders

**Fig. 5** shows the SEM micrographs of  $\text{Co}_x\text{Ni}_{1-x}\text{O}$  powders prepared by the mixed approach (short ball milling + heat treatment of  $\text{Co}_3\text{O}_4 + \text{NiO}$  mixtures) described earlier. For comparison,

the SEM micrographs  $\text{Co}_3\text{O}_4$  and  $\text{NiO}$  used as starting materials are also shown. The particles observed in  $(\text{Co},\text{Ni})\text{O}$  solid solutions have a spherical shape with not sharp edges.

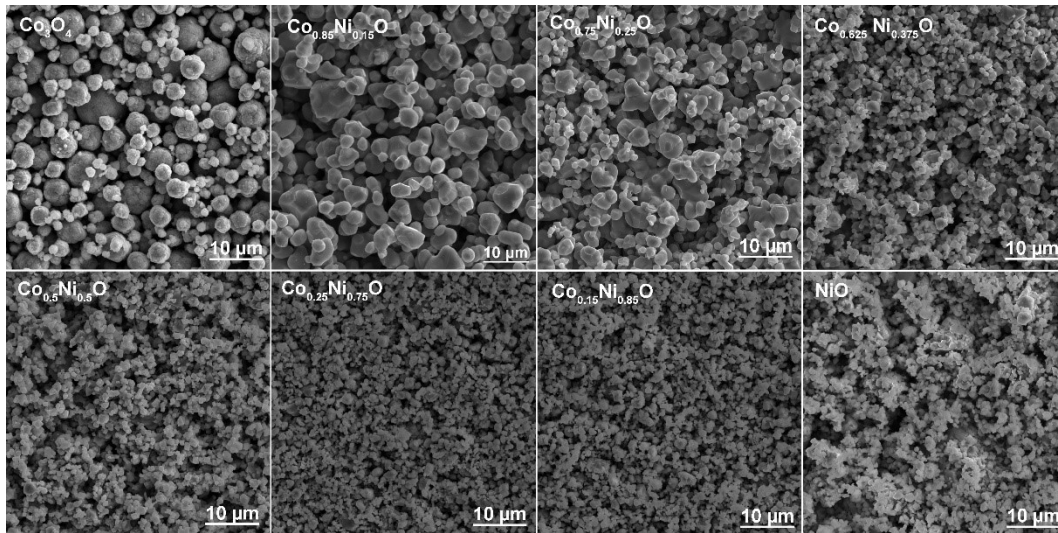


Figure 5. SEM images of the  $(\text{Co},\text{Ni})\text{O}$  powders. The SEM micrographs of the starting materials ( $\text{Co}_3\text{O}_4$  and  $\text{NiO}$ ) are also shown.

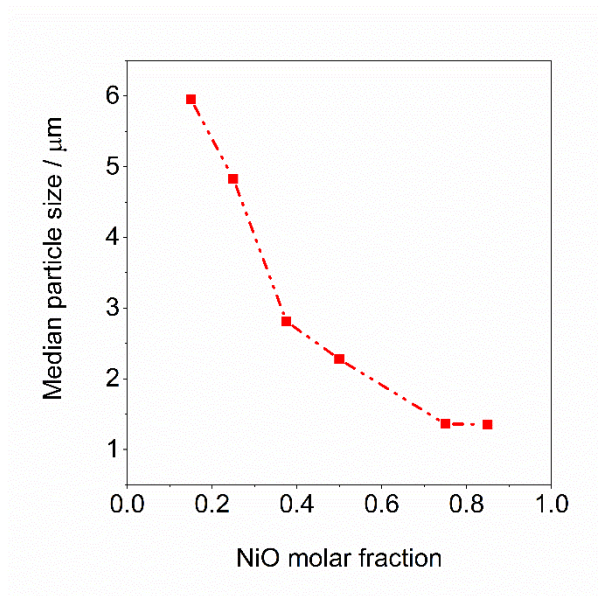


Figure 6. Evolution of the median particle diameter of the  $(\text{Co},\text{Ni})\text{O}$  powders as a function of the  $\text{NiO}$  molar fraction.

The particle size decreases regularly as the  $\text{NiO}$  content gets larger. This trend is confirmed by the PSD measurements. Indeed, as shown in **Fig. 6**, the median particle diameter ( $D_{v,50}$ ) of the  $(\text{Co},\text{Ni})\text{O}$  powder decreases from  $6.0 \mu\text{m}$  for  $\text{Co}_{0.85}\text{Ni}_{0.15}\text{O}$  to  $1.3 \mu\text{m}$  for  $\text{Co}_{0.15}\text{Ni}_{0.85}\text{O}$ . Note that this particle size is too small for APS and HVOF deposition which required larger particles

(typically around 10 - 35  $\mu\text{m}$  in diam.) to be efficient. Thus, further work is required to increase the particle size of (Co,Ni)O solid solutions for use with these deposition techniques. On the other hand, preliminary results of the large-scale synthesis of (Co,Ni)O powders have shown that the size of (Co,Ni)O particles can be easily decreased by a short post-synthesis milling step to the micrometer size range compatible with deposition by suspension plasma spray (SPS). Further work in that direction is underway.

#### **4. Conclusion**

$\text{Co}_x\text{Ni}_{1-x}\text{O}$  materials have been prepared by single step HEBM and two-step (mixed HEBM + heat treatment) procedures. (Co,Ni)O solid solutions produced by prolonged mechanical milling (20 hours) were contaminated by WC due to the erosion of ball milling media. WC contamination is undesirable as it reacts with Co to form  $\text{CoWO}_4$  at high temperature. Thus, in the second method, WC contamination was eliminated by decreasing the ball milling time from 20 hours to 12 minutes and by using a high temperature heat treatment step (10 hours at 1000 °C) to form (Co,Ni)O solid solutions. Pure  $\text{Co}_x\text{Ni}_{1-x}\text{O}$  solid solutions were produced over the whole composition range when  $\text{Co}_3\text{O}_4 + \text{NiO}$  were used as initial powders while a small amount of  $\text{Co}_3\text{O}_4$  was formed at certain composition when  $\text{CoO} + \text{NiO}$  were used instead. At 1000 °C,  $\text{Co}_x\text{Ni}_{1-x}\text{O}$  solid solutions are stable over the whole composition range. In contrast, at 700 and 800 °C,  $\text{Co}_x\text{Ni}_{1-x}\text{O}$  are only stable for  $x \leq 0.22$  and  $x \leq 0.46$ , respectively. The use of single phase (Co,Ni)O powders as raw materials for the preparation by thermal spraying of protective coating on metallic inert anodes is in progress and their anodic behaviour for Al electrolysis will be presented in a near future.

#### **Acknowledgement**

The authors thank the Natural Sciences and Engineering Research Council of Canada (NSERC) (grant STPGP 494283-16), Prima Québec (grant R13-13-001), Metal7 and Kingston Process Metallurgy for supporting this work.

## References

1. Galasiu I, Galasiu R, Thonstad J. Inert anodes for aluminium electrolysis. Düsseldorf: Aluminium-Verlag; 2007: p. 207.
2. Pawlek RP. Inert Anodes: An Update. In: Grandfield J. Light Metals. Springer, Cham; 2014: p. 1309-1313.
3. Beck TR, MacRae CM, Wilson NC. Metal anode performance in low-temperature electrolytes for aluminum production. Metall. Mater. Trans. B. 2011; 42:807–813.
4. Helle S, Pedron M, Assouli B, Davis B, Guay D, Roué L. Structure and high-temperature oxidation behavior of Cu-Ni-Fe based alloys prepared by high energy ball milling for application as inert anodes for aluminum electrolysis. Corros. Sci. 2010; 52:3348-3353.
5. Gavrilova E, Goupil G, Davis B, Guay D, Roué L. On the key role of the Cu content on the oxidation behavior of Cu-Ni-Fe anodes for Al electrolysis. Corros. Sci. 2015; 101:105-113.
6. Goupil G, Jucken S, Poirier D, Legoux JG, Irissou E; Davis B et al. Cold-sprayed Cu-Ni-Fe anode for aluminum electrolysis. Corros. Sci. 2015; 90:259-265.
7. Nguyen T, De Nora. V. De Nora oxygen evolving inert metallic anode. Light Metals. 2006; 385-390.
8. Chen M, Hallstedt B, Gauckler LJ. Thermodynamic assessment of the Co-O system. J. Phase Equilib. 2003; 24:212-227.
9. Vardelle A, Moreau C., Akedo J, Ashrafizadeh H, Berndt CC, Berghaus JO et al. The 2016 thermal spray roadmap. J. Therm. Spray Technol. 2016; 25:1376-1440.
10. Roisnel T, Rodriguez-Carvajal J. WinPLOTR: a windows tool for powder diffraction pattern analysis. Mater. Sci. Forum. 2001; 378:118–123.
11. Kuboon S, Hu YH. Study of NiO–CoO and Co<sub>3</sub>O<sub>4</sub>–Ni<sub>3</sub>O<sub>4</sub> solid solutions in multiphase Ni–Co–O systems. Ind. Eng. Chem. Res. 2011; 50:2015–2020.
12. Moore RJ, White J. Equilibrium relationships in the system NiO-CoO-O<sub>2</sub>. J. Mater. Sci. 1974; 9:1393-1400.
13. Koel GJ, Gellings PJ. The contribution of different types of point defects to diffusion in CoO and NiO during oxidation of the metals. Oxid. Met. 1972; 5:185-203.

### III.5. Article 2: Suspension plasma spray deposition of $\text{Co}_x\text{Ni}_{1-x}\text{O}$ coatings

**Authors:** Saeed Mohammadkhani <sup>a</sup>, Vahid Jalilvand <sup>b</sup>, Boyd Davis <sup>c</sup>, Fadhel Ben Ettouil <sup>b</sup>, Ali Dolatabadi <sup>b</sup>, Lionel Roué <sup>a</sup>, Christian Moreau <sup>b</sup>, Daniel Guay <sup>a</sup>

<sup>a</sup> INRS-Énergie, Matériaux, Télécommunications, Varennes, Québec, Canada

<sup>b</sup> Department of Mechanical, Industrial & Aerospace Engineering, Concordia University, Montreal, Québec, Canada

<sup>c</sup> Kingston Process Metallurgy Inc., Kingston, Ontario, Canada

**Journal:** Surface and Coatings Technology

Published October 2020

**DOI:** <https://doi.org/10.1016/j.surfcoat.2020.126168>

#### **Contributions:**

The suspension plasma spray was carried out by F. Ben Ettouil, V. Jalilvand and the author of this thesis at Concordia University. The powder synthesis as well as characterizations of the coatings by XRD, Rietveld refinement and Particle size distribution were carried out by the author of this thesis. The SEM analysis were performed by V. Jalilvand, A. Dolatabadi, C. Moreau, B. Davis, L. Roué and D. Guay helped interpret the results and correct different versions of the article.

## **Abstract**

Suspension Plasma Spray (SPS) process was used for the deposition of cobalt-nickel oxide solid solutions as potential coatings for inert anodes in primary aluminum production. The effects of SPS process parameters (plasma power, standoff distance, gas mixture, and substrate temperature) on the structure and composition of coatings were investigated. X-ray diffraction measurements, coupled with Rietveld refinement analysis, and scanning electron microscope (SEM) coupled with energy-dispersive X-ray spectroscopy (EDX) analyses were performed. It was shown that substrate temperature is the single most important parameter affecting the nature of the coating, and that uniform, adherent and non-porous  $\text{Co}_x\text{Ni}_{1-x}\text{O}$  coatings made of a single solid solution phase are obtained when the substrate temperature is above 950 °C. Metallic Ni is observed in coatings prepared at lower temperatures and, in that case, the composition of the solid solution phase deviates from that of the starting materials. This work also discusses possible causes for the formation of metallic nickel during spraying.

*Keywords:* (Co,Ni)O solid solution, suspension plasma spray, Al electrolysis

## 1. Introduction

Aluminum is the second most widely used metal in the world. However, primary Al production by electrolysis results in heavy CO<sub>2</sub> emissions [1]. Actually, the aluminum industry is contributing around 1% of the carbon footprint generated by the industrial sector, and 2.1% of global carbon greenhouse gas (GHG) emissions [2]. A relevant approach to produce Al in a greener way is to substitute consumable carbon (CO<sub>2</sub> evolving) anodes by inert (O<sub>2</sub> evolving) anodes. Among the numerous materials studied so far, Cu-Ni-Fe-based alloys appear to be promising, due to their ability to produce a protective nickel ferrite (NiFe<sub>2</sub>O<sub>4</sub>) in low-temperature (700 °C) potassium-based cryolite [3–5]. However, these Cu-Ni-Fe alloys may fluorinate during electrolysis to form non-conductive nickel or iron fluoride, resulting in an increased cell voltage and a decrease in the energy efficiency of the electrolysis process [6].

To protect the CuNiFe alloy from corrosion and prevent the formation of metallic fluorides, the use of (Co,Ni)O-based protective coatings appears promising. Indeed, the work of Nguyen and de Nora [7] demonstrated the effectiveness of this oxide as a fluorination barrier for Ni-Fe metal anodes in a cryolitic medium at 930° C. This is because the CoO phase is very stable with respect to fluorination. However, according to the phase diagram of the Co-O system [8], CoO is likely to be converted to Co<sub>3</sub>O<sub>4</sub> under Al electrolysis conditions, which is undesirable since Co<sub>3</sub>O<sub>4</sub> is an n-type semiconductor that displays a significantly higher O<sub>2</sub> evolution overpotential than p-type semiconducting CoO [7].

Adding Ni atoms to the CoO phase and forming a (Co,Ni)O solid solution makes it possible to avoid the transformation of CoO to Co<sub>3</sub>O<sub>4</sub> [7,9]. The impact of the Ni content on the thermal stability and electrical conductivity of the Co-Ni-O system was highlighted by Moore and White [10]. The thermal stability of Co<sub>x</sub>Ni<sub>1-x</sub>O solid solutions produced by ball milling and calcination has also been studied in our previous work [11].

To make a (Co,Ni)O-based protective coating, a Co-Ni alloy was first electrodeposited onto the anode, followed by an oxidation treatment in air at high temperature to favor the formation of a (Co,Ni)O solid solution [7]. However, due to the change of densities upon oxidation of the metallic Co-Ni alloy, this manner of producing a cohesive, crack-free oxide layer on the inert anode may be challenging.

A potentially relevant method to produce (Co,Ni)O-coated inert anodes is through the direct deposition of (Co,Ni)O oxide compounds, or a mixture of CoO and NiO, via thermal spray deposition techniques. Thermal spraying is a promising, fast and efficient method to deposit thick coatings for various applications in a single step [12]. Various thermal spray techniques exist, including high-velocity oxygen fuel (HVOF), high-velocity air fuel (HVOF), atmospheric plasma spray (APS), and suspension plasma spray (SPS). The latter process was invented in the mid-1990s [13] and has demonstrated its ability to deposit oxide coatings that are usually challenging when using other conventional methods such as electrodeposition, sintering and vacuum-based deposition methods [14]. APS is mainly used for powders that flow easily, and sub-micrometer size powders cannot be used directly due to their low flowability. On the contrary, SPS is ideal for sub-micrometer size particles since they are dispersed and transported by a liquid medium. Also, the main purpose of this study was to prepare coatings made of (Co,Ni)O solid solutions starting from physical mixtures of NiO and CoO powders. During SPS, thinner splats are formed than in APS, which increases the probability that an alloy will form between the two powders.

During SPS, submicron solid particles are injected into a plasma jet from a suspension. The atomization and evaporation of the liquid phase occurs first, followed by the acceleration and melting of particles that travel to and impact the substrate on which they are deposited [15–17]. SPS has been widely used to deposit coatings for a variety of applications; these include biomaterials coatings, wear- and corrosion-resistant coatings, thermal barrier coatings, ceramic filtration membranes, and abrasion-resistant coatings [18–20]. This method's advantages include a relatively high deposition rate, versatility, high scalability, moderate operating cost, and controlled thermal input into substrates [14,21]. With SPS, thick coatings (from 10 to 500  $\mu\text{m}$ ) with sub-micrometer or nanometer scale structures can be produced [22]. Therefore, the ability to create different distinct types of microstructures (columnar-grown, segmented, dense, and porous), the use of fine particles of single or multiphase composition, and even the capability of combining different processes, presents multiple possibilities in terms of thermal spray engineering [23].

In the current study, a novel approach in the preparation of thick, dense, uniform, and single phase (Co,Ni)O coatings using the SPS process is presented. The effects of spraying parameters on the composition and structure of the coatings were studied.

## 2. Experimental

### 2.1 Materials and spray conditions

Cobalt oxide (CoO, Skyspring Nanomaterials, USA) and nickel oxide (NiO, Fuelcellmaterials, USA) were used as starting powders. The particle size distribution was analyzed by laser diffraction using a Malvern Panalytical Spraytec instrument after dispersing the powder in ethanol using a Malvern wet dispersion accessory.

The plasma spraying parameters used for SPS are listed in **Table I**. A first series of tests was performed to explore the deposition parameters space (Part 1, samples S1 to S5). Then, a series of three complementary tests were performed. In the first one, a 50 – 50 mol% CoO + NiO powder mixture was sprayed into water using different plasma powers. The particles were collected, dried in an oven, and analyzed via XRD and SEM. In the second one, NiO and CoO powders were deposited separately on a substrate using the spray conditions listed in Part 1 of **Table I**. Finally, in the third complementary test, a  $\text{Co}_{0.5}\text{Ni}_{0.5}\text{O}$  solid solution powder was used as starting material to prepare coatings. The  $\text{Co}_{0.5}\text{Ni}_{0.5}\text{O}$  solid solution was prepared through a three-step process that involves 12 min ball milling step of a mixture of NiO and  $\text{Co}_3\text{O}_4$  with the targeted 50 – 50 mol% of Co and Ni, followed by a heat treatment at 1000 °C for 10 h and a final 3 h ball milling step to reduce the powder particle size to under 3  $\mu\text{m}$  to meet the SPS requirements. Following these complementary tests, a second and a third series of tests (S6-S7 and S8-S9 samples, respectively) were performed to obtain a single phase coating with low porosity and good adhesion. Square-shaped AISI 304 Stainless steel substrates (2.5 \* 2.5  $\text{cm}^2$  and 0.5 cm thickness) were grit blasted and then rinsed with acetone prior to their use. All substrates have been prepared using the same conditions resulting in a surface roughness,  $R_a$ , of  $1.3 \pm 0.2 \mu\text{m}$ .

Suspensions of CoO and NiO were prepared by mixing 10 wt% of oxide powders with the intended CoO and NiO ratio with 1 wt% of polyvinylpyrrolidone (PVP) as a dispersing agent in ethanol. The injection setup for SPS was developed in-house, and has been described in detail in our previous work [24]. A Mettech's Axial III Plasma Spray System was used in all experiments. This is a high-power, high-efficiency deposition device with axial injection capability (injection of feedstock materials directly into the center of the plasma plume). A FLIR A320 infrared camera (FLIR Systems Inc., USA) was used to monitor substrate temperature during SPS.

Table I. Spray process parameters.

Sample #	Total gas (slm), Ar/N <sub>2</sub> /H <sub>2</sub> (slm), Current (amps)	Power (kW)	Air cooling	Water cooling	Preheating to 200 °C	Inter-pass pauses	Standoff distance (mm)	Substrate temperature
Part 1. Powder suspension of 50% CoO + 50% NiO								
S1	180, 45/45/10, 155	75	Yes	No	Yes	Yes	50	< 600 °C
S2	180, 45/45/10, 167	80	Yes	No	Yes	Yes	50	< 600 °C
S3	180, 45/45/10, 180	85	Yes	No	Yes	Yes	50	< 600 °C
S4	180, 45/45/10, 192	90	Yes	No	Yes	Yes	50	< 600 °C
S5	180, 45/45/10, 210	95	Yes	No	Yes	Yes	50	< 600 °C
Part 2. Powder suspension of 50% CoO + 50% NiO								
S6	180, 45/45/10, 180	85	Yes	Yes	Yes	Yes	50	< 300 °C
S7	180, 45/45/10, 180	85	Yes	Yes	Yes	Yes	70	< 300 °C
Part 3. Powder suspension of 50% CoO + 50% NiO (S8) and 75% CoO + 25% NiO (S9)								
S8	180, 45/45/10, 180	85	No	No	Yes	No	50	ca 950 °C
S9	180, 45/45/10, 180	85	No	No	No	No	50	ca 950 °C

## 2.2. Material characterization

The crystalline structure of coatings was determined by x-ray diffraction (XRD) using a Bruker D8 diffractometer with Cu K<sub>α</sub> radiation. The crystalline structure and unit cell dimensions were obtained through the Rietveld refinement technique, a multi-parameter curve-fitting procedure to extract structural information from the XRD pattern. Refinements of lattice parameters were carried out using the FULLPROF program [25]. The background was removed in the XRD patterns shown below.

As-sprayed specimens were cut using a precision cut-off machine (Secotom-15, Struers A/S, Denmark), then mounted and polished using standard metallographic procedures to a final finish of 0.4 μm. A scanning electron microscope (SEM) coupled with an energy-dispersive X-ray spectroscopy (EDX) elemental analyser (S-3400N, Hitachi High Technologies America, Inc., USA) operating at 15 kV was used for metallographic observation of the deposited samples.

### 3. Results

SEM micrographs of precursor powders are shown in **Fig. 1**. CoO and NiO powders consist of spherical particles. **Fig. 1c and d** shows the corresponding particle size distribution histograms. The particle diameters of CoO powder are centered along a single mode (maximal frequency) at 3  $\mu\text{m}$ , while those of NiO powder are spread over two modes located at 0.5 and 6  $\mu\text{m}$ . The  $D_{10}$ ,  $D_{50}$ , and  $D_{90}$  values are 0.73, 2.3, and 6.1  $\mu\text{m}$  for CoO powder and 0.20, 0.65 and 5.3  $\mu\text{m}$  for NiO powder, respectively.

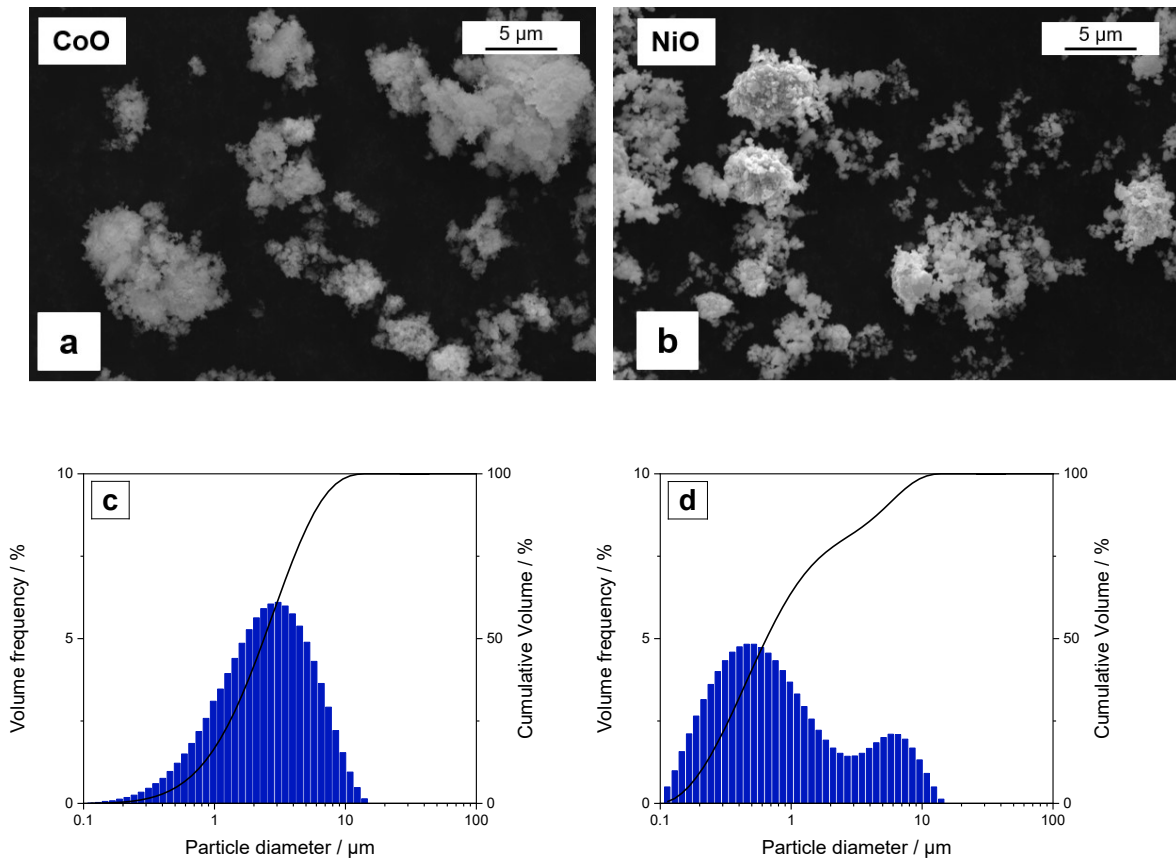


*Fig. 1. SEM micrographs of (a) CoO and (b) NiO precursor powders, and particle size distribution histograms of (c) CoO and (d) NiO precursor powders.*

In the first series of experiments, the suspensions prepared by mixing CoO and NiO powders with 50 - 50 mol% were sprayed using five different input powers ranging from 75 to 95 kW, with all other spray parameters kept constant (see **Table I**). The substrate was maintained below 600  $^{\circ}\text{C}$  by applying inter-pass pauses and air jet cooling to prevent overheating during spraying. **Fig. 2a** presents the XRD patterns of the prepared coatings. Two sets of peaks appear in

the XRD patterns. The main diffraction peaks occur at *ca.*  $2\theta = 37^\circ, 43^\circ, 62^\circ, 75^\circ$  and  $78^\circ$  and are assigned to a *fcc* (Co,Ni)O solid solution. The diffraction peaks of this *fcc* phase are slightly displaced toward larger  $2\theta$  value compared to CoO, suggesting that NiO is dissolved in CoO to form a (Co,Ni)O solid solution. A second set of peaks observed at *ca.*  $2\theta = 44.4^\circ, 51.7^\circ$  and  $76.1^\circ$  are attributed to metallic Ni, indicating that a fraction of the NiO particles is reduced to metallic nickel.

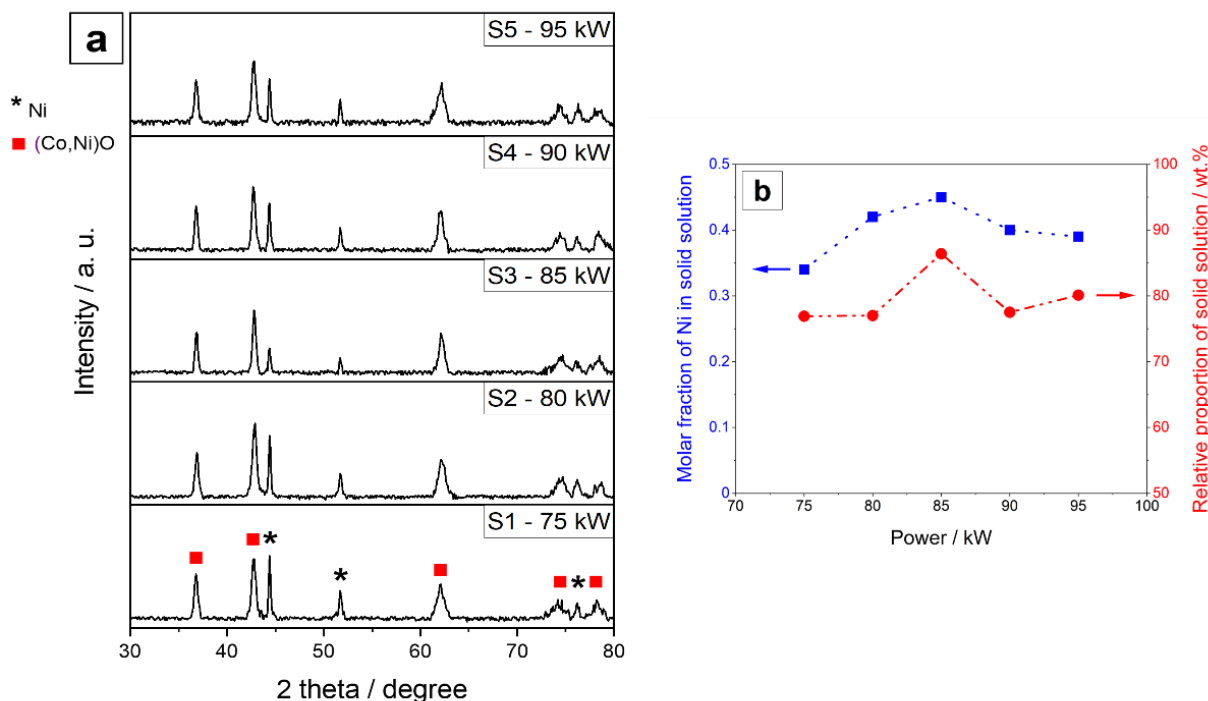


Fig. 2. In (a) XRD patterns of coatings prepared at plasma powers ranging from 75 to 95 kW. In (b), the relative proportion of the solid solution phase, and the Ni content of the solid solution phase are plotted with respect to the plasma power.

A quantitative analysis was conducted via the Rietveld refinement technique to establish the lattice parameters as well as the Co and Ni contents of the solid solutions, and the relative proportions of solid solution and metallic Ni phases. Typical examples of the correspondence between the experimental data and the fitted curve are shown in **Fig. S1**. Based on the existing linear relationship between the lattice parameter and the NiO molar fraction of the  $\text{Co}_x\text{Ni}_{1-x}\text{O}$  solid solution [11], the latter's composition can be ascertained from the lattice parameter value obtained through Rietveld analysis. The coating's total Co and Ni contents may be calculated by considering the relative proportions of solid solution and metallic Ni phases extracted from the Rietveld

analysis, and the weight percent of Co and Ni in the solid solution phase. These values were compared to those of the starting materials in **Table II**. Both sets of data (mass balance) are in reasonably good agreement.

*Table II. Parameters extracted from the Rietveld analysis and the mass balance analysis of samples S1–S9. Note that the Co, Ni and O contents in the powder used for samples S1 to S8 were 39.2, 39.4 and 21.4 wt%, respectively. For sample S9, the Co, Ni and O contents were 59.0, 19.6 and 21.4 wt%, respectively.*

Sample	wt% (Co,Ni)O from Rietveld	wt% Ni from Rietveld	Lattice parameter of (Co,Ni)O phase from Rietveld	Composition of (Co,Ni)O phase (based on lattice parameter)	wt% Co in SS phase	wt% Ni in SS phase	Total wt% Co in coating	Total wt% Ni in coating
S1	76.9	23.1	4.230	Co <sub>0.66</sub> Ni <sub>0.34</sub> O	52.0	26.7	40.0	43.6
S2	77.0	23.0	4.222	Co <sub>0.58</sub> Ni <sub>0.42</sub> O	44.9	33.7	34.6	48.9
S3	86.1	13.9	4.219	Co <sub>0.55</sub> Ni <sub>0.45</sub> O	42.5	36.1	36.6	45.0
S4	77.5	22.5	4.225	Co <sub>0.60</sub> Ni <sub>0.40</sub> O	47.2	31.4	36.6	46.8
S5	82.1	17.9	4.226	Co <sub>0.61</sub> Ni <sub>0.39</sub> O	48.0	30.6	39.4	43.0
S6	47.8	52.2	4.253	Co <sub>0.93</sub> Ni <sub>0.07</sub> O	73.2	5.5	35.0	54.8
S7	51.3	48.7	4.250	Co <sub>0.90</sub> Ni <sub>0.10</sub> O	70.8	7.8	36.3	52.7
S8	100	0	4.216	Co <sub>0.48</sub> Ni <sub>0.52</sub> O	37.8	40.8	37.8	40.8
S9	100	0	4.241	Co <sub>0.77</sub> Ni <sub>0.23</sub> O	60.6	18.0	60.6	18.0

The Ni content of the Co<sub>x</sub>Ni<sub>1-x</sub>O solid solution varied with the input power (**Fig. 2b**). It was maximal at 85 kW, although not as large as expected based on the composition of the injected powder. This is consistent with the variation in the relative proportions of solid solution and metallic Ni phases, which show a maximum at the same power. Thus, NiO and CoO were reacting together to form a Co<sub>x</sub>Ni<sub>1-x</sub>O solid solution phase, but this process was not complete.

**Fig. 3** shows the cross-sectional SEM micrographs of SPS coatings. After 25 deposition passes, these cross-sectional micrographs displayed an approximate coating thickness of 20 to 50 μm, with good adherence to the substrate. All coatings except S3 were composed of light and dark grey areas, parallel to the substrate. The EDX analyzes (not presented here) reveal that the light gray areas did not contain any Co, while the dark gray areas contained both Co and Ni atoms. For

sample S3, the light grey areas were observed only at the interface between the coating and the substrate as well as in a few areas where columnar-growth is observed (**Fig. 3f**). From this point forward, the input power was set at 85 kW, and the spraying parameters were varied to identify the deposition conditions that would give a coating made of a single  $\text{Co}_x\text{Ni}_{1-x}\text{O}$  solid solution phase.

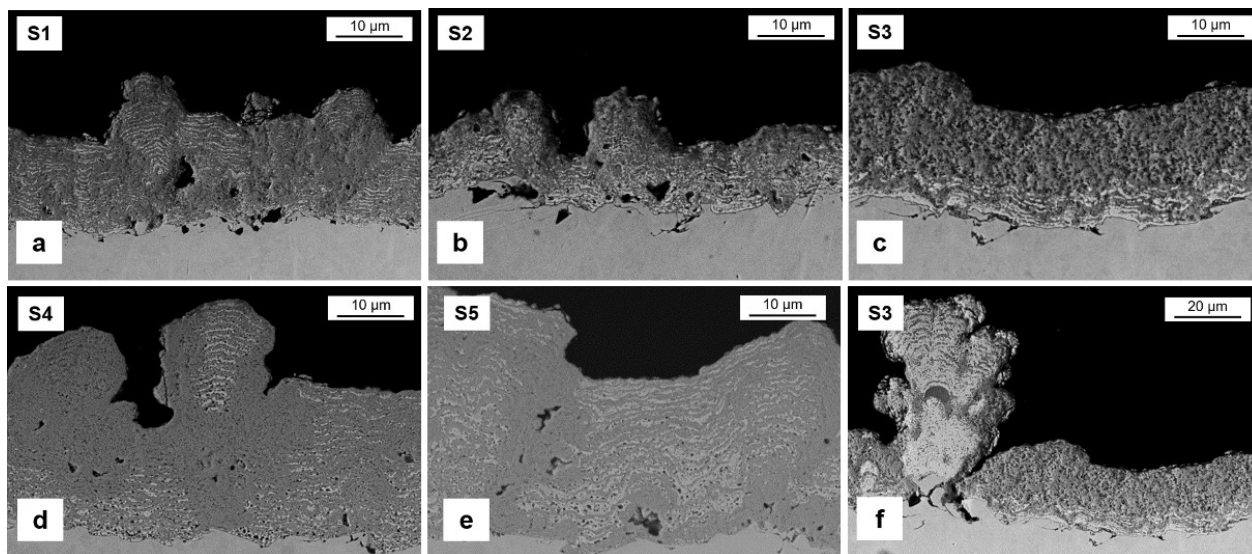


*Fig. 3. Cross-sectional SEM micrographs of coatings prepared at different plasma powers: (a) 75 kW, (b) 80 kW, (c) 85 kW, (d) 90 kW and (e) 95 kW. In (f) the same coating as (c) is shown at a lower magnification. The substrate temperature was always lower than 600 °C.*

**Fig. 4** shows the XRD patterns of the sprayed particles collected from water. Two sets of peaks appear in the XRD patterns, attributed to CoO and NiO phases. Interestingly, the XRD peaks of the solid solution were not observed. This suggests that the formation of the solid solution occurred mostly on the substrate. The XRD peaks of metallic Ni were not observed either, although it is possible that metallic Ni particles were reoxidized upon contact with water. This must be the case since spraying only NiO particles on a substrate using the spray parameters given in Part 1 of **Table I** produced a coating that contains both NiO and metallic nickel phases (**Fig. 5a, 5b** and **5c**). In contrast, spraying only CoO particles using the same spray parameters produced a coating that contains only CoO (**Fig. 5d**).

Then, a powder made of a  $\text{Co}_{0.5}\text{Ni}_{0.5}\text{O}$  solid solution was used as starting material (instead of the previous 50 – 50 mol% physical mixture of CoO + NiO.) The  $\text{Co}_{0.5}\text{Ni}_{0.5}\text{O}$  solid solution was

prepared through a three-step process outlined in our previous work [11]. To provide a less reductive atmosphere, helium rather than hydrogen was used in the plasma gas mixture, and the spraying parameters are listed in **Table III**. Independently of the input power, the XRD pattern showed the characteristic peaks of both the solid solution and the metallic nickel phases (**Fig. 6**). So, metallic Ni is formed even if a solid solution is used as starting material and, most importantly, in the absence of a reductant in the plasma gas mixture.

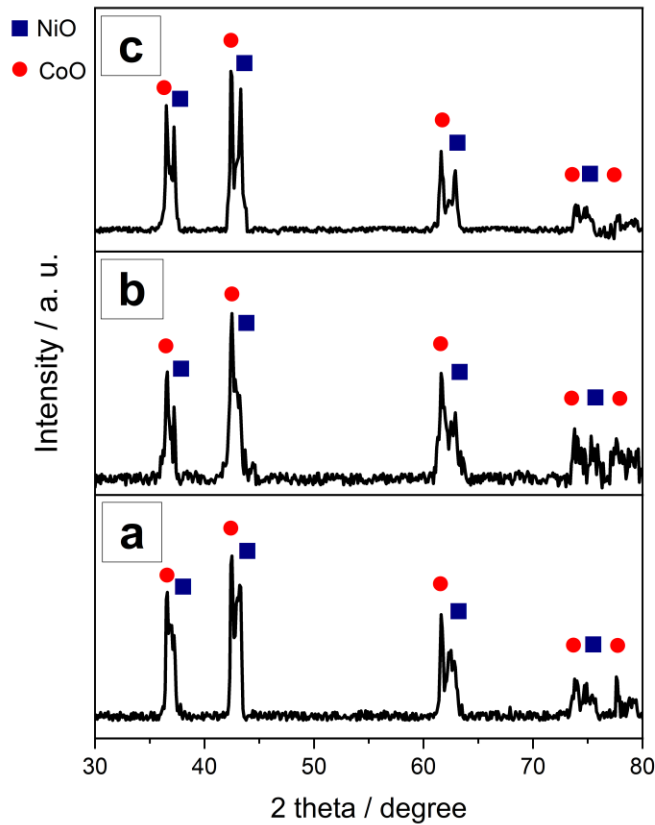


*Fig. 4. XRD patterns of mixed CoO and NiO (50–50 mol%) precursor particles sprayed in water, and then collected and dried in an oven. Different plasma powers were used: (a) 75 kW, (b) 85 kW and (c) 95 kW.*

At 600 °C, the lowest substrate temperature recorded in the previous experiments, NiO is not stable and decomposes to form metallic Ni when the O<sub>2</sub> pressure is less than 10<sup>-18</sup> bar according to the Ni-O phase diagram [26]. The stability domain of Ni-O varies with the temperature. For example, at 300 °C, the decomposition of NiO to Ni occurs when the oxygen pressure is lower than 10<sup>-32</sup> bar. It was inferred from this observation that a lower substrate temperature would decrease the amount of metallic Ni in the coating. Accordingly, in a second series of experiments,

the plasma power was set at 85 kW, and a water-cooled substrate holder and longer inter-pass pauses were introduced to maintain the substrate temperature below 300 °C. The same mixture of CoO and NiO powders (with 50 - 50 mol%) was used. The spraying parameters used for this series of experiments (S6 and S7) are listed in the second part of **Table I**.

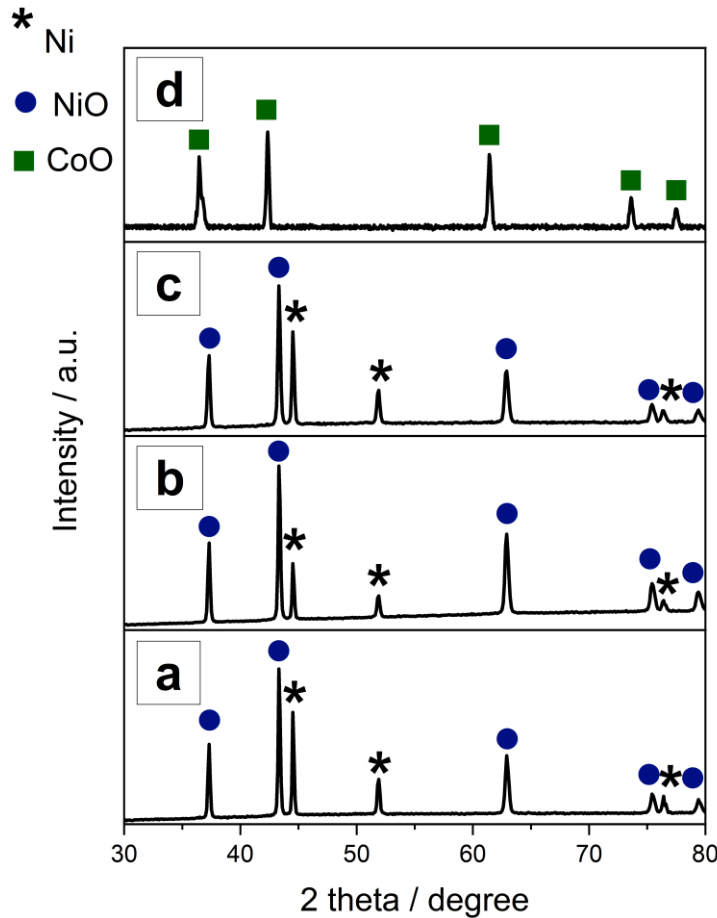


*Fig. 5. XRD patterns of coatings prepared from (a, b and c) NiO powder and (d) CoO powder. The input power was (a) 75 kW, (b and d) 85 kW and (c) 95 kW. All other spraying parameters are listed in Table 1.*

Table III. Spray parameters of a complementary series of experiments. A powder made of a  $\text{Co}_{0.5}\text{Ni}_{0.5}\text{O}$  solid solution was used as starting material and helium was used instead of hydrogen in the plasma gas mixture.

Suspension $\text{Co}_{0.5}\text{Ni}_{0.5}\text{O}$ solid solution								
Sample #	Total gas (slm), Ar/N <sub>2</sub> /He (slm), Current (amps)	Power (kW)	Air cooling	Water cooling	Preheating to 200 °C	Inter-pass pauses	Standoff distance (mm)	Substrate temperature
1	180, 75/10/15, 240	54	Yes	No	Yes	Yes	50	< 600 °C
2	180, 45/45/10, 245	82	Yes	No	Yes	Yes	50	< 600 °C
3	225, 45/45/10, 245	93	Yes	No	Yes	Yes	50	< 600 °C

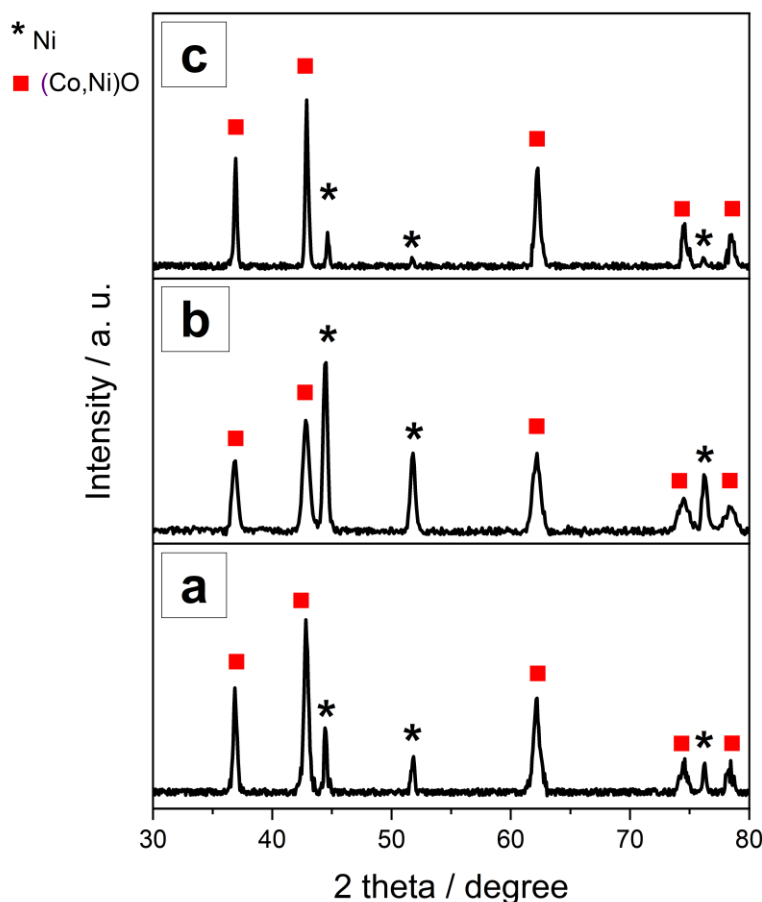
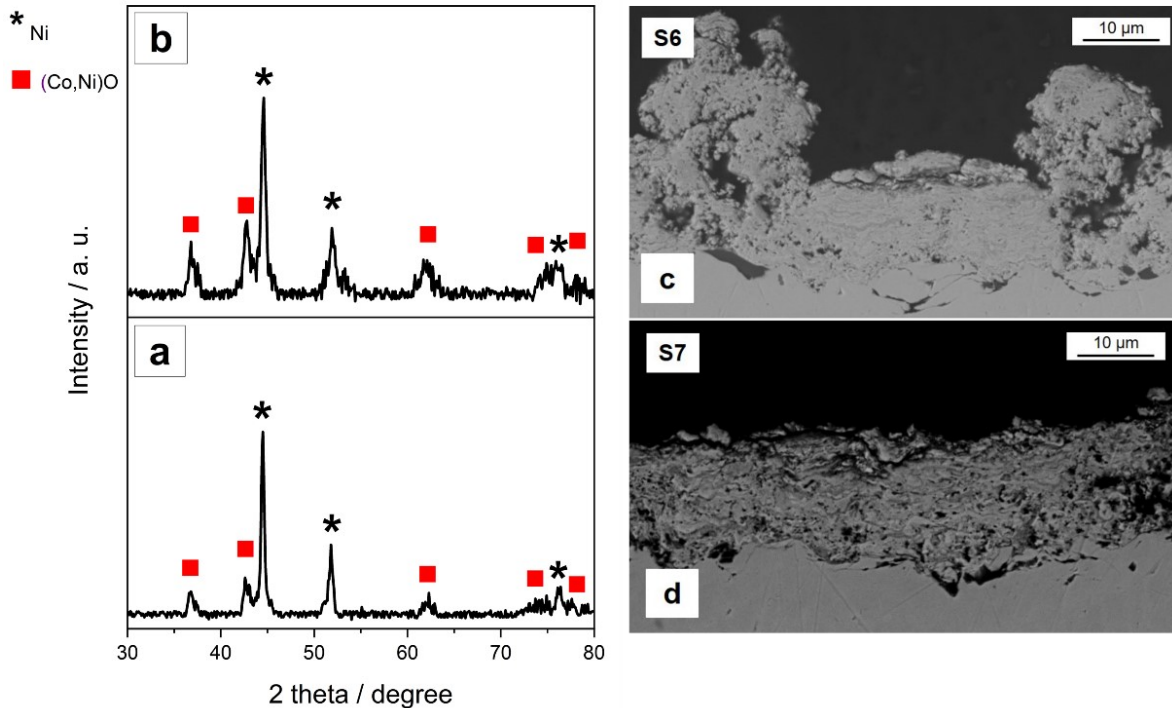


Fig. 6. XRD patterns of coatings prepared using  $\text{Co}_{0.5}\text{Ni}_{0.5}\text{O}$  solid solution powder (instead of a physical mixture of  $\text{CoO} + \text{NiO}$ ) as starting materials and three plasma powers: (a) 54 kW, (b) 82 kW, and (c) 93 kW. In this series of experiments, the gas mixture consisted of Ar/N<sub>2</sub>/He (instead of Ar/N<sub>2</sub>/H<sub>2</sub>) to provide a less reductive atmosphere.

**Fig. 7a and b** displays XRD patterns of samples S6 and S7 that were prepared at two standoff distances (50 and 70 mm) and with the substrate temperature maintained below 300 °C. Increasing the standoff distance may allow the coating to be exposed to more O<sub>2</sub> molecules from the surrounding. For both coatings, two series of peaks were observed, assigned to the solid solution and metallic nickel phases. There was no significant difference between the two XRD patterns, indicating the distance between the nozzle and the substrate is not a critical factor in the formation of metallic Ni. The cross-sectional SEM micrographs in **Fig. 7c and d** indicate that compared to sample S6, increasing the standoff distance (sample S7) made the coating slightly less porous and more uniform.



*Fig. 7. XRD patterns of coatings prepared in the second series of experiments: (a) standoff distance = 50 mm, and (b) standoff distance = 70 mm. In both cases, the plasma power was 85 kW and the substrate temperature was always lower than 300 °C. In (c and d), cross-sectional SEM images of corresponding coatings.*

Thus, no inter-pass pause or additional cooling were applied, and the substrate temperature was allowed to increase to *ca.* 950 °C in the third series of experiments (see **Table I**). **Fig. 8** exhibits the XRD pattern of samples S8 and S9. These samples were prepared from powder mixtures consisting of (50% mol. CoO and 50% mol. NiO) and (75% mol. CoO and 25% mol. NiO), respectively. Both XRD patterns have only a single set of peaks attributed to Co<sub>x</sub>Ni<sub>100-x</sub>O

solid solutions, with no trace of metallic Ni. The  $\text{Co}_x\text{Ni}_{1-x}\text{O}$  composition was  $x = 0.48$  and  $0.77$  for samples S8 and S9, respectively, which is in agreement with the starting powders' compositions.

The cross-sectional SEM images of these two samples are presented in **Fig. 9**. For sample S8, the substrate was pre-heated at  $200\text{ }^\circ\text{C}$  and the coating is uniform and dense. Its surface has a dome-shaped structure and dark grey appearance. Sample S9 has a relatively flat surface. Coating S9 exhibits a light grey area close to the substrate/coating interface, while its upper portion (close to the coating/air interface) has a dark grey appearance. From previous observations, the darker areas and lighter areas were attributed to the solid solution and metallic Ni phases, respectively. The metallic nickel phase in sample S9 is not detected by XRD most probably because it is buried underneath a thicker layer (*ca.*  $50\text{ }\mu\text{m}$  thick) made of only the solid solution phase. The EDX analysis results showed that the cobalt, nickel and oxygen contents in sample S8 were 37, 39 and 24 wt%, while these of sample S9 were 60, 16 and 24, respectively. The EDX results are in good agreement with the quantitative results obtained from Rietveld refinement of the XRD patterns and presented in **Table II**. Based on the EDX analysis results, there was no trace of iron or chromium in the coating, confirming that there was no diffusion of these elements from the substrate.

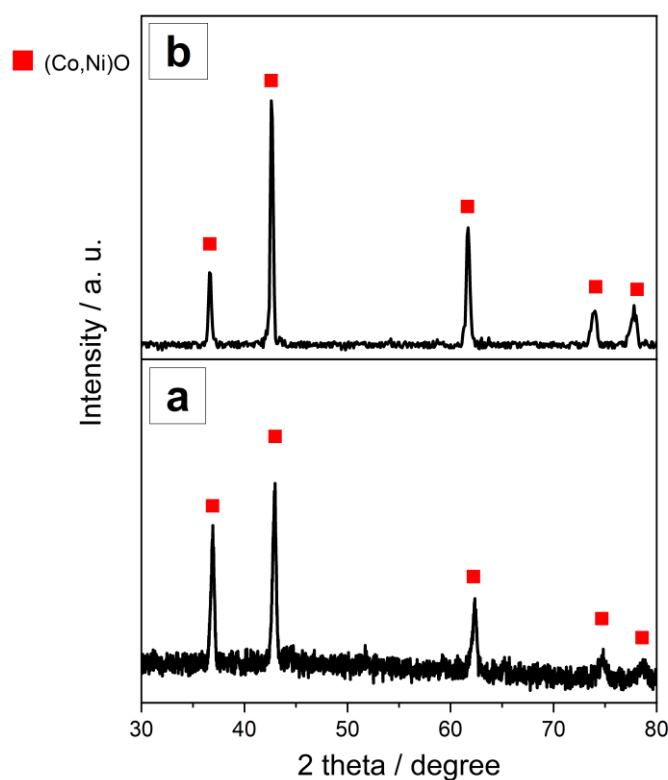


Fig. 8. XRD patterns of coatings prepared in the third series of experiments with (a) [50% mol. CoO + 50% mol. NiO] and (b) [75% mol. CoO + 25% mol. NiO] mixtures. The input power was 85 kW.

The cross-sectional SEM images of these two samples are presented in **Fig. 9**. For sample S8, the substrate was pre-heated at 200 °C and the coating is uniform and dense. Its surface has a dome-shaped structure and dark grey appearance. Sample S9 has a relatively flat surface. Coating S9 exhibits a light grey area close to the substrate/coating interface, while its upper portion (close to the coating/air interface) has a dark grey appearance. From previous observations, the darker areas and lighter areas were attributed to the solid solution and metallic Ni phases, respectively. The metallic nickel phase in sample S9 is not detected by XRD most probably because it is buried underneath a thicker layer (*ca.* 50  $\mu\text{m}$  thick) made of only the solid solution phase. The EDX analysis results showed that the cobalt, nickel and oxygen contents in sample S8 were 37, 39 and 24 wt%, while these of sample S9 were 60, 16 and 24, respectively. The EDX results are in good agreement with the quantitative results obtained from Rietveld refinement of the XRD patterns and presented in **Table II**. Based on the EDX analysis results, there was no trace of iron or chromium in the coating, confirming that there was no diffusion of these elements from the substrate.

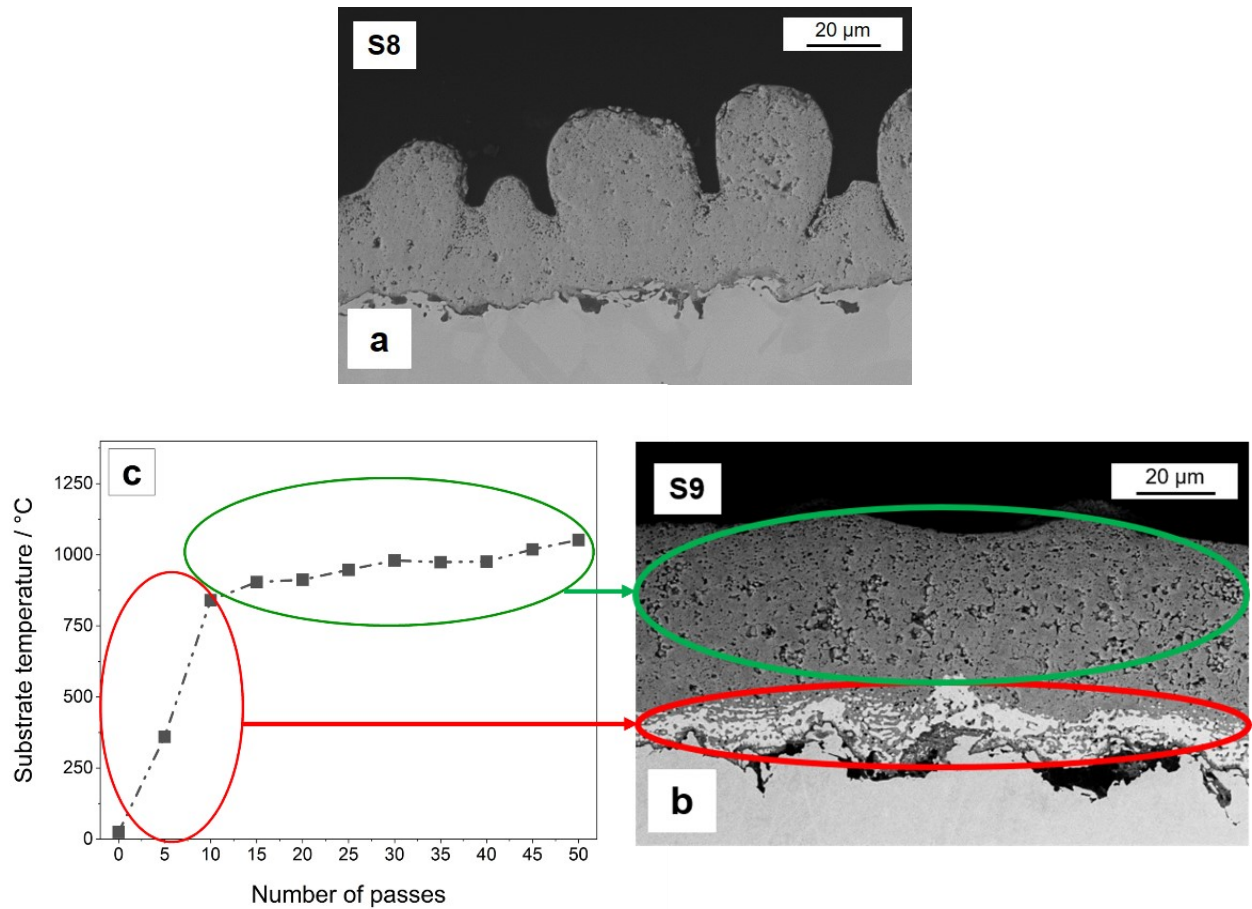


Fig. 9. Cross-sectional SEM micrographs of (a) [50% mol. CoO + 50% mol. NiO] and, (b) [75% mol. CoO + 25% mol. NiO] mixtures. The input power was 85 kW. The variation in substrate temperature with the number of passes is seen in (c).

Variations in substrate temperature with the number of passes are depicted in **Fig. 9c**. The substrate temperature rose to 950 °C in the first ten passes, and remained nearly unchanged over the following 40 passes. The metallic nickel phase in sample S9 was formed in the first few passes of spraying, when the temperature was below 950 °C. Sample S8 does not exhibit a light grey region at the coating/substrate interface. Note that sample S8’s substrate was preheated to 200 °C before beginning the coating process. As a result, it is hypothesized that the substrate reached its maximum temperature faster, which would explain why these light grey strata are not observed in sample S8.

## 4. Discussion

Using a mixture of CoO and NiO as starting materials, it was shown it is possible to use SPS as a deposition technique to prepare  $\text{Co}_x\text{Ni}_{1-x}\text{O}$  coatings that are relatively dense, adherent, and made of a single phase. Our investigation has shown that substrate temperature is the most important parameter affecting the nature of the coating. At low substrate temperature, metallic Ni is formed and the composition of the solid solution phase deviates from that of the starting powders. In contrast, only a single phase is observed in coatings prepared at high temperature, and the composition of the solid solution thus formed is the same as that of the starting materials.

The mechanisms leading to the formation of metallic nickel in the sprayed coatings is not fully understood, and the different factors that can contribute are going to be discussed. One hypothesis to explain the formation of metallic Ni may be that CoO acts as a reducing agent and is further oxidized to  $\text{Co}_3\text{O}_4$ . However,  $\text{Co}_3\text{O}_4$ 's characteristic diffraction peaks were never detected in XRD traces. Also, from the Ni-O and Co-O phase diagrams [8,26], one would not expect CoO to reduce NiO and form  $\text{Co}_3\text{O}_4$ . Moreover, as presented in **Fig. 5**, the reduction of NiO to metallic Ni occurs even in the absence of CoO.

Reduction of NiO to metallic Ni was observed in several studies dealing with plasma-spraying of NiO/yttria-stabilized zirconia (NiO/YSZ) anode coatings for solid oxide fuel cells (SOFCs) [27–29]. In most cases,  $\text{H}_2$  was used in the plasma jet, and reduction of NiO by  $\text{H}_2$  was even used as a strategy to increase the porosity of the coating due to the volume shrinkage between NiO and Ni [29]. Also, oxide reduction of  $\text{ZrO}_2$  to  $\text{Zr}_2\text{O}_3$  in yttria-zirconia thermal barrier coatings prepared by plasma spraying and low-pressure plasma-spraying with a plasma jet consisting of Ar and  $\text{H}_2$  have been observed in the past [30]. The interaction between ceramic particles and the reducing plasma gas was thought to be responsible for the reduction of  $\text{ZrO}_2$  to  $\text{Zr}_2\text{O}_3$ . Partial reduction of  $\text{TiO}_2$  to  $\text{Ti}_n\text{O}_{2n-1}$  (Magnéli phases, where  $n$  is an integer) has also been observed during the spraying of  $\text{TiO}_2$  particles in a mixture of Ar and  $\text{H}_2$  [31].

The occurrence of metallic Ni in coatings prepared by plasma spraying of NiO – nanoagglomerate was also observed in the absence of  $\text{H}_2$  in the plasma jet [28,32], which raises the question of the nature of the reducing agent. It was claimed that collisions of energetic plasma

ions with the sprayed material could be responsible for the observed reduction of NiO during spraying.

NiO can be reduced to metallic Ni at high temperatures through a solid-solid reaction (carbothermal reduction) using coal. NiO can also be reduced through solid-gas reactions using H<sub>2</sub> [33] and CH<sub>4</sub> [34,35]. It was shown recently through a thermodynamic analysis and a series of experimental results that ethanol can be used to reduce NiO to metallic Ni and full conversion of NiO to Ni was observed between *ca* 375 -825 °C [36]. This is because the decomposition products of ethanol (H<sub>2</sub>, CO and C<sub>x</sub>H<sub>y</sub>) are strong reducing agents [37].

The occurrence of C and H species in the plasma (mixture of Ar and He) formed in suspension plasma spraying of YSZ particles dispersed in ethanol was nicely confirmed using optical emission spectra [38]. Indeed, Michaux *et al* attributed the occurrence of metallic Ni in coatings prepared by solution plasma spraying of an ethanolic suspension of NiO and Y<sub>2</sub>O<sub>3</sub>/ZrO<sub>2</sub> powder to reduction of NiO by reducing species resulting from the vaporization/decomposition/ionization of the liquid phase, although H<sub>2</sub> was used as secondary plasma forming gas in their study [28]. So, even in the absence of H<sub>2</sub> in the plasma gas mixture, extensive formation of metallic Ni in coatings prepared at low substrate temperature should not come as a surprise in our SPS experiments since an ethanolic suspension of NiO and CoO powders was used. At high substrate temperature, metallic Ni is oxidized to NiO. This is most particularly evident in sample S9, where metallic Ni is exclusively observed at the substrate/coating interface whilst the substrate temperature was not high enough for Ni to oxidize to NiO before the next pass. Upon reaching a stable substrate temperature of *ca* 950 °C, oxidation of metallic Ni to NiO is fast compared to the transverse motion of the nozzle, allowing the formation of Co<sub>x</sub>Ni<sub>1-x</sub>O coating made of a single solid solution phase.

In summary, different powder mixtures (50% mol CoO + 50% mol NiO) and (75% mol CoO and 25% mol NiO) were used to prepare coatings. The results showed that coatings made of a single phase Co<sub>x</sub>Ni<sub>1-x</sub>O solid solution were obtained as long as the substrate temperature is above 950 °C. It is known from the literature that Co<sub>x</sub>Ni<sub>1-x</sub>O solid solution can be prepared with  $0 \leq x \leq 1$  at temperature higher than *ca* 900 °C [11]. Thus, it is inferred that Co<sub>x</sub>Ni<sub>1-x</sub>O coatings with  $0 \leq x \leq 1$  can be obtained starting from an initial powder mixture with the right composition.

#### **4. Conclusions**

$\text{Co}_x\text{Ni}_{1-x}\text{O}$  coatings were deposited by SPS using CoO and NiO as starting materials. The effects of spraying variables - including input power, standoff distance, and substrate temperature - on coating composition were studied. Substrate temperature was identified as the most critical parameter affecting coating composition. Uniform, adherent and non-porous  $\text{Co}_x\text{Ni}_{1-x}\text{O}$  coatings made of a single solid solution phase were obtained when the substrate temperature was above 950 °C. In the future, the use of inert metallic anodes protected by  $\text{Co}_x\text{Ni}_{1-x}\text{O}$  coatings will be further investigated for the primary production of aluminum.

#### **Acknowledgements**

The authors wish to thank the Natural Sciences and Engineering Research Council (NSERC) through the Strategic program (STPGP/494283-2016), Prima Québec (grant R13-13-001), Metal7 and Kingston Process Metallurgy for supporting this work. Vahid Jalilvand acknowledges a doctoral research scholarship from Fonds de Recherche du Québec - Nature et Technologies (FRQ-NT). Saeed Mohammadkhani also wishes to acknowledge the support of the UNESCO Chair Materials for Energy Conversion, Saving and Storage (MATECSS) Excellence Scholarship.

## References

- [1] D. Paraskevas, K. Kellens, A. Van de Voorde, W. Dewulf, J.R. Dufloy, Environmental Impact Analysis of Primary Aluminium Production at Country Level, *Procedia CIRP*. 40 (2016) 209–213. doi:10.1016/j.procir.2016.01.104.
- [2] M. Gautam, B. Pandey, M. Agrawal, Carbon Footprint of Aluminum Production, in: *Environ. Carbon Footprints*, Elsevier, 2018: pp. 197–228. doi:10.1016/B978-0-12-812849-7.00008-8.
- [3] E. Gavrilova, G. Goupil, B. Davis, D. Guay, L. Roué, On the key role of Cu on the oxidation behavior of Cu–Ni–Fe based anodes for Al electrolysis, *Corros. Sci.* 101 (2015) 105–113. doi:10.1016/j.corsci.2015.09.006.
- [4] G. Goupil, S. Jucken, D. Poirier, J.G. Legoux, E. Irissou, B. Davis, D. Guay, L. Roué, Cold sprayed Cu–Ni–Fe anode for Al production, *Corros. Sci.* 90 (2015) 259–265. doi:10.1016/j.corsci.2014.10.021.
- [5] S. Jucken, M.H. Martin, E. Irissou, B. Davis, D. Guay, L. Roué, Cold-Sprayed Cu-Ni-Fe Anodes for CO<sub>2</sub>-Free Aluminum Production, *J. Therm. Spray Technol.* 29 (2020) 670–683. doi:10.1007/s11666-020-01002-z.
- [6] S. Jucken, B. Tougas, B. Davis, D. Guay, L. Roué, Study of Cu-Ni-Fe Alloys as Inert Anodes for Al Production in Low-Temperature KF-AlF<sub>3</sub> Electrolyte, *Metall. Mater. Trans. B.* 50 (2019) 3103–3111. doi:10.1007/s11663-019-01695-w.
- [7] T. Nguyen, V. De Nora, De Nora oxygen evolving inert metallic anode, *TMS Light Met.* In: Galloway TJ editor, Hoboken, NJ: Wiley - TMS (2006) 385–390.
- [8] M. Chen, B. Hallstedt, L.J. Gauckler, Thermodynamic assessment of the Co-O system, *J. Phase Equilibria.* 24 (2003) 212–227. doi:10.1361/105497103770330514.
- [9] S. Kuboon, Y.H. Hu, Study of NiO–CoO and Co<sub>3</sub>O<sub>4</sub>–Ni<sub>3</sub>O<sub>4</sub> Solid Solutions in Multiphase Ni–Co–O Systems, *Ind. Eng. Chem. Res.* 50 (2011) 2015–2020. doi:10.1021/ie101249r.
- [10] R.J. Moore, J. White, Equilibrium relationships in the system NiO–CoO–O<sub>2</sub>, *J. Mater. Sci.* 9 (1974) 1393–1400. doi:10.1007/BF00552924.
- [11] S. Mohammadkhani, E. Schaal, A. Dolatabadi, C. Moreau, B. Davis, D. Guay, L. Roué, Synthesis and thermal stability of (Co,Ni)O solid solutions, *J. Am. Ceram. Soc.* 102 (2019) 5063–5070. doi:10.1111/jace.16397.
- [12] P.L. Fauchais, J.V.R. Heberlein, M.I. Boulos, *Thermal Spray Fundamentals*, Springer US, Boston, MA, 2014. doi:10.1007/978-0-387-68991-3.
- [13] F. Gitzhofer, E. Bouyer, M.I. Boulos, *Suspension Plasma Spray (SPS)*, US5609921A, 1994.
- [14] M. Aghasibeig, M. Mousavi, F. Ben Ettouill, C. Moreau, R. Wuthrich, A. Dolatabadi, Electrocatalytically Active Nickel-Based Electrode Coatings Formed by Atmospheric and Suspension Plasma Spraying, *J. Therm. Spray Technol.* 23 (2014) 220–226.

doi:10.1007/s11666-013-9997-5.

- [15] P. Fauchais, R. Etchart-Salas, V. Rat, J.F. Coudert, N. Caron, K. Wittmann-Ténéze, Parameters Controlling Liquid Plasma Spraying: Solutions, Sols, or Suspensions, *J. Therm. Spray Technol.* 17 (2008) 31–59. doi:10.1007/s11666-007-9152-2.
- [16] P. Fauchais, G. Montavon, R.S. Lima, B.R. Marple, Engineering a new class of thermal spray nano-based microstructures from agglomerated nanostructured particles, suspensions and solutions: an invited review, *J. Phys. D. Appl. Phys.* 44 (2011) 093001. doi:10.1088/0022-3727/44/9/093001.
- [17] M. Aghasibeig, A. Dolatabadi, R. Wuthrich, C. Moreau, Three-dimensional electrode coatings for hydrogen production manufactured by combined atmospheric and suspension plasma spray, *Surf. Coatings Technol.* 291 (2016) 348–355. doi:10.1016/j.surfcoat.2016.02.065.
- [18] F. Wu, Y. Huang, L. Song, X. Liu, Y. Xiao, J. Feng, J. Chen, Method for preparing porous hydroxyapatite coatings by suspension plasma spraying, US8877283B2, 2009.
- [19] S. Mahade, N. Curry, S. Björklund, N. Markocsan, P. Nylén, R. Vaßen, Functional performance of Gd<sub>2</sub>Zr<sub>2</sub>O<sub>7</sub>/YSZ multi-layered thermal barrier coatings deposited by suspension plasma spray, *Surf. Coatings Technol.* 318 (2017) 208–216. doi:10.1016/j.surfcoat.2016.12.062.
- [20] M. Aghasibeig, C. Moreau, A. Dolatabadi, R. Wuthrich, Fabrication of nickel electrode coatings by combination of atmospheric and suspension plasma spray processes, *Surf. Coatings Technol.* 285 (2016) 68–76. doi:10.1016/j.surfcoat.2015.11.025.
- [21] E. Alebrahim, F. Tarasi, M.S. Rahaman, A. Dolatabadi, C. Moreau, Fabrication of titanium dioxide filtration membrane using suspension plasma spray process, *Surf. Coatings Technol.* 378 (2019) 124927. doi:10.1016/j.surfcoat.2019.124927.
- [22] N. Sharifi, M. Pugh, C. Moreau, A. Dolatabadi, Developing hydrophobic and superhydrophobic TiO<sub>2</sub> coatings by plasma spraying, *Surf. Coatings Technol.* 289 (2016) 29–36. doi:10.1016/j.surfcoat.2016.01.029.
- [23] M. Aghasibeig, F. Tarasi, R.S. Lima, A. Dolatabadi, C. Moreau, A Review on Suspension Thermal Spray Patented Technology Evolution, *J. Therm. Spray Technol.* 28 (2019) 1579–1605. doi:10.1007/s11666-019-00904-x.
- [24] F. Tarasi, M. Medraj, A. Dolatabadi, J. Oberste-Berghaus, C. Moreau, Enhancement of amorphous phase formation in alumina–YSZ coatings deposited by suspension plasma spray process, *Surf. Coatings Technol.* 220 (2013) 191–198. doi:10.1016/j.surfcoat.2012.10.054.
- [25] T. Roisnel, J. Rodríguez-Carvajal, WinPLOTR: A Windows Tool for Powder Diffraction Pattern Analysis, *Mater. Sci. Forum.* 378–381 (2001) 118–123. doi:10.4028/www.scientific.net/MSF.378-381.118.
- [26] M. Kowalski, P.J. Spencer, Thermodynamic reevaluation of the C-O, Fe-O and Ni-O systems: Remodelling of the liquid, BCC and FCC phases, *Calphad.* 19 (1995) 229–243. doi:10.1016/0364-5916(95)00024-9.

- [27] T. Grinys, S. Tamulevicius, I. Prosycevas, S. Meskinis, XRD Analysis of Plasma Sprayed YSZ-NiO-Ni Ceramic Coatings, *Plasma Process. Polym.* 4 (2007) S181–S184. doi:10.1002/ppap.200730607.
- [28] P. Michaux, G. Montavon, A. Grimaud, A. Denoirjean, P. Fauchais, Elaboration of Porous NiO/8YSZ Layers by Several SPS and SPPS Routes, *J. Therm. Spray Technol.* 19 (2010) 317–327. doi:10.1007/s11666-009-9450-y.
- [29] S. Kim, O. Kwon, S. Kumar, Y. Xiong, C. Lee, Development and microstructure optimization of atmospheric plasma-sprayed NiO/YSZ anode coatings for SOFCs, *Surf. Coatings Technol.* 202 (2008) 3180–3186. doi:10.1016/j.surfcoat.2007.11.041.
- [30] G.M. Ingo, Origin of Darkening in 8 wt% Yttria-Zirconia Plasma-Sprayed Thermal Barrier Coatings, *J. Am. Ceram. Soc.* 74 (1991) 381–386. doi:10.1111/j.1151-2916.1991.tb06891.x.
- [31] P. Ctibor, R.C. Seshadri, J. Henych, V. Nehasil, Z. Pala, J. Kotlan, Photocatalytic and electrochemical properties of single- and multi-layer sub-stoichiometric titanium oxide coatings prepared by atmospheric plasma spraying, *J. Adv. Ceram.* 5 (2016) 126–136. doi:10.1007/s40145-016-0181-5.
- [32] M. Poon, O. Kesler, The influence of pore formers on the microstructure of plasma-sprayed NiO–YSZ anodes, *J. Power Sources.* 210 (2012) 204–217. doi:10.1016/j.jpowsour.2012.02.046.
- [33] T. Hidayat, M.A. Rhamdhani, E. Jak, P.C. Hayes, On the Relationships between the Kinetics and Mechanisms of Gaseous Hydrogen Reduction of Solid Nickel Oxide, *Metall. Mater. Trans. B.* 40 (2009) 474–489. doi:10.1007/s11663-009-9239-x.
- [34] M.C. Altay, S. Eroglu, Non-isothermal reduction behavior of NiO in undiluted Ar and CH<sub>4</sub> atmospheres, *Int. J. Miner. Process.* 149 (2016) 50–55. doi:10.1016/j.minpro.2016.02.005.
- [35] R. Alizadeh, E. Jamshidi, H. Ale Ebrahim, Kinetic Study of Nickel Oxide Reduction by Methane, *Chem. Eng. Technol.* 30 (2007) 1123–1128. doi:10.1002/ceat.200700067.
- [36] F. Coskun, S. Cetinkaya, S. Eroglu, Reduction of Nickel Oxide with Ethanol, *JOM.* 69 (2017) 987–992. doi:10.1007/s11837-017-2292-z.
- [37] F. Korkmaz, S. Cetinkaya, S. Eroglu, Thermodynamic Analysis and Reduction of Bismuth Oxide by Ethanol, *Metall. Mater. Trans. B.* 47 (2016) 2378–2385. doi:10.1007/s11663-016-0686-x.
- [38] G. Mauer, A. Guignard, R. Vaßen, D. Stöver, Process diagnostics in suspension plasma spraying, *Surf. Coatings Technol.* 205 (2010) 961–966. doi:10.1016/j.surfcoat.2010.03.007.

## SUPPLEMENTARY SECTION

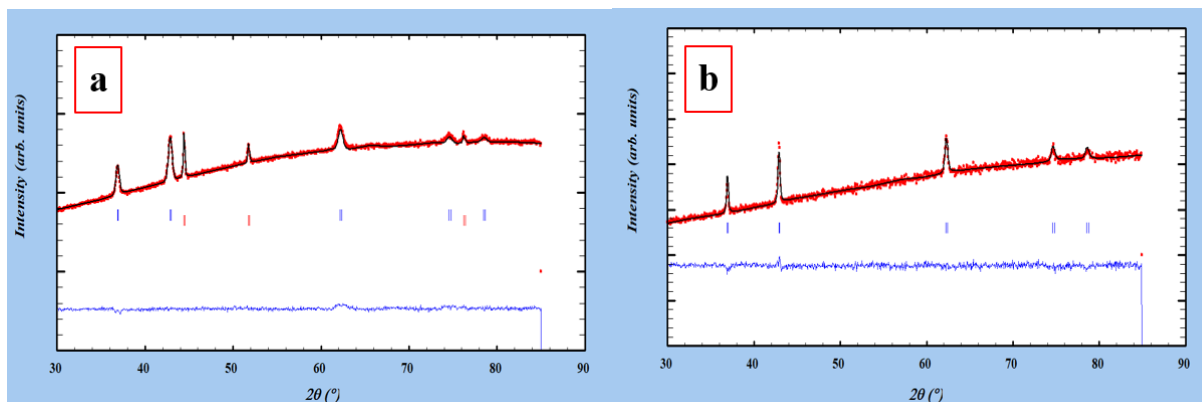


Figure S1. Typical examples of XRD experimental data and Rietveld refinement fitting results: (a) sample S2 that contains two phases and (b) sample S8 that contains a single phase.

### III.6. Article 3: High-temperature behaviour of HVOF (Co,Ni)O coated Cu-Ni-Fe anodes

**Authors:** Saeed Mohammadkhani <sup>a</sup>, Vahid Jalilvand <sup>b</sup>, Boyd Davis <sup>c</sup>, Gilles Henri Gauthier <sup>d</sup>, Ali Dolatabadi <sup>b</sup>, Lionel Roué <sup>a</sup>, Christian Moreau <sup>b</sup>, Daniel Guay <sup>a</sup>

<sup>a</sup> INRS-Énergie, Matériaux, Télécommunications, Varennes, Québec, Canada

<sup>b</sup> Department of Mechanical, Industrial & Aerospace Engineering, Concordia University, Montreal, Québec, Canada

<sup>c</sup> Kingston Process Metallurgy Inc., Kingston, Ontario, Canada

<sup>d</sup> Universidad Industrial de Santander, Grupo INTERFASE, Ciudad Universitaria, Calle 9, Carrera 27, Bucaramanga, Santander, Colombia

**Journal:** Corrosion Science

Published May 2021

**DOI:** <https://doi.org/10.1016/j.corsci.2021.109563>

#### **Contributions:**

The high velocity oxygen fuel spraying was carried out by V. Jalilvand and the author of this thesis at Concordia University. The powder synthesis as well as characterizations of the coatings by SEM-EDS, XRD, Rietveld refinement and particle size distribution were carried out by the author of this thesis. The heat treatments were also performed by the author of this thesis. G. H. Gauthier, A. Dolatabadi, C. Moreau, B. Davis, L. Roué and D. Guay helped interpret the results and correct different versions of the article.

## **Abstract**

Cu-Ni-Fe alloys are promising inert anodes for green Al production but their corrosion resistance must be improved. Here, protective (Co,Ni)O coatings are deposited by high velocity oxygen fuel (HVOF) process on Cu-Ni-Fe alloys. The influence of the coating and substrate compositions on their behaviour is studied at 1000 °C under argon and air. On Cu-rich alloy,  $\text{Co}_x\text{Ni}_{1-x}\text{O}$  coatings with higher nickel content slow down oxygen diffusion to the substrate, as well as copper diffusion to the sample surface. On Ni-rich alloy, the formation of a  $\text{NiFe}_2\text{O}_4$  scale is observed, whose thickness decreases as the Ni content of the  $\text{Co}_x\text{Ni}_{1-x}\text{O}$  coatings increases.

*Keywords:* (Co,Ni)O solid solution, high velocity oxygen fuel, high-temperature oxidation, inert anode, Al electrolysis.

## 1. Introduction

The substitution of consumable carbon anodes emitting CO<sub>2</sub> with inert O<sub>2</sub>-evolving anodes for the primary production of aluminum would reduce considerably the emissions of carbon dioxide and perfluorocarbons from this industry. This substitution would eliminate about 6 Mt of CO<sub>2</sub> eq produced annually by Canadian aluminum smelters, which is equivalent to the amount of CO<sub>2</sub> generated annually by about 2 million cars [1,2]. However, the design of inert anodes is a major challenge because of the severe Al electrolysis conditions that require materials with excellent resistance to corrosion and thermal shock, as well as adequate electrochemical properties. Single phase Cu-Ni-Fe alloys are promising materials for inert anodes due to their ability to form a protective NiFe<sub>2</sub>O<sub>4</sub> layer upon Al electrolysis [3–5]. However, this protective layer needs time to form at the surface of Cu-Ni-Fe alloys, during which fluorination can occur, causing premature degradation of the electrode [6].

In this context, the use of (Co,Ni)O-based protective coatings for metallic anode appears promising. In fact, CoO can work as a barrier for the fluorination of Ni-Fe alloys and the transformation of CoO to CoF<sub>2</sub> occurs only at very low oxygen pressure in cryolite medium [7]. In addition, it has been shown that adding Ni atoms to CoO and forming (Co,Ni)O solid solutions helps in preventing the decomposition of CoO to Co<sub>3</sub>O<sub>4</sub> at elevated temperatures [7–10]. The formation of Co<sub>3</sub>O<sub>4</sub>, which is a n-type semiconductor, should be avoided as it would translate into higher overpotential during Al electrolysis due to its lower conductivity in comparison with p-type semiconductor (Co,Ni)O solid solution [7].

Preparing a single phase, adherent and crack-free oxide layer at the surface of a substrate is challenging. In thermal spraying, thick coatings can be obtained in a single step with a relatively high efficiency [11]. Thermal spray methods can be divided into several categories that include high velocity thermal spraying (high velocity oxygen fuel (HVOF) and high velocity air fuel (HVAF), plasma spraying (suspension plasma spray (SPS), vacuum plasma spray (VPS) and atmospheric plasma spray (APS), combustion flame spraying, detonation gun spraying and arc spraying. However, high velocity thermal spraying techniques are preferred to form coatings with low porosity and good adhesion to the substrate. In these methods, a mixture of oxygen and fuel such as hydrogen, propylene, ethylene or propane is used to produce a supersonic jet through a

Laval nozzle. Powdered materials are injected into the flame, where the particles begin to melt while being accelerated towards a substrate. The high velocity of the particles causes them to form a dense stack of flattened droplets on the substrate, resulting in smooth, uniform coatings with good adhesion to the substrate. Usually, the residence time of the powder in the flame is shorter and the flame temperature is lower than in other thermal spray methods, which further reduces the possibility that the powder is reduced, oxidized or decomposed, or that undesired phase transformation occurs during spraying [11]. Different types of materials, including dense and porous metals, cermets and ceramics have been deposited by HVOF and HVAF, and the targeted applications are diverse such as wear and corrosion resistant coatings, and coatings acting as thermal barrier for high-temperature applications [12–20].

In our previous work, (Co,Ni)O coatings have been prepared by SPS of (Co,Ni)O powders [21]. However, reduction of NiO to Ni has been observed during SPS process. In the work of Nguyen and de Nora [7], (Co,Ni)O coating was deposited on the anode by electrodeposition of a Co-Ni alloy, followed by an oxidation treatment in air. However, producing a crack-free and cohesive oxide layer on the anode using this approach is very challenging as a drastic change in densities occurs upon oxidation of the metallic Co-Ni alloy. Since thick, cohesive and crack-free oxide layers can be directly sprayed using HVOF technique without any changes in their oxidation state, this approach appears more relevant and is evaluated for the first time to produce (Co,Ni)O coatings on CuNiFe substrates.

In the current study, dense, uniform, and single phase  $\text{Co}_x\text{Ni}_{1-x}\text{O}$  coatings, with  $x = 1, 0.75$  and  $0.5$ , are deposited on CuNiFe substrates using the HVOF process. Substrates with two different alloy composition are investigated, namely Cu-20Ni-15Fe (in wt%) (Cu-rich alloy) and Ni-25Fe-10Cu (in wt%) (Ni-rich alloy), which were previously studied as  $\text{O}_2$ -evolving anodes for Al production [6]. The behaviour at  $1000\text{ }^\circ\text{C}$  of the coating/substrate ensembles is investigated in dry inert and oxidizing atmospheres.

## 2. Experimental

$\text{Co}_x\text{Ni}_{1-x}\text{O}$  with  $x = 0.75$  and  $0.5$  was synthesized by mixing  $\text{Co}_3\text{O}_4$  (purity  $\geq 99.7\%$ ,  $-325$  mesh, from Alfa Aesar) and NiO powders (purity  $\geq 99\%$ ,  $-325$  mesh, from Cerac) followed by a 12 h heat treatment at  $1200\text{ }^\circ\text{C}$  in air. Cobalt oxide (CoO) was also prepared by heating  $\text{Co}_3\text{O}_4$  at

1200 °C for 12 hours under an argon flow, with a subsequent rapid cooling to prevent the conversion of CoO to Co<sub>3</sub>O<sub>4</sub> upon cooling. All powders were prepared in kg quantity. They were sieved with -35 and +20 µm screens to remove large particles and avoid clogging the HVOF gun. To determine the particle size, CoO and (Co,Ni)O powders were dispersed in water and analyzed by a Malvern Panalytical Spraytec instrument.

A Diamond Jet 2700-hybrid HVOF gun with a convergent-divergent nozzle from Oerlikon Metco (Westbury, NY, USA) was used to deposit coatings. Propylene and nitrogen were used as fuel and powder carrier gas, respectively. The substrate temperature was monitored during the HVOF coating process by a FLIR A320 infrared camera. The HVOF spraying parameters were first optimized by varying the deposition conditions (H1, H2 and H3 in **Table S1**). Based on the porosity and adherence of the coating on the substrate, the deposition conditions H2 were selected. A detailed description of the optimization procedure is given in the supplementary section.

Two compositions of CuNiFe alloy, Cu-20Ni-15Fe and Ni-25Fe-10Cu (in wt%), were used as substrates. CuNiFe alloys were produced by the casting method and were further homogenized by a heat treatment under argon as explained in our previous work [6,22]. Substrates were cut into disc-shaped specimens of 15 mm diameter and ~7 mm thickness. Then, they were grit-blasted and cleaned by several rinsing in distilled water and acetone. Only one side of the disc-shaped samples was coated by HVOF. All substrates were preheated to 200 °C by performing 5 passes of HVOF jet on the substrate surface before injecting the powder.

CoO, Co<sub>0.75</sub>Ni<sub>0.25</sub>O and Co<sub>0.5</sub>Ni<sub>0.5</sub>O powders were dried in an oven at 75 °C for at least 24 h prior to deposition. HVOF was used to deposit CoO, Co<sub>0.75</sub>Ni<sub>0.25</sub>O and Co<sub>0.5</sub>Ni<sub>0.5</sub>O powders on Cu-20Ni-15Fe (Cu-rich) and Ni-25Fe-10Cu (Ni-rich) substrates using the spray conditions denoted S1 to S6 in **Table S1**. The number of deposition passes was varied from 50 to 55 to achieve coatings with ~100-125 µm thickness.

Coatings were heated at 1000 °C for 20 h in static air and under an argon flow in a muffle furnace and a tubular furnace, respectively. Scanning Electron Microscopy / Energy Dispersive X-ray Spectroscopy (SEM-EDS) observations of as-sprayed and heat treated specimens were undertaken by use of a Tescan Vega3 scanning electron microscope equipped with a Bruker XFlash® 6 | 10 Detector energy dispersive X-ray spectroscope. The crystalline structure of the

starting powders and as-sprayed and heat treated coatings was determined by X-ray diffraction (XRD) using a Bruker D8 diffractometer equipped with Cu  $K_{\alpha}$  radiation.

### 3. Results and discussion

#### 3.1. As-coated samples

SEM micrographs of the starting powders are shown in **Fig. 1a-c**. CoO, Co<sub>0.75</sub>Ni<sub>0.25</sub>O and Co<sub>0.5</sub>Ni<sub>0.5</sub>O powders consist of spherical or near-spherical primary particles that are formed from the agglomeration of smaller particles. The particle size distribution curves of these powders are also shown in **Fig. 1d-f**. The particle diameters of CoO, Co<sub>0.75</sub>Ni<sub>0.25</sub>O and Co<sub>0.5</sub>Ni<sub>0.5</sub>O powders are centered along a single mode, with maximal volume frequency at 21, 19 and 16  $\mu\text{m}$ , respectively. The D<sub>50</sub> and D<sub>90</sub> values are 22 and 35  $\mu\text{m}$  for CoO, 20 and 32  $\mu\text{m}$  for Co<sub>0.75</sub>Ni<sub>0.25</sub>O and 15 and 27  $\mu\text{m}$  for Co<sub>0.5</sub>Ni<sub>0.5</sub>O, respectively.

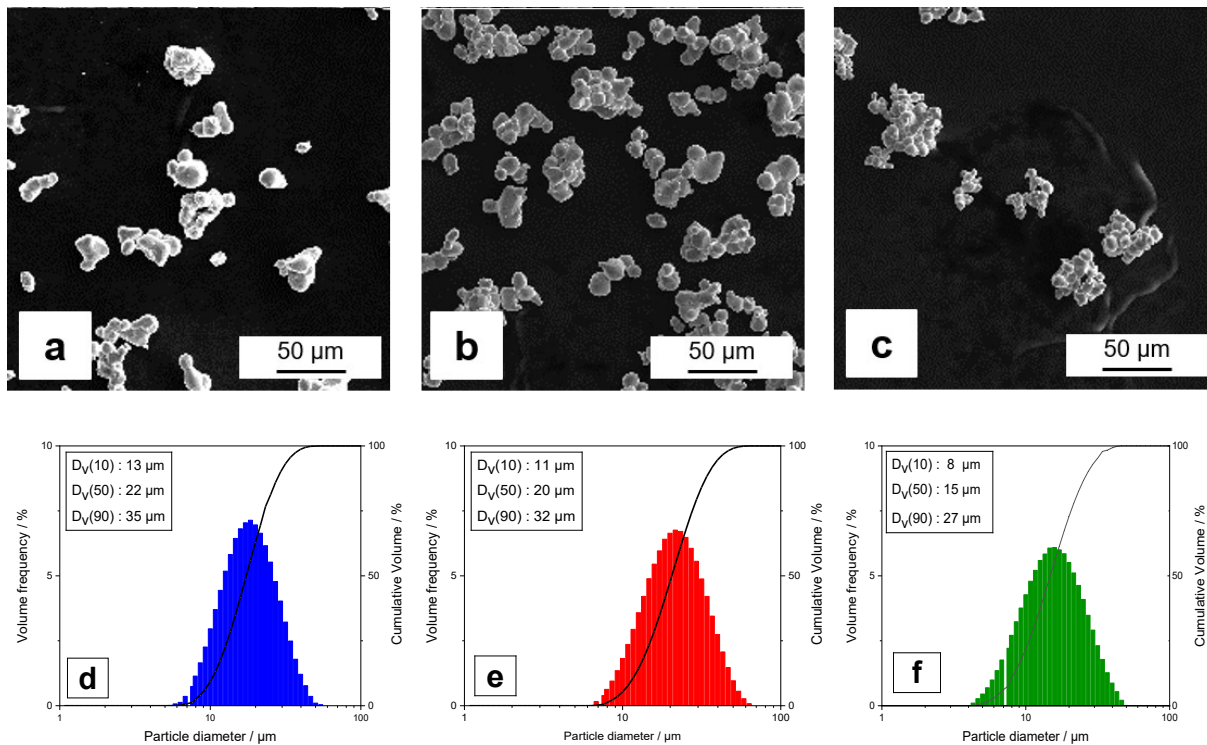


Figure 1. SEM micrographs (a, b and c) and particle size distribution histograms (d, e and f) of (a and d) CoO, (b and e) Co<sub>0.75</sub>Ni<sub>0.25</sub>O and (c and f) Co<sub>0.5</sub>Ni<sub>0.5</sub>O precursor powders.

**Fig. 2** displays the XRD patterns of samples S1-S6. For all coatings, only one set of peaks are observed that are assigned to a *fcc* Co<sub>x</sub>Ni<sub>1-x</sub>O solid solution. The *a* lattice parameter of the Co<sub>x</sub>Ni<sub>1-x</sub>O solid solution was calculated from the position of the diffraction peaks of each coating.

The value of  $x$  was then calculated using the known relationship between  $a$  and the composition of the  $\text{Co}_x\text{Ni}_{1-x}\text{O}$  solid solution [10]. As shown in **Table 1**, the lattice parameters of the  $\text{Co}_x\text{Ni}_{1-x}\text{O}$  coatings and corresponding powders are similar, and their values are in accordance with the nominal composition of the starting powders.

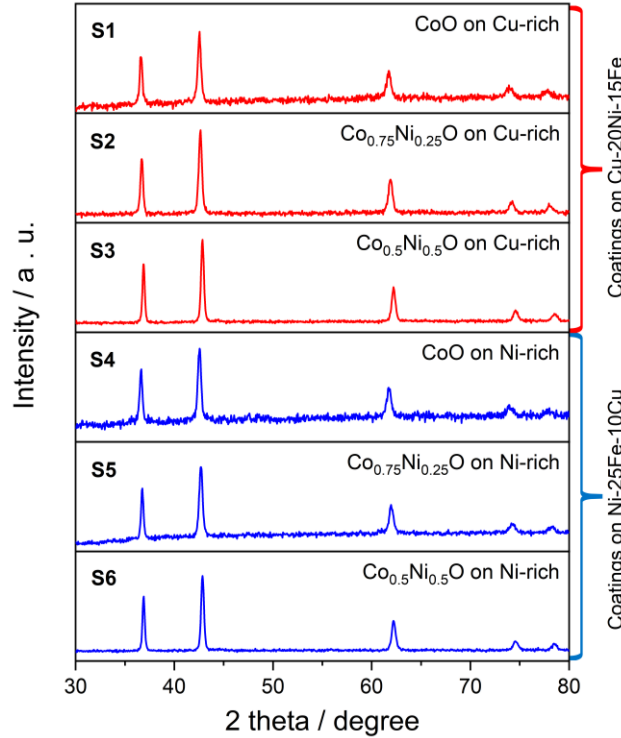
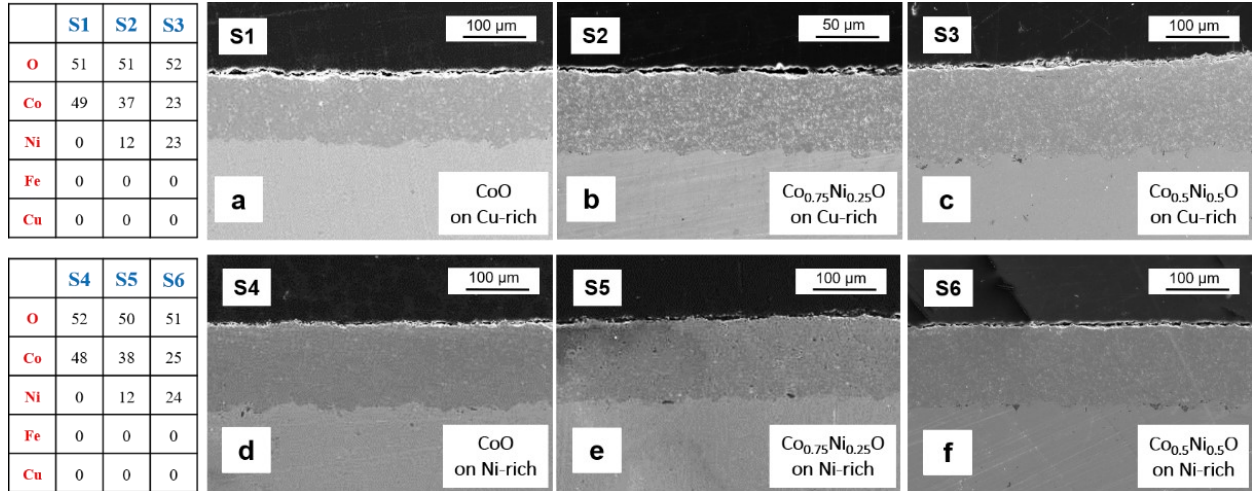


Figure 2. XRD patterns of coatings deposited on Cu-rich substrate (a, b and c) and Ni-rich substrate (d, e and f): CoO (a and d),  $\text{Co}_{0.75}\text{Ni}_{0.25}\text{O}$  (b and e),  $\text{Co}_{0.5}\text{Ni}_{0.5}\text{O}$  (c and f).

Table 1. Structural parameters of (Co,Ni)O coatings.

Sample	Coating composition	Lattice parameter of (Co,Ni)O powders (Å)	Lattice parameter of (Co,Ni)O coatings (Å)	(Co,Ni)O lattice parameter after heat treatment under argon flow (Å)	$\Delta a / a$ after heat treatment under argon flow	(Co,Ni)O lattice parameter after heat treatment in air (Å)
<b>On Cu-20Ni-15Fe substrates</b>						
S1	CoO	4.264	4.263	4.274	0.011	n/a
S2	$\text{Co}_{0.75}\text{Ni}_{0.25}\text{O}$	4.239	4.238	4.251	0.013	n/a
S3	$\text{Co}_{0.5}\text{Ni}_{0.5}\text{O}$	4.221	4.222	4.235	0.013	n/a
<b>On Ni-25Fe-10Cu substrates</b>						
S4	CoO	4.264	4.263	4.273	0.010	4.262
S5	$\text{Co}_{0.75}\text{Ni}_{0.25}\text{O}$	4.239	4.239	4.250	0.011	4.238
S6	$\text{Co}_{0.5}\text{Ni}_{0.5}\text{O}$	4.221	4.221	4.231	0.010	4.223

**Fig. 3** presents the cross-sectional SEM micrographs of coatings. All coatings are uniform and crack-free with very low porosity. The surface of coatings is smooth, and their thickness varies between 110 and 125  $\mu\text{m}$ . The composition of all coatings, as determined by EDS, is very close to that of their respective starting powders, in accordance with the previous XRD data.



*Figure 3. Cross-sectional SEM micrographs of coatings deposited on Cu-rich substrate (a, b and c) and Ni-rich substrate (d, e and f): CoO (a and d),  $\text{Co}_{0.75}\text{Ni}_{0.25}\text{O}$  (b and e),  $\text{Co}_{0.5}\text{Ni}_{0.5}\text{O}$  (c and f). The EDS analysis (at.%) of as-sprayed coatings are presented as well.*

### 3.2. Heat treatment under argon

The heat treatment under argon was carried out to investigate the effect of temperature separately from the effect of oxygen. One of the main concerns of coating metallic alloys with an oxide layer is the difference in their thermal expansion coefficient which can result in continuous cracks in the coating or even its complete or partial delamination from the substrate. When a sample is heated in presence of oxygen, formation of new oxides or changes in the oxidation state can also cause the coating delamination. Thus, a heat treatment in an inert atmosphere shows if the delamination occurs due to thermal expansion and also provides a better understanding of the complex behaviour of the sample during a heat treatment in air.

**Fig. 4** shows the XRD patterns of sample S1-S6 after a 20 h heat treatment at 1000  $^{\circ}\text{C}$  under argon. Only one set of diffraction peaks can be observed in the XRD patterns, indicating that no new phase is formed during heat treatment. However, the XRD peaks of all coatings are shifted to smaller angles, indicating that the lattice parameter of the fcc phase has increased and

thus a change in the composition of the coatings has occurred. The relative change of the lattice parameter, which is given by  $\Delta a / a$ , of coatings deposited on Cu-rich substrates are larger than on Ni-rich substrates (see **Table 1**), indicating that the final composition of the coatings varies with the nature of the substrate. This issue will be discussed in more detail later.

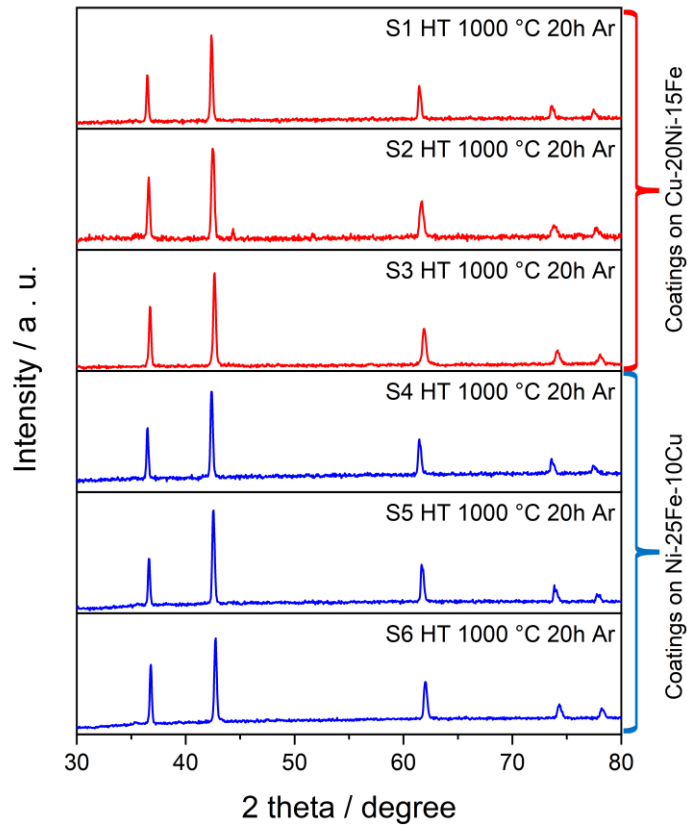
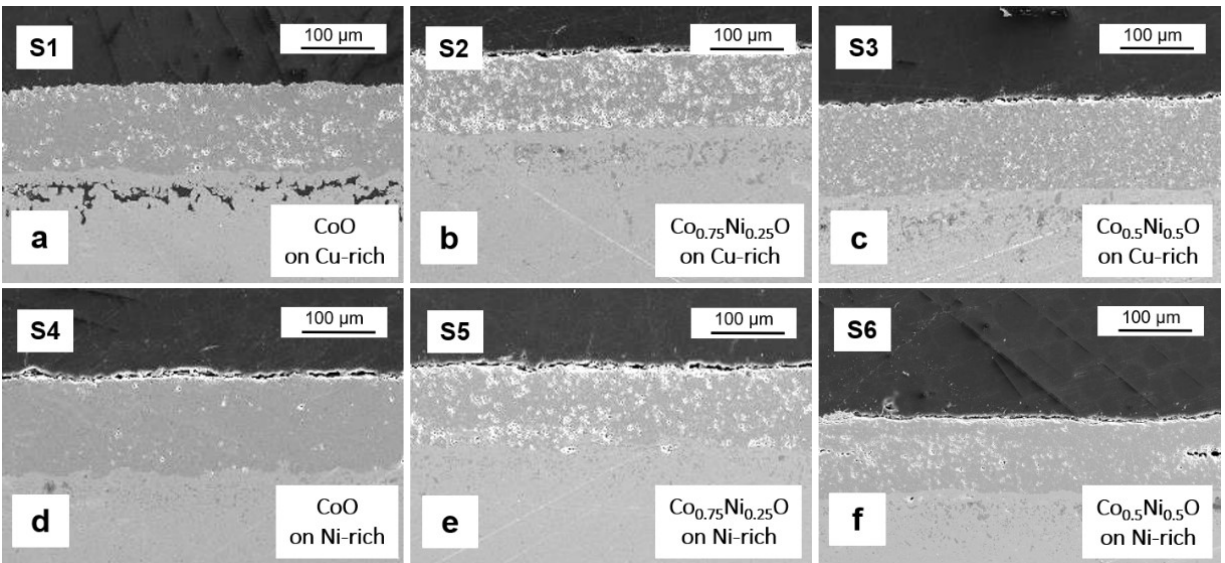


Figure 4. XRD patterns of samples (S1-S6) after 20 h of heat treatment at 1000 °C under an argon flow.



*Figure 5. Cross-sectional SEM micrographs of samples (S1-S6) after 20 h of heat treatment at 1000 °C under an argon flow.*

The cross-sectional SEM micrographs of samples after heat treatment in argon are shown in **Fig. 5**. For coatings deposited on Cu-rich substrates, pores are observed at the coating/substrate interface, especially for the CoO coating. In contrast, coatings deposited on nickel-rich substrates are dense and homogeneous and no porosities are observed at the coating/substrate interface.

**Fig. 6** shows the EDS quantitative and mapping results of CoO coatings on Cu-rich and Ni-rich substrates after heat treatment in argon. Schematic representations of the different compounds formed resulting from heat treatment are also shown. In both cases, three layers are observed, denoted by L1, L2 and L3. Layers 1 and 3 correspond to the coating and substrate, respectively, while L2 is located on the substrate side of the coating/substrate interface. Quantitative EDS analysis was performed in 5 different zones. In Layer 1, EDS results show that diffusion of iron from the substrate to the coating, and that diffusion of cobalt from the coating to the substrate, have occurred. Diffusion of nickel and copper from the substrate to the coating is not observed to any significant extent. On both substrates, zones 1 and 2 in Layer 1 contain the same amount of Fe, indicating there is no Fe concentration gradient in the coating following 20 h of heat treatment. From the EDS results, the atomic ratio  $M / (M + O)$ , where M is the sum of all metallic elements and O is oxygen, is 0.47 and 0.49 in zones 1 and 2, respectively, almost identical to the value measured on as-deposited coatings. This suggests that the average oxidation state of the metallic elements in the coating was not altered during heat treatment.

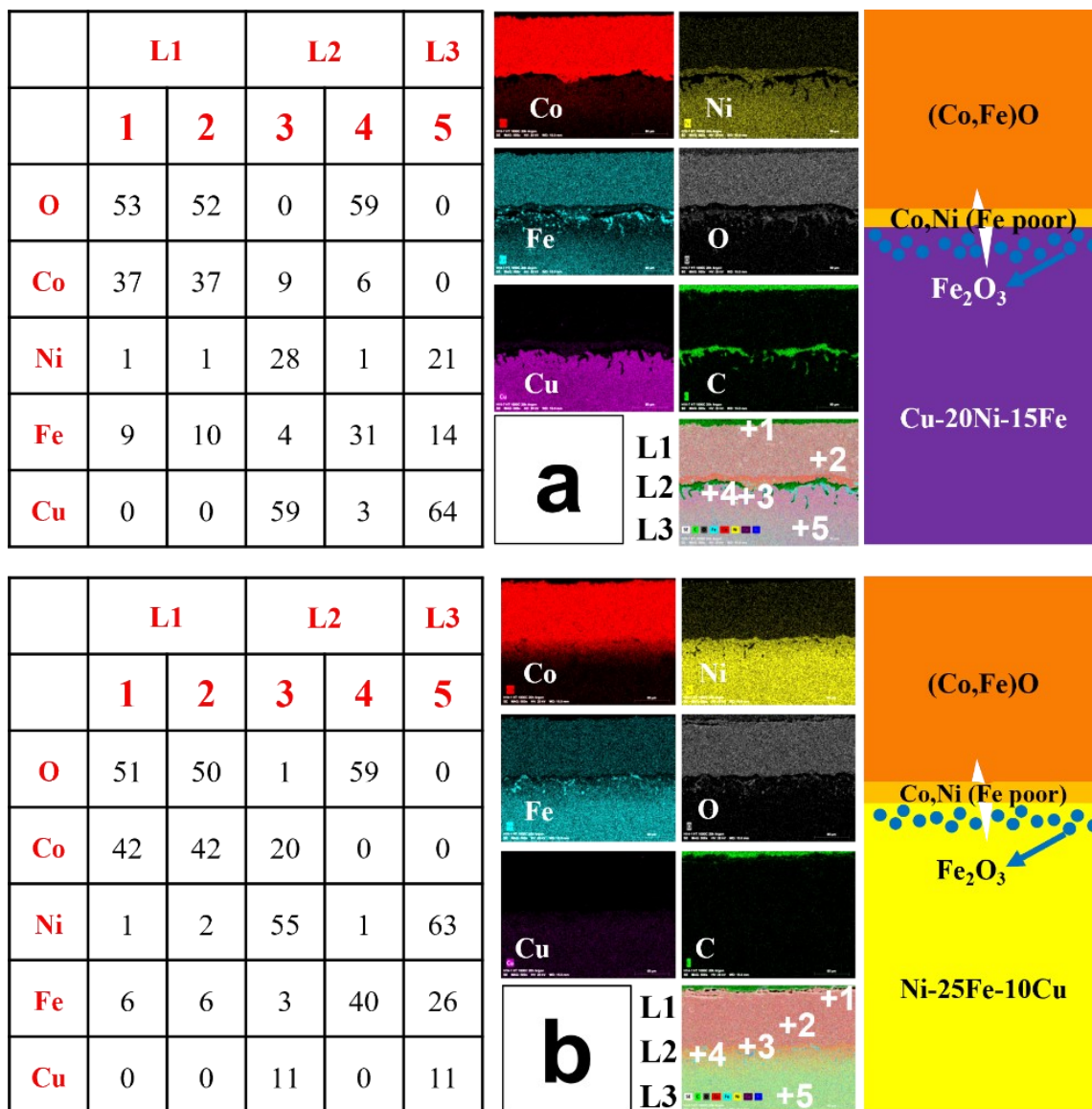


Figure 6. EDS analysis results and schematic illustrations of CoO coatings deposited on (a) Cu-20Ni-15Fe (S1) and (b) Ni-25Fe-10Cu (S4) substrates after 20 h of heat treatment at 1000 °C under an argon flow. The source of carbon is the resin used for the sample preparation.

As noted above, diffusion of Fe atoms to the coating and Co atoms to the substrate is more important on Cu-rich than on Ni-rich substrate. The  $\text{Fe}^{2+}$  and  $\text{Co}^{2+}$  ionic radii are 0.77 and 0.74 Å, respectively [23]. Accordingly, this should translate into a larger relative change of the lattice parameter of coatings deposited on Cu-rich than on Ni-rich substrates, which is consistent with what was observed previously in **Table 1**.

Following Fe diffusion to the coating, a Fe-poor region is formed at the coating/substrate interface of both substrates, where cobalt atoms that have diffused from the coating are concentrated (zone 3 of Layer 2), along with Ni and Cu atoms. Iron atoms in Layer 2 are essentially present as iron oxide inclusions (zone 4 of Layer 2) dispersed in a metallic matrix mainly composed of Cu, Ni and Co atoms (zone 3 of Layer 2). The standard Gibbs free energy of formation,  $\Delta G^{\circ}_f$  (at 1300 K) of FeO, Fe<sub>2</sub>O<sub>3</sub> and Fe<sub>3</sub>O<sub>4</sub> are -188, -487 and -702 kJ mol<sup>-1</sup> of oxide, respectively, compared to -74, -41 and -123 kJ mol<sup>-1</sup> for Cu<sub>2</sub>O, CuO and NiO [24,25]. Based on these data, iron is the most oxidizable element, and the formation of iron oxides, instead of copper and nickel oxide, is not surprising. It is difficult to ascertain the exact nature of the iron oxide compounds formed, but based on the O and Fe stoichiometry, Fe<sub>2</sub>O<sub>3</sub> and Fe<sub>3</sub>O<sub>4</sub> are the most probable.

A mass balance calculation was performed to determine the total amount of Fe and O atoms in Layers 1 and 2. Details of these calculations are given in the supplementary section. Of the total number of Fe atoms initially contained in Layer 2 of the substrate, about 85% are diffusing to the coating (Layer 1) during heat treatment. As mentioned earlier, there is almost no diffusion of Ni and Cu atoms from the substrate to Layer 1. The preferential diffusion of Fe atoms can be understood based on Cu – O, Fe – O and Ni – O phase diagrams [26–28]. During heat treatment in the presence of 99.999% pure Ar, the O<sub>2</sub> partial pressure must be below 10<sup>-10</sup> atm. At this pressure, Cu<sub>2</sub>O is more stable than CuO, Ni is more stable than NiO, and FeO is more stable than either Fe<sub>2</sub>O<sub>3</sub> or Fe<sub>3</sub>O<sub>4</sub>. It is hypothesized that diffusion of Fe<sup>+2</sup> cations in CoO is favored over diffusion of Ni<sup>0</sup> and Cu<sup>+1</sup>. Also, both CoO and FeO have a *fcc* rock-salt crystal structure, and they are known to form a (Co,Fe)O solid solution at high temperature and low oxygen pressure [29]. It is inferred that both factors contribute to promote the diffusion of iron atoms from the substrate to the coating, where they can dissolve homogeneously in the CoO coating to form a (Co,Fe)O phase.

Heat treatment of these samples was conducted in Ar with limited contamination by oxygen (99.999% pure). Accordingly, O atoms found in Layer 2 must originate from the oxide coating (Layer 1). Extending on the previous mass balance calculation (see the supplementary section), the total amount of O atoms in Layer 2 after heat treatment corresponds to only 2-3% of those initially present in the coating (Layer 1). Such a small variation is within the uncertainty of the EDS measurements and would go unnoticed.

The same analysis was conducted for  $\text{Co}_{0.75}\text{Ni}_{0.25}\text{O}$  and  $\text{Co}_{0.5}\text{Ni}_{0.5}\text{O}$  coatings deposited on Cu-rich and Ni-rich substrates, and the results are depicted in **Fig. S3 and S4**. All samples exhibit the same structure, with three well-distinct regions (L1, L2 and L3). However, as shown in **Fig. 7**, the Fe content in Layer 1 varies with the nature of the substrate and the composition of the coating. Interestingly, the iron content in coatings deposited on Cu-rich substrate decreases steadily as the molar fraction of Ni in the (Co,Ni)O coating is increased. This is because the diffusion coefficient of Fe atoms at 1000 °C is smaller in NiO than in CoO ( $2.3 \times 10^{-11}$  vs.  $1.59 \times 10^{-9} \text{ cm}^2 \text{ s}^{-1}$ ) [23]. As a result, increasing the Ni content of the (Co,Ni)O coating decreases the iron diffusivity. On Ni-rich substrates, the Fe content in Layer 1 is almost constant at about 5 at.% and independent of the coating composition. In that case, the diffusion of iron atoms from the Ni-rich substrate is limiting. This is thought to reflect on the smaller diffusion coefficient of Fe atoms in metallic nickel compared to metallic Cu ( $7 \times 10^{-12}$  vs.  $2 \times 10^{-9} \text{ cm}^2 \text{ s}^{-1}$ ) [30,31].

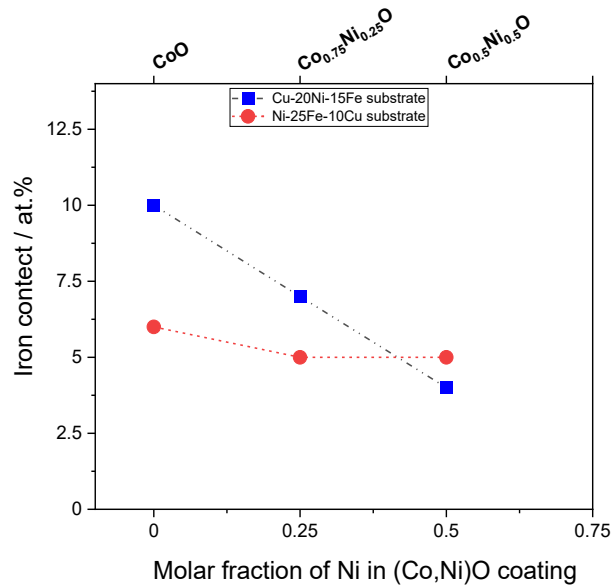


*Figure 7. Iron content in (Co,Ni)O coatings after 20 h of heat treatment at 1000 °C under an argon flow.*

### 3.3. Heat treatment under air

**Fig. 8** illustrates cross-sectional SEM micrographs of HVOF coatings heat treated in air at 1000 °C during 20 h. For comparison, cross-sectional SEM micrographs of bare Cu-rich and Ni-

rich substrates after the same heat treatment are shown as well. Samples heated in air show very different behaviours according to the composition of the substrate. All coatings on Cu-rich substrate (**Fig. 8b-d**) exhibit a thick oxide layer (L2, ~500-1000  $\mu\text{m}$ ) that grows underneath the (Co,Ni)O layer. This oxide layer does not have good adhesion to either the CuNiFe substrate (L3) or the (Co,Ni)O coating (L1) and has been delaminated from both coating and substrate. On Ni-rich substrates (**Fig. 8f-h**), this oxide layer is thinner (L2, ~30-35  $\mu\text{m}$ ) and it is still attached to the HVOF coatings while it has been delaminated from the Ni-rich substrate. Understanding these variations calls for a detailed analysis of the composition of each layer.

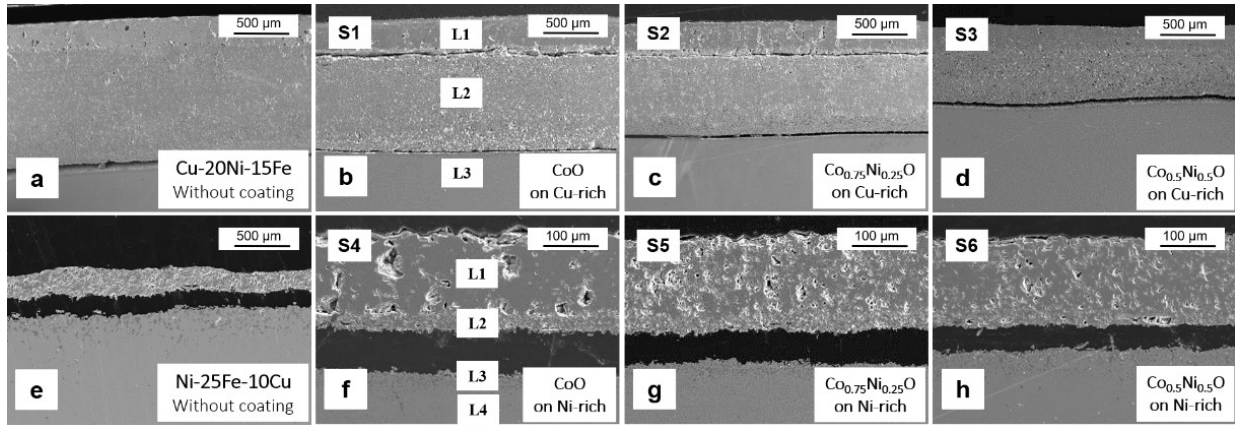


*Figure 8. Cross-sectional SEM micrographs of coatings (samples S1-S6) after 20 h of heat treatment at 1000 °C in static air. Layers 1, 2, 3 and 4 are identified.*

Detailed EDS analysis reveals that the structure and composition of these layers is complex. As shown in **Fig. 9a**, a thin layer of CuO is formed on the outer side (Zone 1) of the CoO coating sprayed on Cu-rich substrate, while a thin layer of Cu<sub>2</sub>O is formed on its inner side (Zone 3). Also, EDS analysis reveals that Cu atoms are dispersed homogeneously in the CoO coating (Zone 2). Unlike heat treatment in argon, no evidence of Fe in the CoO coating was observed. The composition of the (Co,Ni)O coating does not have any drastic effect on the structure of the L1 oxide scale (**Fig. S5 and S6**). Indeed, in all cases, the HVOF coating is sandwiched between a top CuO and a bottom Cu<sub>2</sub>O layer, and Cu atoms are found in the HVOF coating, although there is a gradual decrease of the CuO and Cu<sub>2</sub>O oxide scales as the Ni content of the (Co,Ni)O coatings is increased. According to the Cu–O stability diagram [27,32], the equilibrium O<sub>2</sub> pressure for CuO/Cu<sub>2</sub>O is around 10<sup>-2</sup> atm at 1000 °C. Accordingly, CuO is formed next to the sample surface, where the O<sub>2</sub> pressure is large, whereas Cu<sub>2</sub>O is stable under the CoO oxide coating. The same

CuO and Cu<sub>2</sub>O layered structure was observed in our previous work, where as-cast and homogenized Cu-20Ni-15Fe alloys were used as O<sub>2</sub>-evolving anodes for Al production in KF-based cryolite at 700 °C [6].

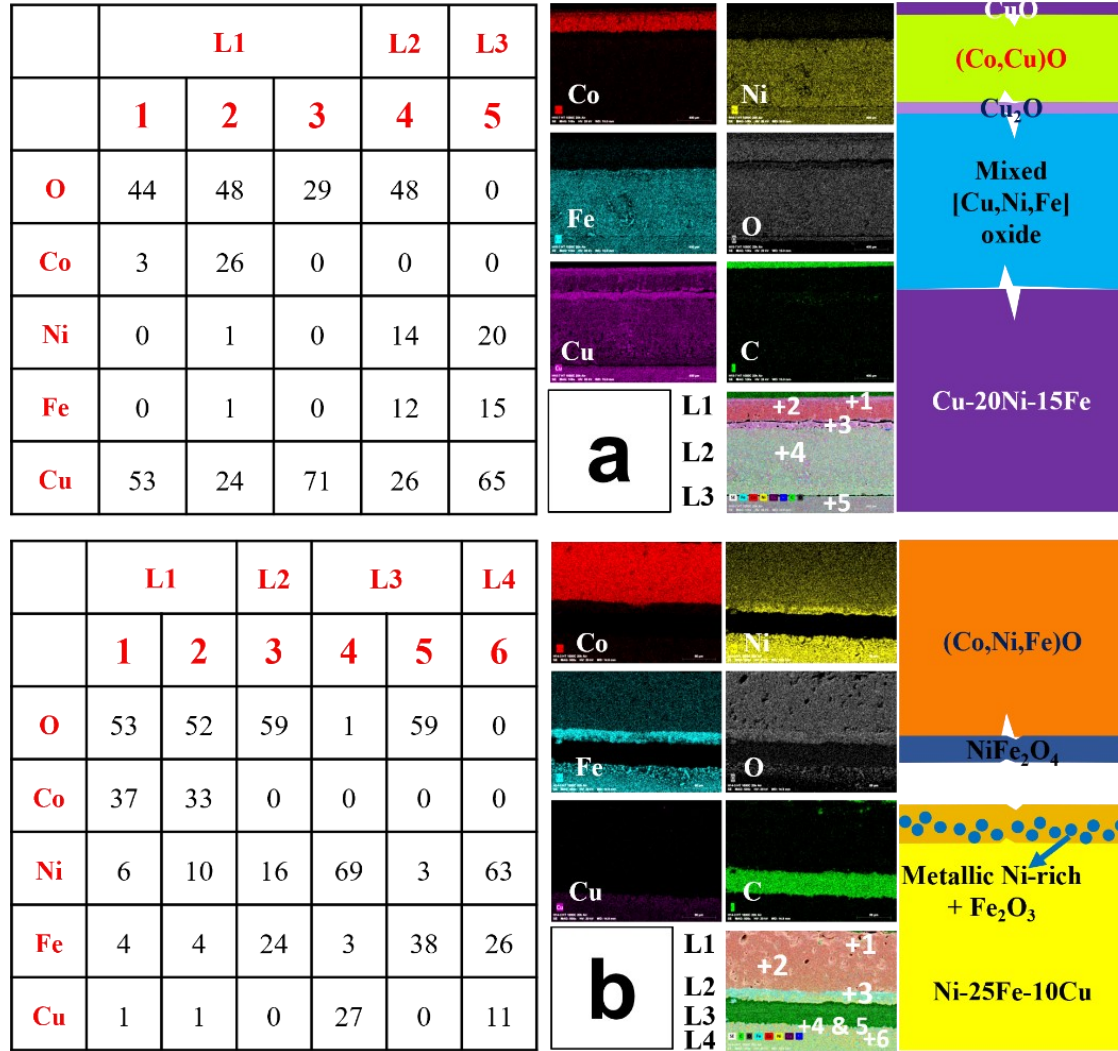


Figure 9. EDS analysis results and schematic illustration of CoO coating deposited on (a) Cu-20Ni-15Fe and (b) Ni-25Fe-10Cu substrate (sample S1 and S4, respectively), after 20 h of heat treatment at 1000 °C in static air. The source of carbon is the resin used for the sample preparation.

The formation of CuO and Cu<sub>2</sub>O follows from the diffusion of Cu atoms from the substrate. Accordingly, Layer 2 is poorer in Cu (Zone 4) in comparison with the substrate (Zone 5). Oxygen atoms are present in Zone 4, along with Cu, Ni and Fe atoms, resulting in the formation of a thick oxide layer. **Figs. S5 and S6** show that the composition of Layer 2 does not change with the

composition of (Co,Ni)O coating. However, as the nickel content in the (Co,Ni)O coating increases, the thickness of L2 decreases significantly (from ~860  $\mu\text{m}$  beneath CoO to ~400  $\mu\text{m}$  beneath  $\text{Co}_{0.5}\text{Ni}_{0.5}\text{O}$ ) (**Fig. 10a**). In comparison, following the same heat treatment process, the thickness of L2 is 1300  $\mu\text{m}$  on bare Cu-rich substrate. Clearly, the (Co,Ni)O coating acts as a semipermeable barrier for the diffusion of O atoms, and this effect is emphasized by the presence of Ni in the coating.

In argon, it was shown previously that Fe atoms from the substrate diffuse preferentially to the coatings, and that Cu atom was almost absent. The situation is very different when the heat treatment is performed under air, where Cu atoms are clearly observed in the coatings. According to the Cu – O and Fe – O phase diagrams, CuO and  $\text{Fe}_2\text{O}_3$  are the more stable phases at 1000  $^\circ\text{C}$  and high oxygen pressure. In these conditions, it is inferred that  $\text{Cu}^{+2}$  diffuses preferentially in the CoO coating to react with oxygen at the coating/air interface to form CuO. The presence of both Co and Cu atoms in the HVOF coating is consistent with a previous report showing that (Co,Cu)O has a *fcc* rock-salt crystal structure similar to CoO and is stable at 1000  $^\circ\text{C}$  in the presence of oxygen [33]. The thickness of the CuO oxide scale is about 70, 45 and 5  $\mu\text{m}$  on CoO,  $\text{Co}_{0.75}\text{Ni}_{0.25}\text{O}$  and  $\text{Co}_{0.5}\text{Ni}_{0.5}\text{O}$  coated Cu-rich substrate. This is a clear indication that the diffusion of Cu atoms from the substrate to the top of the HVOF coating is slowed down considerably as the Ni content of the coating is increased. The same holds true for the diffusion of O atoms to reach the substrate through the coating as the thickness of the  $\text{Cu}_2\text{O}$  oxide scale decreases from about 90, to 70 and then to 45  $\mu\text{m}$  as the fraction of Ni in the coating is increased from 0 to 50%. This is consistent with the previously observed thickness decrease of L2 as the Ni content of (Co,Ni)O coatings is increased.

Under the same conditions, the behaviour of Ni-rich substrate coated with (Co,Ni)O coatings is totally different. For example, with CoO-coated Ni-rich substrate heat treated in air at 1000  $^\circ\text{C}$  during 20 h, copper diffusion and subsequent oxidation are not the predominant phenomena, and the CoO coating is not sandwiched between CuO and  $\text{Cu}_2\text{O}$  oxide layers (**Fig. 9b**). Also, the Cu content of the CoO coating is negligible (1 at.%, Zones 1 and 2). This is because, in CuNiFe alloys, the diffusion and mobility of Cu, Fe and Ni atoms depends strongly on the alloy composition, and thus copper concentration. In Cu-rich alloy, copper is the most mobile element with a diffusion coefficient a hundred-time higher than nickel or iron. However, the diffusion

coefficient of copper is decreased significantly in Cu-poor alloy, varying from  $\sim 10^{-11}$  to  $10^{-9}$   $\text{cm}^2 \text{s}^{-1}$  [34]. Instead, both nickel (6-10 at.%) and iron (4 at.%) are found in the coating (Zones 1 and 2). Iron atoms are dispersed homogeneously in the coating, while there is a gradient of nickel, with 6 at.% in the upper section of the coating (Zone 1) and 10 at.% near the substrate (Zone 2).

A thin layer of nickel ferrite (less than 30  $\mu\text{m}$ ) is formed under the HVOF coating (zone 3 in L2). The formation of a nickel ferrite layer significantly decreases the oxidation rate of Ni-rich substrate. Between the  $\text{NiFe}_2\text{O}_4$  layer and the Ni-rich substrate, there is a layer (L3) made of iron oxide particles dispersed in a metallic matrix made of Cu and Ni. The iron oxide particles have a spherical shape with a few microns diameter. Indeed, the formation of iron oxide is the primary stage for the formation of the nickel ferrite phase that formed once the ratio between iron, nickel and oxygen atoms has the right value [6]. The composition of the (Co,Ni)O coating does not have any significant effect on the structure of L3.

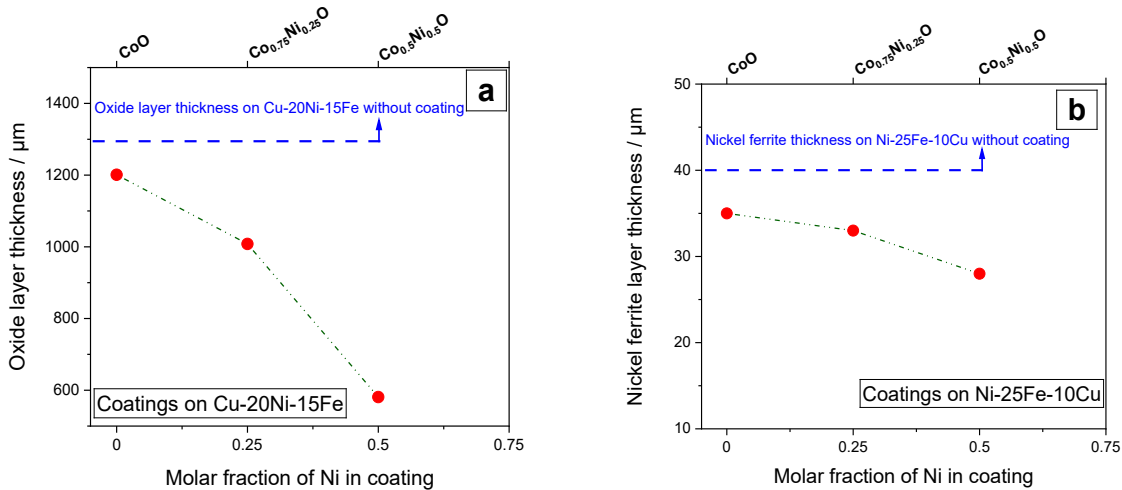


Figure 10. The oxide layer thickness below the HVOF coatings on (a) Cu-20Ni-15Fe substrates and (b) on Ni-25Fe-10Cu substrates after the heat treatment for 20 h at 1000 °C in air (samples S1-S6).

As a summary, **Fig. 10** shows the thickness of the oxide layer (L2 + L3) as a function of the coating composition. On both Cu-rich and Ni-rich substrates, the oxide layer thickness decreases as the nickel content of the (Co,Ni)O coating increases. This is because the oxygen diffusion coefficient in NiO is much lower than in CoO at 1000 °C [35]. The thickness of the oxide layer formed on uncoated Cu-rich substrate is 1300  $\mu\text{m}$  (**Fig. 10a**). Increasing the nickel content of the (Co,Ni)O coating decreases the diffusivity of oxygen, which results in thinner oxide layers

that decreases from 1200 to 600  $\mu\text{m}$  between  $\text{CoO}$  and  $\text{Co}_{0.5}\text{Ni}_{0.5}\text{O}$ . In comparison, the thickness of the  $\text{NiFe}_2\text{O}_4$  oxide layer formed on uncoated Ni-rich substrate is only 40  $\mu\text{m}$ . This is because the formation of a nickel ferrite layer slows down the further oxidation of the underlying substrate [6,36]. In that case, increasing the nickel content of the  $(\text{Co},\text{Ni})\text{O}$  coating results in a less marked effect on the thickness of the oxide layers, although it decreases from 35 to 28  $\mu\text{m}$  between  $\text{CoO}$  and  $\text{Co}_{0.5}\text{Ni}_{0.5}\text{O}$ .

#### 4. Conclusions

$\text{CuNiFe}$  alloy substrates could be used as inert anodes for aluminum electrolysis. However, they are very severely corroded before a protective layer of  $\text{NiFe}_2\text{O}_4$  can form under the aluminum electrolysis conditions, thus slowing down the attack of the electrolyte. In an effort to circumvent this limitation, we have investigated the use of  $(\text{Co},\text{Ni})\text{O}$  coatings as protective layers to slow down the formation of copper oxide known to readily dissolved in the cryolithic medium at high temperature.

So,  $(\text{Co},\text{Ni})\text{O}$  coatings have been deposited by HVOF on both Cu-rich and Ni-rich  $\text{CuNiFe}$  alloy substrates using  $\text{CoO}$ ,  $\text{Co}_{0.75}\text{Ni}_{0.25}\text{O}$  and  $\text{Co}_{0.5}\text{Ni}_{0.5}\text{O}$  powders as starting materials. Using optimized deposition conditions, all coatings are single phase and have a smooth morphology. The oxidation behaviour of these samples was investigated at 1000  $^\circ\text{C}$  in the presence of oxygen to assess the effect of the coatings on the diffusion of Cu and O atoms. Comparison with their high temperature behaviour in inert atmosphere was also performed. After 20 h of heat treatment in air, HVOF coatings on Cu-rich substrates are sandwiched between a top  $\text{CuO}$  and a bottom oxide layer. However, increasing the nickel content of the  $(\text{Co},\text{Ni})\text{O}$  coating from 0 to 0.5 decreases the Cu and O diffusivity, which results in thinner  $\text{CuO}$  and bottom oxide scales. In the case of Ni-rich  $\text{CuNiFe}$  alloy, Cu diffusion to react with O and form  $\text{CuO}$  and  $\text{Cu}_2\text{O}$  is less on an issue because the diffusion of Cu atoms in Ni-rich  $\text{CuNiFe}$  alloys is considerably slowed down. In that case, a nickel ferrite scale is formed between the HVOF coating and the substrate. As expected, the thickness of the  $\text{NiFe}_2\text{O}_4$  layer decreases slightly ( $\sim 15\%$ ) as the Ni content of the  $(\text{Co},\text{Ni})\text{O}$  coating is increased from 0 to 0.5. These coated samples will be used as anodes in Al production and their anodic behaviour in severe aluminum electrolysis conditions will be presented in the near future.

## **Acknowledgement**

The authors thank the Natural Sciences and Engineering Research Council of Canada (NSERC) through the Strategic program (STPGP/494283-2016), Prima Québec (grant R13-13-001), Metal7 and Kingston Process Metallurgy for supporting this work. Vahid Jalilvand acknowledges a doctoral research scholarship from Fonds de Recherche du Québec-Nature et Technologies (FRQ-NT). Saeed Mohammadkhani also acknowledges the support of the UNESCO Chair Materials for Energy Conversion, Saving and Storage (MATECSS) Excellence Scholarship.

## References

- [1] D. Paraskevas, K. Kellens, A. Van de Voorde, W. Dewulf, J.R. Dufloy, Environmental Impact Analysis of Primary Aluminium Production at Country Level, *Procedia CIRP*. 40 (2016) 209–213. doi:10.1016/j.procir.2016.01.104.
- [2] M. Gautam, B. Pandey, M. Agrawal, Carbon Footprint of Aluminum Production, in: *Environ. Carbon Footprints*, Elsevier, 2018: pp. 197–228. doi:10.1016/B978-0-12-812849-7.00008-8.
- [3] E. Gavrilova, G. Goupil, B. Davis, D. Guay, L. Roué, On the key role of Cu on the oxidation behavior of Cu–Ni–Fe based anodes for Al electrolysis, *Corros. Sci.* 101 (2015) 105–113. doi:10.1016/j.corsci.2015.09.006.
- [4] G. Goupil, S. Jucken, D. Poirier, J.G. Legoux, E. Irissou, B. Davis, D. Guay, L. Roué, Cold sprayed Cu–Ni–Fe anode for Al production, *Corros. Sci.* 90 (2015) 259–265. doi:10.1016/j.corsci.2014.10.021.
- [5] S. Jucken, M.H. Martin, E. Irissou, B. Davis, D. Guay, L. Roué, Cold-Sprayed Cu-Ni-Fe Anodes for CO<sub>2</sub>-Free Aluminum Production, *J. Therm. Spray Technol.* 29 (2020) 670–683. doi:10.1007/s11666-020-01002-z.
- [6] S. Jucken, B. Tougas, B. Davis, D. Guay, L. Roué, Study of Cu-Ni-Fe Alloys as Inert Anodes for Al Production in Low-Temperature KF-AlF<sub>3</sub> Electrolyte, *Metall. Mater. Trans. B*. 50 (2019) 3103–3111. doi:10.1007/s11663-019-01695-w.
- [7] T. Nguyen, V. De Nora, De Nora oxygen evolving inert metallic anode, *TMS Light Met. In: Gallow* (2006) 385–390.
- [8] S. Kuboon, Y.H. Hu, Study of NiO–CoO and Co<sub>3</sub>O<sub>4</sub>–Ni<sub>3</sub>O<sub>4</sub> Solid Solutions in Multiphase Ni–Co–O Systems, *Ind. Eng. Chem. Res.* 50 (2011) 2015–2020. doi:10.1021/ie101249r.
- [9] R.J. Moore, J. White, Equilibrium relationships in the system NiO–CoO–O<sub>2</sub>, *J. Mater. Sci.* 9 (1974) 1393–1400. doi:10.1007/BF00552924.
- [10] S. Mohammadkhani, E. Schaal, A. Dolatabadi, C. Moreau, B. Davis, D. Guay, L. Roué, Synthesis and thermal stability of (Co,Ni)O solid solutions, *J. Am. Ceram. Soc.* 102 (2019) 5063–5070. doi:10.1111/jace.16397.
- [11] P.L. Fauchais, J.V.R. Heberlein, M.I. Boulos, *Thermal Spray Fundamentals*, Springer US, Boston, MA, 2014. doi:10.1007/978-0-387-68991-3.
- [12] W. Brandl, D. Toma, J. Krüger, H.J. Grabke, G. Matthäus, The oxidation behaviour of HVOF thermal-sprayed MCrAlY coatings, *Surf. Coatings Technol.* 94–95 (1997) 21–26. doi:10.1016/S0257-8972(97)00470-2.
- [13] J. Oberste Berghaus, J.-G. Legoux, C. Moreau, R. Hui, C. Decès-Petit, W. Qu, S. Yick, Z.

- Wang, R. Maric, D. Ghosh, Suspension HVOF Spraying of Reduced Temperature Solid Oxide Fuel Cell Electrolytes, *J. Therm. Spray Technol.* 17 (2008) 700–707. doi:10.1007/s11666-008-9249-2.
- [14] C.V. Cojocaru, D. Lévesque, C. Moreau, R.S. Lima, Performance of thermally sprayed Si/mullite/BSAS environmental barrier coatings exposed to thermal cycling in water vapor environment, *Surf. Coatings Technol.* 216 (2013) 215–223. doi:10.1016/j.surfcoat.2012.11.043.
- [15] E. Turunen, T. Varis, J. Keskinen, T. Fält, S.P. Hannula, Improved Mechanical Properties by Nanoreinforced Ceramic Composite HVOF Coatings, *Adv. Sci. Technol.* 45 (2006) 1240–1245. doi:10.4028/www.scientific.net/AST.45.1240.
- [16] F. Tarasi, M. Medraj, A. Dolatabadi, J. Oberste-Berghaus, C. Moreau, High-Temperature Performance of Alumina-Zirconia Composite Coatings Containing Amorphous Phases, *Adv. Funct. Mater.* 21 (2011) 4143–4151. doi:10.1002/adfm.201100471.
- [17] C. V. Cojocaru, S.E. Kruger, C. Moreau, R.S. Lima, Elastic Modulus Evolution and Behavior of Si/Mullite/BSAS-Based Environmental Barrier Coatings Exposed to High Temperature in Water Vapor Environment, *J. Therm. Spray Technol.* 20 (2011) 92–99. doi:10.1007/s11666-010-9599-4.
- [18] T. Sahraoui, N.-E. Fenineche, G. Montavon, C. Coddet, Alternative to chromium: characteristics and wear behavior of HVOF coatings for gas turbine shafts repair (heavy-duty), *J. Mater. Process. Technol.* 152 (2004) 43–55. doi:10.1016/j.jmatprotec.2004.02.061.
- [19] M. Jones, A.. Horlock, P.. Shipway, D.. McCartney, J.. Wood, A comparison of the abrasive wear behaviour of HVOF sprayed titanium carbide- and titanium boride-based cermet coatings, *Wear.* 251 (2001) 1009–1016. doi:10.1016/S0043-1648(01)00702-5.
- [20] M. Oksa, E. Turunen, T. Suhonen, T. Varis, S.-P. Hannula, Optimization and Characterization of High Velocity Oxy-fuel Sprayed Coatings: Techniques, Materials, and Applications, *Coatings.* 1 (2011) 17–52. doi:10.3390/coatings1010017.
- [21] S. Mohammadkhani, V. Jalilvand, B. Davis, F. Ben Ettouil, A. Dolatabadi, L. Roué, C. Moreau, D. Guay, Suspension plasma spray deposition of  $\text{Co}_x\text{Ni}_{1-x}\text{O}$  coatings, *Surf. Coatings Technol.* 399 (2020) 126168. doi:10.1016/j.surfcoat.2020.126168.
- [22] S. Jucken, E. Schaal, B. Tougas, B. Davis, D. Guay, L. Roué, Impact of a post-casting homogenization treatment on the high-temperature oxidation resistance of a Cu-Ni-Fe alloy, *Corros. Sci.* 147 (2019) 321–329. doi:10.1016/j.corsci.2018.11.037.
- [23] K. Hoshino, N.L. Peterson, Cation impurity diffusion in CoO and NiO, *J. Phys. Chem. Solids.* 45 (1984) 963–972. doi:10.1016/0022-3697(84)90140-9.
- [24] M.W. Chase, A.I. of Physics., U. States., N.B. of Standards., A.C. Society., JANAF thermochemical tables, American Chemical Society and the American Institute of Physics for the National Bureau of Standards, [New York], 1985. doi:10.18434/T42S31.

- [25] R.D. Holmes, H.S.C. O'Neill, R.J. Arculus, Standard Gibbs free energy of formation for Cu<sub>2</sub>O, NiO, CoO, and Fe<sub>x</sub>O: High resolution electrochemical measurements using zirconia solid electrolytes from 900–1400 K, *Geochim. Cosmochim. Acta.* 50 (1986) 2439–2452. doi:10.1016/0016-7037(86)90027-X.
- [26] G. Ketteler, W. Weiss, W. Ranke, R. Schlögl, Bulk and surface phases of iron oxides in an oxygen and water atmosphere at low pressure, *Phys. Chem. Chem. Phys.* 3 (2001) 1114–1122. doi:10.1039/b009288f.
- [27] J.-P. Wang, W.D. Cho, Oxidation Behavior of Pure Copper in Oxygen and/or Water Vapor at Intermediate Temperature, *ISIJ Int.* 49 (2009) 1926–1931. doi:10.2355/isijinternational.49.1926.
- [28] R. Haugsrud, T. Norby, P. Kofstad, High-temperature oxidation of Cu–30 wt.% Ni–15 wt.% Fe, *Corros. Sci.* 43 (2001) 283–299. doi:10.1016/S0010-938X(00)00080-9.
- [29] I.-H. Jung, S.A. Decterov, A.D. Pelton, H.-M. Kim, Y.-B. Kang, Thermodynamic evaluation and modeling of the Fe–Co–O system, *Acta Mater.* 52 (2004) 507–519. doi:10.1016/j.actamat.2003.09.034.
- [30] S. V. Divinski, F. Hisker, C. Herzig, R. Filipek, M. Danielewski, Self- and Interdiffusion in Ternary Cu-Fe-Ni Alloys, *Defect Diffus. Forum.* 237–240 (2005) 50–61. doi:10.4028/www.scientific.net/DDF.237-240.50.
- [31] K.J. Rönkä, A.A. Kodentsov, P.J.J. Van Loon, J.K. Kivilahti, F.J.J. Van Loo, Thermodynamic and kinetic study of diffusion paths in the system Cu-Fe-Ni, *Metall. Mater. Trans. A.* 27 (1996) 2229–2238. doi:10.1007/BF02651877.
- [32] E.M.M. Hiroaki Okamoto, Mark E. Schlesinger, *Alloy Phase Diagrams*, ASM International, 2016. doi:10.31399/asm.hb.v03.9781627081634.
- [33] L.A. Zabdyr, O.B. Fabrichnaya, Phase equilibria in the cobalt oxide-copper oxide system, *J. Phase Equilibria.* 23 (2002) 149–155. doi:10.1361/1054971023604161.
- [34] I. Gallino, M.E. Kassner, R. Busch, Oxidation and corrosion of highly alloyed Cu–Fe–Ni as inert anode material for aluminum electrowinning in as-cast and homogenized conditions, *Corros. Sci.* 63 (2012) 293–303. doi:10.1016/j.corsci.2012.06.013.
- [35] G.J. Koel, P.J. Gellings, The contribution of different types of point defects to diffusion in CoO and NiO during oxidation of the metals, *Oxid. Met.* 5 (1972) 185–203. doi:10.1007/BF00609658.
- [36] S. Helle, M. Tresse, B. Davis, D. Guay, L. Roué, Mechanically Alloyed Cu-Ni-Fe-O Based Materials as Oxygen-Evolving Anodes for Aluminum Electrolysis, *J. Electrochem. Soc.* 159 (2012) E62–E68. doi:10.1149/2.028204jes.

## SUPPLEMENTARY SECTION

*Table S1. HVOF Spray process parameters.*

Sample #	Oxygen flow (lpm)	Propylene flow (lpm)	Air flow (lpm)	Nitrogen (carrier gas) flow (lpm)	Substrate temperature (°C)	Number of passes	Substrate	Coating composition	Deposition efficiency (%)
<b>Part 1</b>									
H1	279	65	202	15	400	50	Cu-rich	Co <sub>0.75</sub> Ni <sub>0.25</sub> O	18
H2	217	70	167	15	450	50	Cu-rich	Co <sub>0.75</sub> Ni <sub>0.25</sub> O	24
H3	236	55	163	15	350	50	Cu-rich	Co <sub>0.75</sub> Ni <sub>0.25</sub> O	14
<b>Part 2</b>									
S1	217	70	167	15	450	55	Cu-rich	CoO	25
S2	217	70	167	15	450	55	Cu-rich	Co <sub>0.75</sub> Ni <sub>0.25</sub> O	23
S3	217	70	167	15	450	55	Cu-rich	Co <sub>0.5</sub> Ni <sub>0.5</sub> O	24
S4	217	70	167	15	450	55	Ni-rich	CoO	26
S5	217	70	167	15	450	55	Ni-rich	Co <sub>0.75</sub> Ni <sub>0.25</sub> O	29
S6	217	70	167	15	450	55	Ni-rich	Co <sub>0.5</sub> Ni <sub>0.5</sub> O	22

The optimum HVOF spraying conditions were determined using  $\text{Co}_{0.75}\text{Ni}_{0.25}\text{O}$  powder deposited on Cu-20Ni-15Fe (Cu-rich) substrate. Three different sets of spray parameters were tested and they are listed in **Table S1**. No inter pass pauses, air or water cooling was applied during the deposition process. The substrate temperature for sample H1, H2 and H3 was about 350, 450 and 400 °C, respectively. The deposition efficiency for sample H1, H2 and H3 was 18, 24 and 14%, respectively. The XRD patterns of H1, H2 and H3 coatings are shown in **Fig. S1**. In all cases, only one set of peaks appears in the XRD patterns. The diffraction peaks occur at  $2\theta = 36.7^\circ, 42.7^\circ, 61.9^\circ, 74.2^\circ$  and  $78.1^\circ$  and are assigned to *fcc* (Co,Ni)O solid solution. The composition of the solid solutions was obtained by calculating the *a* lattice parameter of the *fcc* phase based on the position of the XRD peaks. The composition of the (Co,Ni)O solid solution was  $\text{Co}_{0.73}\text{Ni}_{0.27}\text{O}$  for samples H1, H2 and H3, very close to the starting powder.

The cross-sectional SEM micrographs of H1, H2 and H3 coatings are presented in **Fig. S2**. The coating thickness is between 60 to 85  $\mu\text{m}$  after 50 deposition passes. The SEM images show a uniform microstructure, low porosity, very low surface roughness and good bonding to the substrate. However, sample H2 has the lowest porosity. While layers of melted splats can still be seen in sample H1 and H3, the splats observed in sample H2 formed a uniform structure, most probably because the particles were better accelerated/melted during the deposition process.

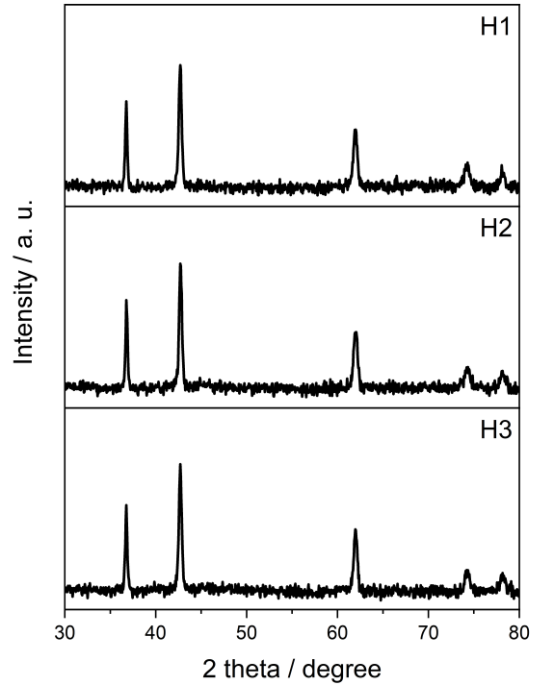


Figure S1. XRD patterns of coatings prepared in the first series of experiments using different HVOF gas compositions ranging.

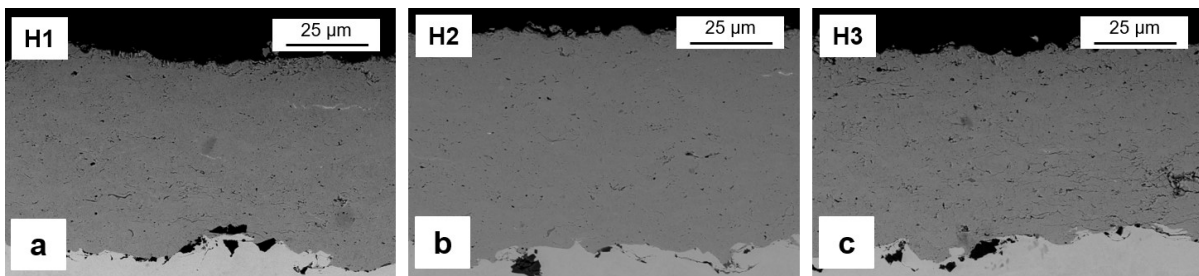


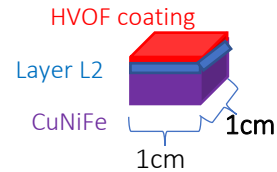
Figure S2. Cross-sectional SEM micrographs of coatings prepared in the first series of experiments using different HVOF gas compositions ranging.

A mass balance calculation was performed to determine the total amount of Fe and O atoms in Layer 1 and 2 of CoO coatings on Cu-rich substrate after heat treatment under argon:

	<b>Thickness</b>	<b>Lattice parameter</b>
HVOF coating (before HT)	$118 * 10^{-4} \text{ cm}$	$4.264 * 10^{-8} \text{ cm}$
HVOF coating (before HT)	$118 * 10^{-4} \text{ cm}$	$4.274 * 10^{-8} \text{ cm}$
Fe-poor layer	$50 * 10^{-4} \text{ cm}$	$3.60 * 10^{-8} \text{ cm}$

Cu-20Ni-15Fe in wt% =  $\text{Cu}_{62.7}\text{Ni}_{20.9}\text{Fe}_{16.4}$  in at.%

If we consider the sample size is  $1 \text{ cm} * 1 \text{ cm} \Rightarrow$



Before heat treatment:

Total oxygen in  $118 \mu\text{m}$  thickness CoO:

If we consider the total coating volume is  $0.0118 \text{ cm} * 1 \text{ cm} * 1 \text{ cm} = 0.0118 \text{ cm}^3$

CoO unit cell volume is:  $(4.264 * 10^{-8} \text{ cm})^3 = 77.527 * 10^{-24} \text{ cm}^3$

In  $0.0118 \text{ cm}^3$  there are:  $0.0118 \text{ cm}^3 / 77.527 * 10^{-24} \text{ cm}^3 = 1.522 * 10^{20}$  CoO unit cells

Each CoO unit cell contains 4 atoms of O and 4 atoms of Co, therefore,

In this volume, there are  $6.088 * 10^{20}$  atoms of oxygen.

Total Fe in  $50 \mu\text{m}$  thickness of CuNiFe (Layer L2):

Cu-rich unit cell volume is:  $(3.60 * 10^{-8} \text{ cm})^3 = 46.656 * 10^{-24} \text{ cm}^3$

If we consider the total substrate volume is  $0.005 \text{ cm} * 1 \text{ cm} * 1 \text{ cm} = 0.005 \text{ cm}^3$

In  $0.005 \text{ cm}^3$  there are:  $0.005 \text{ cm}^3 / 46.656 * 10^{-24} \text{ cm}^3 = 1.071 * 10^{20}$  CuNiFe unit cells

Each CuNiFe unit cell (FCC) contains 4 atoms, 0.656 atoms Fe + 0.836 atoms Ni + 2.508 atoms Cu (Cu-20Ni-15Fe in wt% =  $\text{Cu}_{62.7}\text{Ni}_{20.9}\text{Fe}_{16.4}$  in at.%).

So, there are totally  $0.702 * 10^{20}$  atoms of Fe.

After heat treatment:

Total iron in 118  $\mu\text{m}$  thickness of  $(\text{Co,Fe})\text{O}$ :

If we consider the total coating volume is  $0.0118 \text{ cm} * 1 \text{ cm} * 1 \text{ cm} = 0.0118 \text{ cm}^3$

$(\text{Co,Fe})\text{O}$  unit cell volume is:  $(4.274 * 10^{-8} \text{ cm})^3 = 78.073 * 10^{-24} \text{ cm}^3$

In  $0.0118 \text{ cm}^3$  there are:  $0.0118 \text{ cm}^3 / 78.073 * 10^{-24} \text{ cm}^3 = 1.511 * 10^{20}$   $\text{CoO}$  unit cells

Each  $(\text{Co,Fe})\text{O}$  unit cell contains 4  $(\text{Co,Fe})$  atoms and 4 O atoms, 0.4 atoms Fe, 3.6 atoms Co [ $(\text{Co}_{0.4}\text{Fe}_{0.1})\text{O}$ ].

Therefore, there are  $0.604 * 10^{20}$  atoms of iron (Number of Fe atoms that diffused from L2 into  $\text{CoO}$  coating).

Remaining Fe atoms in L2 after HT:

#Fe atoms before HT - #Fe atoms diffused into  $\text{CoO}$  after HT:

$0.702 * 10^{20} - 0.604 * 10^{20}$  atoms of iron =  $0.098 * 10^{20}$  atoms of iron

To oxidize all these Fe atoms ( $\text{Fe}_2\text{O}_3$ ):  $0.147 * 10^{20}$  atoms of oxygen is required.

Total O in  $\text{CoO}$  before HT was:  $6.088 * 10^{20}$  atoms of oxygen.

2.414 at.% of O from  $\text{CoO}$  is required to oxidize the remaining Fe in L2.

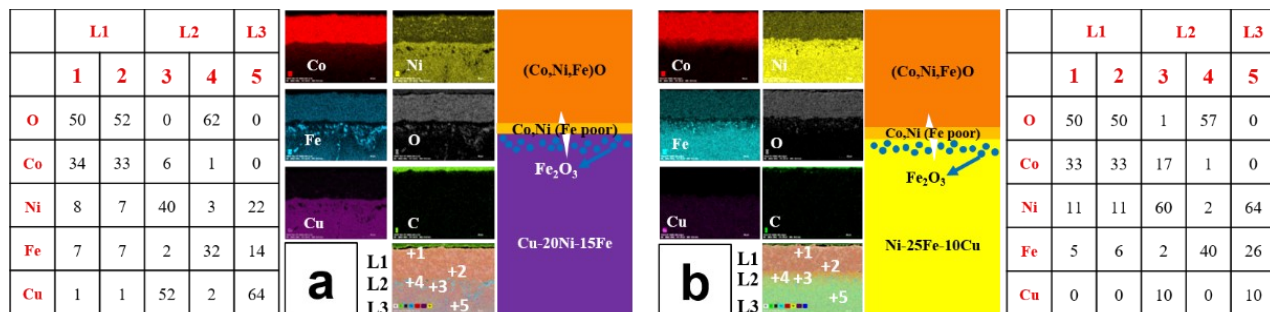


Figure S4. EDS analysis results and schematic illustrations of  $Co_{0.75}Ni_{0.25}O$  coatings deposited on (a) Cu-20Ni-15Fe and (b) Ni-25Fe-10Cu substrates (sample S2 and S5, respectively), after 20 h of heat treatment at 1000 °C under an argon flow. The source of carbon is the resin used for the sample preparation.

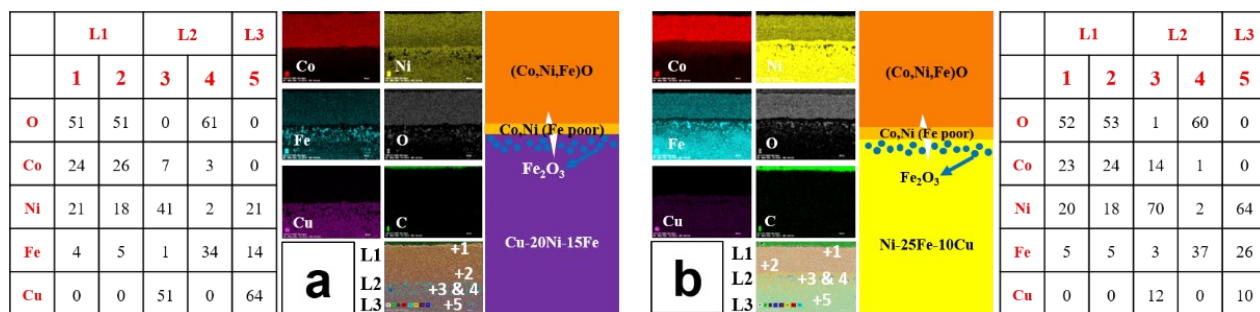


Figure S4. EDS analysis results and schematic illustrations of  $Co_{0.5}Ni_{0.5}O$  coatings deposited on (a) Cu-20Ni-15Fe and (b) Ni-25Fe-10Cu substrates (sample S3 and S6, respectively), after 20 h of heat treatment at 1000 °C under an argon flow. The source of carbon is the resin used for the sample preparation.

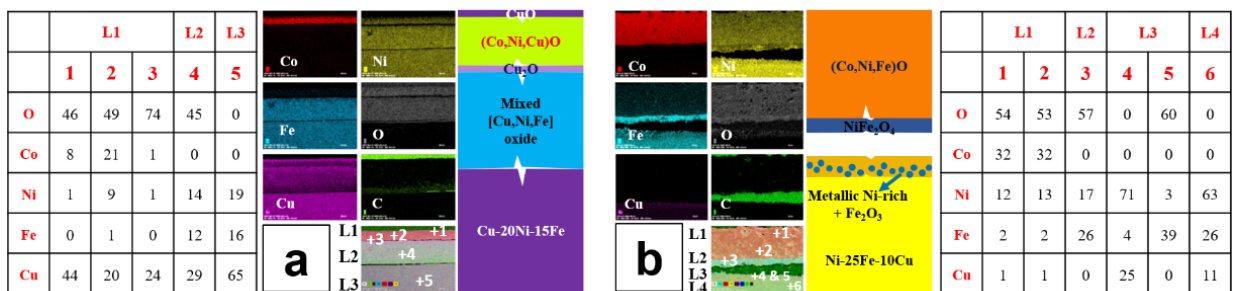


Figure S5. EDS analysis results and schematic illustration of  $Co_{0.75}Ni_{0.25}O$  coating deposited on (a)  $Cu-20Ni-15Fe$  and (b)  $Ni-25Fe-10Cu$  substrate (sample S2 and S5, respectively), after 20 h of heat treatment at 1000 °C in static air. The source of carbon is the resin used for the sample preparation.

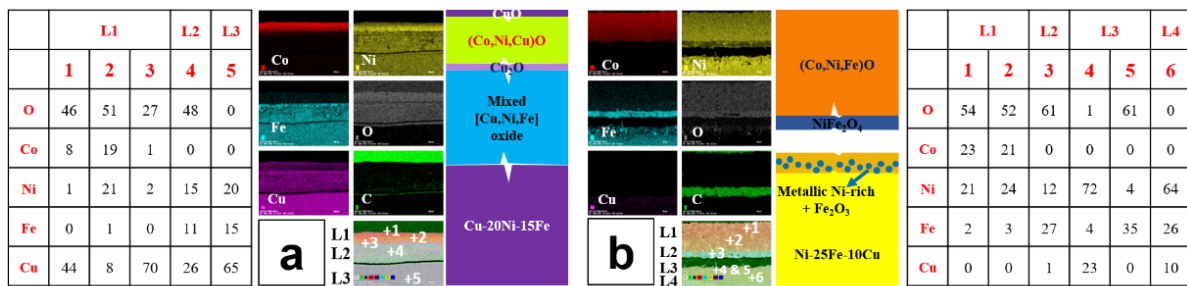


Figure S6. EDS analysis results and schematic illustration of  $Co_{0.5}Ni_{0.5}O$  coating deposited on (a)  $Cu-20Ni-15Fe$  and (b)  $Ni-25Fe-10Cu$  substrate (sample S3 and S6, respectively), after 20 h of heat treatment at 1000 °C in static air. The source of carbon is the resin used for the sample preparation.

### **III.7. Solubility of (Co,Ni)O in molten cryolite and anodic behaviour of (Co,Ni)O coated Cu-Ni-Fe electrodes**

#### **Contributions:**

The solubility measurements and electrolysis tests were carried out by the author of this thesis at INRS. The ICP analysis were carried out at INRS-ETE and the obtained results were treated by the author of this thesis. The characterizations of the anodes after aluminum electrolysis tests by SEM-EDS and XRD were performed by the author of this thesis.

As explained in previous sections, one of the most important characteristics for the materials used as anodes in aluminum electrolysis is low solubility in molten cryolite. The dissolution rate of NiO as a function of composition of cryolite and time has been studied [1–3] but to our knowledge, the solubility of CoO and (Co,Ni)O in molten electrolyte has never been measured. Here, dissolution rates of  $\text{Co}_x\text{Ni}_{1-x}\text{O}$  solid solutions in sodium and potassium-based electrolytes at 1000 and 700 °C, are studied. As mentioned before, Cu-Ni-Fe alloys are promising inert anodes for green aluminum production but their corrosion resistance must be improved. Protective (Co,Ni)O coatings have been successfully deposited on Cu-Ni-Fe by SPS and HVOF methods [4,5]. Uniform, adherent and non-porous  $\text{Co}_x\text{Ni}_{1-x}\text{O}$  coatings were obtained using both thermal spray techniques. However, reduction of NiO to Ni was observed during SPS process. Dense, uniform, and single phase  $\text{Co}_x\text{Ni}_{1-x}\text{O}$  coatings, with  $x = 1, 0.75$  and  $0.5$ , were deposited on two compositions of CuNiFe alloys (Cu-20Ni-15Fe and Ni-25Fe-10Cu (in wt%)) using the HVOF process. The behaviour of coated samples at 1000 °C under argon and air atmospheres was studied and the impact of the coating and substrate compositions on their behaviour was investigated. Also, it was shown that to prevent undesired formation of  $\text{Co}_3\text{O}_4$ , a (Co,Ni)O solid solution rich in nickel must be used [6]. Here, the use of Cu-Ni-Fe anodes protected by  $\text{Co}_x\text{Ni}_{1-x}\text{O}$  coatings prepared by HVOF for the primary production of aluminum is presented.

## Experimental

- Solubility measurements

To perform solubility measurements, sintered pellets of  $\text{Co}_x\text{Ni}_{1-x}\text{O}$  were prepared.  $\text{Co}_x\text{Ni}_{1-x}\text{O}$  ( $x = 1, 0.75, 0.5, 0.25$  and  $0$ ) powders were mixed separately with a PVA solution (5 wt% in water) then were cold-pressed under 50 MPa for 5 minutes. The pellets were left to dry in an oven then were heated 16 h in air at 1350 °C to be sintered. Sintered CoO pellet was heated again at 950 °C under argon flow for 3h and then was left to cool down under argon flow to obtain a pure CoO pellet and prevent its conversion to  $\text{Co}_3\text{O}_4$ . Prior to solubility measurements, the crystal structure of sintered pellets was analyzed by XRD. Apparent densities of produced pellets were about 89 % of their theoretical densities.

200 grams of NaF and KF-based electrolyte powders were dried 24 h in oven prior to solubility measurements. The NaF-based electrolyte was composed of 82.15 wt%  $\text{Na}_3\text{AlF}_6$  + 9.85

wt%  $\text{AlF}_3$  + 8 wt%  $\text{Al}_2\text{O}_3$  (CR=2.3) and the KF-based electrolyte consisted of 45 wt% KF + 50 wt%  $\text{AlF}_3$  + 5 wt%  $\text{Al}_2\text{O}_3$  (CR=1.3). Sintered pellets were put under electrolyte powder mixture at the bottom of alumina crucibles. For solubility measurements at 1000 °C, NaF-based electrolytes were heated under argon flow and after 3, 6, 8 and 9 h of immersion, ~2 grams of molten electrolyte were taken out using a graphite tube and left to cool down at room temperature. The obtained samples were crushed using a mortar and pestle to be analyzed by ICP. After 9 h at 1000 °C, electrolytes were cooled down in the furnace and solid electrolytes were cut into smaller pieces. All sintered pellets remained at the bottom of crucible. For solubility measurements at 700 °C, KF-based electrolytes were heated at 700 °C under argon flow for 60 hours and sampling was carried out every 20 h (20, 40 and 60 h) using the same procedure as explained above. As a reference, 200 grams of each sodium and potassium-based electrolytes without any sintered pellets were heated at 1000 and 700 °C, respectively, and 2 grams of molten electrolytes were taken out and analyzed by ICP.

- Aluminum electrolysis

$\text{Co}_x\text{Ni}_{1-x}\text{O}$  powders with  $x = 0.75$  and  $0.5$  were prepared in kg quantity as described in our previous work. Cu-20Ni-15Fe and Ni-25Fe-10Cu (in wt%) substrates were produced by the casting method and were further homogenized by a heat treatment under argon as explained in a previous work [7,8]. Substrates were cut into disc-shaped specimens of 15 mm diameter and ~7 mm thickness. Then, they were grit-blasted and cleaned by several rinsing in distilled water and acetone. Only one side of the disc-shaped samples was coated by HVOF and coatings with ~100-125  $\mu\text{m}$  thickness were prepared. The HVOF spraying parameters and HVOF setup are described in detail in our previous work [5].

Aluminum electrolysis tests were carried out in a laboratory electrolysis cell as explained in the second chapter of this thesis. Disc-shaped coated anode was connected to a stainless steel 316 threaded rod which was placed inside an alumina tube. Prior to heating process, the HVOF-coated anode was placed inside the cell (5 cm above solid electrolyte), then cathode, anode and electrolyte were heated slowly ( $2\text{ }^\circ\text{C}\cdot\text{min}^{-1}$ ) up to the electrolysis temperature to prevent thermal shock into the coating layer. The anode was then inserted into the electrolyte and aluminum electrolysis started. The electrolysis experiments were conducted at 700, 850 and 1000 °C under argon atmosphere at an anode current density of  $0.5\text{ A}\cdot\text{cm}^{-2}$  using a two-electrode configuration

cell controlled by VMP3 potentiostat/galvanostat. The graphite crucible containing the electrolyte (~150 cm<sup>2</sup> in contact with the molten bath) was considered as the counter electrode.

The electrolyte (~400 g) was composed of 82.15 wt% Na<sub>3</sub>AlF<sub>6</sub> + 9.85 wt% AlF<sub>3</sub> + 8 wt% Al<sub>2</sub>O<sub>3</sub> (CR=2.3) for electrolysis at 1000 °C while for electrolysis at 700 and 850 °C, electrolyte consisted of 45 wt% KF + 50 wt% AlF<sub>3</sub> + 5 wt% Al<sub>2</sub>O<sub>3</sub> (CR=1.3) was used. Electrolyte powders were dried in an oven at 150 °C for at least 24 hours before the experiments. Alumina powder (which was dried with the same procedure) was periodically added to the electrolyte with an automatic feeder to keep the alumina concentration at saturation during the electrolysis. After electrolysis, anode was removed from the electrolyte and left to slowly cool down inside the electrolysis cell. Then, the anodes were detached from the stainless-steel threaded rod. The coated side of the anodes used for electrolysis at 700 and 850 °C were analyzed by XRD. The anodes used at 1000 °C was embedded in resin to prevent the delamination of the oxide layer from the anode surface due to thermal and mechanical shocks. Samples were then polished using standard metallographic procedures and their cross-sections were analyzed by a scanning electron microscopy (SEM) in secondary electron (SE) mode using a Tescan Vega3 scanning electron microscope equipped with a Bruker XFlash® 6 | 10 Detector energy dispersive X-ray spectroscope (EDX).

## Results and discussion

- Solubility measurements

**Fig. 1** shows the dissolution rate of cobalt and nickel from Co<sub>x</sub>Ni<sub>1-x</sub>O in molten KF and NaF-based electrolytes at 700 and 1000 °C as a function of the immersion time. For comparison, cobalt and nickel contaminations of as-received potassium and sodium-based electrolytes are presented as well (blank samples). As shown in **Fig. 1a**, dissolution rates of cobalt and nickel from Co<sub>x</sub>Ni<sub>1-x</sub>O pellets at 700 °C is between 0.5 to 2.2 ppm and between 1 to 8 ppm, respectively, while cobalt and nickel contaminations in the as-received potassium-based electrolyte (blank sample) are 1.3 and 4.5 ppm, respectively. Also, increasing immersion time from 20 to 60 h does not seem to have a considerable effect on solubility of cobalt or nickel in the molten KF cryolite. This means that there is no significant dissolution of the Co<sub>x</sub>Ni<sub>1-x</sub>O materials in KF-based electrolyte at 700 °C. At 1000 °C in sodium-based electrolyte, solubility the amount of dissolved Co from Co<sub>x</sub>Ni<sub>1-x</sub>O solid solutions measured after 9 h of immersion varies from 16 ppm for x = 0.25 to 65 ppm for

$x = 1$  while the amount of dissolved Ni varies from 9 ppm for  $x = 0.75$  to 23 ppm for  $x = 0$ . Cobalt and nickel contaminations in the as-received sodium-based electrolyte (blank sample) are 0.4 and 5 ppm, respectively. Because of the higher dissolution rate of Co versus Ni, increasing the Co content in  $\text{Co}_x\text{Ni}_{1-x}\text{O}$  solid solutions increases its global (Ni + Co) dissolution rate as shown in **Fig. 1e.**, however, the global contamination of NaF-based electrolysis with cobalt and nickel from  $(\text{Co},\text{Ni})\text{O}$  materials was lower than 80 ppm for all compositions of  $\text{Co}_x\text{Ni}_{1-x}\text{O}$  solid solutions, showing their low solubility in molten electrolyte.

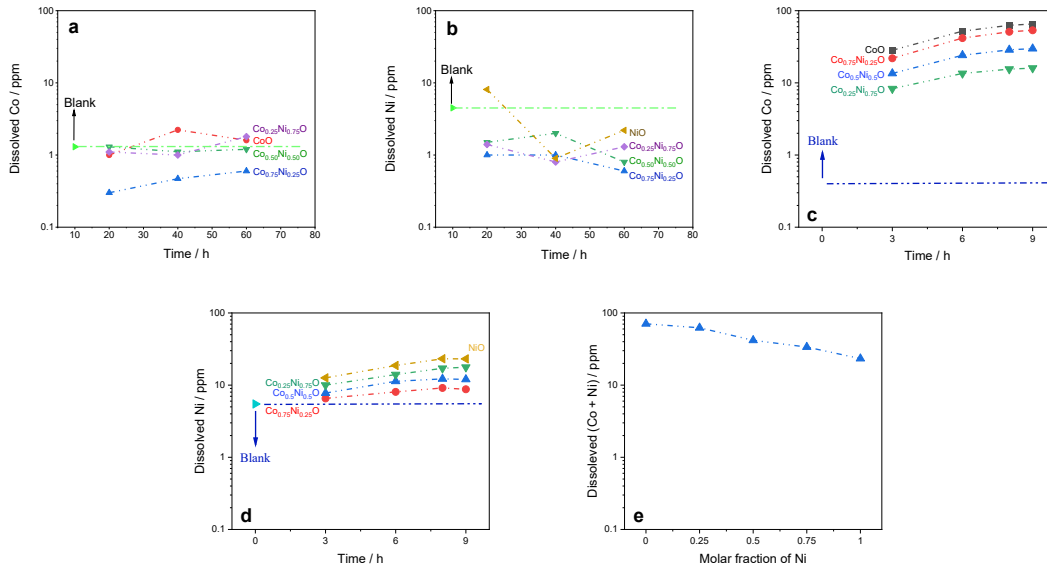


*Figure 1. Dissolution rate of (a) Co and (b) Ni in molten KF-based electrolyte at 700 °C and of (c) Co and (d) Ni in molten NaF-based electrolyte at 1000 °C for  $\text{Co}_x\text{Ni}_{1-x}\text{O}$  (with  $x = 0, 0.75, 0.5, 0.25$  and 1) as a function of time and (e) as a function of  $x$  for  $t = 9\text{h}$  in molten NaF-based electrolyte at 1000 °C.*

- Cell voltage evolution

**Fig. 2a-d** shows the cell voltage evolution during the Al electrolysis performed at different temperatures (700, 850 and 1000 °C) using the Cu-20Ni-15Fe or Ni-25Fe-10Cu anodes coated with  $\text{Co}_{0.5}\text{Ni}_{0.5}\text{O}$  or  $\text{Co}_{0.75}\text{Ni}_{0.25}\text{O}$ . The cathode potential and the ohmic drop related to the electrolyte and electrical connections are expected to be stable and similar for the different electrolysis experiments. Consequently, the variations of the cell voltage shown in **Fig. 2** are considered as indicative of the variation of the anode potential. It must be noted that only one side of the disc-shaped substrates was coated by HVOF, thus the variation of the cell voltage is

representative of the variation of the anode potential in both coated and bare parts of Cu-Ni-Fe alloys.

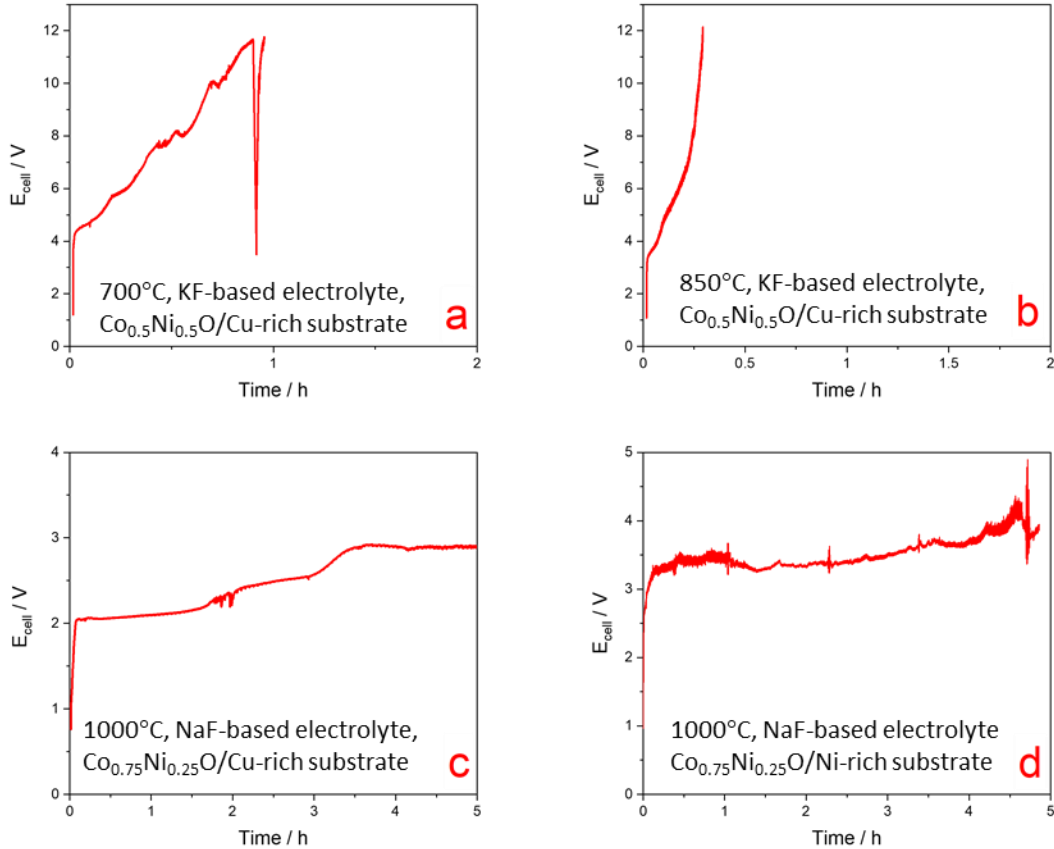


Figure 2. Cell voltage vs. electrolysis time at (a) 700, (b) 850 °C in KF-based electrolyte and (c,d) 1000 °C in NaF-based electrolyte for the Cu-20Ni-15Fe anodes coated with  $\text{Co}_{0.5}\text{Ni}_{0.5}\text{O}$  (a,b), with  $\text{Co}_{0.75}\text{Ni}_{0.25}\text{O}$  (c) and the Ni-25Fe-10Cu anode coated with  $\text{Co}_{0.75}\text{Ni}_{0.25}\text{O}$  (d).

At 700 °C in KF-based electrolyte (**Fig. 2a**), the cell voltage reached ~4 V in a few minutes for the Cu-20Ni-15Fe anode coated with  $\text{Co}_{0.5}\text{Ni}_{0.5}\text{O}$ , which is related to the  $\text{O}_2$  evolution reaction. Then cell voltage increased from 4 V to 12 V in about 1 hour, where electrolysis stopped due to high cell voltage. Then, as the electrolysis restarted, the cell voltage reached 12 V in few minutes and electrolysis stopped again. The same evolution of cell voltage is observed during the Al electrolysis at 850 °C using a similar anode (**Fig. 2b**). These rapid increases in the cell potential were not observed when a bare Cu-20Ni-15Fe was used as an anode and thus, were associated

with the decomposition of (Co,Ni)O and the formation of Co<sub>3</sub>O<sub>4</sub> on the coated side of the anode as supported by the XRD analysis (not shown here). As mentioned earlier, the formation of Co<sub>3</sub>O<sub>4</sub> is not desired since Co<sub>3</sub>O<sub>4</sub> is an n-type semiconductor that displays a significantly higher O<sub>2</sub> evolution overpotential than p-type semiconducting (Co,Ni)O. One must however note that the potential increase observed here is much higher than expected on the basis of the de Nora's work showing an increase of about 1V of the oxygen evolution overpotential for Co<sub>3</sub>O<sub>4</sub> versus (Co,Ni)O coatings measured at 930 °C in molten cryolite (see Fig. I-13 in chapter 1). As explained in detail in our previous work [6], the decomposition of (Co,Ni)O to Co<sub>3</sub>O<sub>4</sub> depends on temperature, oxygen partial pressure and composition of (Co,Ni)O. It was shown that Co<sub>x</sub>Ni<sub>1-x</sub>O solid solutions are only stable for  $x \leq 0.46$  and  $x \leq 0.22$  at 800 °C and 700 °C, respectively, when heated in air. At higher oxygen pressures, only solid solutions with even higher nickel contents are stable at these temperatures. Our experimental results confirmed that Co<sub>0.5</sub>Ni<sub>0.5</sub>O is stable in pure oxygen atmosphere only at temperatures higher than ~900 °C. Thus, it is predictable that Co<sub>0.5</sub>Ni<sub>0.5</sub>O coating decomposes to Co<sub>3</sub>O<sub>4</sub> during the aluminum electrolysis at 700 and 850 °C. Unfortunately, we were not able to manufacture Cu-Ni-Fe electrodes coated with (Co,Ni)O having a higher Ni content due to the impossibility to produce such as powder in sufficient quantity and with the appropriate particle size at the time the HVOF equipment was available.

For electrolysis at 1000 °C in NaF-based electrolyte, two compositions of Cu-Ni-Fe alloys (Cu-rich Cu-20Ni-15Fe and Ni-rich Ni-25Fe-10Cu) coated with Co<sub>0.75</sub>Ni<sub>0.25</sub>O were used as the anodes. For the Cu-rich coated alloy (**Fig. 2c**), the cell voltage reached about 2.1 V in a few minutes and remained stable until almost 2 hours of electrolysis, then it increased slowly to 2.8 V at 3.5 hours of electrolysis and remained unchanged until the end of the electrolysis. The slight increase in the cell potential at 1000 °C after 2 hours of electrolysis may be due to the formation of a continuous, thick, porous and poorly conductive oxide layer on the bare parts of Cu-Ni-Fe alloy as well as the formation of a nickel ferrite layer on the Co<sub>0.75</sub>Ni<sub>0.25</sub>O coated parts of Cu-Ni-Fe alloy, as supported by the SEM-EDX analyses presented in **Fig. 4**. As mentioned above, only one side of the disc-shaped anodes was coated by (Co,Ni)O, thus the variation of the cell voltage is representative of the variation of the anode potential in both coated and uncoated parts of Cu-Ni-Fe anodes. The cell potentials in the first few hours of electrolysis at 1000 °C, was about 2.1 V which is less than the reversible potential for O<sub>2</sub> evolution reaction (2.248 V at 960 °C, see Fig.

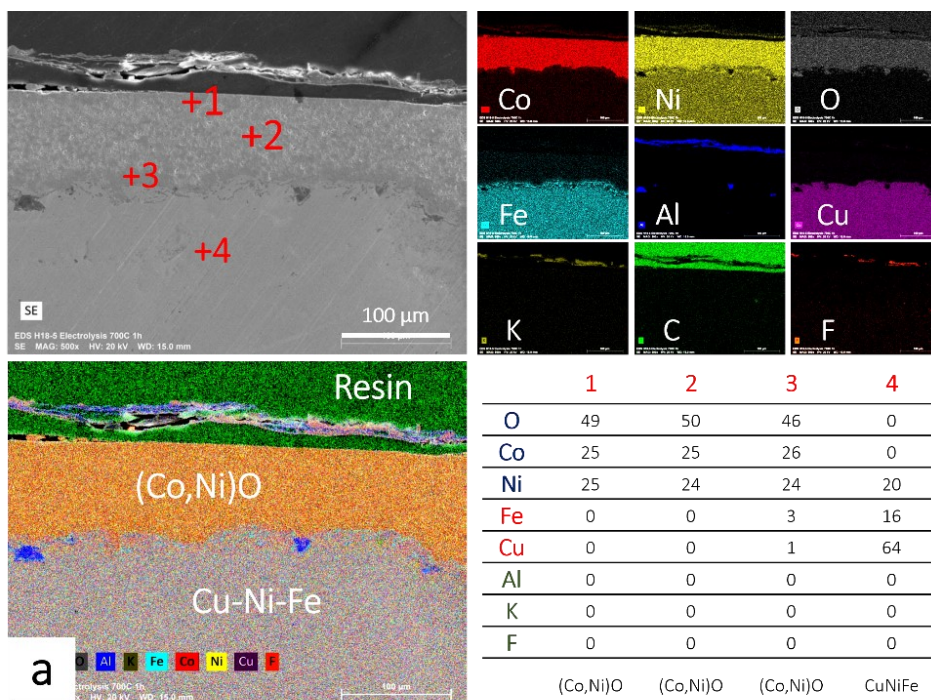
I2b in Chap. I). This indicates that in the first few hours of electrolysis, the observed cell potential is probably related to the oxidation of Cu, Ni and Fe elements on the uncoated side of the anode.

For Ni-rich alloy coated with  $\text{Co}_{0.75}\text{Ni}_{0.25}\text{O}$ , the cell voltage reached 3 V at the beginning of electrolysis within few minutes and then rapid fluctuations and a continuous increase can be seen in the cell voltage, as shown in **Fig. 2d**. Cell voltage remained more stable for two hours after the first hour of electrolysis but then increased to 4 V accompanied with rapid fluctuations at the end of electrolysis. The rapid fluctuation in the cell voltage is probably due to formation and delamination of thin layers (20 – 50  $\mu\text{m}$ ) of oxide on both coated and not-coated sides of Ni-rich anode coated with  $\text{Co}_{0.75}\text{Ni}_{0.25}\text{O}$  as shown in the SEM-EDX analyses in **Fig. 4**.

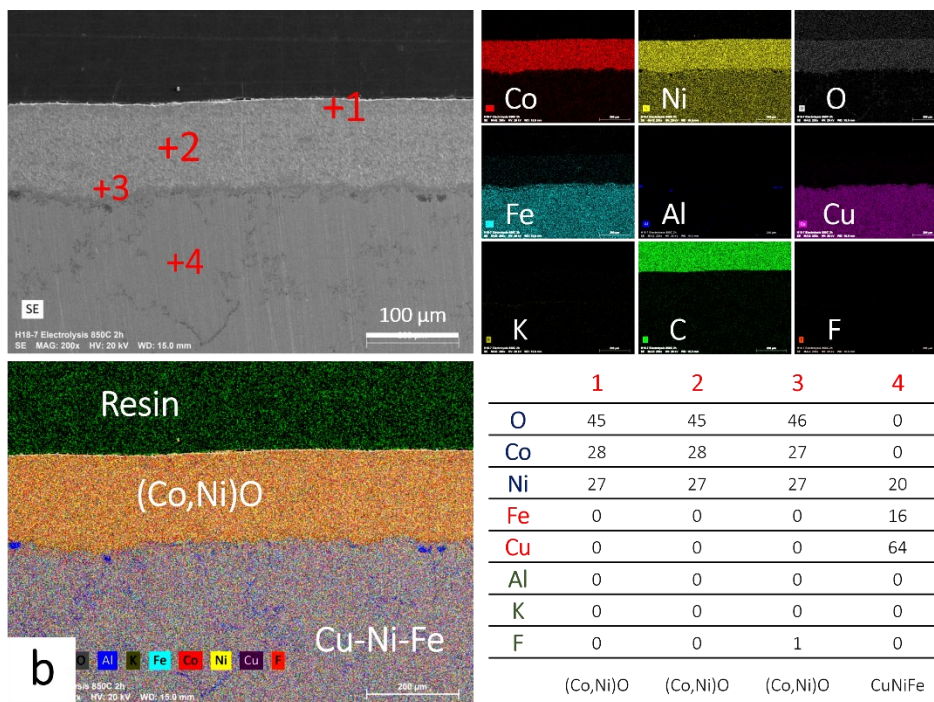
- Characterization of the anodes after Al electrolysis

**Figs. 3 and 4** show cross-sectional SEM micrographs as well as elemental EDS mappings of Co, Ni, O, Cu, Ni, Fe, Al, Fe and Na or K of Cu-Ni-Fe anodes coated with (Co,Ni)O after the aluminum electrolysis at 700, 850 and 1000 °C. For comparison, cross-sectional SEM micrographs of both coated and bare parts of Cu-Ni-Fe anodes after the Al electrolysis are shown.

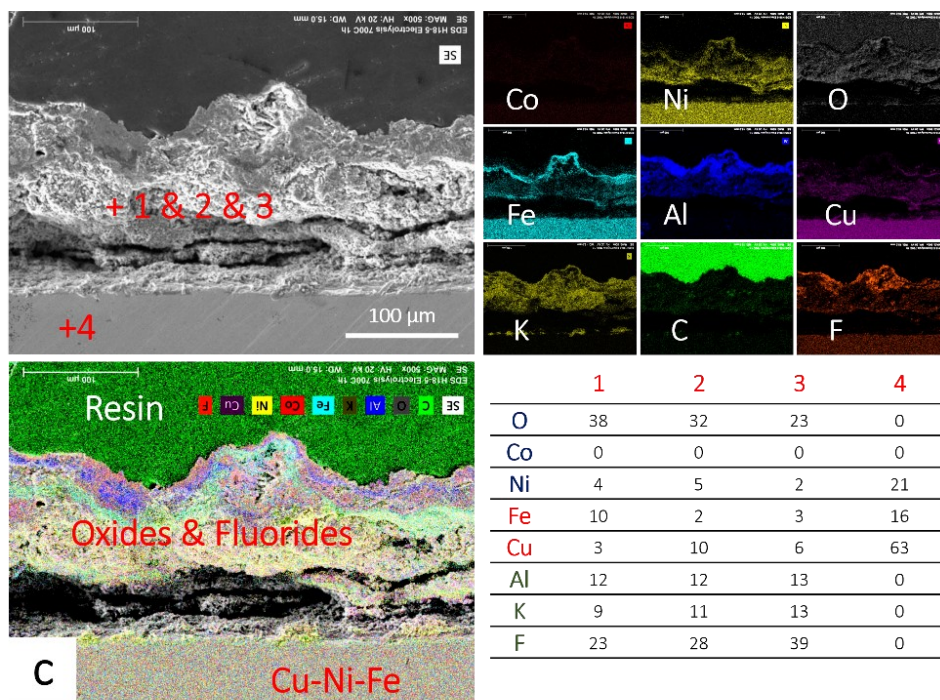
After 1 hour electrolysis at 700 and 850 °C,  $\text{Co}_{0.5}\text{Ni}_{0.5}\text{O}$  coating is still well-attached to the Cu-Ni-Fe substrate and there is no sign of delamination, as shown in **Fig. 3a and b**. On the not-coated parts of these samples, a layer of oxides (about 50  $\mu\text{m}$  thick) is formed which is delaminated in some parts (**Fig. 3c**). The delaminated oxide layers are composed of thick copper oxide and thin iron oxide layers as well as aluminum oxide and fluoride. Some Cu-poor regions composed of iron and nickel oxides and fluorides are also formed on the not-coated parts of the anode. The impact of HVOF coated layer on the resistance corrosion of the anode is evident even after one hour of electrolysis, since oxidation and fluorination reactions occurred on the not-coated parts of the anode while on the coated parts, oxygen or fluorine diffusion did not happen.



(a)  $\text{Co}_{0.5}\text{Ni}_{0.5}\text{O}$  coated part of the Cu-rich alloy after 1 h of electrolysis at 700 °C.



(b)  $\text{Co}_{0.5}\text{Ni}_{0.5}\text{O}$  coated part of the Cu-rich alloy after 1 h of electrolysis at 850 °C.



(c) Uncoated part of the Cu-rich alloy after 1 h of electrolysis at 700 °C.

Figure 3. Cross-sectional SEM images and EDS analysis results of Cu-20Ni-15Fe anodes coated with (Co,Ni)O after aluminum electrolysis at (a & c) 700, (b) 850 °C for 1h. The source of carbon is the resin used for the sample preparation. SEM-EDS analyses presented in (c) are taken from the not-coated parts of the anode after 1 electrolysis at 700 °C.

**Fig. 4a-b** shows the cross-section SEM images and EDX mapping analyses taken from the coated and not-coated parts of Cu-20Ni-15Fe anode after electrolysis for 5 hours at 1000 °C. On the coated parts of the anode, the upper part of the scale is  $\text{Co}_{0.75}\text{Ni}_{0.25}\text{O}$  coating and a continuous dense layer of nickel ferrite ( $\sim 30 \mu\text{m}$ ) is formed on the inner side of the (Co,Ni)O coating while both  $\text{NiFe}_2\text{O}_4$  and (Co,Ni)O layers have been delaminated. The delamination probably happened after the electrolysis when the anode was cooling down as no electrolyte infiltration was detected in this delamination area. The thickness of (Co,Ni)O layer is not uniform which suggests its partial delamination or dissolution during the aluminum electrolysis. A region rich in copper is formed at the interface of the substrate and the coating, as a result of the outward diffusion of iron and nickel.

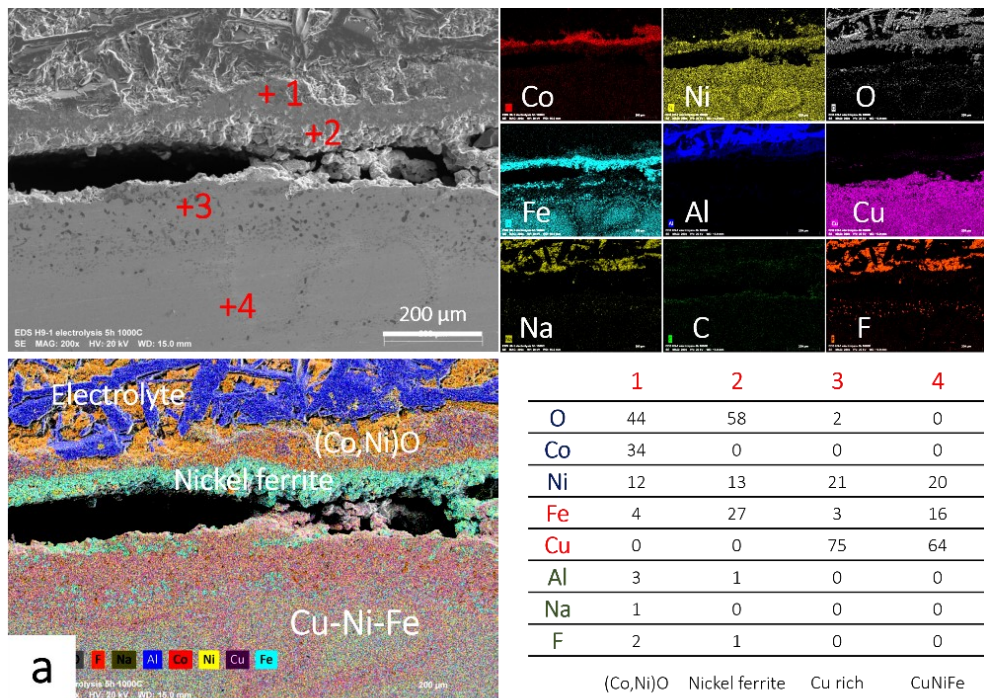
On the not-coated parts of the anode, a thick layer of [Cu & Ni & Fe] oxides with 300-400  $\mu\text{m}$  thickness is formed. The upper part of the scale on the not-coated parts of the anode is richer

in iron while some discontinuous regions of  $\text{NiO} + \text{Fe}_2\text{O}_3 + \text{CuO}_x$  are observed in the inner parts of the scale. The composition of the oxides in different regions of this scale is not uniform and is composed of different ratios of  $\text{NiO} + \text{Fe}_2\text{O}_3 + \text{CuO}_x$ . The nickel ferrite layer can not be seen on the not-coated parts of the anode and fluorination has occurred at the surface of the Cu-Ni-Fe alloy underneath the thick oxide layer. These results suggest that the HVOF coating layer protected the Cu-Ni-Fe alloy and significantly decreases the corrosion rate of the sample by providing the required time for the formation of the nickel ferrite layer. Long-term electrolysis experiments at using a larger size anode will have to be performed to confirm the ability of (Co,Ni)O coating in protecting the Cu-Ni-Fe alloy from fluorination.

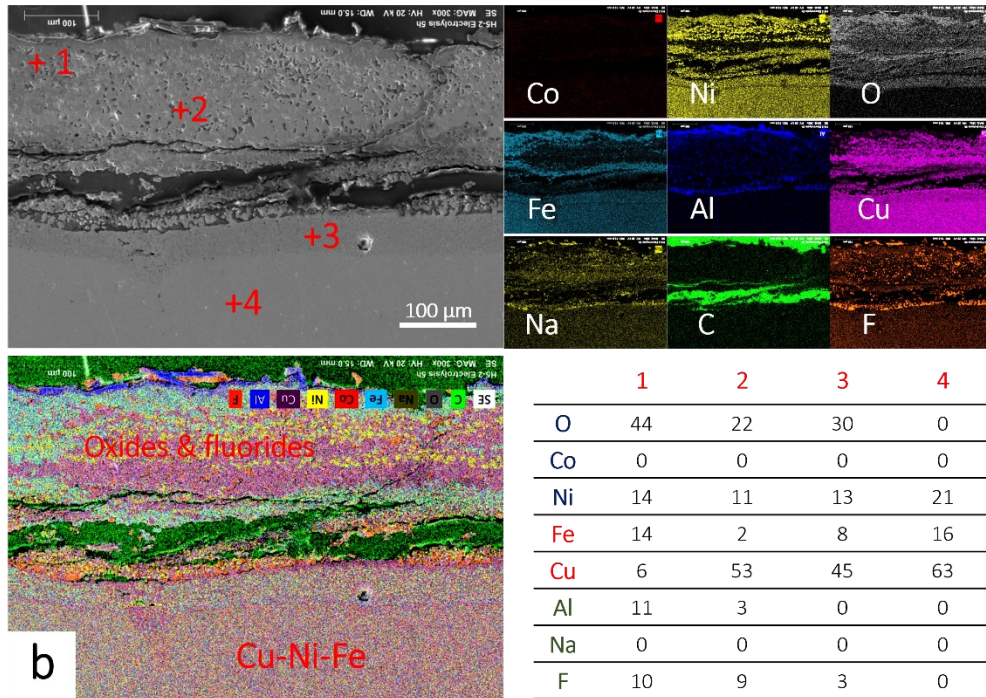
**Fig. 4c-d** shows the cross-section SEM images and EDX mapping analyses taken from the coated and not-coated parts of Ni-25Fe-10Cu anode after electrolysis for 5 hours at 1000 °C. On the coated part of the anode,  $\text{Co}_{0.75}\text{Ni}_{0.25}\text{O}$  coating is completely delaminated and several thin layers (5 – 20  $\mu\text{m}$ ) of oxides are formed underneath the HVOF coating which are also completely delaminated. These thin oxide layers are composed of iron and nickel oxides and are richer in nickel indicating that the Ni/Fe ratio has not been optimal to favor the solid-state reaction yielding the formation of a nickel ferrite layer. On the not-coated parts of the Ni-rich anode, a multilayered structure composed of a succession of separated thin layers of oxides (5-10  $\mu\text{m}$  thick) is formed and electrolyte has penetrated between the layers of oxides, similar to the thin delaminated layers of oxides on the coated side, as shown in **Fig 4d**. It shows that unlike Cu-rich alloy, Ni-rich alloy is incapable of forming a continuous adherent oxide layer which can prevent infiltration of electrolyte and its spallation. The composition of different layers of the formed oxides have been analyzed by SEM-EDS and the results showed that all layers are richer in nickel oxide and the nickel ferrite phase is formed neither on the coated side nor on the not-coated side of Ni-rich alloy.

The dry oxidation behaviour at 1000 °C of bare Cu-rich and Ni-rich Cu-Ni-Fe alloys as well as coated by  $\text{Co}_x\text{Ni}_{1-x}\text{O}$  has been studied in our previous work [5]. It was shown that when heated in air, in Cu-rich alloy, copper is the first element that is oxidized. In this alloy, the outward diffusion of Cu from the substrate and formation of a  $\text{CuO}_x$  layer at the surface of the alloy, is accompanied by the inward diffusion of oxygen. The Cu-poor layer formed between the  $\text{CuO}_x$  scale and the substrate is then oxidized resulting in the formation of a  $\text{NiO} + \text{Fe}_2\text{O}_3 + \text{CuO}_x$  layer. The formation of these two layers slightly slows down the oxidation of the substrate but the

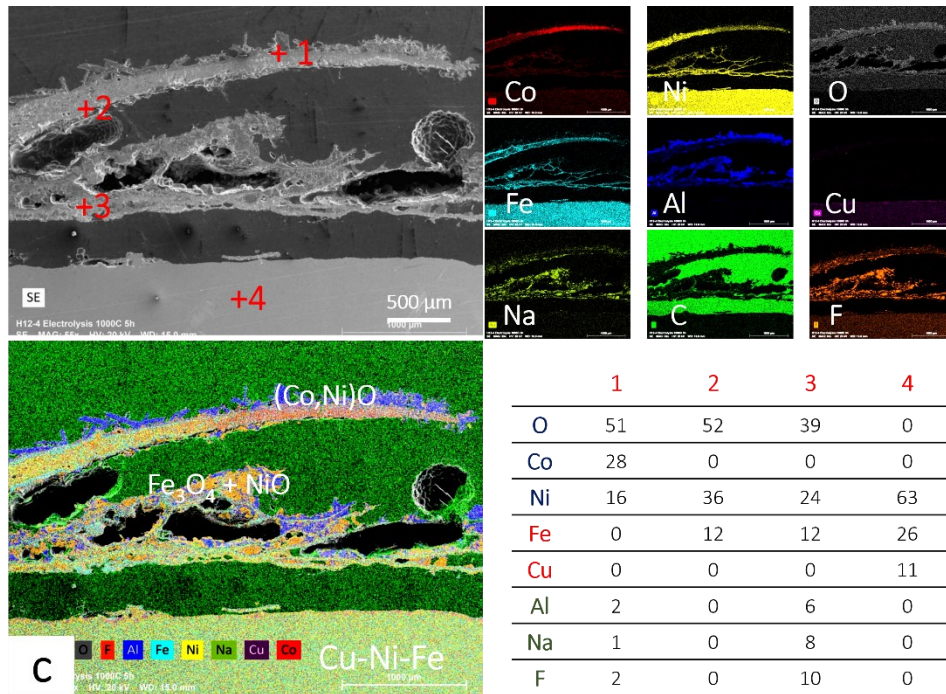
oxidation continues and the scale thickness increases by increasing the heating time. The oxidation of Cu-rich alloy stops (or significantly slows down) only if a continuous layer of nickel ferrite is formed which is not the case during the dry oxidation tests. Even a  $\text{Co}_x\text{Ni}_{1-x}\text{O}$  coating can only slow down the outward diffusion of copper and inward diffusion of oxygen on the Cu-rich substrate but it can not completely block the diffusion processes. When heated in air at 1000 °C, the  $\text{Co}_x\text{Ni}_{1-x}\text{O}$  coating is sandwiched between two layers of copper oxides and a thick layer of  $\text{NiO} + \text{Fe}_2\text{O}_3 + \text{CuO}_x$  is formed between the (Co,Ni)O coating and Cu-rich substrate. In fact, the (Co,Ni)O coating decreases the diffusivity of copper and oxygen, which results in thinner oxide layers whose thicknesses reduce from 1400 to 600  $\mu\text{m}$  between bare and coated Cu-rich substrates. During aluminum electrolysis at 1000 °C, the outward diffusion of copper and inward diffusion oxygen occurs on both bare and coated sides of Cu-rich anode. However, after 5 h electrolysis, only on the coated side, the dissolution of copper oxide in molten cryolite and the protection of (Co,Ni)O coating provide the optimal conditions ( $\text{NiO} + \text{Fe}_2\text{O}_3$  formed with the correct ratio between the (Co,Ni)O coating and Cu-rich substrate) for the formation of a continuous thick layer of  $\text{NiFe}_2\text{O}_4$ .



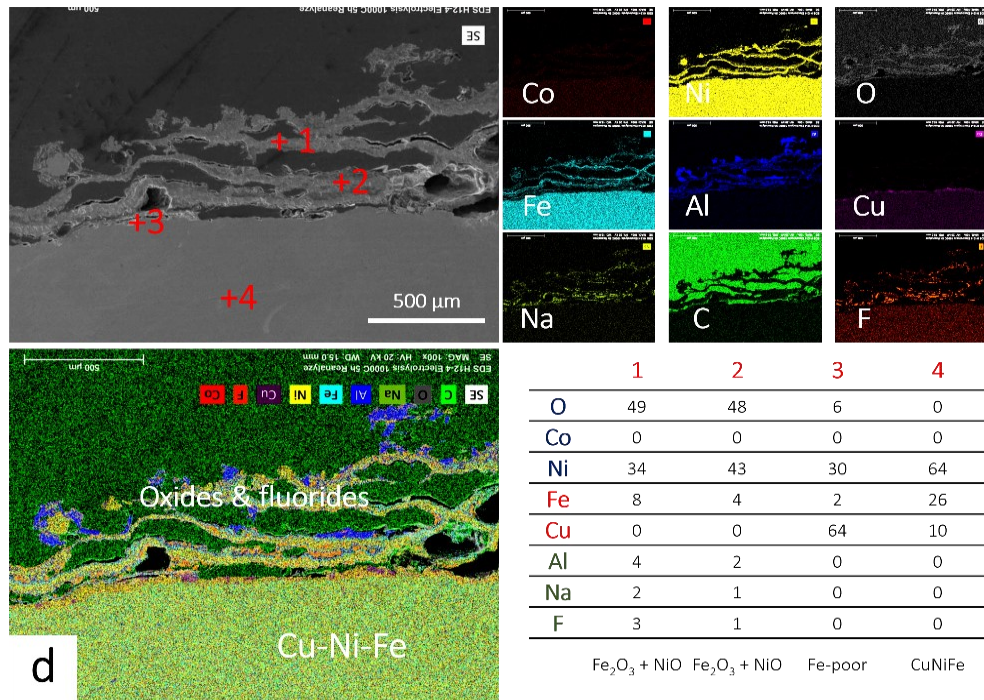
(a)  $\text{Co}_{0.75}\text{Ni}_{0.25}\text{O}$  coated part of the Cu-rich alloy after 5h of electrolysis at 1000 °C



(b) Uncoated part of the Cu-rich alloy after 5h of electrolysis at 1000 °C.



(c)  $\text{Co}_{0.75}\text{Ni}_{0.25}\text{O}$  coated part of the Ni-rich alloy after 5 h of electrolysis at 1000 °C.



(d) Uncoated part of the Ni-rich alloy after 5h of electrolysis at 1000 °C.

Figure 4. Cross-sectional SEM images and EDS analysis results of Cu-20Ni-15Fe anodes (a) and Ni-25Fe-10Cu (b) coated with (Co,Ni)O after aluminum electrolysis at 1000 °C for 5h. The source of carbon is the resin used for the sample preparation. SEM-EDS analyses presented in (b & d) are taken from the not-coated parts of the anodes.

The dry oxidation behaviour of Ni-rich alloy in air at 1000 °C is totally different from that of the Cu-rich alloy. In Ni-rich alloy, diffusion and mobility of Cu is much lower than in Cu-rich alloy, hence,  $\text{CuO}_x$  layer does not form at the surface of Ni-rich alloy. Instead, oxidation of nickel and iron will result in the formation of a  $\sim 35 \mu\text{m}$  thick nickel ferrite layer which significantly decreases the oxidation rate of Ni-rich substrate. In this alloy, iron is the first element that oxidizes, and spherical iron oxide particles are formed and dispersed in metallic matrix of Ni and Cu (rich in Ni). The formation of iron oxide followed by the formation of nickel oxide are the primary stages for the formation of the nickel ferrite phase that formed once the ratio between iron, nickel and oxygen atoms has the right value. A  $\text{Co}_x\text{Ni}_{1-x}\text{O}$  coating slightly decreases the oxygen diffusion into the Ni-rich substrate, when heated in air at 1000 °C, resulting in the formation of a slightly thinner nickel ferrite layer beneath (Co,Ni)O coating ( $\sim 28 \mu\text{m}$ ). Also, iron (about 4 at%) and nickel (6-10 at%) were both diffused and dispersed in the (Co,Ni)O layer during the dry oxidation

tests. However, during the aluminum electrolysis, the nickel ferrite phase was never formed on either coated or uncoated sides of the Ni-rich substrate. This is probably due to the continuous dissolution of thin iron and nickel oxides layers in the molten electrolyte and that optimal NiO/Fe<sub>2</sub>O<sub>3</sub> ratio for the formation of NiFe<sub>2</sub>O<sub>4</sub> is never occurred. As mentioned earlier, the fluctuations in the cell potential observed when using Ni-rich alloy as an anode might be due to the continuous formation and dissolution of these iron and nickel oxides phases.

## Conclusion

The global (Ni + Co) contamination of molten NaF-based electrolytes from Co<sub>x</sub>Ni<sub>1-x</sub>O solid solutions is very low. At 1000 °C in NaF-based electrolyte, less than 80 ppm of (Co + Ni) was detected after solubility measurements. Despite a great mechanical stability at 700 and 850 °C, it is not feasible to use Cu-Ni-Fe alloy coated with Co<sub>0.5</sub>Ni<sub>0.5</sub>O or Co<sub>0.75</sub>Ni<sub>0.25</sub>O as an anode in low-temperature aluminum electrolysis. The decomposition of Co<sub>x</sub>Ni<sub>1-x</sub>O to Co<sub>3</sub>O<sub>4</sub> will result in a rapid increase in the cell potential due to the lower electrical conductivity of Co<sub>3</sub>O<sub>4</sub>. At 1000 °C, the cell potential is relatively stable since decomposition of Co<sub>x</sub>Ni<sub>1-x</sub>O to Co<sub>3</sub>O<sub>4</sub> will not occur at 1000 °C. It was shown that coating Cu-20Ni-15Fe alloy with a (Co,Ni)O layer leads to a significant increase in the corrosion resistance of the alloy and a coherent NiFe<sub>2</sub>O<sub>4</sub> layer was formed on the coated parts of the alloy beneath the (Co,Ni)O layer. On the bare Cu-20Ni-15Fe alloy a relatively thick layer of nonhomogeneous NiO + Fe<sub>2</sub>O<sub>3</sub> + CuO<sub>x</sub> was formed. There was no sign of the formation of nickel ferrite layer on the not-coated parts of the alloy after 5 hours electrolysis in sodium-based electrolyte. This points to the critical role of HVOF (Co,Ni)O coating layer in the formation of nickel ferrite layer as well as prevention of Cu-Ni-Fe alloy from fluorination. However, the thickness of (Co,Ni)O layer after 5 hours of electrolysis is not uniform which shows its partial delamination or dissolution. It was also shown that the composition of the Cu-Ni-Fe alloy plays a key role on the NiFe<sub>2</sub>O<sub>4</sub> formation since this latter was not observed on the (Co,Ni)O coated side nor on the not-coated side of the Ni-rich Ni-25Fe-10Cu alloy.

## References

- [1] D.H. DeYoung, Solubilities of oxides for inert anodes in cryolite-based melts, *Light Met. R.E. Mille* (1896) 1073.
- [2] T.E. Jentoftsen, O.-A. Lorentsen, E.W. Dewing, G.M. Haarberg, J. Thonstad, Solubility of some transition metal oxides in cryolite-alumina melts: Part I. Solubility of FeO, FeAl<sub>2</sub>O<sub>4</sub>, NiO, and NiAl<sub>2</sub>O<sub>4</sub>, *Metall. Mater. Trans. B.* 33 (2002) 901–908. doi:10.1007/s11663-002-0073-7.
- [3] A.D. McLeod, J.-M. Lihmann, J.S. Haggerty, D.R. Sadoway, Selection and Testing of inert anode materials for Hall cells, 1987.
- [4] S. Mohammadkhani, V. Jalilvand, B. Davis, F. Ben Ettouil, A. Dolatabadi, L. Roué, C. Moreau, D. Guay, Suspension plasma spray deposition of Co<sub>x</sub>Ni<sub>1-x</sub>O coatings, *Surf. Coatings Technol.* 399 (2020) 126168. doi:10.1016/j.surfcoat.2020.126168.
- [5] S. Mohammadkhani, V. Jalilvand, B. Davis, G.H. Gauthier, A. Dolatabadi, C. Moreau, L. Roué, D. Guay, High-temperature behaviour of HVOF (Co,Ni)O coated Cu-Ni-Fe anodes, *Corros. Sci.* 189 (2021) 109563. doi:10.1016/j.corsci.2021.109563.
- [6] S. Mohammadkhani, E. Schaal, A. Dolatabadi, C. Moreau, B. Davis, D. Guay, L. Roué, Synthesis and thermal stability of (Co,Ni)O solid solutions, *J. Am. Ceram. Soc.* 102 (2019) 5063–5070. doi:10.1111/jace.16397.
- [7] S. Jucken, B. Tougas, B. Davis, D. Guay, L. Roué, Study of Cu-Ni-Fe Alloys as Inert Anodes for Al Production in Low-Temperature KF-AlF<sub>3</sub> Electrolyte, *Metall. Mater. Trans. B.* 50 (2019) 3103–3111. doi:10.1007/s11663-019-01695-w.
- [8] S. Jucken, E. Schaal, B. Tougas, B. Davis, D. Guay, L. Roué, Impact of a post-casting homogenization treatment on the high-temperature oxidation resistance of a Cu-Ni-Fe alloy, *Corros. Sci.* 147 (2019) 321–329. doi:10.1016/j.corsci.2018.11.037.

## General conclusions and perspectives

The main objective of this thesis was to design a surface treatment for Cu-Ni-Fe anodes to slow down the attack of the electrolyte and allow the formation of the  $\text{NiFe}_2\text{O}_4$  protective layer to occur. This protective layer should therefore have low porosity, good adhesion, good electrical conductivity, low solubility in the electrolyte, low affinity for fluorides and low overvoltage for the  $\text{O}_2$  release reaction. The material that seems most appropriate is  $(\text{Co,Ni})\text{O}$ . Thus, in a first step, powders of  $\text{Co}_x\text{Ni}_{1-x}\text{O}$  were prepared by mechanosynthesis or heat treatment. The microstructure, morphology and thermal stability as well as solubility in cryolitic media of the  $(\text{Co,Ni})\text{O}$  powders were studied depending of their Ni/Co ratio. The results revealed that  $(\text{Co,Ni})\text{O}$  solid solutions produced by prolonged mechanical milling (20 hours) are contaminated by WC due to the erosion of ball milling media. WC contamination is undesirable as it reacts with Co to form  $\text{CoWO}_4$  at high temperature. Thus, in the second method, a high temperature heat treatment (12 hours at 1200 °C) was used to form  $(\text{Co,Ni})\text{O}$  solid solutions. With this method, pure  $\text{Co}_x\text{Ni}_{1-x}\text{O}$  solid solutions were produced over the whole composition range using  $\text{Co}_3\text{O}_4 + \text{NiO}$  as initial powders. Regarding thermal stability of  $(\text{Co,Ni})\text{O}$  solid solutions, at 1000 °C,  $\text{Co}_x\text{Ni}_{1-x}\text{O}$  solid solutions are stable over the whole composition range. In contrast, at 700 and 800 °C in air,  $\text{Co}_x\text{Ni}_{1-x}\text{O}$  is only stable for  $x \leq 0.78$  and  $x \leq 0.54$ , respectively. Further analysis showed that the thermal stability of  $(\text{Co,Ni})\text{O}$  materials also depends on the oxygen partial pressure.

Selected  $(\text{Co,Ni})\text{O}$  compositions were then deposited on Cu-Ni-Fe alloys by High Velocity Oxygen Fuel (HVOF) and Suspension Plasma Spray (SPS) methods. The thermal spray parameters were optimized to obtain thick, dense and single phase coatings.  $\text{Co}_x\text{Ni}_{1-x}\text{O}$  coatings were deposited by SPS using  $\text{Co}_x\text{Ni}_{1-x}\text{O}$  powders or mixtures of CoO and NiO powders as starting materials. In SPS, the effects of spraying variables - including input power, standoff distance, and substrate temperature - on coating composition were studied. Substrate temperature is identified as the most critical parameter affecting coating composition. Undesired reduction of NiO to metallic Ni was observed in some of the coatings prepared by SPS. Uniform, adherent and non-porous  $\text{Co}_x\text{Ni}_{1-x}\text{O}$  coatings made of a single solid solution phase were obtained when the substrate temperature was above 950 °C. Since deposition of a dense, smooth and single phase  $(\text{Co,Ni})\text{O}$  coating was challenging with SPS,  $(\text{Co,Ni})\text{O}$  coatings were prepared by HVOF method. In HVOF, powder particles are sprayed with a much higher velocity and a lower temperature. In HVOF, the

residence time of the powder in the flame is shorter and the flame temperature is lower than in other thermal spray methods, which further reduces the possibility that the powder is reduced, oxidized or decomposed, or that undesired phase transformation occurs during spraying. So, (Co,Ni)O coatings were deposited by HVOF on both Cu-rich and Ni-rich Cu-Ni-Fe alloy substrates using CoO, Co<sub>0.75</sub>Ni<sub>0.25</sub>O and Co<sub>0.5</sub>Ni<sub>0.5</sub>O powders as starting materials. Using optimized deposition conditions, all coatings were single phase and have a smooth morphology. The oxidation behaviour of these samples was investigated at 1000 °C in the presence of oxygen to assess the effect of the coatings on the diffusion of Cu and O atoms. Comparison with their high temperature behaviour in inert atmosphere was also performed. After 20 h of heat treatment in air, HVOF coatings on Cu-rich substrates are sandwiched between a top CuO and a bottom Cu<sub>2</sub>O layer. However, increasing the nickel content of the (Co,Ni)O coating from 0 to 0.5 decreases the Cu and O diffusivity, which results in thinner CuO, Cu<sub>2</sub>O and bottom oxide scales. In the case of Ni-rich Cu-Ni-Fe alloy, Cu diffusion to react with O and form CuO and Cu<sub>2</sub>O is less on an issue because the diffusion of Cu atoms in Ni-rich Cu-Ni-Fe alloys is considerably slowed down. In that case, a nickel ferrite scale is formed between the HVOF coating and the substrate. As expected, the thickness of the NiFe<sub>2</sub>O<sub>4</sub> layer decreases slightly (~ 15%) as the Ni content of the (Co,Ni)O coating is increased from 0 to 0.5.

In the last step, the dissolution rates of Co and Ni from Co<sub>x</sub>Ni<sub>1-x</sub>O (with x = 1, 0.75, 0.5, 0.25 and 0) were measured in two types of cryolites at 700 and 1000 °C. The results revealed that both (Co,Ni)O materials have very low solubility in molten cryolites. The solubility of cobalt from Co<sub>x</sub>Ni<sub>1-x</sub>O solid solutions is less than 2.2 and 65 ppm at 700 and 1000 °C, respectively. The dissolution of nickel from different compositions of Co<sub>x</sub>Ni<sub>1-x</sub>O is less than 8 and 23 ppm at 700 and 1000 °C, respectively. Also, selected (Co,Ni)O coated Cu-Ni-Fe materials were evaluated as inert anodes for Al electrolysis. For electrolysis at 700 and 850 °C, Cu-20Ni-15Fe alloys coated with Co<sub>0.5</sub>Ni<sub>0.5</sub>O were used as anodes. Despite a great mechanical stability at 700 and 850 °C, it is not feasible to use Cu-Ni-Fe alloy coated with Co<sub>0.5</sub>Ni<sub>0.5</sub>O or Co<sub>0.75</sub>Ni<sub>0.25</sub>O as anodes for aluminum electrolysis. The decomposition of Co<sub>x</sub>Ni<sub>1-x</sub>O to Co<sub>3</sub>O<sub>4</sub> will result in a rapid increase in the cell potential due to the lower electrical conductivity of Co<sub>3</sub>O<sub>4</sub>. At 1000 °C, Cu-Ni-Fe alloys coated with Co<sub>0.75</sub>Ni<sub>0.25</sub>O were used as anodes for aluminum electrolysis. The cell potential during electrolysis at 1000 °C is relatively stable since decomposition of Co<sub>x</sub>Ni<sub>1-x</sub>O to Co<sub>3</sub>O<sub>4</sub> will not occur at 1000 °C. It was shown that coating Cu-20Ni-15Fe alloy with a Co<sub>0.75</sub>Ni<sub>0.25</sub>O layer leads

to a significant increase in the corrosion resistance of the alloy and a coherent  $\text{NiFe}_2\text{O}_4$  layer was formed on the coated parts of the alloy beneath the  $(\text{Co,Ni})\text{O}$  layer. On the bare Cu-20Ni-15Fe alloy a relatively thick layer of nonhomogeneous  $\text{NiO} + \text{Fe}_2\text{O}_3 + \text{CuO}_x$  was formed. There was no sign of formation of nickel ferrite layer on the not-coated parts of the alloy after 5 hours electrolysis in sodium-based electrolyte. This points to the critical role of HVOF  $(\text{Co,Ni})\text{O}$  coating layer in the formation of nickel ferrite layer as well as prevention of Cu-Ni-Fe alloy from fluorination. However, the thickness of  $(\text{Co,Ni})\text{O}$  layer after 5 hours of electrolysis is not uniform which shows it partial delamination or dissolution. The composition of the Cu-Ni-Fe alloy also plays a key role on the  $\text{NiFe}_2\text{O}_4$  formation since the latter was not observed on the  $(\text{Co,Ni})\text{O}$  coated side and uncoated side of the Ni-25Fe-10Cu alloy.

## Perspectives

Although the coated anodes studied in this thesis have been tested in short time electrolyses, the obtained results are encouraging. Longer duration (e.g., 100 h) and pilot scale (e.g., 100 A) electrolyses must be carried out to confirm the potential of these anodes for industrial use. Large Cu-Ni-Fe anodes can be coated with a layer of  $(\text{Co,Ni})\text{O}$  using HVOF and then used as anodes under electrolysis conditions closer to the current conditions of industrial primary aluminum production. Another approach to improve the corrosion resistance of the anodes, and in particular to reduce the contamination of electrolyte, would be to deposit a layer of nickel ferrite using thermal spray techniques. Cu-Ni-Fe anodes can be coated with a single layer of nickel ferrite or a double layer coating composed of nickel ferrite and  $(\text{Co,Ni})\text{O}$  and the anodic behaviour of coated anodes must be examined to confirm the effectiveness of this approach for application in industrial aluminum production.

To further increase the oxidation resistance of Cu-Ni-Fe alloy, it is possible to coat it with a Ni-Cr bond-coat layer and a  $(\text{Co,Ni})\text{O}$  top-coat layer using HVOF process. The high resistance of nickel–chromium alloys to high-temperature oxidation and corrosion makes them widely used as thermally sprayed coatings in fossil fuel-fired, boilers, waste incineration boilers, electric furnaces, etc. When heated, a thin layer of  $\text{Cr}_2\text{O}_3$  will form at the surface of the coating which blocks the diffusion of oxygen into the underlying alloy and prevents the sample from further oxidation. As shown in our previous work, a continuous inward diffusion of oxygen and outward

diffusion of copper occurs when Cu-20Ni-15Fe alloy is heated in air at 1000 °C. HVOF sprayed  $\text{Co}_x\text{Ni}_{1-x}\text{O}$  coatings could slow down the inward diffusion of oxygen and outward diffusion of copper but they are not able to completely block the diffusion and oxidation processes. Therefore, coating Cu-20Ni-15Fe alloy with a Ni-Cr bond-coat layer and a (Co,Ni)O top-coat layer could protect the Cu-Ni-Fe alloy from oxidation as well as from the fluorination during aluminum electrolysis. Primary results of our work on [Cu-Ni-Fe substrate + Ni-Cr bond-coat +  $\text{Co}_{0.5}\text{Ni}_{0.5}\text{O}$  top-coat] samples prepared by HVOF revealed the efficiency of these coatings in protecting the underlying alloy from oxidation. The samples were heat treated for 20 hours in air at 1000 °C and the Ni-Cr layer could successfully prevent the oxygen inward diffusion and the copper outward diffusion. Also, no cracks or porosities were formed and both Ni-Cr bond-coat and (Co,Ni)O top-coat layers were well-attached to the Cu-Ni-Fe substrate after the heat treatment. The anodic behaviour of these coated samples will be investigated in severe aluminum electrolysis conditions in the near future.

**Étude d'anodes Cu-Ni-Fe revêtues de (Co,Ni)O  
pour l'électrolyse de l'aluminium**

## Introduction

L'aluminium est le deuxième métal le plus utilisé dans le monde. Cependant, la production d'aluminium primaire par électrolyse est toujours réalisée selon le procédé Hall-Héroult qui engendre de fortes émissions de CO<sub>2</sub>. La substitution des anodes de carbone consommables émettant du CO<sub>2</sub> par des anodes inertes émettant de l'O<sub>2</sub> pour la production primaire d'aluminium réduirait considérablement les émissions de dioxyde de carbone et de perfluorocarbures de cette industrie. Cette substitution éliminerait environ 6 Mt d'équivalent CO<sub>2</sub> produites annuellement par les alumineries canadiennes, ce qui équivaut à la quantité de CO<sub>2</sub> produite annuellement par environ 2 millions de voitures. Cependant, la conception d'anodes inertes est un défi majeur en raison des conditions sévères d'électrolyse de l'aluminium qui nécessitent des matériaux présentant une excellente résistance à la corrosion et aux chocs thermiques, ainsi que des propriétés électrochimiques adéquates. Parmi les nombreux matériaux étudiés jusqu'à présent, les alliages à base de Cu-Ni-Fe semblent prometteurs, en raison de leur capacité à produire une ferrite de nickel protectrice (NiFe<sub>2</sub>O<sub>4</sub>) dans de la cryolithe à base de potassium à basse température (700 °C). Cependant, cette couche protectrice a besoin de temps pour se former à la surface des alliages Cu-Ni-Fe, au cours de laquelle une fluoration peut se produire, provoquant une dégradation prématurée de l'électrode.

Dans ce contexte, l'utilisation de revêtements protecteurs à base de (Co,Ni)O pour anode métallique apparaît prometteuse. En fait, CoO peut fonctionner comme une barrière pour la fluoration des alliages Ni-Fe et la transformation de CoO en CoF<sub>2</sub> ne se produit qu'à très basse pression d'oxygène en milieu cryolite. De plus, en ajoutant des atomes de Ni à CoO pour former des solutions solides (Co,Ni)O aide à prévenir la décomposition indésirable de CoO en Co<sub>3</sub>O<sub>4</sub> à des températures élevées. La production d'alliages Cu-Ni-Fe avec un revêtement protecteur monophasique, dense et sans fissures à base de (Co,Ni)O est difficile en utilisant des méthodes conventionnelles telles que l'électrodéposition d'alliage métallique Co-Ni suivie d'une étape d'oxydation. En effet, des fissures se forment dans le revêtement en raison du changement de densité lors de l'oxydation de l'alliage métallique Co-Ni. Cependant, dans les techniques de projection thermique (oxy-combustible à grande vitesse (HVOF) et projection plasma en suspension (SPS)), des revêtements épais peuvent être obtenus en une seule étape avec un rendement relativement élevé.

## Les objectifs de la thèse:

Les objectifs de cette thèse sont les suivants:

- Optimiser les conditions de synthèse pour produire des solutions solides  $\text{Co}_x\text{Ni}_{1-x}\text{O}$  monophasées avec un procédé évolutif, économique et rapide.
- Étudier la stabilité thermique et le taux de dissolution dans la cryolite fondue de matériaux (Co, Ni)O à des températures élevées.
- Optimiser les paramètres de projection SPS et HVOF afin d'obtenir des revêtements (Co,Ni)O denses, uniformes et monophasiques sur les anodes Cu-Ni-Fe.
- Étudier le comportement en oxydation sèche à haute température d'alliages Cu-Ni-Fe revêtus de solutions solides  $\text{Co}_x\text{Ni}_{1-x}\text{O}$ .
- Étudier le comportement anodique des alliages Cu-Ni-Fe revêtus en conditions d'électrolyse de l'aluminium et caractériser les couches d'oxyde formées à la surface des anodes pour évaluer l'impact du revêtement sur la résistance à la corrosion de l'alliage.

Cette thèse se compose de trois chapitres:

**Le premier chapitre** est une revue bibliographique du procédé actuel de production d'aluminium ainsi que les impacts potentiels et les défis du remplacement des anodes en carbone par des anodes inertes. Ensuite, les systèmes Cu-Ni-Fe et Co-Ni-O sont présentés. Les procédures de synthèse et de revêtement sont aussi introduites.

## Section expérimentale

**Le deuxième chapitre** fournit les détails expérimentaux. Les méthodes de synthèse et de projection des matériaux étudiés ainsi que les différentes techniques de caractérisation utilisées, incluant les tests d'électrolyse de l'aluminium, sont présentées en détails.

## Résultats et discussions

Dans **le troisième chapitre**, trois articles publiés sont présentés. Ces articles résument les principaux résultats obtenus dans le cadre de cette thèse. La séquence des articles suit l'avancement du travail effectué. L'article 1 porte sur la synthèse des solutions solides (Co,Ni)O ainsi que sur

leur stabilité thermique. Deux méthodes de projection thermique utilisées pour revêtir les alliages Cu-Ni-Fe d'une couche de (Co,Ni)O monophasée et dense et le comportement à haute température des échantillons revêtus sont présentés dans les articles 2 et 3. Un résumé de chaque article est présenté suivi des 3 articles publiés. Dans la dernière partie de ce chapitre, des résultats non publiés à ce jour sur la solubilité du (Co,Ni)O dans la cryolite fondue et le comportement anodique des électrodes de Cu-Ni-Fe revêtues de (Co,Ni)O sont présentés.

Les solutions solides de (Co,Ni)O sont considérées comme des matériaux de protection prometteurs des anodes à évolution d'O<sub>2</sub> pour la production d'aluminium. Dans ce contexte, deux méthodes de synthèse à l'état solide, à savoir le broyage mécanique à haute énergie et la calcination, ont été évaluées pour la synthèse de solutions solides de (Co,Ni)O. Avec ces deux procédures, les solutions solides de Co<sub>x</sub>Ni<sub>1-x</sub>O peuvent être formées sur toute la plage de composition. Cependant, un contaminant WC indésirable est observé en utilisant la méthode broyage mécanique à haute énergie en raison de l'érosion des outils de broyage (**Figure R1**). Dans la deuxième méthode, la contamination WC a été éliminée en diminuant le temps de broyage de 20 heures à 12 minutes et en utilisant une étape de traitement thermique à haute température (10 heures à 1000 °C) pour former les solutions solides (Co,Ni)O. Des solutions solides pures de Co<sub>x</sub>Ni<sub>1-x</sub>O ont ainsi été produites sur toute la plage de composition lorsque Co<sub>3</sub>O<sub>4</sub> + NiO ont été utilisés comme matériaux de départ (**Figure R2**).

La stabilité thermique des matériaux (Co,Ni)O a été examinée à haute température sous air. Les résultats illustrés à la **Figure R3** ont révélé qu'à 1000 °C, les solutions solides de Co<sub>x</sub>Ni<sub>1-x</sub>O sont stables sur toute la plage de composition. En revanche, à 700 et 800 °C, Co<sub>x</sub>Ni<sub>1-x</sub>O ne sont stables que pour  $x \leq 0,22$  et  $x \leq 0,46$ , respectivement.

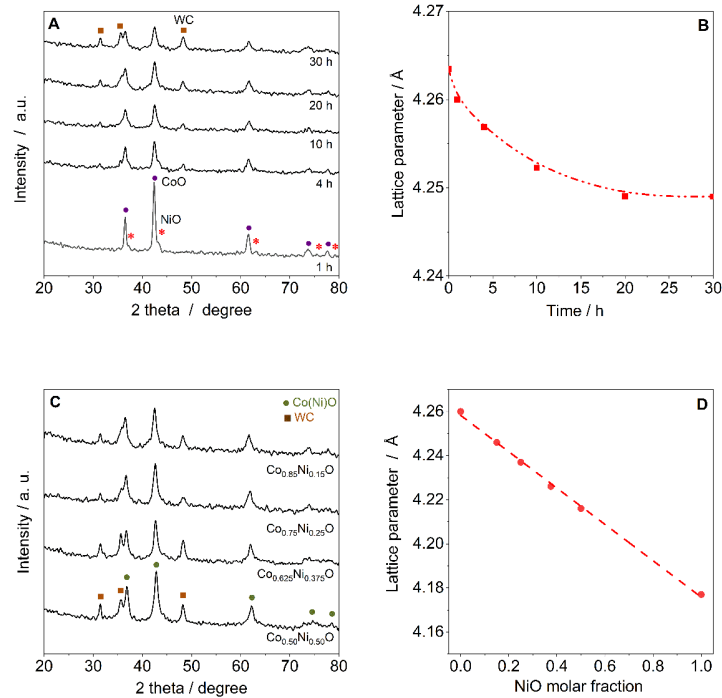


Figure R1. A, diagrammes de diffraction des rayons X (DRX) de 85 % en moles de CoO + 15 % en moles de NiO après différents temps de broyage. B, Variation du paramètre de maille de la phase (Co,Ni)O avec le temps de broyage. C, diagrammes DRX de poudres  $\text{Co}_x\text{Ni}_{1-x}\text{O}$  ( $x = 0,85, 0,75, 0,625$  et  $0,50$ ) après 20 heures de broyage. D, Variation du paramètre de maille des solutions solides de (Co,Ni)O par rapport à la fraction molaire de NiO.

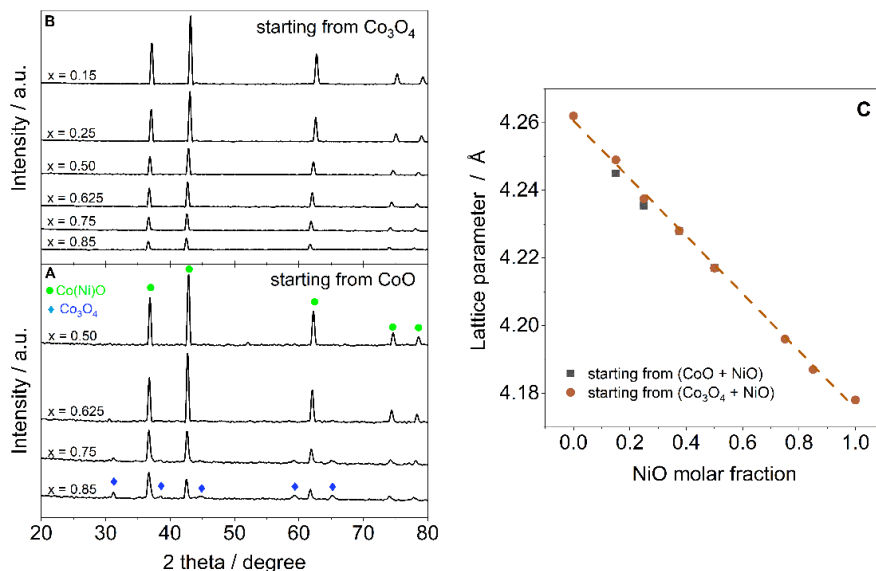


Figure R2. A, Diagrammes de diffraction des rayons X de  $\text{Co}_x\text{Ni}_{1-x}\text{O}$  avec  $x = 0,85, 0,75, 0,625$  et  $0,50$  obtenus après 12 minutes de broyage d'un mélange (CoO + NiO) suivi d'un traitement thermique à  $1000^\circ\text{C}$  pendant 10 heures dans l'air. B, diagrammes DRX de  $\text{Co}_x\text{Ni}_{1-x}\text{O}$  avec  $x = 0,85, 0,75, 0,625, 0,50, 0,25$  et  $0,15$  obtenus après 12 minutes de broyage de  $(\text{Co}_3\text{O}_4 + \text{NiO})$  suivi d'un traitement thermique à  $1000^\circ\text{C}$  pendant 10 heures à l'air. C, Comparaison de la relation entre le paramètre de maille des solutions solides de (Co,Ni)O et la fraction molaire de NiO préparées à partir de (CoO + NiO) et  $(\text{Co}_3\text{O}_4 + \text{NiO})$ .

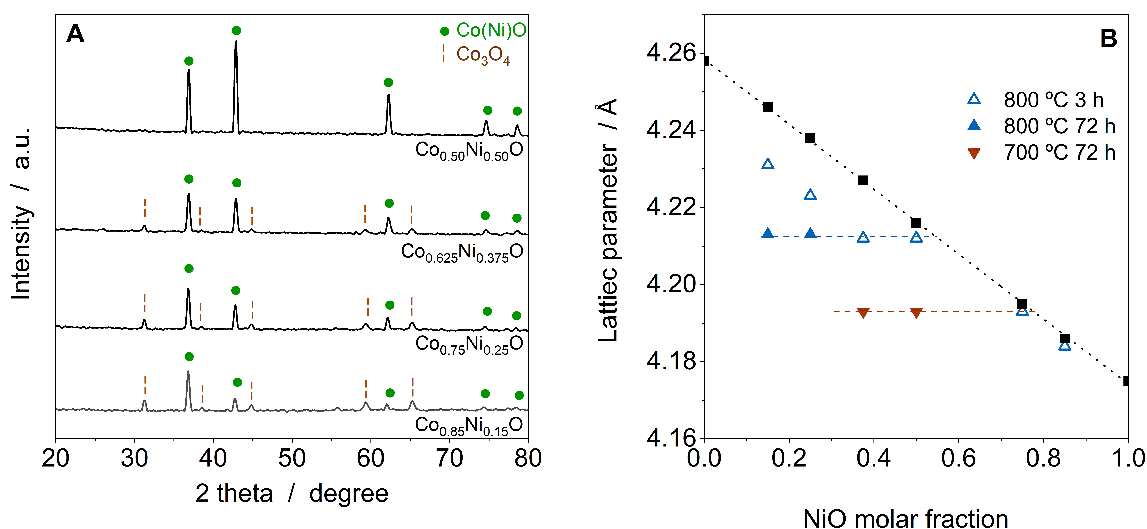


Figure R3. A, Diagrammes de diffraction des rayons X de solutions solides de (Co,Ni)O après traitement thermique à 800 °C pendant 3 heures ; B, Variation du paramètre de maille des solutions solides (Co,Ni)O après traitement thermique à différentes températures et durées. La relation linéaire entre le paramètre de maille des solutions solides  $\text{Co}_x\text{Ni}_{1-x}\text{O}$  et la fraction molaire NiO est également indiquée comme référence (ligne pointillée noire).

Pour augmenter la résistance à la corrosion des alliages Cu-Ni-Fe et éviter leur fluoruration prématurée, il est indispensable de les revêtir d'une couche protectrice (Co,Ni)O. Le CoO est une barrière à la fluoruration et l'ajout d'atomes de nickel au CoO empêchera sa transformation indésirable en un semi-conducteur de type n moins conducteur  $\text{Co}_3\text{O}_4$  pendant l'électrolyse de l'aluminium. Cependant, le revêtement d'alliages Cu-Ni-Fe avec une couche d'oxyde cohésive et sans fissure en utilisant des méthodes conventionnelles telles que l'électrodéposition ou le frittage est très difficile. Une méthode potentiellement pertinente pour produire des anodes inertes revêtues de (Co,Ni)O consiste à déposer directement des composés (Co,Ni)O, ou un mélange de CoO et NiO, via des techniques de dépôt par projection thermique.

Dans un premier temps, le procédé de projection plasma de suspension (SPS) a été évalué pour le dépôt de solutions solides (Co,Ni)O. Une étude approfondie a été menée sur les effets des paramètres de projection (puissance d'entrée, composition du gaz plasma, distance de projection et température du substrat) sur les caractéristiques du revêtement. Un revêtement dense, uniforme et monophasé a été déposé avec succès. Il a été montré (**Figure R4**) que la température du substrat est le paramètre le plus important affectant la nature du revêtement. Des revêtements  $\text{Co}_x\text{Ni}_{1-x}\text{O}$  uniformes, adhérents et non poreux constitués d'une seule phase de solution solide sont obtenus

lorsque la température du substrat est supérieure à 950 °C. La présence de Ni métallique est observée dans les revêtements préparés à des températures plus basses et, dans ce cas, la composition de la phase de solution solide s'écarte de celle attendue. Ce travail traite également des causes possibles de la formation de nickel métallique lors de la pulvérisation

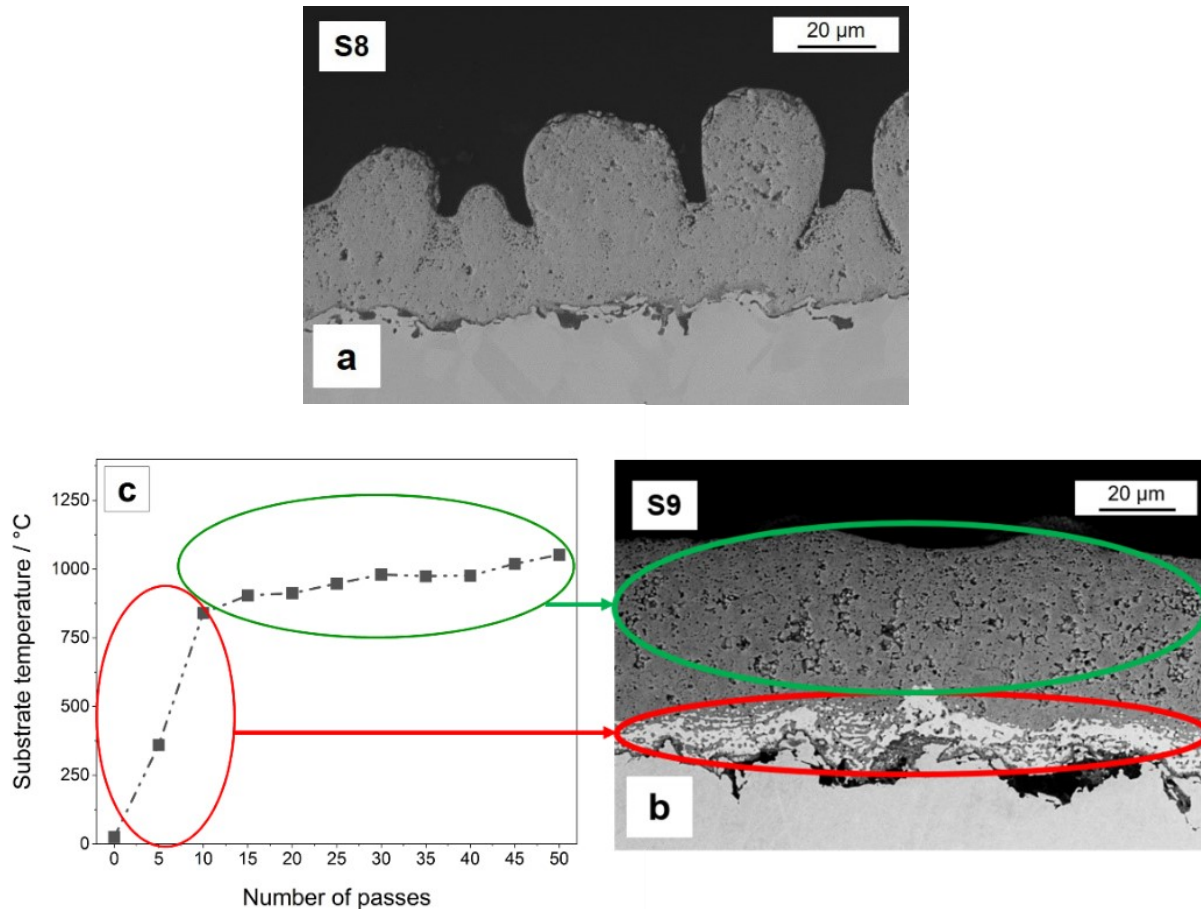
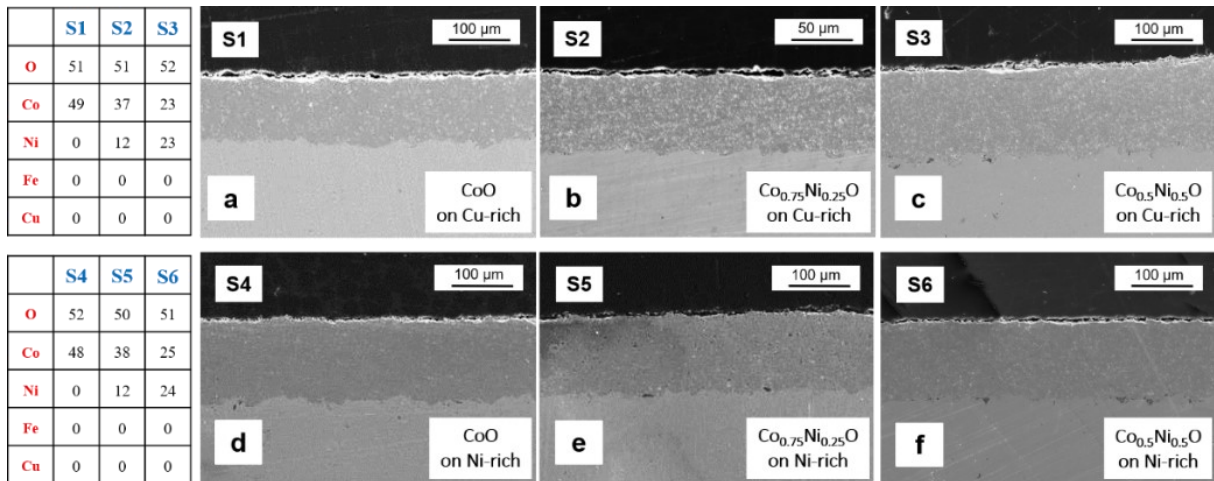


Figure R4. Images MEB en coupe transversale de (a) [50 % mol. CoO + 50 % mol. NiO] et, (b) [75 % mol. CoO + 25% mol. NiO mélanges]. La puissance d'entrée était de 85 kW. La variation de la température du substrat avec le nombre de passages est vue en (c).

Des revêtements  $\text{Co}_x\text{Ni}_{1-x}\text{O}$  adhérents et non poreux ont été obtenus en utilisant la technique SPS, cependant, une réduction de NiO en Ni a été observée au cours du processus SPS conduisant à la formation d'un revêtement à deux phases. Ainsi, à l'étape suivante, des revêtements  $\text{Co}_x\text{Ni}_{1-x}\text{O}$  ( $x = 1, 0,75$  et  $0,5$ ) sont déposés par procédé HVOF (combustible à l'oxygène à grande vitesse) sur des alliages Cu-Ni-Fe. L'influence des compositions du revêtement et du substrat sur leur comportement est étudiée à 1000 °C sous argon et air.

La **Figure R5** présente les micrographies MEB en coupe transversale des revêtements. Tous les revêtements sont uniformes et sans fissures avec une très faible porosité. La surface des revêtements est lisse et leur épaisseur varie entre 110 et 125  $\mu\text{m}$ . La composition de tous les revêtements, telle que déterminée par EDS, est très proche de celle de leurs poudres de départ respectives et sur la base des résultats DRX, tous les revêtements préparés sont monophasiques.



*Figure R5. Images MEB en coupe transversale des revêtements déposés sur substrat riche en Cu (a, b et c) et substrat riche en Ni (d, e et f) : CoO (a et d),  $\text{Co}_{0.75}\text{Ni}_{0.25}\text{O}$  (b et e),  $\text{Co}_{0.5}\text{Ni}_{0.5}\text{O}$  (c et f). L'analyse EDS (at.%) des revêtements tels que pulvérisés est également présentée.*

Après un traitement thermique de 20h à 1000  $^{\circ}\text{C}$  dans l'argon, les atomes de fer et de nickel ont légèrement diffusé du substrat dans la couche de  $\text{Co}_x\text{Ni}_{1-x}\text{O}$  et leur diffusion est réduite quand la teneur en nickel dans la couche de (Co,Ni)O augmente. Après 20 h de traitement thermique sous air, les revêtements HVOF sur des substrats riches en Cu sont pris en sandwich entre une couche supérieure de CuO et une couche inférieure d'oxyde de  $\text{Cu}_2\text{O}$ . Cependant, l'augmentation de la teneur en nickel du revêtement (Co,Ni)O de 0 à 0,5 diminue la diffusivité du Cu et de l'O, ce qui entraîne des écailles de CuO et d'oxyde de fond plus fines. Dans le cas des alliages Cu-Ni-Fe riches en Ni, la diffusion de Cu pour réagir avec O et former CuO et  $\text{Cu}_2\text{O}$  est moins problématique car la diffusion des atomes de Cu dans les alliages Cu-Ni-Fe riches en Ni est considérablement ralentie. Dans ce cas, une couche de ferrite de nickel se forme entre le revêtement HVOF et le substrat. L'épaisseur de la couche  $\text{NiFe}_2\text{O}_4$  diminue légèrement ( $\sim 15\%$ ) lorsque la teneur en Ni du revêtement (Co,Ni)O passe de 0 à 0,5 (**Figure R6**).

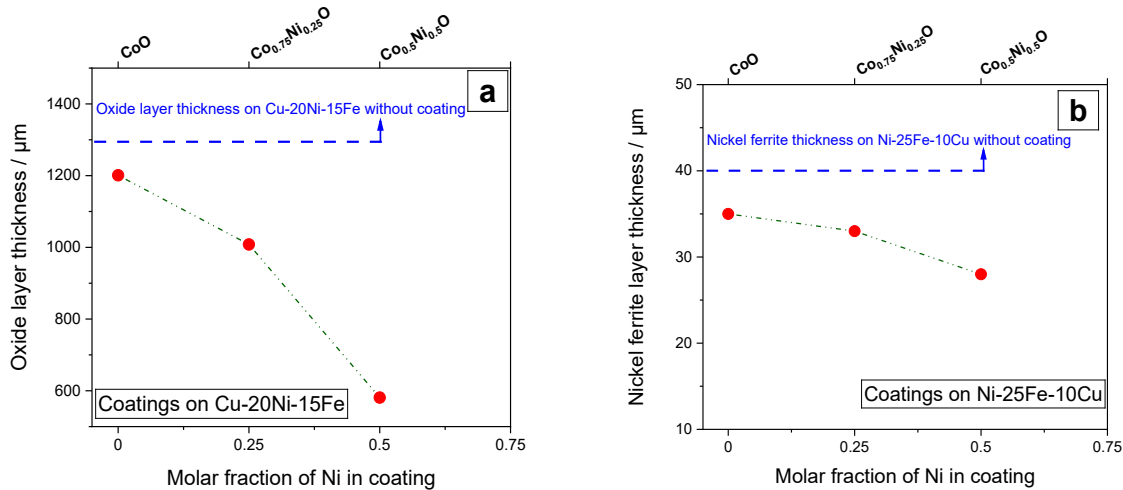
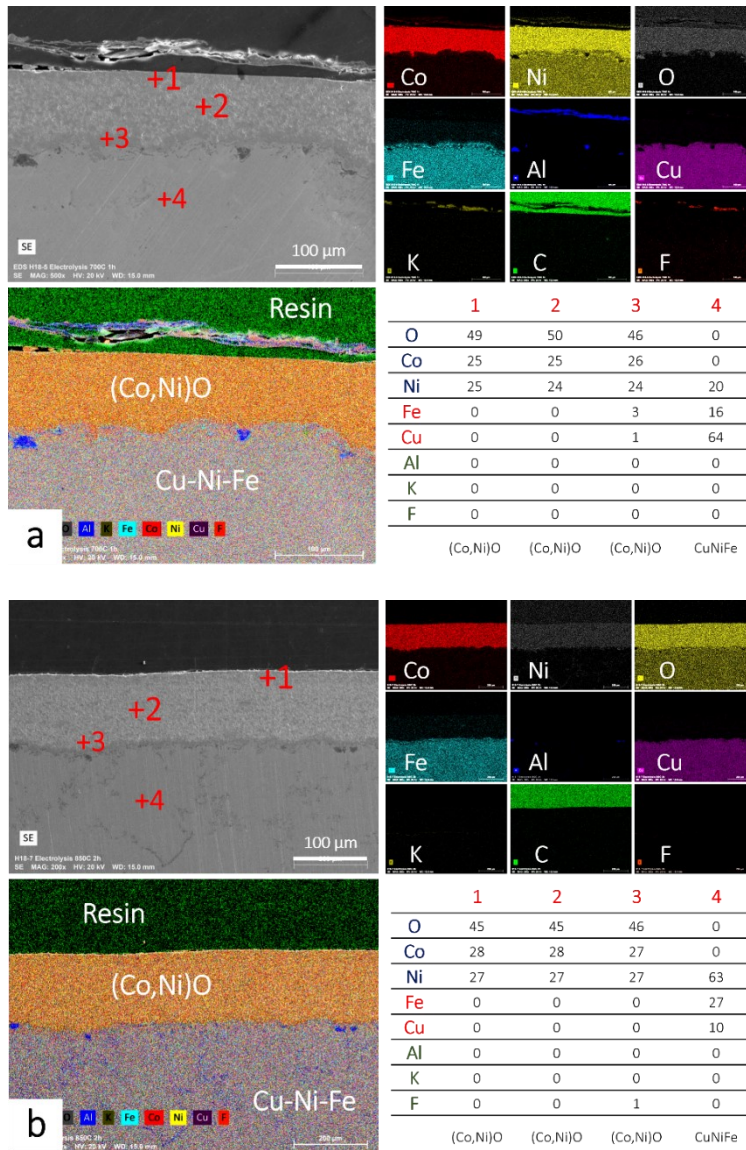


Figure R6. L'épaisseur de la couche d'oxyde sous les revêtements HVOF sur (a) des substrats Cu-20Ni-15Fe et (b) sur des substrats Ni-25Fe-10Cu après le traitement thermique de 20 h à 1000 °C dans l'air.

L'une des caractéristiques les plus importantes des matériaux utilisés comme anodes pour l'électrolyse de l'aluminium est la faible solubilité dans la cryolite fondue. La vitesse de dissolution de NiO en fonction de la composition de la cryolithe et du temps a été étudiée mais à notre connaissance, la solubilité de CoO et (Co,Ni)O dans l'électrolyte fondu n'a jamais été mesurée. Dans cette étude, les taux de dissolution de solutions solides  $\text{Co}_x\text{Ni}_{1-x}\text{O}$  dans des électrolytes à base de sodium et de potassium à 1000 et 700 °C sont étudiés. Dans la dernière étape, l'utilisation d'anodes Cu-Ni-Fe protégées par des revêtements  $\text{Co}_x\text{Ni}_{1-x}\text{O}$  préparés par HVOF pour la production primaire d'aluminium a été étudiée.

Les taux de dissolution du cobalt et du nickel des pastilles de  $\text{Co}_x\text{Ni}_{1-x}\text{O}$  à 700 °C se situent respectivement entre 0,5 et 2,2 ppm et entre 1 et 8 ppm, tandis que les contaminations par le cobalt et le nickel dans l'électrolyte à base de potassium tel que reçu (le blanc) sont de 1,3 et 4,5 ppm, respectivement. De plus, l'augmentation du temps d'immersion de 20 à 60 h ne semble pas avoir d'effet significatif sur la solubilité du cobalt ou du nickel dans la cryolithe KF fondue. Cela signifie qu'il n'y a pas de dissolution significative des matériaux  $\text{Co}_x\text{Ni}_{1-x}\text{O}$  dans l'électrolyte à base de KF à 700 °C. A 1000 °C dans un électrolyte à base de sodium, la solubilité du Co des solutions solides de  $\text{Co}_x\text{Ni}_{1-x}\text{O}$  mesurée après 9 h d'immersion varie de 16 ppm pour  $x = 0,25$  à 65 ppm pour  $x = 1$  tandis que la solubilité du Ni varie de 9 ppm pour  $x = 0,75$  à 23 ppm pour  $x = 0$ . Les contaminations par le cobalt et le nickel dans l'électrolyte à base de sodium tel que reçu (échantillon vierge) sont de 0,4 et 5 ppm, respectivement.

Malgré une grande stabilité mécanique à 700 et 850 °C (**Figure R7**), il n'est pas envisageable d'utiliser l'alliage Cu-Ni-Fe revêtu de  $\text{Co}_{0.5}\text{Ni}_{0.5}\text{O}$  ou  $\text{Co}_{0.75}\text{Ni}_{0.25}\text{O}$  comme anode pour l'électrolyse de l'aluminium à basse température. En effet, la décomposition de  $\text{Co}_x\text{Ni}_{1-x}\text{O}$  en  $\text{Co}_3\text{O}_4$  conduit à une augmentation rapide du potentiel de la cellule en raison de la conductivité électrique inférieure du  $\text{Co}_3\text{O}_4$ .



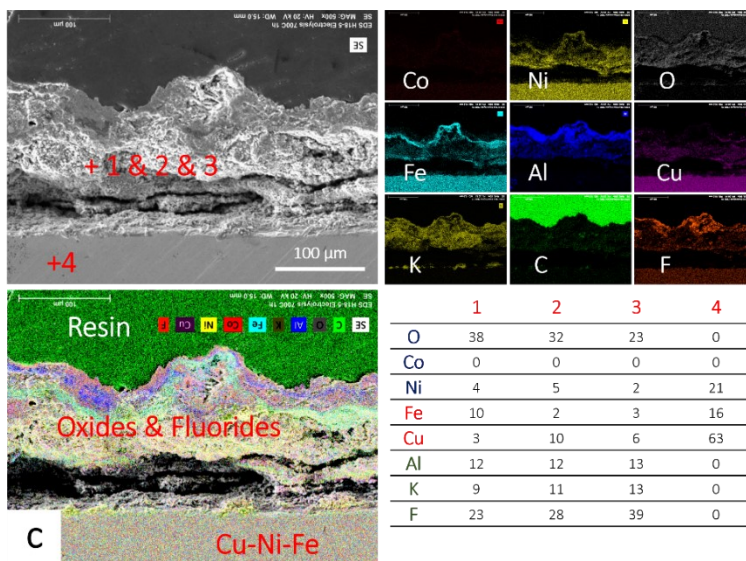
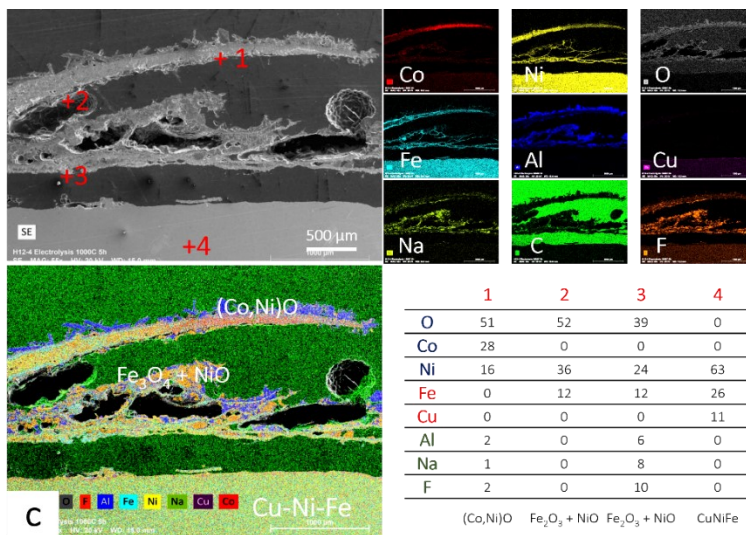
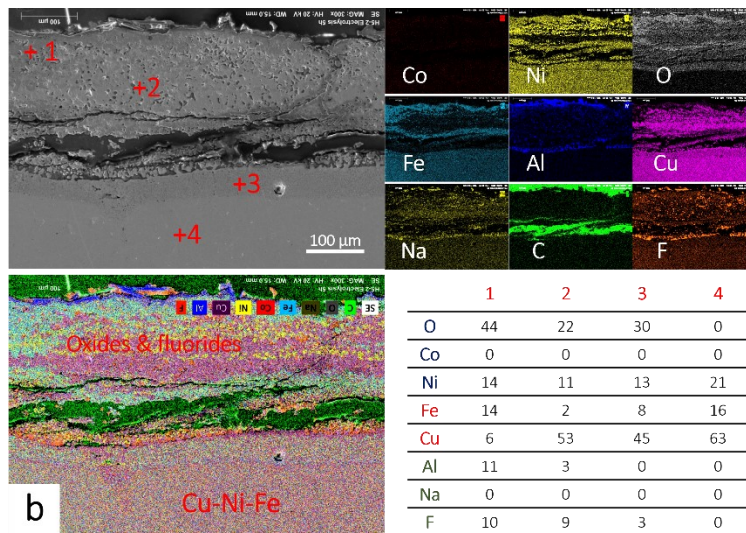
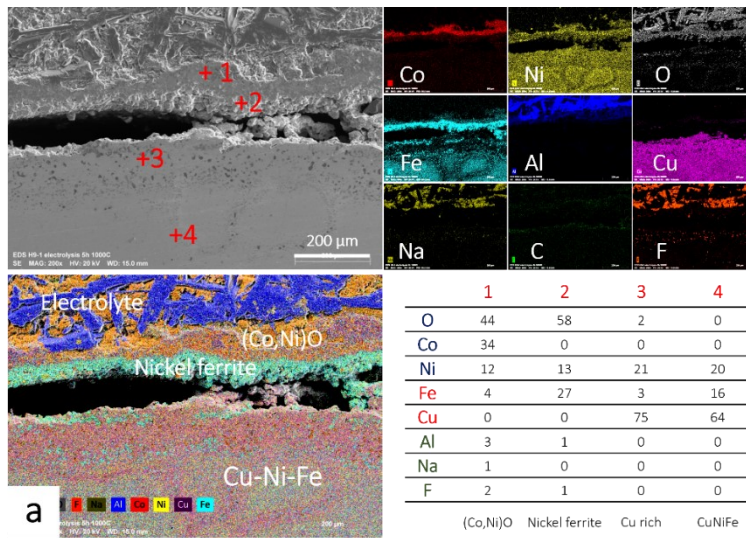


Figure R7. Images MEB en coupe et résultats d'analyse EDS des anodes Cu-20Ni-15Fe revêtues de (Co,Ni)O après électrolyse de l'aluminium à (a & c) 700, (b) 850 °C pendant 1h. La source de carbone est la résine utilisée pour la préparation des échantillons. Les analyses MEB-EDS présentées en (c) sont prélevées sur les parties non revêtues de l'anode après 1 électrolyse à 700°C.

À 1000 °C, le potentiel de la cellule est relativement stable puisque la décomposition de  $\text{Co}_x\text{Ni}_{1-x}\text{O}$  en  $\text{Co}_3\text{O}_4$  ne se produit pas à 1000 °C. Il a été montré que le revêtement de l'alliage Cu-20Ni-15Fe avec une couche de (Co,Ni)O entraîne une augmentation significative de la résistance à la corrosion de l'alliage et qu'une couche cohérente de  $\text{NiFe}_2\text{O}_4$  s'est formée entre l'alliage et le revêtement de (Co ,Ni)O (**Figure R8**). Sur l'alliage Cu-20Ni-15Fe nu, une couche relativement épaisse de  $\text{NiO} + \text{Fe}_2\text{O}_3 + \text{CuO}_x$  non homogène s'est formée. Il n'y a aucun signe de formation d'une couche de ferrite de nickel sur les parties non revêtues de l'alliage après 5 heures d'électrolyse dans un électrolyte à base de sodium. Cela souligne le rôle critique du revêtement HVOF de (Co,Ni)O dans la formation de la couche de ferrite de nickel ainsi que pour la prévention de la fluoration de l'alliage Cu-Ni-Fe. Cependant, l'épaisseur de la couche de (Co,Ni)O après 5 heures d'électrolyse n'est pas uniforme ce qui montre une délamination partielle ou une dissolution. Il a également été montré que la composition de l'alliage Cu-Ni-Fe joue un rôle clé sur la formation de  $\text{NiFe}_2\text{O}_4$  puisque cette dernière n'a pas été observée du côté revêtu de (Co,Ni)O ni du côté non revêtu de l'alliage Ni-25Fe-10Cu (**Figure R8**).



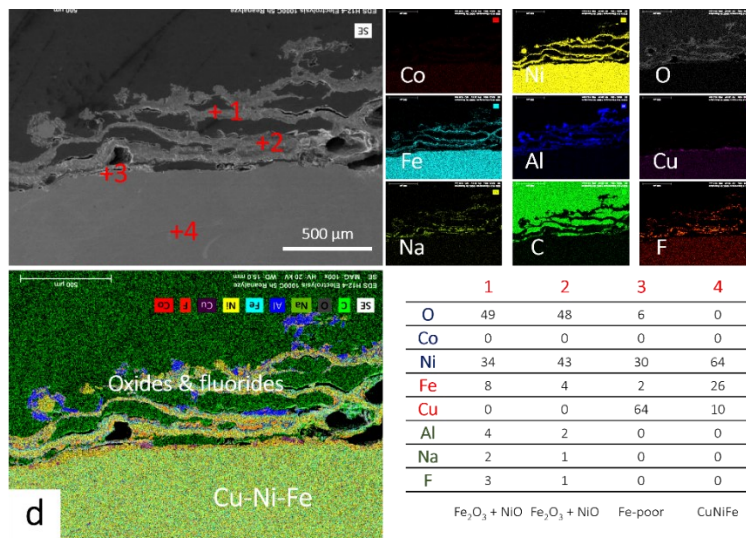


Figure R8. Images MEB en coupe et résultats d'analyse EDS des anodes Cu-20Ni-15Fe (a) et Ni-25Fe-10Cu (b) recouvertes de (Co,Ni)O après électrolyse de l'aluminium à 1000 °C pendant 5h. La source de carbone est la résine utilisée pour la préparation des échantillons. Les analyses MEB-EDS présentées en (b & d) sont issues des parties non revêtues des anodes.

## Conclusions

Cette partie résume brièvement les principaux résultats de ma recherche et présente les défis et perspectives dans ce domaine. En outre, les perspectives de cette recherche pour augmenter encore la résistance à l'oxydation de l'alliage Cu-Ni-Fe sont présentées.

L'objectif principal de cette thèse était de concevoir un traitement de surface des anodes Cu-Ni-Fe pour ralentir l'attaque de l'électrolyte et permettre la formation de la couche protectrice de  $\text{NiFe}_2\text{O}_4$ . Cette couche protectrice doit donc présenter une faible porosité, une bonne adhérence, une bonne conductivité électrique, une faible solubilité dans l'électrolyte, une faible affinité pour les fluorures et une faible surtension pour la réaction de libération d' $\text{O}_2$ . Le matériau qui semble le plus approprié est le (Co,Ni)O. Ainsi, dans une première étape, des poudres de  $\text{Co}_x\text{Ni}_{1-x}\text{O}$  ont été préparées par mécanosynthèse ou traitement thermique. La microstructure, la morphologie et la stabilité thermique ainsi que la solubilité en milieu cryolitique des poudres de (Co,Ni)O ont été étudiées en fonction de leur rapport Ni/Co. Les résultats ont révélé que les solutions solides de (Co,Ni)O produites par broyage mécanique prolongé (20 heures) sont contaminées par le WC en raison de l'érosion des outils de broyage. La contamination par WC est indésirable, car elle réagit

avec le Co pour former du  $\text{CoWO}_4$  à haute température. Ainsi, pour la seconde méthode, un traitement thermique à haute température (12 heures à  $1200\text{ }^\circ\text{C}$ ) a été utilisé pour former des solutions solides de  $(\text{Co,Ni})\text{O}$ . Avec cette méthode, des solutions solides pures de  $\text{Co}_x\text{Ni}_{1-x}\text{O}$  ont été produites sur toute la plage de composition en utilisant  $\text{Co}_3\text{O}_4 + \text{NiO}$  comme précurseurs. Concernant la stabilité thermique des solutions solides  $(\text{Co,Ni})\text{O}$ , à  $1000\text{ }^\circ\text{C}$ , les solutions solides  $\text{Co}_x\text{Ni}_{1-x}\text{O}$  sont stables sur toute la plage de composition. En revanche, à  $700$  et  $800\text{ }^\circ\text{C}$  dans l'air,  $\text{Co}_x\text{Ni}_{1-x}\text{O}$  n'est stable que pour  $x \leq 0,78$  et  $x \leq 0,54$ , respectivement. Une analyse plus poussée a montré que la stabilité thermique des matériaux  $(\text{Co,Ni})\text{O}$  dépend également de la pression partielle d'oxygène.

Des compositions de  $(\text{Co,Ni})\text{O}$  sélectionnées ont ensuite été déposées sur des alliages Cu-Ni-Fe par les méthodes High Velocity Oxygen Fuel (HVOF) et Suspension Plasma Spray (SPS). Les paramètres de projection thermique ont été optimisés pour obtenir des revêtements épais, denses et monophasiques. Les revêtements  $\text{Co}_x\text{Ni}_{1-x}\text{O}$  ont été déposés par SPS en utilisant des poudres  $\text{Co}_x\text{Ni}_{1-x}\text{O}$  ou des mélanges de poudres CoO et NiO comme matières premières. Pour la technique SPS, les effets des variables de pulvérisation sur la composition du revêtement, tels que la puissance d'entrée, la distance de sécurité ou encore la température du substrat  $t$  ont été étudiés. La température du substrat est identifiée comme le paramètre le plus critique affectant la composition du revêtement. Une réduction indésirable de NiO en Ni métallique a été observée dans certains des revêtements préparés par SPS. Des revêtements  $\text{Co}_x\text{Ni}_{1-x}\text{O}$  uniformes, adhérents et non poreux constitués d'une seule phase de solution solide ont été obtenus lorsque la température du substrat était supérieure à  $950\text{ }^\circ\text{C}$ . Étant donné que le dépôt d'un revêtement  $(\text{Co,Ni})\text{O}$  dense, lisse et monophasé était difficile à obtenir avec le SPS, le revêtement  $(\text{Co,Ni})\text{O}$  a été préparé par la méthode HVOF. Pour la technique HVOF, les particules de poudre sont pulvérisées avec une vitesse beaucoup plus élevée et une température plus basse. En HVOF, le temps de séjour de la poudre dans la flamme est plus court et la température de la flamme est plus basse que dans les autres méthodes de projection thermique, ce qui réduit encore la possibilité que la poudre soit réduite, oxydée ou décomposée, ou qu'une transformation de phase indésirable se produise pendant la pulvérisation. Ainsi, des revêtements de  $(\text{Co,Ni})\text{O}$  ont été déposés par HVOF sur des substrats en alliage Cu-Ni-Fe riches en Cu et en Ni en utilisant des poudres de CoO,  $\text{Co}_{0,75}\text{Ni}_{0,25}\text{O}$  et  $\text{Co}_{0,5}\text{Ni}_{0,5}\text{O}$  comme précurseurs. En utilisant des conditions de dépôt optimisées, tous les revêtements étaient monophasés et ont une morphologie lisse. Le comportement à l'oxydation de

ces échantillons a été étudié à 1000 °C en présence d'oxygène pour évaluer l'effet des revêtements sur la diffusion des atomes de Cu et O. Une comparaison avec leur comportement à haute température en atmosphère inerte a également été effectuée. Après 20 h de traitement thermique sous air, les revêtements HVOF sur des substrats riches en Cu sont pris en sandwich entre une couche supérieure de CuO et une couche intérieure de Cu<sub>2</sub>O. Cependant, l'augmentation de la teneur en nickel du revêtement Co<sub>x</sub>Ni<sub>1-x</sub>O de 0 à 0,5 diminue la diffusivité du Cu et de l'O, ce qui entraîne la formation des écailles de CuO, Cu<sub>2</sub>O et d'oxyde de fond plus fines. Dans le cas des alliages Cu-Ni-Fe riches en Ni, la diffusion de Cu pour réagir avec O et former CuO et Cu<sub>2</sub>O est moins problématique, car la diffusion des atomes de Cu dans les alliages Cu-Ni-Fe riches en Ni est considérablement ralentie. Dans ce cas, une calamine en ferrite de nickel se forme entre le revêtement HVOF et le substrat. Comme prévu, l'épaisseur de la couche de NiFe<sub>2</sub>O<sub>4</sub> diminue légèrement (~ 15 %) lorsque la teneur en Ni du revêtement Co<sub>x</sub>Ni<sub>1-x</sub>O passe de 0 à 0,5.

Dans la dernière étape, les vitesses de dissolution du Co et du Ni de Co<sub>x</sub>Ni<sub>1-x</sub>O (avec x = 1, 0,75, 0,5, 0,25 et 0) ont été mesurées dans deux types de cryolites à 700 et 1000 °C. Les résultats ont révélé que les deux matériaux (Co,Ni)O ont une très faible solubilité dans les cryolites fondues. La solubilité du cobalt des solutions solides de Co<sub>x</sub>Ni<sub>1-x</sub>O est inférieure à 2,2 et 65 ppm à 700 et 1000 °C, respectivement. La dissolution du nickel de différentes compositions de Co<sub>x</sub>Ni<sub>1-x</sub>O est inférieure à 8 et 23 ppm à 700 et 1000 °C, respectivement. De plus, des matériaux Cu-Ni-Fe revêtus de (Co,Ni)O ont été évalués en tant qu'anodes inertes pour l'électrolyse de l'aluminium. Pour l'électrolyse à 700 et 850 °C, des alliages Cu-20Ni-15Fe revêtus de Co<sub>0,5</sub>Ni<sub>0,5</sub>O ont été utilisés comme anodes. Malgré une grande stabilité mécanique à 700 et 850 °C, il n'est pas envisageable d'utiliser l'alliage Cu-Ni-Fe revêtu de Co<sub>0,5</sub>Ni<sub>0,5</sub>O ou Co<sub>0,75</sub>Ni<sub>0,25</sub>O comme anodes pour l'électrolyse de l'aluminium. La décomposition de Co<sub>x</sub>Ni<sub>1-x</sub>O en Co<sub>3</sub>O<sub>4</sub> entraînera une augmentation rapide du potentiel de la cellule en raison de la conductivité électrique inférieure du Co<sub>3</sub>O<sub>4</sub>. À 1000 °C, des alliages Cu-Ni-Fe revêtus de Co<sub>0,75</sub>Ni<sub>0,25</sub>O ont été utilisés comme anodes pour l'électrolyse de l'aluminium. Le potentiel de la cellule pendant l'électrolyse à 1000 °C est relativement stable puisque la décomposition de Co<sub>x</sub>Ni<sub>1-x</sub>O en Co<sub>3</sub>O<sub>4</sub> ne se produira pas à 1000 °C. Il a été montré que le revêtement de l'alliage Cu-20Ni-15Fe avec une couche de Co<sub>0,75</sub>Ni<sub>0,25</sub>O conduit à une augmentation significative de la résistance à la corrosion de l'alliage et qu'une couche cohérente de NiFe<sub>2</sub>O<sub>4</sub> s'est formée sur les parties revêtues de l'alliage sous la couche de (Co,Ni)O. Sur l'alliage Cu-20Ni-15Fe nu, une couche relativement épaisse de NiO + Fe<sub>2</sub>O<sub>3</sub> + CuO<sub>x</sub> non

homogène s'est formée. Il n'y avait aucun signe de formation de couche de ferrite de nickel sur les parties non revêtues de l'alliage après 5 heures d'électrolyse dans un électrolyte à base de sodium. Cela souligne le rôle critique de la couche de revêtement HVOF (Co,Ni)O dans la formation de la couche de ferrite de nickel ainsi que la prévention de la fluoration de l'alliage Cu-Ni-Fe. Cependant, l'épaisseur de la couche de (Co,Ni)O après 5 heures d'électrolyse n'est pas uniforme ce qui montre une délamination partielle ou une dissolution. La composition de l'alliage Cu-Ni-Fe joue également un rôle clé sur la formation  $\text{NiFe}_2\text{O}_4$  puisque cette dernière n'a pas été observée du côté (Co,Ni)O revêtu et du côté non revêtu de l'alliage Ni-25Fe-10Cu.